Energy storage systems based on lithium-ion batteries and supercapacitors: characterization, modelling and integration with renewable energies

Ph. D. dissertation prepared to
obtain the Doctor degree by

Alberto Berrueta Irigoyen

Supervisors

Alfredo Ursúa Rubio

Pablo Sanchis Gúrpide

upna
Universidad
Pública de Navarra
Nafarroako
Unibertsitate Publikoa

Department of Electrical and Electronic Engineering

Pamplona, December 2017

Summary

Environmental, social and economic drawbacks of fossil and nuclear fuels are leading to an increased use of renewable energy sources. The strong technological development of renewable-based generation systems during the last years, especially in the case of wind and photovoltaic systems, has led to an impressive reduction of production costs and made these technologies competitive with conventional power plants. At present, the main barrier that limits their massive integration into the electrical grid is their reduced manageability due to the intermittent nature of renewable resources. Distributed energy storage systems, particularly lithium-ion batteries and supercapacitors, arise as one of the best options to provide manageability to these systems and help operate an electrical grid increasingly based and dependent on renewable power plants.

This thesis analyses in depth both energy storage technologies, in particular when they operate in renewable generation systems. The main research lines of the thesis are:

- Analysis of the state of the art of lithium-ion battery and supercapacitor technologies.
- Study of the influence of thermodynamic, electrochemical and thermal phenomena on the operation of these storage technologies.
- Electrochemical and thermal modelling of both technologies.
- Estimation of the state of charge and ageing of lithium-ion batteries.
- Experimental validation of the proposed models under different operating conditions.
- Development of methodologies for the optimal design and operation of storage systems based on lithium-ion batteries in renewable environments, and implementation in photovoltaic power plants.

Resumen

Los inconvenientes medioambientales, sociales y económicos que presentan los combustibles fósiles y nucleares están propiciando un uso cada vez mayor de fuentes de energía renovables. El fuerte desarrollo tecnológico de los sistemas de generación basados en estas fuentes de energía, especialmente de los sistemas eólicos y fotovoltaicos, ha abaratado enormemente sus costes de producción, resultando ya tecnologías competitivas en relación con las plantas convencionales. Actualmente, el principal obstáculo que limita su integración masiva en la red eléctrica es su gestionabilidad, dada la naturaleza intermitente del recurso renovable. Los sistemas de almacenamiento energético distribuidos, y en particular las baterías de litio y los supercondensadores, surgen como una de las mejores alternativas para mejorar la gestión de esta energía y facilitar la operación de una red eléctrica cada vez más basada en sistemas renovables.

Esta tesis analiza en profundidad ambas tecnologías de almacenamiento, especialmente cuando funcionan en entornos de generación renovable. Las principales líneas de trabajo de la tesis son:

- Análisis del estado actual de las tecnologías.
- Estudio de la influencia de los fenómenos termodinámicos, electroquímicos y térmicos en el funcionamiento de estos sistemas de almacenamiento.
- Modelado electroquímico y térmico de ambas tecnologías de almacenamiento.
- Estimación del estado de carga y del envejecimiento en baterías de litio.
- Validación experimental de los modelos propuestos ante diferentes condiciones de funcionamiento.
- Desarrollo de metodologías para el diseño y funcionamiento óptimo de sistemas de almacenamiento basados en baterías de litio en entornos renovables y particularización para centrales fotovoltaicas.

Zusammenfassung

Die ökologischen, sozialen und wirtschaftlichen Nachteile von fossilen und nuklearen Brennstoffen führen zu einer zunehmenden Nutzung erneuerbarer Energiequellen. Die schnelle technische Entwicklung dieser allem voran auf Windkraft sowie Fotovoltaik beruhende Energiegewinnung, brachte eine enorme Senkung der Produktionskosten mit sich, die diese neue Art der Energieförderung mit den herkömmlichen Kraftwerken konkurrenzfähig machte. Das gegenwärtige Haupthindernis, das eine starke Integration in das Stromnetz begrenzt, ist ihre reduzierte Verwaltbarkeit aufgrund der intermittierenden Beschaffenheit nachwachsender Rohstoffe.Distributive Energiespeichersysteme, insbesondere Lithiumbatterien und Superkondensatoren, entwickeln sich zu einer der besten Alternativen, um die Verwaltung dieser Energie zu verbessern und den Betrieb eines Stromnetzes zu erleichtern, das zunehmend auf erneuerbaren Systemen basiert.

Diese Arbeit untersucht eingehend beide Energiespeichertechnologien, insbesondere wenn sie in erneuerbaren Erzeugungsanlagen eingesetzt werden. Die Hauptthemen dieser Arbeit stellen die folgenden Punkte dar:

- Analyse der aktuellen Lage der Technologien.
- Untersuchung des Einflusses thermodynamischer, elektrochemischer und thermischer Phänomene auf den Betrieb dieser Speichersysteme.
- Elektrochemische und thermische Modellierung beider Speichertechnologien.
- Einschätzung des Ladezustands und der Alterung in Lithiumbatterien.
- Experimentelle Validierung der vorgeschlagenen Modelle vor verschiedenen Betriebsbedingungen.
- Entwicklung von Methoden zur optimalen Gestaltung und zum Betrieb von Speichersystemen auf der Basis von Lithiumbatterien in erneuerbaren Umgebungen und Spezialisierung für Photovoltaikanlagen.

Agradecimientos — *Danksagungen*

En los viajes que se emprenden en la vida la felicidad no está en el destino, sino en el camino. A lo largo del viaje que ha supuesto esta tesis ha habido muchas personas que me han acompañado en el camino, a las cuales me gustaría dedicarles unas líneas de agradecimiento:

A mis directores de tesis, Alfredo y Pablo, por la relación de confianza y afecto que hemos mantenido durante la tesis y por su apoyo en los aspectos técnicos, especialmente en los momentos más complicados de la investigación.

A Idoia, por ser quien despertó mi interés hacia los sistemas de almacenamiento y por los valiosos consejos que me ha dado a lo largo de la tesis.

A todos los miembros del grupo Ingeper, entre los que existe un ambiente de compañerismo y amistad sin el cual estos años no habrían sido lo mismo. ¡Que no decaigan los Ingebikes!

A los miembros del grupo ITF, por ceder sus laboratorios y, en particular, a Patricia, por su colaboración en el diseño del modelo térmico de baterías presentado en la sección 4.5 de la tesis.

An die Mitarbeiter des Teams Batterietechnik des Frauenhofer ISE, die mich sowohl mit ihrem technischen Wissen, ihrem Beitrag in Kapitel 6 dieser Arbeit sowie durch die interessanten Diskussionen, die wir führten, tatkräftig unterstützten. Gleichermaßen möchte ich mich für die herzliche Gastfreundschaft während meines gesamten Aufenthalts bedanken.

A los compañeros de la asociación Aperna, por hacer que la Universidad sea mucho más que un lugar de estudio o de trabajo.

A mis amigos, por los buenos momentos que pasamos juntos y que son tan necesarios para afrontar con motivación cada nueva semana.

Y por último, pero no menos importante, a mi familia, especialmente a mis padres. Soy quien soy gracias a ellos, y sin su ejemplo y apoyo esta tesis no habría sido posible.

Muchas gracias, vielen Dank.

Contents

List of Figures

List of Tables

Chapter 1

Introduction

Begin at the beginning – the King said, gravely
– and go on till you come to an end; then stop.

– Lewis Carroll, *Alice in Wonderland*

The evolution and development of a society is linked with the energy consumption [CHA98]. Society complexity, worldwide population and quality of life during human history have been linked to their energy consumption. After the primitive nomadic gatherer societies, whose only energy input was the food found along their wandering, agriculture and farming were developed to provide a safer source of energy for the society. Then, the animal power was used to perform useful work and the forests were felled in search of wood for goods manufacturing and heating.

The energy consumption has skyrocketed since XIX century, when enormous amounts of energy were required in order to expand the Industrial Revolution around the world, as shown in Figure 1.1 (a). This growth brought the global annual energy consumption in 2016 to surpass 45 million TWh. This current scenario is considered by many people as non-sustainable, given that the energy resources that we are using to fuel the world are not replenished at the same rate.

In this context of rising energy demand, a number of technologies aimed at energy use find a favourable scenario for its accelerated installation. Renewable energy generators and, specially, wind and photovoltaic (PV) systems are clear examples. In spite of this fast and encouraging growth of renewable energy systems, the world is currently immersed in the Era of Fossil Fuels, as can be inferred from Figure 1.1 (b). This figure shows the primary origin of the worldwide consumed energy during the last 51 years (1965–2016). Renewable

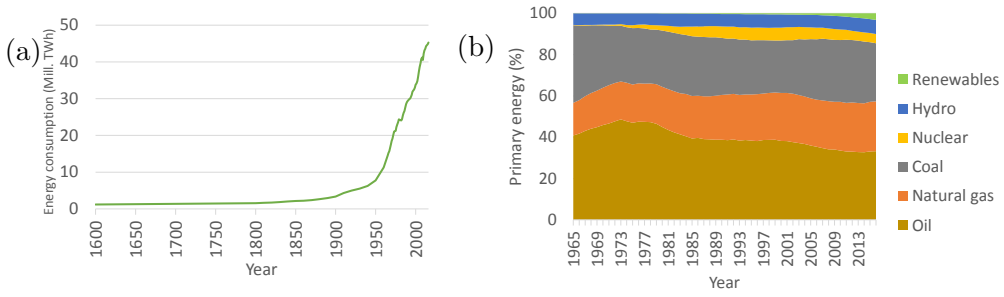

Figure 1.1: Global annual energy consumption: total energy consumed from 1600 to 2016 (data from [SMI16]) (a) and primary origin of the energy from 1965 to 2106 (data from [DUD17]) (b).

energies had a total share during 2016 slightly greater than 3% by the first time since the outburst of the Industrial Revolution. If hydraulic power is also accounted as renewable, the total share in 2016 reaches 10%. Meanwhile, fossil fuels (coal, oil and natural gas) accounted for 85% of the global primary energy.

Fossil fuels entail important problems that are encouraging the development of energy policies aimed at reducing their use. The most serious problem is related with the pollution they generate, which causes both local problems (such as the deterioration of air quality in cities which entails health problems [CAR18, YAN18, MAJ18]) and global problems (greenhouse effect, global heating, extinction of species, etc. [IPC13]). Besides this main, pollution issue, there are other problems related with the uneven location of fossil fuels, that make the world energy-dependent on countries with energy resources. This dependency provokes, on the one hand, self-sufficiency concerns in dependent countries, such as most of European countries, and, on the other hand, huge social inequality in countries with energy resources; combination that too often leads to armed conflicts [LEI14, HUN17].

In this respect, renewable energies arise as a more sustainable resource, much less pollutant, more equal from the social and geographical point of view and virtually ever-lasting. The fast cost reduction accomplished during the last years has eliminated the overrun that this kind of energy used to entail when compared with other energy generation technologies. As a matter of fact, a number of companies have been allowed in Spain to install 4.6 GW of wind power and 3.9 GW of PV power during 2018 and 2019, receiving just the usual remuneration of the electricity market. These companies being willing to invest are a sign of the current profitability of these renewable technologies with no further requirements of fed-in tariffs [PEÑ17]. Therefore, more and

more countries are adding this kind of technologies in their energy generation mix, what is happening both in developed countries such as Germany, USA, Japan and Spain, and developing countries, such as China, India and Mexico [MAS17].

Once this cost barrier has been overcome, the next problem preventing the increasing penetration of renewable energy in the electricity grid is its manageability. Given that renewable energy resource is unpredictable and that renewable plants exhibit a low inertia compared to the traditional power plants based on large synchronous generators, renewable energy units cannot properly contribute to the grid frequency and voltage regulation [STE17a, KÖH17]. Storage systems are presented as a good option to deal with these problems. On the one hand, they can play the role of an electrical inertia to allow for the grid voltage and frequency regulation and, on the other hand, the stored energy can be managed to improve the predictability and quality of the generated power.

Energy storage for electricity grid has been traditionally carried out through reversible pumped-storage hydro systems, which need a lower and upper water reservoir and are able to pump water up when excessive electricity availability and turbine it down when needed. These systems require suitable locations with large differences in hight to build both water reservoirs. In the new paradigm of decentralized electricity grid, with distributed generation and electrical microgrids, the decentralized energy storage is gaining interest, bringing batteries into prominence. Actually, Bloomberg predicts an increase in small-scale battery systems installed by households and businesses alongside PV systems to account for 57% of installed storage capacity worldwide by 2040 [NEW17]. The battery technology that has been traditionally used for grid storage has been the lead–acid batteries. [SAN13]. However, these batteries present problems related with the lead toxicity, its short useful life and low efficiency. These characteristics reduce the interest on lead–acid batteries to be used for electricity grid storage.

Lithium-ion batteries are currently undergoing a fast development process, leaded by the automotive sector in their search for an efficient, lightweight, safe and inexpensive storage system that allows the transition from the current internal-combustion vehicles to the electric vehicle. Thus, the performance of Li-ion batteries is being enhanced while their cost is sinking. This fact brings Li-ion battery forward as a main actor for the energy panorama expected for the upcoming years. In fact, the cost reduction experienced by Li-ion batteries during the last years meant a price reduction from $ 1000 per kWh in 2008 to $ 268 per kWh in 2015, that is a 73% reduction in battery cost in seven years [CAZ16]. This trend is expected to continue during the following years,

reaching $100 per kWh by year 2020 [CAZ16, HYB]. This price reduction comes along with a fast increase in the Li-ion battery demand expected for the upcoming years. Several studies predict a 40% increase in the global Li-ion battery market between 2017 and 2020 driven mainly by the electric vehicle sector. In the mid term, Li-ion batteries are expected to jump to the electricity grid.

Besides Li-ion batteries, supercapacitors (SCs) can also play a main role in electricity grid voltage and frequency regulation, as well as in renewable energy firming. Their outstanding cycle life, efficiency and ability to operate in extreme environmental conditions open a wide range of possibilities for SCs to be used as ESS in many applications or as auxiliary ESS to be hybridized with Li-ion batteries or other main ESS. The use of SCs is also expected to experience a great growth during the upcoming years due to the increasing requirements of fast-dynamic storage in energy systems. Several SC market outlooks predict a Compound Annual Growth Rate between 20 and 25% per year during the next seven years [GRA16, ACC16].

The modelling of electrochemical systems is a handful tool to exploit their electrochemical principles and optimise their management. The understanding of the physical principles that affect each particular application and their account during the design of the management strategies are of most importance for a suitable design of an ESS. As reviewed through this thesis, uncountable models for Li-ion batteries and SCs have been published, each of them emphasising different aspects of the ESS. However, better understanding of electrochemistry, new material designs and manufacturing processes, new requirements for the ESSs, new computational capabilities, and other continuous technology improvements need to be taken into account and studied from the modelling point of view, so that they can be incorporated into the decision-making procedures related with ESSs.

According to this scenario, four objectives are tackled along this thesis. The first one consists on reviewing and synthesising the fundamentals governing the operation of lithium-ion batteries. This compilation is made with a special focus put on the final usage of these batteries when operating with renewable energy generation systems and on the main influences that each electrochemical phenomenon has on these applications.

The second objective consists on the development of a lithium-ion battery model useful for the management and control of such a battery in renewable energy scenarios. This objective is in turn subdivided into three sub-objectives. The first one consists on the analysis of different estimation methods for state of charge (SOC) calculation and the identification of the most suitable method

for each application. The second sub-objective deals with the modelling of the battery electrical performance and its relationship with the physico-chemical phenomena that affect it. The third sub-objective consists on the development of a thermal model able to interact with the electrical model in order to maintain the high accuracy of the electrical model in a wide range of operating conditions.

The third objective consists on the analysis of the integration of lithium batteries in a renewable generation plant from the point of view of the optimisation of an objective function using the battery models developed in this thesis.

Finally, the fourth objective consists on the analysis of the performance of supercapacitors (SCs) and their useful characteristics to support Li-ion batteries in a hybrid ESS, thereby improving the overall characteristics. This objective is also divided into two sub-objectives. Firstly, an analysis of the current state of SCs technology including its applicability and a market review is presented. Secondly, an electro-thermal model is proposed with the aim of simulating the SC performance. This SC model can be integrated into the above-mentioned Li-ion battery model to allow the analysis of hybrid ESS.

This thesis, divided in seven chapters, is structured to orderly tackle the four objectives. After this introduction, in Chapter 2, Li-ion batteries are contextualized, the most important milestones that have triggered their technology evolution are summarized, and the basic battery concepts used along the thesis are defined. Moreover, the components of this battery technology are described and Li-ion batteries are classified according to shape and materials, identifying positive and negative aspects of each Li-ion battery. Finally, some directives concerning the future development of battery technology expected for the upcoming years are mentioned.

After this, in Chapter 3, the physico-chemical principles of lithium-ion batteries are reviewed, summarised and analysed. Specifically, thermodynamic of insertion electrodes, electrochemical principles of this kind of redox reactions, the main phenomenons provoking battery ageing and the main processes related to thermal behaviour are covered.

In Chapter 4, a Li-ion battery model is proposed, based on the physical principles of the battery performance. After detailed simplification processes, these principles are represented as an equivalent circuit. Firstly, different algorithms for SOC estimation are covered, based both on accurate current measurement and on the use of an equivalent circuit. Improved methods that combine both approaches are also analysed. Moreover, the modelling of the electrochemical performance of the battery is covered by the development

of two models for different applications. Both general methods are particularised for a specific battery and experimentally validated through laboratory tests. Subsequently, thermal modelling is also covered, proposing a model able to estimate the operation temperature of the Li-ion battery. This model is combined with the previously-mentioned electrochemical model enhancing its capabilities. Finally, a battery ageing model is proposed and validated by means of computer simulation comparing the results with a commercial battery datasheet.

The work presented in Chapter 5 was developed during a research stay in Fraunhofer Institute for Solar Energy System (Freiburg im Breisgau, Germany). The integration of Li-ion batteries in renewable energy plants is covered in this chapter. With this aim, the sizing method and management strategies are tackled through mathematical optimisation aimed at maximising or minimising the value of an objective function. The proposed method is particularised for a medium-size photovoltaic plant, a type of power plant where energy storage systems are expected to play a main role during the upcoming years. This sizing and management optimisation strategy is based on the battery models proposed in Chapter 4, as well as on models of other components of the generation plant which are also briefly described in Chapter 5. A comparison of the economical revenue obtained from the storage system by applying the proposed methodology and by using an intuitive strategy is included at the end of this chapter. This comparative study proves the usefulness of the proposed optimisation tool to get the most out of an Li-ion battery.

Subsequently, Chapter 6 analyses the role of SCs as complementary ESS to be installed with Li-ion batteries in applications requiring fast charge–discharge cycles or high frequency performance. With this aim, the current state of SCs technology is analysed, starting from the basic principles of operation and following with their electrical characteristics, different modelling trends proposed in the bibliography and examples of successful engineering applications. The chapter goes on with the proposal of an electrochemical-thermal model for SCs in which, using an equivalent methodology to the one used for battery modelling, the operating principles are simplified in order to build a model valid for the analysis of a wide range of frequencies as high as the typical electronic converter commutation range. Given the similarities between this SC model and the Li-ion battery model proposed in previous chapters, both models can be combined to allow for the analysis of the hybridization of both ESS.

Finally, Chapter 7 summarises the final conclusions of this thesis. Moreover, the contributions of the research work are compiled and future research

lines that can contribute to move forward in the research topics covered in the thesis are proposed.

Chapter 2

Lithium technology

You must be ready to give up even the most attractive ideas when experiment shows them to be wrong.

– Alessandro Volta

2.1 Why lithium?

Lithium is the lightest and smallest of all metals and has the lowest standard reduction potential. Firstly, its small size eases its intercalation inside the crystal lattice of electrode materials provoking low mechanical stress and thereby minimizing cracks associated with charge–discharge cycles. Moreover, its low standard reduction potential gives rise to negative electrodes with a very low potential, which enlarges the battery working voltage (greater than 3 V) and its power and energy density. These properties make lithium a very attractive material to be used for a battery.

These characteristics are attractive for diverse industrial sectors, which has driven an increasing interest in Li-ion battery technology during the last years. During the decade of 2000s, the communication sector headed the Li-ion battery research and development aimed at replacing the previous Ni–Cd and Ni–MH batteries, with poor functionality. During that decade, lithium batteries copped the portable device market, being currently the storage system used in virtually all electronic devices. During the decade of 2010s, the electrochemical energy storage turned compelling for the automotive sector, given the interest on electric vehicles. This is currently causing a fast improve-

ment of the technology, along with an unprecedented increasing demand. This improved functionality is catching the interest of a third main sector, the stationary applications, given than Li-ion batteries can be attractive for grid connected applications such as domestic self-consumption, renewable energy generation improvement, electricity grid support, etc.

But, is there enough lithium available at a reasonable price to cover this increasing demand? Lithium is a sparse material, both in the universe and in the Earth's crust. Hydrogen and helium are estimated to make up roughly 74% and 24% of all baryonic matter in the universe respectively. The other elements are just 2% of the ordinary matter. The material abundance in the universe follow a trend consisting of heavier nuclei being less common as lighter, given that shortly after the Big Bang (within a few hundred seconds) only light elements were produced in a process known as Big Bang nucleosynthesis. Specifically, only hydrogen, helium and lithium were produced in this process. Heavier elements were mostly generated much later, inside of stars. Lithium has been originated through three main processes, which are the Big Bang nucleosynthesis (23% of the available Li in the universe), the nuclear reactions that take place in dying low-mass stars (64%) and nuclear fission caused by cosmic rays (13%) [CRO95].

Even though lithium nuclei are very light, this metal is an exception to the above-mentioned abundance trend. The reason for this exception is that the nucleus of the lithium atom verges on instability. Actually, the two stable lithium isotopes found in nature have among the lowest binding energies per nucleon of all stable nuclides. Because of its relative nuclear instability, lithium is less common in the solar system than 25 of the first 32 chemical elements [VAN99].

Interesting for industrial uses is the availability of lithium in the surface of the Earth. As a whole, the Earth's crust contains approximately 20 parts per million of lithium, and the oceans contain 0.17 parts per million [EMS01]. Lithium is therefore not a prevailing material, but it is more common than metals such as cobalt, tin or lead, as shown in Figure 2.1 (a) (note the logarithmic scale). According to estimates of the US Geological Survey, there are 40 million tonnes of lithium mineable globally, 65% of that alone in the South American countries of Bolivia, Chile and Argentina, as shown in Figure 2.1 (b) [AG16].

For standardization reasons, the unit used to refer to lithium production is tones of LCE (lithium carbonate equivalent) which allows for the comparison of production quantities of different lithium materials. In 2015 the global lithium production was approximately 175 000 tonnes LCE. According to pro-

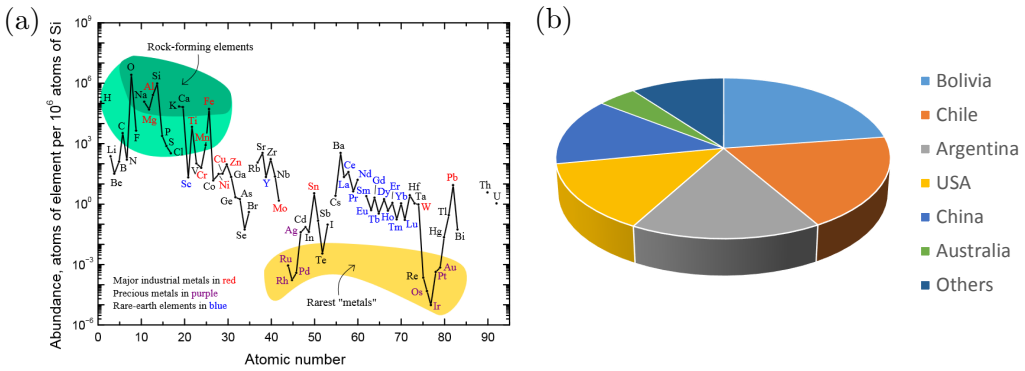

Figure 2.1: Lithium availability in Earth's crust: abundance of the chemical elements in Earth's upper continental crust as a function of atomic number, reproduced from Wikipedia (a) and location of the main lithium reserves by country (b).

jections, this amount will increase to 300 000 tonnes LCE by 2020, as shown in Figure 2.2, and continue growing to reach 700 000 tones LCE in 2025 [AG16]. This increasing demand is rising the cost of lithium, as shown in Figure 2.3 (a) following typical demand–supply rules. However, this fact is not crucial for the price of Li-ion batteries, given the small amount of lithium required to build these batteries. Actually, as mentioned in the table shown in Figure 2.2, 50 kg of LCE (112 lb) are required for an 85 kWh Tesla battery (this is equivalent to 110 g of Li per kWh). The lithium price of a battery is around \$5.3 kWh^{-1}, which represents 2% of the overall battery price (roughly \$250 kWh^{-1}).

Some concerns have been reported related to the availability of other materials required for the cathode of Li-ion batteries. Most of them are related with cobalt, which is a key cathode component for portable electronics batteries, it is scarcer than lithium (see Figure 2.1) and 65% of its global production comes from Democratic Republic of the Congo, a country that is extremely politically unstable and has deeply-rooted corruption structures. However, there is a wide variety of Li-ion batteries, as reported in the following sections, with different cobalt requirements (a high amount of cobalt is required for a $LiCoO_2$ cathode used in a cell phone battery, but no cobalt is used in a $LiMn_2O_4$ cathode used for a Nissan Leaf battery). Therefore, a cathode material is not as crucial as lithium for the Li-ion battery industry to expand, given the multiple cathodes that have already been designed and tested (cobalt, nickel, manganese, aluminium, etc.).

Having said this, although some materials required for Li-ion batteries are not broadly found in the Earth's crust, the current increasing demand of these materials is still far from the global production capacity and from the global

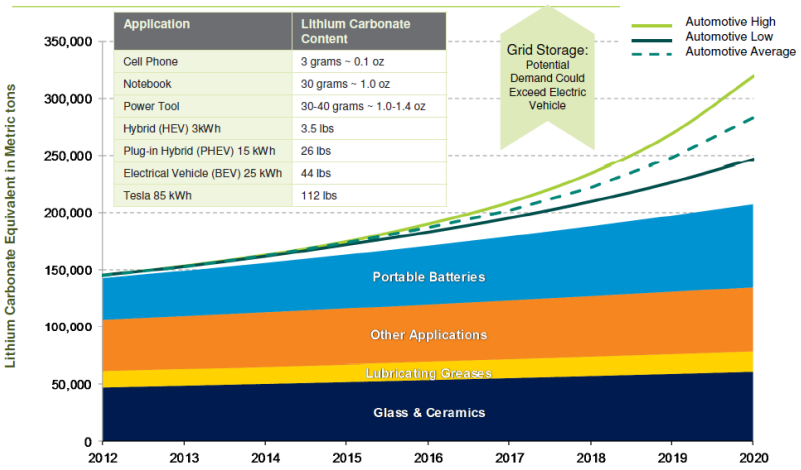

Figure 2.2: Global lithium production and consumer sector. Current data and prognosis for the future years. Reproduced from [ALB16] with data from Bloomberg.

reserves. Actually, a demand of 300 000 tones LCE is predicted for year 2020 while the reserves are estimated to be 40 million tones LCE, which means 133 year availability at the production rate predicted for 2020. If the production rate predicted for 2025 (700 000 tones LCE) is used for this calculation, 66 years of lithium supply are guaranteed. This numbers should be taken with care, given the fast growing expectancies for this market during the upcoming years. However, based on these results, lithium can be considered, not as the definitive solution for energy storage, but as the best current and mid-term alternative while other technologies are developed.

Actually, the effect of the increasing battery production is nowadays a significant reduction of Li-ion battery cost, given that scale economies, improvements of the manufacturing processes and discovery of cheaper battery materials have a bigger impact on battery cost than the increase on raw material prices. The battery price evolution from 2008 to 2015 is shown in Figure 2.3 (b). A cost reduction from \$1000 kWh^{-1} in 2008 to \$250 kWh^{-1} in 2015 is reported, which means a 75% price reduction in eight years. The DOE has set a target for the year 2022 of \$120 kWh^{-1}, which was considered by the IEA as a realistic value [CAZ16]. Two of the most remarkable companies involved in the sector of electrical mobility placed even more challenging targets, which consist of battery costs lower than \$100 kWh^{-1} for year 2020 (Tesla) and 2022 (General Motors), as represented in Figure 2.3.

Therefore, rather than worrying about a lack of lithium for the increasing demand placed by the electric vehicle market in the short term, perhaps we

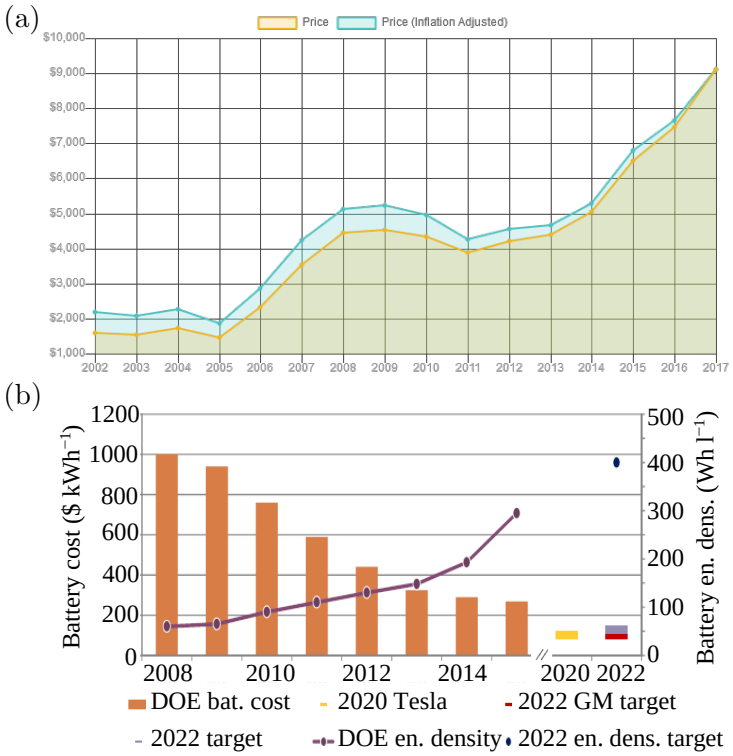

Figure 2.3: Price indicators related to Li-ion batteries: price of lithium from 2002 to 2017 in $ per tone LCE (a) and battery cost from 2008 to 2015, along with expected values for 2020 and 2022 in $ per kWh (b). Reproduced from [CAZ16].

should think about plausible shortages of rare earth materials. Such materials are used to build the permanent magnet for the electric motors. China controls about 95% of the global market for rare earth metals and expects to use most of these resources for its own production.

2.2 Technology evolution

Lithium was discovered in a mineral called petalite by Johann August Arfvedson in 1817, as shown in Figure 2.4. This alkaline material was named *lithion/lithina*, from the Greek word $\lambda\iota\theta o\zeta$ (transliterated as lithos, meaning "stone"), to reflect its discovery in a solid mineral, as opposed to potassium, which had been discovered in plant ashes, and sodium, which was known partly for its high abundance in animal blood. Lithium was first isolated in 1821 by William Thomas Brande and Sir Humphrey Davy through the electrolysis of

lithium oxide (Li_2O).

Some technical developments had to be tackled before lithium could be used as a battery material, given that traditional electrolytes were based on water, which has a decomposition voltage lower than the working voltage of a lithium-ion battery (LIB). Therefore, new organic electrolytes needed to be developed, the first of which was polyvinylpyridine (PVP). This first LIB has its genesis in research work done at the Jet Propulsion Laboratory published in 1967 [GUT67]. It was a primary battery (single-use, non-rechargeable battery). A few years later, in 1972, Moser and Schneider invented the lithium/iodine battery [MOS72a, MOS72b], which used a lithium metal anode and an iodine-based cathode. This movement from a zinc-based to a lithium-based battery achieved a five-times improvement of energy density (from 50 Wh/kg to 250 Wh/kg) [GRE92]. The lithium–iodine battery was soon identified as a suitable power source for cardiac pacemakers [GRE71], which had a tremendous impact on patient comfort, since its use in these devices resulted in a reduced weight and an extension from two UP to ten years in the device operational life [HOL01].

Figure 2.4 shows a chronology with the most important millstones for the development of LIBs. Under the time line, the main discoveries and advances are shown, along with the main inventors. Above the line, the most remarkable dates are written in red colour and a main characteristic of the technology development status during each period is summarized.

The fast widespread of consumer electronics during the 1970s stimulated an interest in moving to secondary, rechargeable systems. In theory, there was no difficulty on the anode side, since the ions formed from the lithium metal anode during discharge were expected to plate back to rebuild the metal anode during charge. Indeed, lithium deposition from carbonate-based solutions had been already demonstrated [HAR58]. Therefore, the research efforts were focused on cathode materials. The first insertion (or intercalation) cathode was proposed in 1978, which was titanium sulphide (TiS_2) [WHI78]. Insertion electrodes are able to reversibly accept and release lithium ions from their open structure assuming various valence states, thereby allowing several charge–discharge battery cycles. The first commercial prototypes of secondary Li-ion battery appeared in the late 1970s. However, some operational faults, including fire incidents, revealed problems concerning the battery anode. Due to the high reactivity of lithium metal, it reacts readily with the electrolyte, building the so-called solid–electrolyte interface (SEI). Irregularities at this layer can lead to uneven lithium deposition and dendrite formation, which may short the cells causing thermal runaway, fire or explosion.

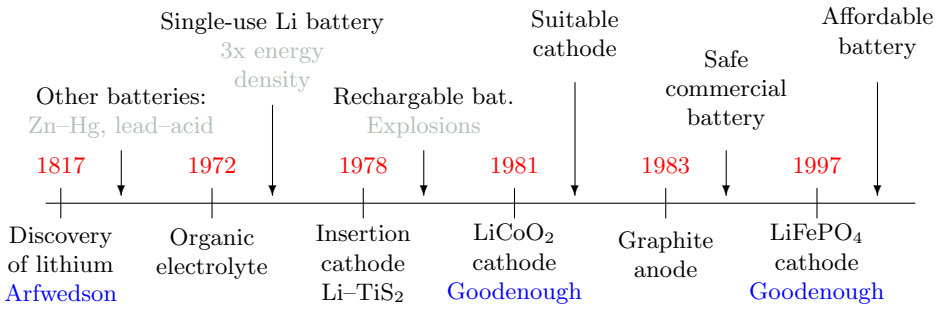

Figure 2.4: Main milestones during the early development of lithium batteries.

The use of a reversible graphite electrode for the anode can be considered as the key advance that enabled commercial lithium-ion batteries [BAS83, YOS87]. The choice of graphite is rather surprising, since it is unstable in the stability window of most common electrolytes. The electrolyte, in fact, decomposes at the graphite surface, forming an electronically blocking but ionically conductive layer that stops the decomposition while allowing the electrochemical process to continue. Therefore, graphite is thermodynamically unstable but kinetically protected. This protective layer is also called solid–electrolyte interface (SEI). Graphite is nowadays the most commonly-used anode material for lithium-ion batteries.

In contrast, a wide variety of cathode materials is used for Li-ion batteries. The cathode must be capable of providing lithium ions to assure the electrochemical process, as well as to accept them back in a reversible matter to provide Li-ion batteries with long lifetime. These requirements were firstly fulfilled by $LiCoO_2$, a material with a layered crystal structure discovered by Goodenough and co-workers in 1981 [MIZ81]. This is the cathode normally used nowadays for portable devices like cell phones or laptops.

In the search for a cheaper Li-ion battery capable of delivering higher power, Goodenough's group designed in 1997 a lithium iron phosphate ($LiFePO_4$) cathode [PAD97], which is currently the flagship of the olivine components used as battery cathodes. This material is significantly cheaper than $LiCoO_2$, but suffers form a very high intrinsic resistance, which requires special electrode preparations involving sophisticated coating processes.

During the 21st century, an intensive research work has been accomplished and several materials have been proposed as cathode materials. Among them, a layered compound deserves special attention due to its widespread use, it is $Li(Ni_xMn_xCo_{1-2\cdot x})O_2$. It exhibits outstanding electrochemical properties by combining the high capacity of $LiNiO_2$ and the thermal stability and low cost

of manganese in $LiMnO_2$, and stable electrochemical characteristics of $LiCoO_2$ [PAR12].

The current need of long-lasting Li-ion batteries has risen the interest for lithium titanium oxide as anode material to replace graphite. The negligible changes in the lattice structure upon accepting and releasing lithium ions and the lack of SEI interface due to the stability of this material inside the battery operation voltage enlarge the lifetime and the reliability of the batteries. Companies like Leclanché are already selling lithium titanium oxide (LTO) batteries.

The wide variety of materials available nowadays for lithium battery electrodes turns into an extensive catalogue of Li-ion batteries with different properties determined by the used materials and the manufacturing process. The most commonly-used materials and associated batteries are covered through the following sections, along with their characteristics, advantages and disadvantages and the most suitable applications for each of them.

2.3 Important concepts about batteries

Electrochemical cell vs. battery

An electrochemical cell is the smallest unit of a device that converts chemical energy to electric energy, or vice versa. Conversely, a battery can be built by the connection of multiple electrochemical cells. However, the word *battery* is normally used as the generic term to refer to either cells or batteries. Therefore, when the battery operation principles are explained in this thesis, the word *battery* is used for an easier argumentation and with no ambiguity, even though the processes described and explained take place in a single cell.

Full cell vs. half cell

A full cell is the normal electrochemical cell that can be found in the market, where electrochemical reactions occur at both the cathode and the anode, and allows direct measurement of battery characteristics and performance. Similarly, a half cell also has two electrodes (otherwise, there would be neither voltage nor current). However, one of them is the electrode under study; while the other one (also known as counter electrode) is a standard electrode used to facilitate measurements and analysis of activities at the working voltage.

There are several standard electrodes, being the best known the standard hydrogen electrode (SHE), whose standard electrode potential (v_{eq}^0) is declared to be zero volts at all temperatures. For the analysis of Li-ion batteries, the

Li/Li^+ electrode is typically used as reference. The redox reaction in the Li/Li^+ electrode is:

$$Li^+ + e^- \rightleftharpoons Li\ (s)$$

whose standard potential relative to SHE is -3.0401 V [HAY12].

The analysed electrodes of two half cells can be assembled together to build a full cell (discarding the counter electrodes) to build a full cell. Figure 2.5 schematically represents the potential vs. Li/Li^+ of (a) a generic anode (low potential) and (b) a generic cathode (high potential). Note that lithium content increases from left to right in Figure 2.5 (a) and from right to left in Figure 2.5 (b). It is reasonable that an increasing lithium content leads to an approach of the electrode potential to the reference Li/Li^+ electrode, which means a reduced potential for increasing lithium content. The vertical lines represent the maximum and minimum lithium content in each electrode for the electrochemical reaction to be reversible. Given the high voltage difference between both electrodes, they are suitable to be placed together to build a full cell, such as the schematic shown in Figure 2.5 (c). The cell voltage is the difference between the cathode and anode voltage, as shown below:

$$v_{cell} = v_{c,\ vs\ Li/Li^+} - v_{a,\ vs\ Li/Li^+} \tag{2.1}$$

As shown in Figure 2.5 (c), the charge (right) and discharge (left) lithium concentration limits are the most restrictive between anode and cathode, which, in this schematic, are the cathode discharging limit and the anode charging limit. The Li ions are deintercalated from an electrode while intercalated in the other electrode. This is the reason why discharging arrows in Figure 2.5 are labelled as Li intercalation for the cathode and Li deintercalation for the anode.

Polarization

Polarization (v_η) is a lack or excess of electrode potential compared with the equilibrium potential (v_{eq}). v_{eq} is the battery voltage when it is kept in open circuit conditions enough time for all the dynamic processes to reach its steady state. When current flows between the two terminals of the battery, the actual potential v is always larger (charging) or smaller (discharging) than the v_{eq}:

$$v_\eta = v - v_{eq} \tag{2.2}$$

This effect result in power losses during battery operation, either it is being charged or discharged.

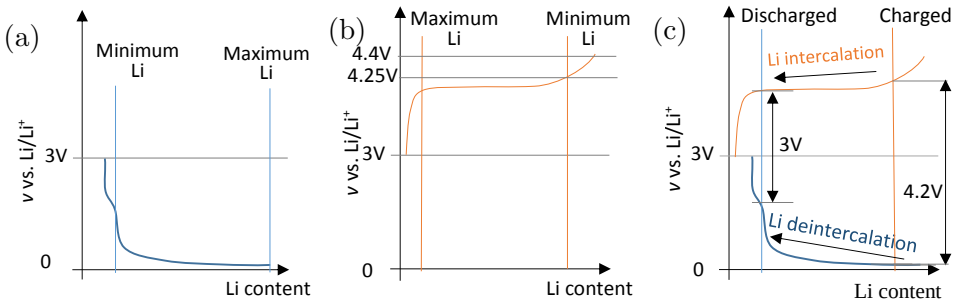

Figure 2.5: Half-cell and full-cell potential schematics: anode material (a), cathode material, note that maximum Li intercalation is on left side of the graph (b) and full cell, whose potential is measured between cathode and anode potential (c).

Capacity (C)

Is the amount of electrical charge (Ah) that a battery is able to store. This unit should not be confused with the capacitance of a capacitor, which is measured in Farad (F).

Its value is determined by the amount of active material. As explained in the following chapters of the thesis, the active material of a battery usually decreases as it gets older, due to ageing mechanisms that electrically disconnect regions of the electrodes, turning them into passive material. Besides, there is usually an excess of one of the electrodes, so that the ageing mechanism can be minimized, and not all the active material can be used during battery charge and discharge due to irreversibilities occurring at extreme charged and discharged states. Therefore, a direct measurement of the cell capacity via determination of the amount of active materials is hard to realize.

The following measurement procedure is used along this thesis to define capacity: The cell capacity C is the actual amount of charge which can be extracted from a fully charged cell during discharge at a current rate of 0.5C (see following paragraph) at an ambient temperature of 20 °C. Besides the real cell capacity, there is a term called nominal capacity C_N which is specified by the cell manufacturer. The actual capacity of a fresh cell is usually above the nominal capacity, and it becomes lower as ageing mechanisms take place.

Rate of charging/discharging (C-rate)

It is a commonly-used magnitude to standardise the battery current. It is defined as the current (i) that would be needed for a battery with nominal capacity to be fully charged or discharged in one hour (if it was possible to

accomplish a full charge or discharge with this constant current). Therefore, the following relationship can be stated for a C-rate I_{rate}:

$$\text{C-rate current} = \frac{i}{C_N} \tag{2.3}$$

where i is the battery current whose C-rate equivalence wants to be calculated. It is commonly assumed, when talking about lithium-ion batteries, that a battery current of 4C means four times C-rate. This means, for example, that a current of 4C in a 20 Ah battery is $i = 4 \cdot 20 = 80$ A.

Cut-off voltage

To prevent the battery from permanent damages and to avoid safety hazards, the cell must only be operated inside specified voltage limits. Therefore, the battery voltage should not sink below a lower limit nor exceed an upper limit. These limits are called cut-off voltages.

Energy density

This magnitude is defined as the amount of energy stored in a battery per unit mass or volume. This is an important factor to be taken into account for battery design and analysis. Sometimes energy density data is provided at an electrode level (taking into account only the mass or volume of the electrode material), other times at cell level (considering the size of the cells) and, others, at a battery pack level (considering the whole battery pack mass and volume).

Care should be taken in order to compare equivalent magnitudes of different technologies or products, given that the energy density of an electrode is bigger than that of a cell, and this is also greater than the energy density of the whole battery pack.

Power density

This is an analogous magnitude to energy density. It is defined as the power manageable per unit mass or volume of a battery. The same attention needs to be paid to the element referred to with this magnitude (electrode, cell or battery pack).

Charge throughput (CT)

This is a term adopted by some authors to measure the use of a battery. It is defined as the accumulation of the overall charge accepted and extracted by

the cell during the analysed time lapse. It is defined by Equation 2.4:

$$CT = \int_{t_0}^{t} |i(\tau)|\, d\tau \tag{2.4}$$

State of charge (SOC)

The state of charge is one of the main battery variables. It is the measurement of the charge stored in the battery, and its units are % of the battery capacity, or, alternatively, per unit. For easier calculations, the per-unit value is used in the equations of this thesis.

$$SOC = \frac{\text{Stored charge (Ah)}}{C_N} \tag{2.5}$$

Cycle

A cycle is the process of charging and discharging (or discharging and charging) a cell following a specified procedure. The SOC at the end of the cycle is the same as at the beginning.

Depth of discharge (DOD)

This is a property of a battery cycle, i. e. we usually talk about the depth of discharge during a cycle. It is defined as the charge throughput during the cycle divided by two times the battery capacity C:

$$DOD = \left.\frac{CT}{2 \cdot C}\right|_{cycle} \tag{2.6}$$

Internal resistance (R_i)

Is the equivalent-circuit representation of the non-ideal battery behaviour. Due to dynamic phenomena, its value depends on the studied frequency. A common convection is to measure its value at a frequency of 1 kHz. This parameter contains information about battery efficiency, heat dissipation, battery ageing, etc., as detailed through this thesis.

Coulombic efficiency (η_c)

Is the ratio between the charge extracted from the battery and de charge that needs to be charged to return the battery to its initial state:

$$\eta_c = \left.\frac{\int_{dis} i \cdot dt}{\int_{ch} i \cdot dt}\right|_{cycle} \tag{2.7}$$

The origin of coulombic inefficiency are parasitic reactions and it is a main parameter for battery materials design. Its main effect is a premature ageing of the battery, given that these reactions cannot be reverted.

Energy efficiency (η_e)

Is the ratio between the energy extracted from the battery and de energy that needs to be charged to return the battery to its initial state:

$$\eta_e = \left. \frac{\int_{dis} i \cdot v \cdot dt}{\int_{ch} i \cdot v \cdot dt} \right|_{cycle} \tag{2.8}$$

The origin of energy inefficiency, besides the own coulombic efficiency, are non-ideal phenomena (also known as overvoltages) related with the battery performance, which are represented by the internal resistance (R_i) and described in detail in Section 3.3. This is an important parameter from the point of view of the battery user, given taht its main effects are power losses during battery operation and augmented generated heat which needs to be evacuated from the battery.

Equivalent full cycle

It is a unit to standardise the total charge throughput CT and make it comparable between batteries with different capacities. It is equal to two times the nominal cell capacity. For example, a 10 Ah battery undergoes an equivalent full cycle when it handles a charge throughput of 20 Ah (10 Ah charging and 10 Ah discharging).

Cycle ageing

Is the effect that non-reversible phenomena due to battery charging and discharging have in battery parameters. The most remarkable effects are capacity fade and impedance rise.

Calendar ageing

Is the effect of only time-dependent phenomena in the battery parameters. The most affected parameter are also capacity and impedance.

State of Health (SOH)

It is a measurement of the actual state of a cell at any time during its lifetime compared to the characteristics of the new battery. This magnitude can be defined as a ratio between the actual capacity and the nominal capacity:

$$SOH = \frac{C(t)}{C_N} \tag{2.9}$$

or as a ratio between battery impedance, or more commonly internal resistance (R_i):

$$SOH = 1 - \frac{R_i(t) - R_{i,N}}{R_{i,N}} \tag{2.10}$$

Given that both capacity fade and impedance rise are signs of battery ageing, SOH is sometimes defined as the most restrictive of these two expressions. However, since most of the ageing phenomena imply a combination of capacity fade and impedance rise, as explained in Section 3.5, the two SOH definitions usually provide similar results.

End of life (EOL)

The end of life of a battery denotes the point in its lifetime, when it is considered to be not further usable for the particular application where it is being used. The EOL criteria is usually defined as a level of SOH. Its value is usually between 70% and 80% SOH, given the non-linear, accelerated battery ageing phenomena associated with $SOH < 0.7$.

Even though, there are proposals of second-life applications for Li-ion batteries that use aged batteries (the EOL criteria for its original application was surpassed). These are usually situations in which the battery energy and power densities are not so crucial and a less restrictive criteria can set in order to extend the use of these low-price, aged batteries.

Battery life

Is the duration of the battery (measured in time and/or in cycles) until it reaches the defined end of life (EOL) criteria. The battery life is a consequence of a superposition of cycle and calendar ageing effects.

2.4 Components of a lithium-ion cell

A lithium-ion battery cell consists on two electrodes, which are usually referred as anode (negative) and cathode (positive), separated by an ion-conductive membrane, as shown in Figure 2.6. The main part of each electrode is the active material, which takes par in the electrochemical reaction and determines the battery performance. Besides the active material, each electrode has a current collector, which is a good electronic conductor material on which the active material is deposited. It provides the electrode with the required structural stability and conducts the electrons to the external electric circuit. Finally, both active materials and the membrane are immersed in an electrolyte,

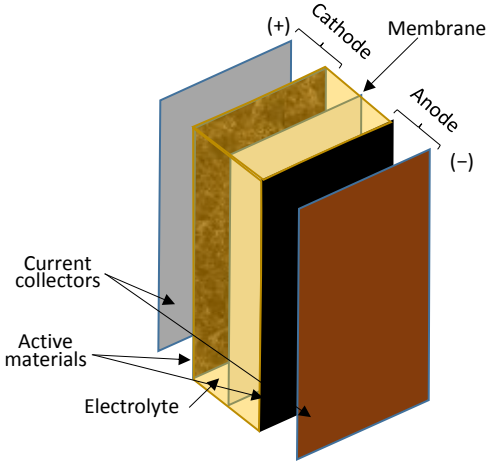

Figure 2.6: Schematic of the main components of a Li-ion cell.

which allows the ion movement between both electrodes. There are a wide variety of different Li-ion batteries which use different materials and manufacturing processes for each of these components. The main choices, remarkable parameters and main characteristics for each of them are covered through the following subsections.

2.4.1 Negative electrode active material

The negative electrode of a lithium battery is often referred to as *anode*, since oxidation takes place during discharge. The anode material has an important influence on the battery performance, including safety, energy density, power density and cycle life. These materials should fulfil the following conditions:

- Low potential vs. Li/Li^+, which allows a larger cell potential when placed with a cathode, as mentioned in Section 2.3.
- No significant change in the crystal structure should occur due to the intercalation and deintercalation of lithium ions, thereby leading to an extended battery lifetime.
- The electrochemical reactions should be highly reversible, ideally with $\eta_c = 1$.
- High diffusion of lithium ions through the crystal lattice.
- High electrode conductivity.

- High amount of charge stored per unit mass.

The characteristics, advantages, disadvantages and challenges of the most used anode materials are covered through the following subsections and summarized inTable 2.1.

2.4.1.1 Lithium metal

As mentioned in Section 2.2, metallic lithium was used as anode for the first family of lithium batteries. Since it is purely lithium, the totality of the atoms can be ionized and used as charge carriers, providing an outstanding energy density (3860 $Ah\,kg^{-1}$ [KOR13]). Its electrochemical potential is also really low (−3.05 V vs. standard hydrogen electrode [HAY12]). These two characteristics yield an energy density as high as 600 $Wh\,kg^{-1}$ on the cell level [KOR13]. The safety problems associated with high lithium reactivity with air and water, as well as short circuits occurred as a consequence of dendrite formation on the metallic surface made this anode unsuitable for practical batteries.

Some studies have been published attempting to stabilize lithium metal by coating the surface with polymeric or inorganic substances. Despite these efforts, lithium metal is not used nowadays as anode material.

2.4.1.2 Graphite

Graphite is made of carbon atoms arranged in a planar, layered structure[1]. The electrochemical activity of carbon is due to the intercalation of Li between the graphene planes[2] (as much as 1 Li atom per 6 carbons can be stored). The main advantages of graphite are its low cost, abundance, low potential vs. Li/Li^+ (see Figure 2.7), high Li diffusivity, high electrical conductivity and low volume change during lithiation and delithiation [NIT15].

For a closer analysis of the graphite anode, let's take a $Li_xC_6/Li_{1-x}CoO_2$ battery as an example, as the one shown in Figure 2.8. Li_xC_6 denotes the

[1]There are only three naturally occurring allotropes of carbon, whose difference is the structure and bonding of the atoms within the allotropes: diamond, which enjoys a diamond lattice crystalline structure, graphite, having a honeycomb lattice structure, and amorphous carbon (such as coal or soot), which does not have a crystalline structure.

[2]Note that graphite is made of hundreds of thousands of layers of graphene stacked together. The graphene used for some Li-ion batteries (sometime called graphene batteries) are separated single layers of graphite which are used as structural support for the active electrode materials. Therefore, graphene is not the active material in graphene batteries.

Table 2.1: Main characteristics of anode materials. Data from [SCR13, PAR12].

Material	Theoretical C ($mAh\,g^{-1}$)	Real C ($mAh\,g^{-1}$)	Avg. pot. (V)	Advantages	Issues
Li metal	3800	—	0	Energy density	High reactivity, dendrite growth, fires, explosions
Graphite	372	~ 360	~ 0.1	Mature technology	Outside electrolyte stability
Cokes	—	~ 170	~ 0.15	High capacity and cycle life	High consumption of Li
Li_xSi_y	4200	~ 1000	~ 0.16	High capacity, low cost	Volume changes, nanostructures
Li_xSn_y	790	~ 700	~ 0.4	High capacity, low cost	Volume changes, nanostructures
$Li_4Ti_5O_{12}$ (LTO)	170	~ 145	~ 1.55	Low volume expainsion, chemical and thermal stability	Low specific capacity, high voltage

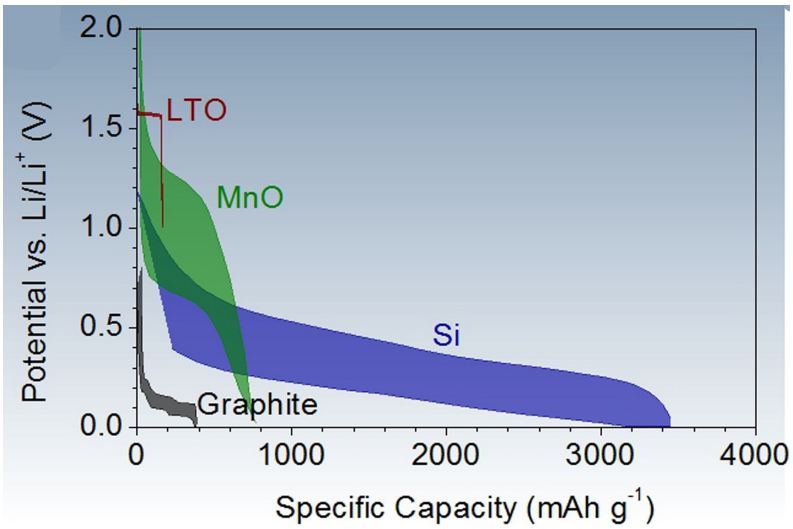

Figure 2.7: Potential and specific capacity of several anode materials at low charge/discharge rates to shown voltage hysteresis. Reprinted from [NIT15], with permission from Elsevier.

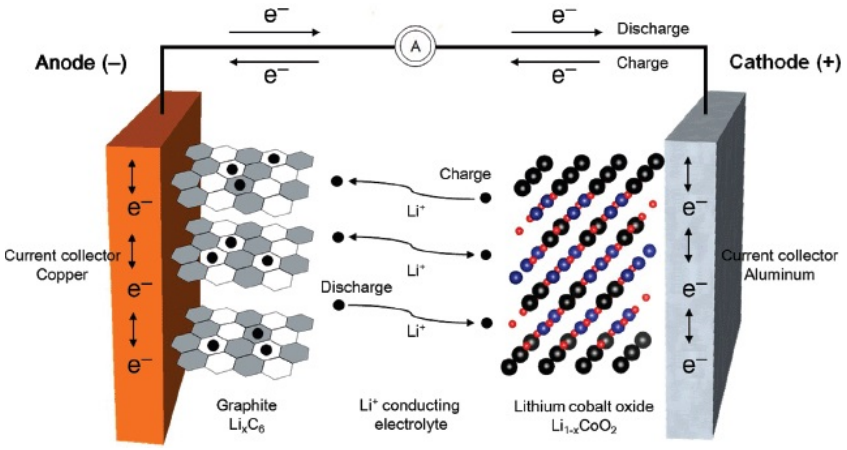

Figure 2.8: Movement of Li^+ in an electrolyte and insertion/extraction of Li^+ within electrodes in a lithium secondary battery. Reprinted from [PAR12], with permission from John Wiley & Sons, Inc.

graphite anode, in which one lithium reacts theoretically with six carbons, as shown in the equation below. The potential of pristine graphite is 3.0 V vs. Li/Li^+, but rapidly declines when a small portion of lithium is intercalated and it ranges from 0.05 to 0.25 vs. Li/Li^+ in the battery operation region.

$$Li_x\, C_6 \rightleftharpoons C_6 + x\, Li^+ + x\, e^-$$

Decomposition of the electrolyte occurs at the surface of the anode during charging, given that its reduction potential is higher than that of graphite. Such decomposition not only causes the formation of solid–electrolyte interface (SEI) but also suppresses the electron transfer reactions between the anode and the electrolyte, thus preventing further electrolyte decomposition. If the SEI is broken during normal battery operation and the anode gets in touch with the electrolyte a new SEI is created to passivate the exposed area, thereby reducing the coulombic efficiency and battery lifetime, as explained in Subsection 3.2.2 and Section 3.5.

Besides this SEI, the main drawbacks of graphite anodes are, firstly, their bad combination with the most common Li-ion battery electrolytes, which are based on propylene carbonate (PC). PC intercalates together with Li between the graphitic planes, leading to electrode exfoliation. Secondly, graphitic planes that build each particle are stacked in the same direction, leading to an uniaxial 10% strain along the edge planes due to lithium insertion and extraction, damaging the protective SEI. Some proposals to solve these problems

suggest the use of amorphous carbon to protect the vulnerable edge planes from electrolyte, thereby achieving higher coulombic efficiency [NOZ09].

2.4.1.3 Amorphous carbon

Amorphous carbon behave like small graphitic grains with disordered orientation, which makes them much less susceptible to electrolyte exfoliation and reduced and isotropic volume expansion, giving as a result a high capacity and high cycle life material. However, the high fraction of exposed edge planes increases absolute quantity of SEI formed , reducing the coulombic efficiency during the first cycles and consuming an important part of the limited active Li available in a fresh cell [NIT15].

2.4.1.4 Lithium titanium oxide ($Li_4Ti_5O_{12}$ or LTO)

LTO is a good anode material for low energy, b ut high power, high cycle life and safe Li-ion batteries. Its combination of thermal stability, high rate, relatively high volumetric capacity and high cycle life compensate the high cost of titanium, which increases the price of LTO batteries. However, this material has a larger potential vs. Li/Li^+ (which reduces the cell voltage) and lower specific capacity than other materials, as shown in Figure 2.7.

Its small volumetric change due to lithium insertion and extraction (0.2% change in volume [SCH99, WAG06]) reduces the strain of the electrode and the associated particle cracks. Moreover, its high potential prevents Li dendrite growth and electrolyte decomposition (since the electrolyte is stable at this potential). Unfortunately, surface reactions are not completely avoidable, suffering from gassing between the organic electrolyte and the LTO active material. Therefore, carbon has been proposed as a particle coating [HE13, SON14a], but this material catalyses and accelerates electrolyte decomposition by the building of an SEI.

Even so, LTO anodes can last for tens of thousands of cycles, giving this electrode a distinct advantage over most other anode materials for high power and long life applications, specially when no high energy density is needed [NIT15].

2.4.1.5 Alloying materials

Alloying materials refer to elements which electrochemically alloy and form compound phases with Li at a low potential. The most used alloying mate-

rials for Li-ion battery cathodes are Si and Sn. These components can reach extremely high gravimetric capacity (see Li_xSi_y in Table 2.1), but usually suffer for extreme volume changes (several times its original volume) during lithiation and delithiation. This cause particles to fracture and lose electrical contact [WAN14a], shortening its cycle life and increasing the cell impedance. Some proposals related to particle encapsulation in a carbon shell or electrolyte additives to stabilise the SEI [BOR14] have been published aimed at the improvement of these anode materials.

Silicon is the alloying material that has received the most attention due to its relatively low delithiation potential (~ 0.16 V), extremely high capacity (theoretically 4200 $mAh\,g^{-1}$, see Table 2.1 for comparison), abundance, low cost, chemical stability and non-toxicity [NIT15]. The alloy built with lithium is Li_xSi_y.

Tin (Li_xSn_y) has also been of some interest, given that it has similar properties than silicon, but with a higher conductivity that can counteract its lower gravimetric capacity and slightly lower cell voltage (see Table 2.1).

2.4.2 Positive electrode active material

The positive electrode of a lithium battery is often referred to as *cathode*, since reduction takes place during discharge. As shown in Figure 2.8, when the battery is discharging, the cathode material is reduced by the electrons flowing from the cables, while the lithium ions are intercalated. Conversely, during charge process, the emitted electrons and deintercalated ions are transported to the anode through the external circuit and the electrolyte by means of a non-spontaneous oxidation reaction.

A suitable cathode material is that which fulfils the following conditions:

- Reversible behaviour and a flat potential with the intercalation–deintercalation of Li ions.
- It should be light and densely packed, and have high electrical and ionic conductivities for high power.
- Side reactions unrelated to Li ion circulation should have a minimal weight in the total performance of the cathode.
- Small changes in the crystal lattice volume in order to avoid active material desorption from current collectors.

- They should have electrochemical[3] and thermal[4] stability.

The development of Li-ion batteries has favoured the rise of a wide variety of cathode materials, each of them having advantages and disadvantages, as detailed below and summarized in Table 2.2. Despite the continuous appearance of new families as cathode materials (conversion materials, fluorine and chlorine compounds, etc.), the most commonly-used options are intercalation compounds [NIT15]. Intercalation materials have a crystal structure in which Li-ions can be reversibly intercalated and de-intercalated provoking a small volume change. There are four crystal structures used for Li-ion batteries cathode materials whose main characteristic and representative materials are detailed below.

2.4.2.1 Layered structure compounds

The firstly-discovered and most used structure is the layered lattice, in which the lattice consists of several parallel layers and the lithium ions are intercalated between these layers, as shown in Figure 2.9 (a). These ions have a 2D mobility along the interlayer spaces, resulting in adequate ionic diffusivity in most of layered materials. Besides the traditional $LiCoO_2$, there are other layered materials used as battery cathodes, most of them aimed at reducing cobalt costs:

$LiCoO_2$ (LCO) This is the first and mos commercially successful Li-ion cathode material. It has a relatively high specific capacity (274 $mAh\,g^{-1}$), low self discharge, high discharge voltage and good cycling performance. The major limitations are the high cost of cobalt, low thermal stability and fast capacity fade at high current rates or during deep cycling. Deep cycling (delithiation above 4.2 V, which means approximately 50% of Li extraction) induces lattice distortion from hexagonal to monoclinic symmetry, deteriorating its cycling performance. Many different metals have been proposed as dopants, demonstrating promising but limited results [CHO01].

$LiNiO_2$ (LNO) This material has the same crystal structure as LCO and a similar theoretical specific capacity of 275 $mAh\,g^{-1}$ (see Table 2.2). However

[3]Electrochemical stability is achieved when reactions with the electrolyte are not spontaneous.

[4]Thermal stability refers to exothermic release of oxygen when the cathode is heated above a certain point, resulting in a runaway reaction.

Table 2.2: Main characteristics of cathode materials. Data from [SCR13, PAR12, NIT15].

Material	Theoretical C ($mAh\,g^{-1}$)	Real C ($mAh\,g^{-1}$)	Avg. pot. (V)	Advantages	Issues
LCO	274	~ 150	3.9	Field-tested operation	High cost, low thermal stability
LNO	275	215	3.7	Energy density, low cost	Thermal stability, Li blocking
NCA	200	~ 150	3.6	Long calendar life	Fast ageing at high T
LMO	148	~ 130	4.0	Price, environmental friendly	Reduced cycle life
NMO	280	180	3.8	Energy density, cost	Low Li diffusivity
NMC	278	170	3.7	High capacity	Relatively high price
LFP	170	~ 160	3.4	Low cost, safety, environmental compatibility	Low electronic conductivity and potential

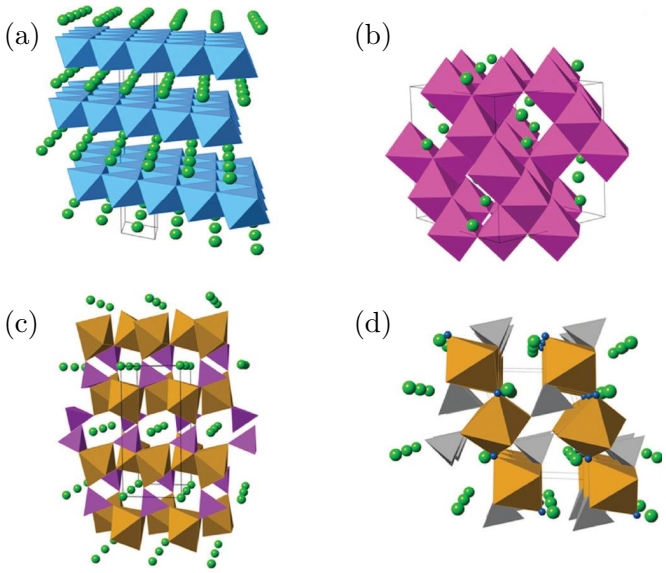

Figure 2.9: Representative crystal structures of cathode materials for lithium-ion batteries: layered $LiCoO_2$ (a), cubic $LiMn_2O_4$ spinel (b), olivine structured $LiFePO_4$ (c) and tavorite-type $LiFeSO_4F$ (d). Li ions are shown as light green spheres. Reproduced from [ISL14b] — Published by The Royal Society of Chemistry.

pure LNO cathodes are not favourable, given than the Ni^{2+} ions have a tendency to substitute Li^{+} sites during synthesis and delithiation, blocking the Li diffusion pathways [ROU96]. Moreover, it is even more thermally unstable than LCO. Partial substitution of Ni with Co is an effective way to reduce cationic disorder [KAL05], and a small amount of Al can improve both thermal stability and electrochemical performance [CHE04], building the NCA material explained hereafter.

$LiNi_{0.8}Co_{0.15}Al_{0.05}O_2$ (NCA) Its high usable discharge capacity and long storage calendar life have made from this material a widespread cathode for commercial applications. For example, the cathode of the Panasonic cells manufactured for Tesla EVs is NCA. However, this material has been reported to have a severe capacity fade when subjected to high temperatures [BLO03, ITO05].

$LiMnO_2$ (LMO) This is a cheaper and less toxic compared with previous layered materials. The lattice structure does not have a high stability, and therefore the layered structure has a tendency to irreversibly change to spinel structure. Moreover, the carbon anode impedance increases when Mn is solved in the electrolyte, problem which is avoided with LTO anodes.

$Li(Ni_{0.5}Mn_{0.5})O_2$ (NMO) This cathode can maintain similar energy density to LCO, while reducing cost by using lower cost transition metals. However, it has a lower Li diffusivity, which may result in unappealing rate capability [ROS92].

$LiNi_{0.33}Co_{0.33}Mn_{0.33}O_2$ (NMC) It has a similar achievable specific capacity than LCO and similar operating voltage, while having lower cost by reducing the Co requirements. This material has been reported to have a good cycle stability, and several rates of Ni, Co and Mn have been proposed in order to achieve different characteristics. Even concentration gradient of these three transition metals in each material particle has been proposed in some research papers [SUN09].

2.4.2.2 Spinel structure compounds

Spinel structures are cubic close-packed oxides with two tetrahedral and four octahedral sites per formula unit, where Li ions can be inserted, as represented in Figure 2.9 (b). $LiMn_2O_4$ is a representative spinel active material.

$Li_2Mn_2O_4$ (LMO) Care should be taken with the acronym LMO, since it is sometimes used to refer to the layered $LiMnO_2$ cathode. In this section concerns the spinel $Li_2Mn_2O_4$ cathode (page 31). It has several benefits related to the abundance, cost and environmental friendliness of Mn. In this structure, Mn is located in the octahedral spinel sites and Li in the tetrahedral sites. Therefore, Li^+ can diffuse through vacant tetrahedral and octahedral interstitial sites in the 3D structure. However, this cathode suffers from insufficient long-term cyclability, which is believed to be originated by Mn dissolution and formation of tetragonal $Li_2Mn_2O_4$.

2.4.2.3 Olivine structure compounds

The olivine structure is a hexagonal, close-packed array of oxygen ions with half of the octahedral sites occupied with a metal and one-eighth of the tetrahedral sites occupied by a non-metal, as represented in Figure 2.9 (c). The representative olivine structure used as Li-ion cathode material is $LiFePO_4$.

$LiFePO_4$ (LFP) LFP has a good thermal stability and high power capability. However, the major weakness is its low average potential. This issue is normally tackled by substituting oxygen by large polyanions (XO_4^{y-}in the crystal lattice. The strong X–O bond reduces the Fe–O bond, increasing the ionization tendency of Fe^{3+}/Fr^{2+} and improving voltage [TU06, LIN14]. Reduction in particle size, carbon coating and cationic doping have been proven to be effective in increasing the rate performance of this material [NIT15].

2.4.2.4 Tavorite structure compounds

Tavorite materials have 1D diffusion channels, as represented in Figure 2.9 (d). They have been proposed to exhibit low activation energies, allowing charge and discharge at very high rates, comparable to those observed in small olivine particles. Some of these materials contain vanadium, which raises concern about toxicity and environmental impact. The previously-explained material families have been way more widely used than tavorite components [NIT15, PAR12].

2.4.3 Electrolyte

The electrolyte of a Li-ion battery is the medium for the movement of ions. Besides allowing the ion flow, the intercalation reaction takes place on the

interface between the electrodes and the electrolyte. Therefore, an electrolyte for Li-ion batteries should meet the following requirements [PAR12]:

- High ionic conductivity. The movement of ions at the electrodes and diffusion within the electrolyte are especially important when the battery is rapidly charged or discharged.
- High chemical and electrochemical stability toward electrodes. Given the electrochemical reactions that take place in a battery, the electrolyte should be electrochemically stable within the potential range of redox reactions at both electrodes. Besides, it should be chemically stable toward the metals and polymers constituting the cathode, anode and other parts of the cell.
- Characteristics kept over a wide temperature range. A common temperature for Li-ion batteries is considered to range from –20 to 60 °C, and a proper electrolyte should keep its characteristics through the whole range.
- High safety. Some materials used in electrolytes are flammable and may cause fires or explosions when heated to high temperatures during short circuits. Higher ignition points are favoured, and non-flammable materials should be used when possible. The electrolyte should also have a low toxicity in case of leakage or disposal.
- Low cost. Given the fierce market competition for Li-ion batteries, expensive materials are unlikely to be adopted.

Four types of materials have been proposed to be used as electrolytes for Li-ion batteries. Their characteristics, advantages and disadvantages are covered in the following subsubsections and summarised in Table 2.3. From these four types of electrolytes, liquid electrolytes are present in most of the Li-ion battery that is nowadays in the market. On the other hand, solid polymers have not been commercially used. As explained below, gel polymers are used to manufacture the so-called lithium-polymer (LiPO) batteries and ionic liquids are a developing research area in which several promising results are being published.

2.4.3.1 Liquid electrolytes

Liquid electrolytes, consisting on lithium salts dissolved in organic solvents, are the most widely used electrolyte in commercially-available batteries. Organic

Table 2.3: Comparative chart of electrolyte materials [PAR12].

	Liquid electrolytes	Ionic liquid electrolytes	Solid polymer electrolytes	Gel polymers electrolytes
Composition	Organic solvents + Li salt	RT ionic liquids + Li salt	Polymer + Li salt	Org. solvents + polymer + Li salt
Ion conduct.	High	High	Low	Relatively high
Low-temp. performance	Relatively good	Poor	Poor	Relatively good
Thermal stability	Poor	Good	Excellent	Relatively good
Applicability	Most used	Promising future	Not used	Some pouch cells

solvents are used instead of aqueous electrolytes because of the high potential of Li-ion batteries. The greater disadvantage of organic solvents is their low dielectric constant. A higher dielectric constant results in greater dissociation as it is inversely proportional to the Coulombic force between cations and anions of the lithium salt. The working temperature is conditioned by the melting and boiling points of the solvent, which should remain liquid at any operation temperature and keep its ability to dissolve the lithium salt also at low temperatures. Some examples of solvents used in Li-ion batteries are ethylene carbonate (EC), propylene carbonate (PC), dimethyl carbonate (DMC), ethylmethyl carbonate (EMC) and other organic solvents.

Besides the solvent, attention should be paid to the dissolved lithium salt. Specifically, the salts with bigger ions are favoured, given that Li salts having delocalized anions tend to dissociate more readily. However an increase in ionic radius leads to less movement of anions, which can prevent lithium movement through the electrolyte.

2.4.3.2 Ionic liquid electrolytes

An ionic liquid refers to a salt in the liquid state, formed by organic cations and inorganic anions. In particular, those found in the liquid state at room temperature are called room-temperature ionic liquids. The main characteristics of ionic liquids that should be taken into account for their use as a battery electrolyte are:

- They are liquid in a wide temperature range.
- They have high ionic conductivity due to the high concentration of ions

- They are non flammable and thermally resistant.
- They are chemically stable.
- They have a relatively high polarity and ionic conductivity.

Ionic liquids are a large family of materials that offers multiple options for the material design. Due to this issue, high expectancies are put on ionic liquids to replace the problematic liquid electrolytes of Li-ion batteries, and intensive research on this topic has been made in recent years, as summarised by Efterkhari et. al in their review paper [EFT16]. A promising possibility related to ionic liquids, which is still at an early stage of development, is supercooled ionic liquid crystals for fast ion diffusion through the guided channels of a liquid-like medium. If this option is materialised, it will be a breakthrough for general electrochemistry, far beyond Li-ion batteries [EFT16].

2.4.3.3 Solid polymer electrolytes

Solid electrolytes have several advantages over liquids, such as higher energy density and reliability, no risk of leakage, no release of combustible gases at high temperature and no membrane requirement. Solid polymer electrolytes consist solely on a polymer and salt. The polymers should ease the lithium ions transport and salt dissociation. Most research related with solid polymer electrolytes has focused on synthesising new polymers to enhance ionic conductivity [KIM06, HUA01]. Ionic conductivity, mechanical strength and electrode/electrolyte surface characteristics can be enhanced by adding inorganic particles to solid polymer electrolytes.

Despite such active research, Li-ion batteries with solid polymer electrolyte have yet to be fully commercialised. Compared to liquid electrolytes, solid polymer electrolytes have low ionic conductivity at room temperature, weak mechanical properties and poor interfacial characteristics [PAR12].

2.4.3.4 Gel polymer electrolytes

These electrolytes are formed by polymers, organic solvents and lithium salts and are produced by mixing organic electrolytes with solid polymer matrices. Even though there is a polymeric phase, the ionic conductivity of gel electrolytes is between that of liquids and solid polymers, due to the electrolyte encapsulated in the polymer chains. Representative polymers used as matrices are polyacrylonitrile, poly(vinylidene fluoride) and poly(methyl methacrylate).

The lithium batteries with gel polymer electrolytes are called lithium–polymer batteries (LiPO batteries). The low ionic conductivity of gel polymers compared to liquid electrolytes is the main reason for the little advancement in the development of LiPO batteries. Poor interfacial contact with electrodes is another problem arising from gel polymer electrolytes, which has special significance when the battery is charged or discharged at high current rates.

2.4.4 Membrane

The membrane (or separator) is a non-active material (which does not participate in the electrochemical reaction) which must be an electric insulator but ionic conductor. Together with electrodes and electrolyte, separators play an important role in determining the battery performance and safety [LEE14]. A picture of a disassembled 40 Ah commercial Li-ion cell is shown in Figure 2.10, where the membrane can be seen as a white, plastic film to separate both electrodes. The cell consists in 48 stacked electrodes connected in parallel to the connection taps (top part of the closed cell). An anode and a cathode are shown on the opened cell. The black part is the active material (graphite for the anode and NMC for the cathode), half of which was removed to shown the copper an aluminium current collectors. The membrane, which is intercalated between the electrodes, is shown at the right of the opened cell.

The membranes are microporous polymer films with pores ranging from nanometres to micrometers. The most used material are polyethylene and polypropylene, which have various advantages including outstanding mechanical strength, stability and low cost [HOH64, JON89]. These materials have a low thermal shut-down temperature (135–165 ^{o}C), at which the membrane melts and the pores get blocked, restricting ion movement and thus improving battery safety.

The most important characteristics to take into account for membrane design are its thickens, electrical resistance, permeability, pore size, porosity, shut-down temperature, chemical stability, etc.

2.4.5 Current collectors

Current collectors are electrical conductors that supply or deliver electrons from the electrode active material. Given the required electronic conductivity, electrochemical stability and mechanical strength, metal are commonly used as material for current collectors. Specifically, thin films (10–20 μm of aluminium and copper are used at the cathode and anode, respectively. For the battery manufacturing, electrode active materials are coated on these current

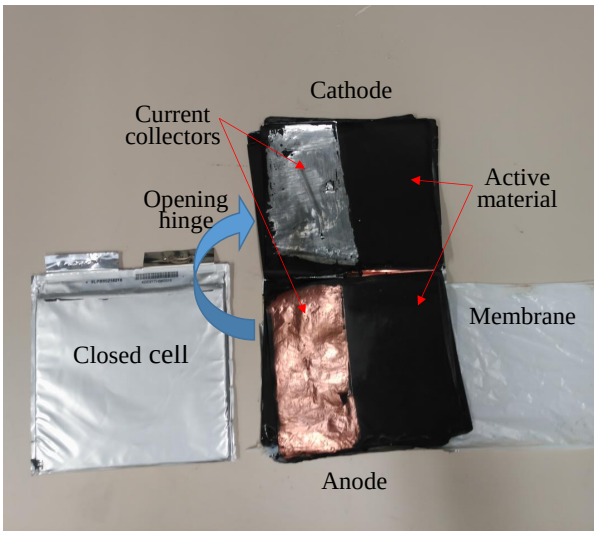

Figure 2.10: Disassembled 40 Ah pouch cell with graphite anode and NMC cathode.

collectors. Figure 2.10 , where the current collectors can be seen to be made of aluminium and copper.

Copper is used as anode current collector, given its low price and electrochemical stability at 0–3V vs. Li/Li^+, which is the working potential of carbon electrodes. However, copper cannot be used as cathode current collector, given that its oxidation occurs at 3 V vs. Li/Li^+ and cathodes have higher working potential. Taking this voltage limitation and cost into account, aluminium is the most appropriate material to be used as cathode current collector.

2.5 Classification

The different manufacturing techniques for Li-ion cells and materials covered in Section 2.4 can be combined to give a wide variety of different Li-ion batteries. Lithium is the active material in all of them, which can be either ionized while in solution or bound to an electrode; but never exists as metal. This is why these batteries are called Li-ion batteries. This variability of materials and manufacturing processes gives rise to multitude Li-ion battery types with different functionalities and prices.

Two usual classifications for Li-ion batteries are presented in this section. The first of them is based on the battery manufacturing technique (and therefore shape), while the second one is based on its main materials. It is note-

worthy that *Li-ion battery* is a broad concept that groups several families of batteries which have in common the use of lithium as active material with no presence of lithium metal. Given the vast number of possible combination between different anodes, cathodes, electrolytes and membranes, an exhaustive classification of every Li-ion battery cannot be presented. However, the most typical batteries commercialized nowadays are classified through the following subsections.

2.5.1 Based on cell shape

The cell shape is an important parameter from several points of view, including manufacturing technique, battery pack assembly and cooling method. Four are the most common layouts of Li-ion battery cells:

2.5.1.1 Cylindrical cell

This is the most typical shape for a battery cell. Its main advantages are ease of manufacture and good mechanical stability. Most cylindrical cells have a pressure relief mechanism to avoid risk of explosion. The simplest design consists on a membrane that is broken under high pressure. Re-sealable vents with a spring valve are the preferred design.

For easier use, standardization of the cell sizes has resulted in a number of available formats, being the 18650 cell shown in Figure 2.11 (a) the most used one. These number mean that the cylinder measurements are 18 mm in diameter and 650 mm in length. The 18650 cell could be the most optimized cell, offering one of the lowest costs per Wh and with good reliability records. Typical applications of this cell format are power tools, medical instruments, laptops and e-bikes. Tesla electric vehicles also use 18650 cells for now. However, Tesla, Panasonic and Samsung have decided to move to a larger 21700 cell for easy of manufacturing, optimal capacity and other benefits.

At a first glance, the fact that cylindrical cells do not fully utilize the space of a battery pack due to its circular shape can be seen as a disadvantage concerning power and energy density of the whole battery pack. However, the higher energy density reached with cylindrical cells (248 $\mathrm{Ah\,kg^{-1}}$ vs. 140 $\mathrm{Ah\,kg^{-1}}$ given by pouch cells) counteracts this issue. Moreover, the empty space can be used for cooling to improve battery thermal management. This separation has also advantages referred to safety issues, since cylindrical cells are always spaced apart to prevent thermal runaway propagation.

(a) (b) (c) (d)

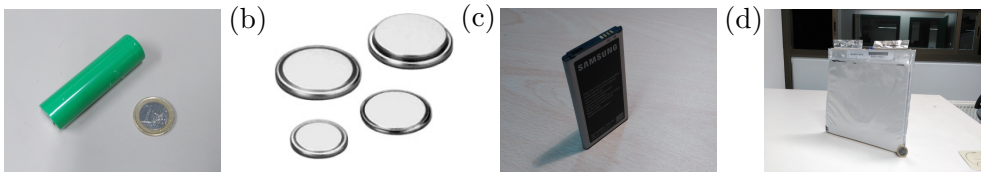

Figure 2.11: Lithium-ion cell shapes: cylindrical 18650 (a), button (b), prismatic (c) and pouch (d).

2.5.1.2 Button cell

Button cells are also known as coin cells, used to be attractive designs for small electronics, medical devices and security wands at airports. As shown in Figure 2.11 (b), they are small and inexpensive to build and can be stacked to achieve higher voltage. However, their main drawback is the low charging capability, given that they have to be charged no faster than 10 or 16 hours. This issue makes other battery format more attractive than button cells. Today, most button cells are non-rechargeable and can be found in medical implants, watches, hearing aids, car keys and memory backup.

2.5.1.3 Prismatic cell

As shown in Figure 2.11 (c), prismatic cells are wound and flatted into a pseudo-prismatic jelly roll. They make an optimal use of the space and are found in mobile phones, tablets and low-profile laptops. There are not universal standard measurements, and it is common for each manufacturer to design its own cells. These cells require a firm enclosure to achieve compression, and some swelling due to gas build up should be expected. This build up must be taken into account in order to allow battery growing. Actually, a 5 mm cell could grow to 8 mm after only 500 cycles.

2.5.1.4 Pouch cell

This cell design was firstly proposed in 1995 by substituting the metallic cylinder case by a fully sealed plastic bag, as shown in Figure 2.11 (d). This design is simple, flexible and light. It makes the most efficient use of space, achieving 90–95% packaging efficiency. Similarly to prismatic cells, no standardised sizes exist, and each manufacturer fabricates its cells with the required size.

Given their flat shape, heat can be easily evacuated from these cells, making them very suitable for high-power applications such as drones, electric vehicles, etc. Although easily stackable, provision must be made for swelling,

as shown in Figure 2.12. Pouch cells can grow 8–10% after 50 cycles. Therefore, it is best not to stack them on top of each other but to lay them flat, side by side or allow extra space in between them. The pressure created by a swollen pouch cell in an electronic device could break the display and electronic circuitry.

Pouch cells are manufactured by stacking electrodes, previously cut with the cell shape, intercalated with the membrane. During the first charge process, when the SEI is built, some gas is released. Therefore, a *gasbag* must be temporarily placed on the side to collect this gas and let the pouch cell with its flat shape. After this formation process the gasbag is cut off and the pack is resealed to form the finished product. Subsequent charges should produce minimal gases, however, gas generation, cannot be fully avoided. It is caused by electrolyte decomposition during normal operation.

2.5.2 Based on materials

The different materials that can be used to build different parts of the battery have been covered in Section 2.4. All the viable combinations of those materials give rise to a wide variety of Li-ion batteries, which are named after their characteristic material. Six battery types are highlighted in this section for being the most used technologies. Most of them are named after their cathode material, given the wider variety of materials for this electrode.

Isidor Buchman presents in his book Batteries in a Portable World [BUC16] radar charts to compare several characteristics of different Li-ion battery technologies, which are reproduced in Figure 2.13. The six chosen characteristics to be compared are specific energy and power, safety, performance, life span and cost. Each of these characteristics represented in radar charts is graded from the central point to the outer, representing the middle point the worst grade and the most external mark on each axis the best grade. Therefore, for a general comparison between technologies, the larger the polygon area (coloured dark green in Figure 2.13), the better the battery characteristics.

With the support of these charts, the main advantages and disadvantages of each battery type, along with their main applications are summarised hereinafter.

2.5.2.1 LCO

LCO is the most mature Li-ion battery chemistry. These batteries are characterised for having $LiCoO_2$ as cathode material. They have high nominal

Figure 2.12: Fresh and swollen pouch cells used in an iPhone cellular.

voltage (3.9 V) and high energy density. However, they are expensive (because of their cobalt content), have relatively short lifespan and have poor thermal stability, provoking safety concerns, as represented in Figure 2.13 (a). Moreover, they have limited power capability, and should not be charged and discharged faster than 1C.

LCO batteries are mostly used in portable electronic devices, but are recently losing favour to other options such as LMO and, especially, NMC and NCA because of the high cost of cobalt and improved performance by blending with other active cathode materials.

2.5.2.2 LMO

LMO batteries use $LiMn_2O_4$ as cathode active material. They achieve higher nominal voltage than LCO (4.05 V), but lower energy density (approximately 20% less). They are inexpensive, given that Manganese is much cheaper than cobalt, and safer than LCO. Moreover, their low internal resistance enables fast charging and high-current discharging. However, they are moderate in overall performance, especially at high temperature and have limited cycle and calendar ageing, as shown in Figure 2.13 (b).

There are important research trends towards blending LMO with NMC and/or NCA as active cathode material to improve the specific energy and prolong the life span. This combination brings out the best in each system, and the LMO (NMC) is chosen for most electric vehicles, such as the Nissan Leaf, Chevy Volt and BMW i3. The LMO part of the battery, which can be about 30%, provides high current boost on acceleration while the NMC part gives the long driving range.

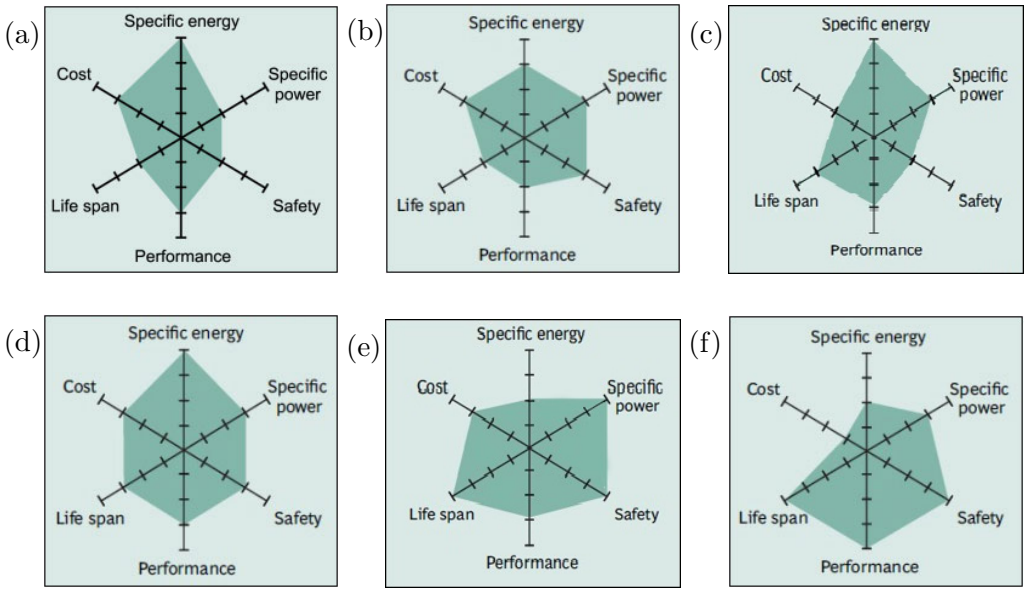

Figure 2.13: Characteristics of main Li-ion batteries: LCO (a), LMO (b), NCA (c), NMC (d), LFP (e) and LTO (f). Reprinted form [BUC16].

2.5.2.3 NCA

The cathode of these batteries is made of $LiNiCoAlO_2$. It offers the highest specific capacity (up to 200 $mAh\,g^{-1}$) which results in high energy and power density, even though they suffer from reduced nominal voltage in comparison with LCO or LMO. Less convenient are safety and cost of these batteries, as represented in Figure 2.13 (c).

This technology is the one chosen by Tesla for its electric vehicles. The increasing manufacturing requirements of this kind of batteries associated with the EV market is expected to bring reduced costs in the upcoming years.

2.5.2.4 NMC

The cathode of these batteries is made of $LiNiMnCoO_2$, in which different proportions of each transition metal can be used to achieve particular performance requirements. There are NMC batteries tailored to serve as energy cells or as power cells. For example, NMC in an 18650 cell for moderate load condition has a capacity of about 2800 mAh and can deliver 4 A to 5 A; NMC in the same cell optimized for specific power has a capacity of only about 2000 mAh but delivers a continuous discharge current of 20 A [BUC16].

NMC is the battery of choice for many power tools, e-bikes and stationary applications. Given their lower cost and similar characteristics than LCO batteries, they are increasing their market share.

2.5.2.5 LFP

LFP batteries are built with a $LiFePO_4$ cathode. Its specific capacitance, which is similar to that of LCO batteries, but lower nominal voltage (3.3 V) bring a low energy density to these batteries. They are tolerant to full charge conditions and are less stressed than other batteries if kept at high voltage for a prolonged time. As a trade-off, they have a higher self-discharge rate, which can lead to problems related with imbalance between cells. As shown in Figure 2.13 (e), LFP batteries are very safe and provide long lifetime, while having high power capability during both charge and discharge.

LFP batteries are used in some hybrid electric vehicles, but their main applications are stationary systems, in which specific energy is not a critical issue when compared to life span, specific power and cost.

2.5.2.6 LTO

These batteries are named after their anode material, given that the traditional carbonaceous anode is substituted by $Li_4Ti_5O_{12}$. Their cathode is usually lithium manganese oxide or NMC. This type of batteries provides the longest lifetime, very safe performance and thermal stability as well as high specific power, even at low operation temperature, as shown in Figure 2.13 (f). However, its nominal voltage of 2.4 V also entails the lowest energy density (65 $Wh\,kg^{-1}$).

LTO batteries are very suitable for stationary energy storage applications where extremely long lifetime is required. They are also used in UPS and electric powertrains such as Mitsubishi i–MiEV and Honda Fit EV.

Given that energy density is a main parameter for many battery applications, a comparative graph between the value of this magnitude for different battery technologies is presented in Figure 2.14. Besides the above-mentioned Li-ion options, coloured in orange, tentative figures of lead–acid (brown), Ni–Cd and Ni–MH batteries (green) are included in the comparative. In general, Li-ion batteries are seen to provide much higher values of specific energy than the other battery types. In this figure, a big difference between Li-ion batteries is appreciated, whose specific energy ranges from 80 $Wh\,kg^{-1}$ of LTO batteries to 250 $Wh\,kg^{-1}$ offered by NCA.

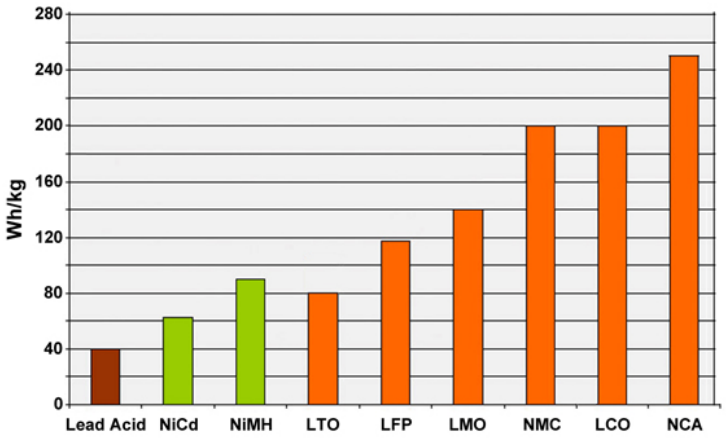

Figure 2.14: Specific energy of different types of Li-ion batteries and other chemistries. Reproduced from [BUC16].

A number of studies have been published with the aim of forecasting the most promising Li-ion battery technology for the upcoming years. For instance, a study published by *Cairn Energy Research Advisors* [JAF17] predicts the share of the increasing Li-ion battery market during the next 10 years (2017–2026), as shown in Figure 2.15. Based on this report, the most promising battery cathode material in the mid term is NMC, followed by LFP and NCA. Due to the high cost of Co, LCO batteries are expected to have a decreasing interest during the upcoming years.

2.6 A look into the future of lithium

The first Li-ion battery boom took place in the 2000s and was related to portable device, the second one is currently happening and is related to electric vehicles and electrical mobility in general, and the third one is expected to happen during the following decades, with rapid grow of stationary energy storage, specially small-scale batteries installed in households and PV systems. According to Bloomberg, Li-ion batteries for energy storage will become a $20 billion per year market by 2040 [NEW17]. Due to this growing Li-ion battery demand, both in quantity and in technical requirements, important research efforts are being made at every level aimed at improving this technology and cover the market demands.

Concerning engineering research in Europe aimed at optimizing the existing materials and getting the most out of each battery, a research project called

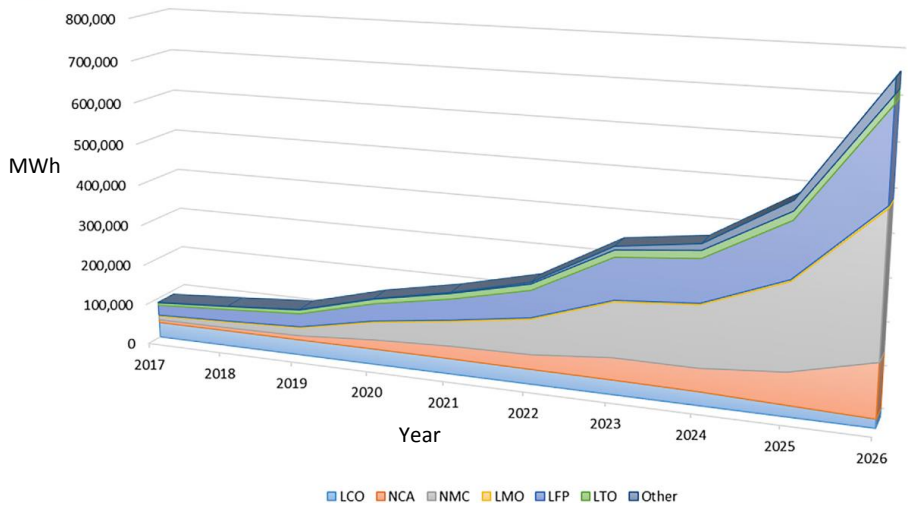

Figure 2.15: Lithium-ion battery market forecast divided by type. Reprinted from [JAF17].

Batteries 2020 was recently concluded [EU16]. The Spanish IK4–IKERLAN research centre led this project, which counted with first-level research partners from universities and companies such as the research group led by D. U. Sauer at the RWTH Aachen University, Aalborg University, Leclanché and Abengoa. This consortium could increase both the energy density and lifetime of large format NMC pouch lithium-ion batteries towards the goals targeted for automotive batteries (250 $\mathrm{Wh\,kg^{-1}}$ at cell level and over 4000 cycles at 80% depth of discharge). Three strategies were tackled at the same time: (*i*) materials developments, specifically two new generations of NMC cathode materials were developed to improve the performance, stability and cyclability of existing battery cells, (*ii*) better understanding of the ageing phenomena and (*iii*) reduction of battery cost by considering second life of batteries already used in electric vehicle applications [SWI16, TIM16].

Great steps are taken in the USA towards cheaper and more reliable Li-ion batteries. The engineering research done by Tesla and the construction of the factory known as *Gigafactory 1* in Nevada are remarkable examples of the expected battery development during the upcoming years. The Tesla Gigafactory 1 is already operational while finishing construction work at the Tahoe Reno Industrial Center, Nevada. Two construction phases are shown in Figure 2.16, along with the final planned size. The factory started limited production of Powerwalls and Powerpacks in the first quarter of 2016 [JOH16] using battery cells produced elsewhere, and began mass production of cells in January 2017 [RAN17]. Given the expectations of building new gigafacto-

Figure 2.16: Gigafactory 1 construction phases. It doubled its size from July 2016 to January 2017, when 30% of the factory was completed.

ries, Tesla began to refer to the SolarCity Gigafactory at Buffalo, New York, in February 2017, as *Gigafactory 2*. The projected Europe Gigafactory will be named either Gigafactory 3, 4, or 5 and the location is expected to be announced in 2017 [DOW17].

At material level, there are several research lines aimed at improving battery materials. The major challenge is to move a step forward passing from the current intercalation chemistry to novel concepts that may lead to advanced batteries.

Lithium-metal Rechargeable lithium-metal batteries were manufactured before Li-ion, but the dendrite growing prevented its widespread commercialisation. In 2010, a trial Li-metal with a capacity of 300 $\mathrm{Wh\,kg^{-1}}$ was installed in an experimental electric vehicle. DBM Energy, the German manufacturer, claims 2500 cycles, short charge times and competitive pricing [BUC16]. 300 $\mathrm{Wh\,kg^{-1}}$ would be the highest achieved energy density, given that NCA batteries in the Tesla S 85 has 250 $\mathrm{Wh\,kg^{-1}}$ and LMO batteries of the BMW i3 have 120 $\mathrm{Wh\,kg^{-1}}$.

Lithium–air Similarly to fuel cells, the battery uses the oxygen from the air to make the electrochemical reaction of the cathode, while the anode is made of lithium. The theoretical specific energy of Li–air batteries is 13 $\mathrm{kWh\,kg^{-1}}$. If only one quarter of this theoretical value is reached, the combined battery energy density and high efficiency of an electric motor ($\sim$90%) could be on par with a gasoline tank (13 $\mathrm{kWh\,kg^{-1}}$) and its low-efficient thermal motor

(25–30%).

However, the specific power of Li–air batteries is low, especially at cold temperatures. Air purity is also important for these batteries, and it may need to be filtered for its use in a battery. As a result, the battery may end up with compressors, pumps and filters which increase its size and weight and consume part of the battery power. Another problem of Li–air batteries is the so-called *sudden death syndrome* due to the lithium peroxide films built by the reaction of lithium and oxygen, which prevents electron movement and results in an abrupt reduction in the battery's storage capacity. Research efforts are being made with additives that reduce the lithium peroxide formation and improve the cycle life.

Lithium–sulphur Li–S batteries are based on the dissolution of lithium from anode and its incorporation into alkali metal polysulfide salts during discharge, and reverse plating to the anode while charging. These batteries get ride of the intercalation material needed for Li-ion batteries. On the one hand, the intercalation graphite can be removed from the anode and metallic lithium can be used. On the other hand, the metal oxide cathode is replaced by cheaper and lighter sulphur. Each sulphur atom can host two lithium ions while the typical amount hosted by a Li-ion battery cathode material ranges from 0.5 to 0.7 lithium ions per host atom.

These batteries have a theoretical energy density on the order of 2600 $\mathrm{Wh\,kg^{-1}}$, and a European H2020 Research Project ended in 2016 called ALISE reached a value of 500 $\mathrm{Wh\,kg^{-1}}$ in a Li-S battery for cars developing new and optimised components regarding anode, cathode, electrolyte and separator [ALI17]. Some issues that need to be solved to allow further development of Li–S batteries are the low conductivity and massive volume change of sulphur during charging and discharging. Carbon coating is being studied to improve the electrical conductivity of the sulphur cathode, bot these issues are still not solved. Moreover, the achieved cycle life for Li–S batteries is still too short to allow its commercialisation. While S and $\mathrm{Li_2S}_n$ are relatively insoluble in the electrolyte, many intermediate polysulfides are not, and its dissolution in the electrolyte causes irreversible loss of active sulphur. The use of a protective layer has been studied to improve this issue, but more research is still needed [JEO07, ISL14a].

Solid-state lithium Solid-state technology replaces the liquid electrolyte of current Li-ion batteries by a solid polymer or a ceramic separator. A solid electrolyte allows to plate and strip alkali metals on both the cathode and

the anode side without dendrites, which simplifies battery cell fabrication and eliminates the intercalation material, thereby reducing the mass of the battery.

In January 2017, the team leaded by Professor Goodenough (Figure 2.17), published a paper reporting the development of a low-cost all-solid-state battery that is noncombustible and has a long cycle life with a high volumetric energy density and fast rates of charge and discharge [BRA17]. This battery is claimed to have three times as much energy density as regular Li-ion batteries while allowing for a greater number of charge–discharge cycles.

However, part of the research community is sceptical about this finding. Dan Steingart, a professor of mechanical engineering at Princeton, said: "If you could accomplish what this paper claims, it would rewrite the way we think about chemistry", and "As revered and important as John Goodenough is, the mechanism described to account for the anomalous capacity appeared to be in conflict with the first law of thermodynamics" [STE17b]. Matthew J. Lacey, a researcher at the Ångström Advanced Battery Centre at Uppsala University, Sweden, is also sceptical, and he provides the following explanation to the published results: "There is considerable reason (and precedent) to suspect that the energy stored and released by the cell is significantly influenced by decomposition reactions of the electrolyte and/or reactions of impurities in the electrolyte".

As usually happens in science, other researches will repeat the proposed method in the upcoming months, take different measurements, critically analyse the results and, thereby confirm or disprove this all-solid-state battery.

Sodium-ion These batteries use the operation principles used by Li-ion, but using sodium (Na) ion as charge carriers. The advantages of Na-ion batteries

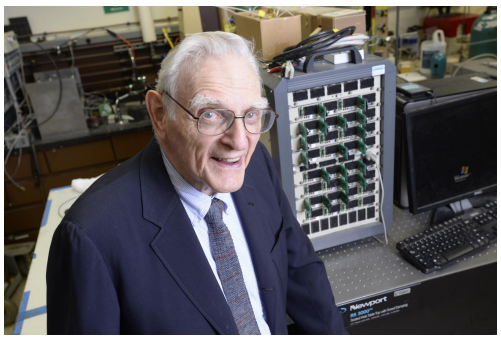

Figure 2.17: John B. Goodenough in the laboratory where he researches, at the University of Texas at Austin, at the age of 94 years (2017).

are the low cost and abundance of Na compared to Li, their ability to fully discharge with no damage to the cells, reducing the risk of short circuits and ignition when batteries are stored (Li-ion batteries have a 30% of irreversible capacity that cannot be discharged).

A drawback of Na-ion batteries is its lower energy density, which may reduce its use to sectors where size and weight are not major issues, such as stationary energy storage and renewable energy plants. Moreover, the large expansion and contraction of electrode size during charge and discharge lead to a reduced lifetime of Na-ion batteries, and intensive research is aimed at improving the characteristics of this promising battery technology [PAN13, STE00, ZHU13, SAA14].

Chapter 3

Fundamentals of lithium-ion batteries

I'm old enough to know you can't close your mind to new ideas.

– John B. Goodenough, 2017

3.1 Introduction

The main physico-chemical processes that are the basis of the performance of lithium-ion batteries are presented in this chapter. These principles are used as the foundation for subsequent discussion presented in the following chapter of this thesis. These fundamentals are crucial for a wide variety of aspects related with lithium-ion batteries, such as the improvement and cheapening of manufacturing processes, the analysis of ESS through modelling, the control of the power converters connected to the ESS, the design of management strategies for a battery system, etc. In all these situations, the accurate knowledge of the fundamental principles that drive the battery performance allows for the design and manufacturing of a suitable battery for the desired application or for the maximization of the performance of a battery in a particular energy system.

Along this chapter, four different phenomena are analysed. Firstly, Section 3.2 concerns thermodynamic processes, which analyse steady-state systems. Thermodynamic applied to batteries means open circuit analysis (no current flow through the battery). The equilibrium potential in typical Li-ion

batteries electrodes is addressed in this section, as well as the equilibrium between the anode and the electrolyte. This equilibrium has particular interest in Li-ion batteries, since the electrolyte is not stable at the working potentials of the negative electrode. The equilibrium is only possible through the formation of a so-called solid–electrolyte interface (SEI) which is a hot research topic for the manufacturing processes and which has a main importance in the performance and ageing of Li-ion batteries.

Secondly, in Section 3.3, the most important electrochemical processes are gathered, i.e. the effects that the electrochemical reaction has on the battery. Therefore, electrochemical principles are applied when current is driven through the battery. The phenomena covered in this section are ohmic phenomena, related with the opposition of battery materials to the movement of electrons and ions; the electrochemical of the redox reactions driven by the Butler–Volmer equation, which us the causing of the so-calling activation losses; and the effects of ion transport through the electrolyte and in the electrode, which is governed by the diffusion laws and cause the diffusion (or concentration) losses. The result of these phenomena are overvoltages that lead to energy losses in the battery, as detailed in Section 3.3.

Thirdly, the ageing phenomena are analysed in Section 3.5, explaining the battery components involved in each ageing mechanism and the working conditions that determine the battery degradation rate. Moreover, the implications that these mechanisms have on the battery applications (capacity fade and power fade) are explained and the concepts of calendar and cycle ageing are introduced, which are often used to model the ageing of a Li-ion battery.

Finally, the most remarkable thermal phenomena taking place in Li-ion batteries are analysed in Section 3.4. The effect that operation temperature has on the battery performance is presented, which motivates a further study of thermal issues for practical applications. Besides, the heat generation mechanisms are gathered, empathising the difference between reversible and irreversible heat generation. The heat transmission and evacuation to the surroundings is also covered, summarising the fundamental concepts concerning heat conduction and convection.

These fundamental processes are related one to each other, given that the battery is a single physical system in which each phenomenon affects the others. Actually, battery ageing and operation temperature affect its thermodynamic and electrochemical performance, and in turn the temperature affects the ageing phenomena. Meanwhile, electrochemical processes are the main cause of heat generation and of ageing phenomena. Therefore, a Li-ion battery is a complex physical system, which has important benefits and po-

tential, but also entail thrilling challenges concerning its study, understanding and management.

3.2 Thermodynamics

Thermodynamics is the branch of physics that addresses the fundamentals of the physical and chemical behaviour of equilibrium matter [MOR04]. Therefore, thermodynamic laws are used to explain the state of a battery when it is kept at equilibrium, i.e. when it is kept in open circuit and, therefore, neither electrons nor ions circulate through the system. The equilibrium potential of the typical Li-ion battery insertion electrodes is explained in the following subsection. Thereafter, in Subsection 3.2.2, the reason why the graphite electrode and the organic electrolyte can be used to build a Li-ion battery, even though the thermodynamic equilibrium potential between these materials when the battery is charged would lead to a spontaneous reaction and the consequential destruction of the battery.

3.2.1 Equilibrium potential of insertion electrodes

The electrochemical reaction at the electrode–electrolyte interphase can be expressed as follows:

$$\mathrm{Li}^{+} + \mathrm{e}^{-} + \theta_s \rightleftharpoons [\mathrm{Li}^{+\delta} - \theta^{-\delta}]$$

where the expression $\left[\mathrm{Li}^{+\delta} - \theta^{-\delta}\right]$ represents the intercalated species, denoted hereafter by subscript $_{\zeta}$. The following relationship can be established based on thermodynamic principles:

$$F \cdot v_{eq} = \mu^{0}_{Li} + \mu_{\psi} - \mu_{\zeta} \tag{3.1}$$

where F is the Faraday constant. Note that the chemical potential μ_j ($j = \zeta, \psi$) is not dependent on the composition of the host material. The chemical potential of a species j in any condition can be related to the potential in other temperature and concentration conditions through activity coefficient (γ_j) and molar fraction (x_j) [KAR08]. In a Li-ion battery, the forces caused by the interaction between positively-charged Li ions and negatively-charged host material cause the non-ideal behaviour [KAN92]. Therefore, activity a_j, is defined as follows, being $j = \zeta$ or ψ:

$$a_j = \gamma_j \cdot x_j \tag{3.2}$$

Therefore, the chemical potential can be calculated from reference chemical potential (μ_j^0), which is tabulated, through Equation 3.3:

$$\mu_j = \mu_j^0 + R \cdot T \cdot \ln(a_j) \tag{3.3}$$

being R and T the gas constant and the temperature respectively. Substituting Equation 3.3 in Equation 3.1:

$$\begin{aligned} F \cdot v_{eq} &= \mu_{Li}^0 + \mu_\psi^0 - \mu_\zeta^0 + R \cdot T \cdot \ln\left(\frac{x_\psi}{x_\zeta}\right) + R \cdot T \cdot \ln\left(\frac{\gamma_\psi}{\gamma_\zeta}\right) \\ &= F \cdot v_{eq}^0 + R \cdot T \cdot \ln\left(\frac{x_\psi}{x_\zeta}\right) + R \cdot T \cdot \ln\left(\frac{\gamma_\psi}{\gamma_\zeta}\right) \end{aligned} \tag{3.4}$$

being v_{eq}^0 the equilibrium potential corresponding with the reference chemical potentials μ_ζ^0 and μ_ψ^0. The deviation from ideal behaviour, represented by the last term in Equation 3.4, is due to the pseudo binary interactions between Li ions and the host matrix during intercalation and deintercalation processes. In the specific case where $\gamma_j = 1$, Equation 3.4 is called *Nernst Equation*.

Since γ_j is related to Gibbs energy [TAT14, SAB15], the Redlich-Kister equation can be used to obtain the following expression, where the terms b_k are constant coefficients used to represent, by means of the sum of N elements, the non-ideal interactions (v_{INT}):

$$\begin{aligned} F \cdot v_{eq,\,j} = F \cdot v_{eq,\,j}^0 &+ R \cdot T \cdot \ln\left(\frac{1 - x_{\zeta,j}}{x_{\zeta,j}}\right) \\ &+ \sum_{k=0}^{N} b_k \cdot \left[(2 \cdot x_{\zeta,j} - 1)^{k+1} - \frac{2 \cdot x_{\zeta,j} \cdot k\,(1 - x_{\zeta,j})}{(2 \cdot x_{\zeta,j} - 1)^{1-k}}\right] \end{aligned} \tag{3.5}$$

$$v_{eq,\,j} = v_{eq,\,j}^0 + \frac{R \cdot T}{F} \cdot \ln\left(\frac{1 - x_{\zeta,j}}{x_{\zeta,j}}\right) + v_{INT,j} \tag{3.6}$$

Thus, the equilibrium potential of a cell is:

$$v_{eq} = v_{eq,\,c} - v_{eq,\,a} \tag{3.7}$$

By substituting Equation 3.6 in Equation 3.7 an expression for the equilibrium voltage can be obtained:

$$v_{eq} = v_{eq,c}^0 - v_{eq,a}^0 + \frac{R \cdot T}{F} \cdot \ln\left(\frac{(1 - x_{\zeta,c}) \cdot x_{\zeta,a}}{x_{\zeta,c} \cdot (1 - x_{\zeta,a})}\right) + v_{INT,c} - v_{INT,a} \tag{3.8}$$

3.2.2 Equilibrium between the anode and the electrolyte: Solid–electrolyte interface

The solid–electrolyte interface (SEI) is a passive layer created between the electrolyte and the graphite anode, whose existence is crucial for the reversibility of Li-ion batteries. Some authors use the term SEI also to refer to a similar surface built between the cathode and the electrolyte, even tough the most common term for this interface is "passivation film" or "surface layer". More effort has been devoted to the study of the SEI than of the surface layer, given that the cathodes are stable by themselves in their interaction with the electrolyte. Conversely, without the SEI, the anode and electrolyte would spontaneously react and the battery would be destroyed. Actually, electrolyte solvents are unstable below 0.8 V versus Li^+/Li and above 4.5 V versus Li^+/Li in the presence of the electrode materials, which are strongly reducing/oxidizing [PAL16], while the working potential of a carbon-based anode ranges from 0 to 1 V versus Li^+/Li [VER96].

The SEI results from the reduction of some components of the electrolyte, such as EC and $LiPF_6$, with active lithium [THA98]. The SEI consists of several layers. An inorganic part (LiF, Li-oxide or Li_2CO_3) is deposited next to the anode surface. This layer has a high lattice energy due to its iono-covalent bonds, which prevents the diffusion of organic molecules. Therefore, the passivating effect of the SEI is assigned to this layer [AUR99]. Outside this inorganic layer, there is a layer of organic decomposition products [THA98].

Prior to its market release, each Li-ion battery has undergone a SEI formation process, therefore it has a stable SEI when acquired by the user. This formation process consists in a slow charge during which the electrolyte solvent degradation reaction takes place at the electrode–electrolyte interface, which often also involves the electrolyte salt and water impurity traces. The resulting insoluble products form a solid protective psasivation layer adhering to the surface of the negative electrode, which is the SEI. Even though an ideal SEI would be built before the battery is put on the market and stay stable after that, there are irreversible side reactions that etail battery ageing, as explained in Subsubsection 3.5.2.1.

The SEI is a productive and on-going materials research topic, given that specific additives are mixed with the electrolyte in order to create a stable layer with the following requirements:

- Electron transference number = 0. Otherwise, the electrons would bypass the SEI and the electrode would decompose.
- High ionic conductivity. With this property there is no opposition to

lithium ion intercalation and de-intercalation into the anode.

- Uniform morphology and chemical composition in order to get an homogeneous current distribution.
- Suitable adhesion to the carbon anode.
- Outstanding mechanical strength and flexibility that allows the expansion and contraction of the carbon crystal lattice due to the lithium intercalation and de-intercalation process.
- Low solubility in the electrolyte, so that the SEI is not decomposed consuming the available lithium and irreversibly reducing the battery capacity.

3.3 Electrochemistry

Electrochemistry is the study of electron transfer caused by redox reactions at the interface of an electron conductor, such as a metal, and an ionic conductor, such as an electrolyte. Therefore, the electrochemical theory is the most suitable tool to explain the phenomena taking place in a battery when it is out of its thermodynamic equilibrium, i.e. when it is being charged or discharged. The three main electrochemical phenomena that take place during the battery charging and discharging processes are described through the following subsections.

3.3.1 Ohmic phenomena

Ohmic losses represent the voltage drop due to the transfer of electrons in the electric circuit and the movement of ions through the electrolyte and membrane.These phenomena are determined, on the one hand, by the electronic conductivity of the electrodes and of the current collectors (usually copper and aluminium) and, on the other hand, by the ionic conductivity of the electrolyte and membrane. Since the electrolyte does not store energy, its properties are unchanged for any value of SOC. However, the variation in the electrode lithium content leads to a conductivity change, making the ohmic phenomena SOC dependent. With regard to temperature, there are opposite effects over electronic and ionic conductivity. The electronic conductivity decreases for increasing temperature in most of conductive materials, whereas the ionic conductivity is increased by higher temperature. Given that the ef-

fect over ionic conductivity is greater than that over electronic conductivity [PAR12], ohmic losses decrease when the temperature is increased.

3.3.2 Polarizable electrodes

Any electrochemical reaction required some energy to take place, which is called *activation energy*. This means, in a Li-ion battery, that the electrodes need to be polarised, i. e. there has to be a voltage drop between each electrode and the electrolyte for the battery to get charged or discharged. This voltage drop entails an increased energy required for battery charging and reduced energy available when discharging. These power losses are known as activation losses or activation overpotential.

3.3.2.1 Double layer effect

The current managed by a battery can be divided into a faradaic current (i_F) and a capacitive current, also called non-faradaic or double layer current (i_{dl}):

$$i = i_F + i_{dl} \tag{3.9}$$

In the previous equation, i_F is the current generated by the redox reaction, while i_{dl} is a consequence of differences in the Fermi levels of the electrode and electrolyte, which induces a slight current flow in one direction or the other, thereby creating an electric field in the area of the electrolyte closest to the electrode. Meanwhile, the excess charge in the electrode metal material is located on the contact surface. The relationship between charge (z) and the potential gradient in the electrode $\left(\frac{d^2 v_{eq,j}}{dl^2}\right)$ is represented with Poisson Equation [BAR05]:

$$\frac{d^2 v_{eq,j}}{dl^2} = -\frac{1}{\epsilon \cdot \epsilon_0} \cdot \sum_j z_j \cdot F \cdot x_j^0 \cdot \exp\left(-\frac{z_j \cdot F \cdot v_{eq,j}}{R \cdot T}\right) \tag{3.10}$$

where ϵ_0 is the vacuum permittivity and ϵ is the relative permittivity of the material. The sum refers to the local species j. Equation 3.10 can be solved [BAR05], giving an expression for this distributed capacitance, also known as double layer capacitance, C_{dl}:

$$C_{dl} = S_{SEI} \cdot \left(\frac{2 \cdot z^2 \cdot F^2 \cdot \epsilon \cdot \epsilon_0 \cdot x_j^0}{R \cdot T}\right)^{\frac{1}{2}} \cdot \cosh\left(\frac{z \cdot F \cdot v_{eq,j}}{2 \cdot R \cdot T}\right) \tag{3.11}$$

3.3.2.2 Kinetics of chemical reaction: Butler–Volmer Equation

Let A and B be two chemical species, correlated by an elemental, unimolecular chemical reaction:

$$\mathrm{A} \underset{k_b}{\overset{k_f}{\rightleftharpoons}} \mathrm{B}$$

Both reaction are always active and their reaction speed depends on the concentration of the reactants, as shown in Equation 3.12 and Equation 3.13:

$$vel_f = k_f \cdot c_A \tag{3.12}$$

$$vel_b = k_b \cdot c_B \tag{3.13}$$

The constant reactions k_f and k_b have dimensions of s^{-1} and are the reciprocal of the average lifetime of A and B. The net conversion rate of A into B is:

$$vel_{net} = k_f \cdot c_A - k_b \cdot c_B \tag{3.14}$$

When the process reaches the equilibrium, the net conversion rate is 0. Therefore:

$$\frac{k_f}{k_b} = \frac{c_B}{c_A} \longrightarrow \text{constant} \tag{3.15}$$

Accordingly with the thermodynamic results, the kinetic theory predicts a constant concentration ration in the equilibrium state. This agreement is required of any kinetic theory. In the limit of equilibrium, the kinetic equations must collapse to relations of the thermodynamic form; otherwise the kinetic picture cannot be accurate. Thermodynamics gives information about the required mechanism to keep the equilibrium, while the kinetic theory describes the evolution of the mass flow along the system, both in its approach to the equilibrium and in a dynamic state.

The conversion rate of A into B at equilibrium, shown in Equation 3.15, is called exchange velocity of the reaction, vel_{ex}, and it is an important concept related with the electrode kinetics:

$$vel_{ex} = k_f(c_A)_{eq} = k_b(c_B)_{eq} \tag{3.16}$$

In a general electrode reaction that involves a number n of electrons, the equilibrium state defined by the thermodynamics theory is expressed by the Nest Equation (Equation 3.4). Following the notation of a redox reaction, the reactants are named oxidants (O) and the products reducers (R):

$$\mathrm{O} + n\,\mathrm{e}^- \underset{k_b}{\overset{k_f}{\rightleftharpoons}} \mathrm{R}$$

Besides the equilibrium state, the kinetic theory should explain the relationship between current (i) and voltage (v) for different values of i. This current is often limited by the velocity at which the reactants are transported from the bulk electrodes to the surface. This limitations does not concern the kinetic theory of the interfase, but is in agreement with the relationship proposed by Tafel in 1095:

$$v_\eta = b_0 + b_1 \cdot \log i \tag{3.17}$$

A suitable electrochemical interpretation must explain the Tafel equation in an electrochemical system.

Let $c_O(l,\ t)$ be the concentration of the oxidant species at a distance l of the interface in a time instant t, and vel_f the reaction rate of the forward half-reaction. Based on Equation 3.12, the following expression can be written:

$$vel_f = k_f \cdot c_O(0,\ t) = \frac{i_c}{n \cdot F \cdot S} \tag{3.18}$$

Given that the forward half-reaction is a reduction reaction, there is a cathodic current i_c which is proportional to vel_f. If an equivalent analysis is done for the inverse half-reaction:

$$vel_b = k_b \cdot c_R(0,\ t) = \frac{i_a}{n \cdot F \cdot S} \tag{3.19}$$

where i_a is the anodic component of the total current and $c_R(x,\ t)$ is the concentration of the reducing species. Therefore, the net reaction rate is:

$$vel_{net} = vel_f - vel_b = k_f \cdot c_O(0,\ t) - k_b \cdot c_R(0,\ t) = \frac{i}{n \cdot F \cdot S} \tag{3.20}$$

Therefore, the net current is:

$$i = i_c - i_a = n \cdot F \cdot S\,[k_f \cdot c_O(0,\ t) - k_b \cdot C_R(0,\ t)] \tag{3.21}$$

Let's assume a redox process in which the species O and R react through the transference of a single electron ($n = 1$), as shown in the following chemical equation:

$$\mathrm{O} + \mathrm{e}^- \underset{k_b}{\overset{k_f}{\rightleftharpoons}} \mathrm{R}$$

The equilibrium voltage v_{eq} is taken as the reference potential to develop the kinetic theory. This reference is valid as long as the two chemical species taking part in the reaction are present, thereby defining the equilibrium. If a situation such as the one represented in Figure 3.1 takes place, in which there is a potential change Δv_{eq} in the electrode until a level $v_{elec} = v_{eq} + \Delta v$ is reached, the energy of an electrode electron varies in $-F \cdot \Delta v$, moving the curve

O+e shown in Figure 3.1 this quantity upwards or downwards. It can be seen in Figure 3.1 that the oxidation barrier ΔG_a has been reduced in a fraction of the total energy change of the electron. Let this fraction be $(1-\alpha)$, where α is the transfer coefficient, which takes values between 0 and 1. Therefore:

$$\Delta G_a = \Delta G_a^0 - (1-\alpha)\cdot F\cdot(v_{elec}-v_{eq}) \tag{3.22}$$

Analogously, for the cathode reaction:

$$\Delta G_c = \Delta G_c^0 + \alpha\cdot F\cdot(v_{elec}-v_{eq}) \tag{3.23}$$

It is reasonable to assume that the kinetic constants k_f and k_b in Equation 3.21 have an Arrhenius-type temperature behaviour. Therefore, Equation 3.22 and Equation 3.23 can be rewritten as follows, being $f = F/(R\cdot T)$:

$$k_f = S_f\cdot\exp\left(-\frac{\Delta G_c}{R\cdot T}\right) = S_f\cdot\exp\left(-\frac{\Delta G_{0c}}{R\cdot T}\right)\cdot\exp\left(-\alpha\cdot f\cdot(v_{elec}-v_{eq})\right) \tag{3.24}$$

$$k_b = S_b\cdot\exp\left(-\frac{\Delta G_a}{R\cdot T}\right) = S_b\cdot\exp\left(-\frac{\Delta G_{0a}}{R\cdot T}\right)\cdot\exp\left((1-\alpha)\cdot f\cdot(v_{elec}-v_{eq})\right) \tag{3.25}$$

Equation 3.24 and Equation 3.25 can be inserted in Equation 3.21 to get the so-called Butler-Volmer equation:

$$\begin{aligned} i_F = & F\cdot S_{SEI}\cdot k^0\cdot[c_0(0,t)\cdot\exp\left(-\alpha\cdot f\cdot(v_{elec}-v_{eq})\right) \\ & -c_R(0,t)\cdot\exp\left((1-\alpha)\cdot f\cdot(v_{elec}-v_{eq})\right)] \end{aligned} \tag{3.26}$$

where S_{SEI} stands for the area of the electrode–electrolyte interphase, v_{eq} is the equilibrium electrode potential, v_{elec} the electrode potential when subject to a current and α the apparent cathodic transfer coefficient.

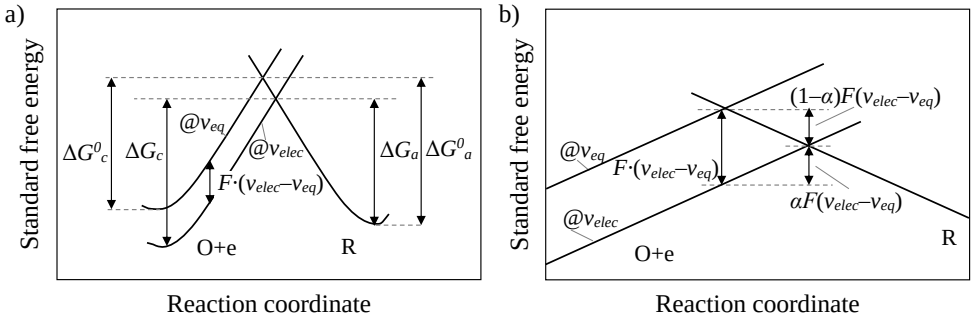

Figure 3.1: Effects of a potential change on the standard free energies of activation for oxidation and reduction. Complete picture (a) and magnified view of the crossing area (b) [BAR01].

The voltage difference required for the reaction to take place ($v_{elec} - v_{eq}$ in Equation 3.26), combined with the faradaic current i_F, leads to the power losses called activation losses.

3.3.3 Ion transport

Diffusion or concentration phenomena are described by Fick's laws of diffusion, which relate the diffusive flux to the concentration. The fist law, Equation 3.27, states the relationship assuming steady state; while the second law, Equation 3.28, predicts how diffusion causes the concentration to change with time.

$$\dot{m} = -\rho \cdot D \cdot \nabla x \tag{3.27}$$

$$\frac{\delta x}{\delta t} = D \cdot \Delta x \tag{3.28}$$

Fick's diffusion coefficient D depends on the temperature, as expressed by the following equation:

$$D = D_0 \cdot \exp\left(-\frac{E_A}{R \cdot (T - T^0)}\right) \tag{3.29}$$

Diffusion phenomena have two main effects on the performance of a Li-ion battery. On the one hand, the ion diffusion through the crystal lattice in the electrodes creates a difference between the ion concentration at the electrode–electrolyte interphase, and the average electrolyte concentration, $c_{\bar{Li}}$. Given the fact that the electrochemical reaction takes place on the interphase, the equilibrium voltage and the activation phenomena are defined defined by the concentration on this surface. This ion concentration gradient produces a concentration voltage drop during battery operation. On the other hand, ion diffusion through the membrane has also a major impact on the battery behaviour, particularly during low temperature operation [SAB15]. This process induces a voltage drop in the battery with characteristic dynamics, which is different from the electrode diffusion and needs to be separately analysed. Both phenomena lead to energy losses in the battery and are called diffusion or concentration losses.

3.4 Thermal phenomena

Heat generation is a fact in every energy system, and Li-ion batteries are not the exception. The inefficiencies of real processes prevent the total amount of

energy to be useful and a portion is dissipated as heat. This dissipative process takes place in the bulk of the battery cells, where the electrochemical reactions and the electron and ion movement go on. Therefore, this energy must be conducted from the inner to the surface of the cell and finally dissipated to the ambient. As detailed in the following subsections, the temperature has a remarkable influence on the battery performance, and it can limit the battery functionality in some cases. Therefore, a good understanding of the heat generation phenomena and suitable cell and battery pack designs that optimize the thermal performance are important factors to achieve a good battery pack. Actually, TESLA Inc., a company that is taking great steps towards the Li-ion battery technical improvement and price decrease, owns over forty patents directly related with thermal issues in this kind of batteries, which include battery management strategies to limit thermal generation [KEL17], heat dissipation [MAR14c, STR15], thermal event detection [LEP15], avoidance of thermal propagation [RAW14, HER13], etc.

The most remarkable issues about the influence that temperature has on Li-ion batteries, the thermal generation mechanisms and the basics of thermal dissipation are covered through the following subsections.

3.4.1 Effect of temperature on battery performance

It is well known that the performance of Li-ion batteries reaches its maximum when operating at moderate, homogeneous ambient temperatures (between 20 and 40 °C). Both high and low temperatures have negative effects on its performance, and the optimal temperature is a trade-off between these issues that depends on the anode, cathode and electrolyte components [BAN11]. The pejorative effects that different thermal conditions have on battery performance are addressed in the following lines.

3.4.1.1 High temperature

Energy and power fade These are the two main battery ageing phenomena explained in Section 3.5. Energy fade takes place when the active material inside the battery is turned into inactive material, reducing the battery capacity, which also cuts down the energy that can be stored in the battery. Power fade is related with impedance rise, which reduces the battery operating discharging voltage and increases its charging voltage.

Several experimental studies concerning the performance of Li-ion batteries at high temperature have been published. They analyse batteries with different anodes, cathodes and electrolytes reaching similar conclusions which

points to an accelerated energy and power fade triggered by high temperature. Ramadass et al. cycled several C/$LiCoO_2$ batteries [RAM03] obtaining accelerate ageing rates for temperatures higher than 50 °C. Ehrlich obtained similar conclusions with Li/$LiMn_2O_4$ batteries [RED10] and Amine et al. [AMI05] and Liu et al. [LIU10] for LFP batteries. Similarly, when the batteries are not cycled but just stored at different temperatures, higher power and energy fade is measured for higher temperatures [THO03a, SCH17].

Thermal runaway This is one of the most hazardous and undesirable processes that can take place in a Li-ion battery, and great research and development efforts are aimed at the detection, prevention and restraint of this effect [WAN12]. Actually, thermal runaway in two Li-ion batteries was the reason for the grounding of the whole fleet of Boeing 787 Dreamliners on January 2013, the first aircraft equipped with lithium-ion batteries [WIL13].

The thermal runaway event occurs in batteries when elevated temperatures trigger heat-generating exothermic reactions and the generated heat cannot be effectively dissipated, thereby activating further exothermic processes, as represented in Figure 3.2. These exothermic reactions were reviewd by Spotnitz and Franklin [SPO03], who identified the metastable components of the SEI to exothermically decompose at a temperature between 90 and 120 °C. After this breakdown, when the electrolyte is in contact with the anode, the electrolyte solvent starts to decompose at a temperature of 100 °C, with the reaction peaking at 200 °C, as shown in Figure 3.2. The positive electrode can also react with the electrolyte or give off oxygen that reacts with the electrolyte in a highly exothermic reaction triggered only with high temperatures ($\approx$ 180 °C, as shown in Figure 3.2). In the presence of this released oxygen, organic electrolytes can combust once vaporized. By this point, the separator should have melted, which can cause battery short circuits, which further increases the temperature. After these concatenated phenomena, the battery would probably have exploded and/or taken fire.

The temperature at which the thermal runaway phenomena are triggered depend on a number of factors, such as the composition of the electrodes and electrolytes (and therefore the SEI) and the SOC (higher SOC has been proven to reduce the thermal runaway trigger temperature [HAL99]).

Self-discharge Besides the irreversible performance loss addressed before, lithium-ion batteries also suffer from reversible self-discharge. Even though this effect has only a slight importance in typical lithium-ion battery applications, high temperatures have been detected to be an accelerator of self-

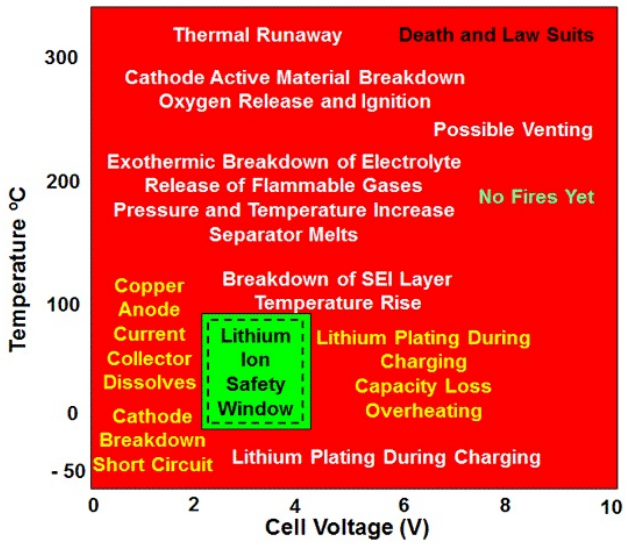

Figure 3.2: Lithium-ion cell operating window and destructive processes taking place out of this window. Reproduced from The Electropaedia (www.electropaedia.com).

discharge processes [JOH98, AUR05, RED10]. Therefore, if the battery is used in an application where long storage periods are required, temperature is a parameter that has to be taken into account in order to calculate its self-discharge.

3.4.1.2 Low temperature

Most of the batteries available in the market, including the Li-ion technologies, have reduced features when performing at low temperature, given the reduced ion conductivity of the involved materials and the lower reaction rate of the redox processes (which normally follow an Arrhenius trend) [ZHU15]. However, the requirements of the automotive sector, in which the batteries must be able to operate at sub-zero temperatures, encouraged the U.S. Department of Energy (DOE) to set a goal of 20% battery power performance with a temperature of –30 °C. Therefore, commercial HEV manufacturers usually employ battery heating strategies to prevent battery degradation due to low temperatures.

Although low temperatures reduce the ionic conductivity of the SEI and electrolyte and lithium ions have more difficulties to diffuse through the graphite anode, Zhang et al. [ZHA04] identified the poor charge transfer at the electrode–electrolyte interface as the performance limiting factor of Li-ion batteries at

low temperatures.

Besides, when the lithium ions diffusion in the anode is deteriorated by low temperatures and their transport rate is kept high because of high current, the metallic lithium is deposited on the surface of the SEI, which causes a new SEI formation process, thereby consuming active material and reducing the usable electrode–electrolyte contact area. As explained in Section 3.5, lithium deposition (or plating) is one of the most degrading effects concerning Li-ion batteries with carbonaceous anodes and can lead to the build of dendrites, which can eventually punch the separator and short circuit the battery.

However, low temperature in Li-ion batteries is counter balanced by the increased heat generation that takes place in these situations due to increased battery resistance. Some studies concerning this issue have been published, such as [JI13], where an isothermal discharge at –20 °C is compared with an adiabatic discharge starting at the same temperature, obtaining a discharge capacity of 100 mAh for the first experiment and 2200 mAh for the second one. In spite of this negative feedback, extra warm-up of batteries is required for their performance in cold environments [STU04].

3.4.1.3 Temperature imbalance

Given the influence that temperature has on battery performance and ageing, overheating and non-uniform temperature distribution of the cells along the battery pack can lead to excessive degradation and failure of some of the cells. In the past, many researchers overlooked the effects of thermal imbalances in Li-ion battery packs, and assumed the electrochemical performance among individual cells of a battery pack to be identical [BAN11]. However, more recent studies pay attention to this topic. This concern began around 2011, when Bandhauer et al. [BAN11] revealed that electrical imbalance could lead to serious battery failures if thermal runaway is induced. Meanwhile, White [GUO11b] studied the battery thermal phenomena and simulated the electrical and thermal performances of batteries connected in parallel.

More recently, Yang et al. [YAN16c] present simulation and experimental results of the discharging process of two parallel-connected cells with different temperatures. A larger current is observed within the cell of higher temperature, which aggravate the capacity deviation between the two cells and accelerate the capacity losses of the battery pack. Parallel-connected cells are also studied in [BRU16] by means of experimental results, concluding that the unavoidable variations in cell properties affect the ageing process of the cells and the heating and temperature distribution within the battery assembly.

Huang et al. [HUA17] examine the operating current, temperature distribution and heat generation of each cell in a battery pack and study the impact of thermally-driven imbalances obtaining useful results and conclusions for practical applications, such as the variation of internal resistances shown in Figure 3.3, which may need to be taken into account for the battery control and management.

There are also research works proposing individual cell temperature control aimed at using the temperature imbalance to improve the performance of the battery. In this line, relative temperatures have been proposed to be used as the balancing target, and several advantages of this strategy are identified. The authors of [LI16c] proposed two algorithms aimed at balancing the battery cells by means of relative thermal management. The main advantages of this strategy highlighted in this paper are:

- With an accurate temperature control, the affection of thermal issues to the battery lifetime and performance can be minimized.
- The individual cell temperature control degrades the cells uniformly and improves the overall characteristics of the battery.
- The slow dynamics typical from temperature processes make this strategy ideal for slow balancing processes.
- The thermal management system can assume the balancing function, allowing the removal of other cell balancing systems that are required for traditional strategies.

3.4.2 Heat generation

The electrochemical phenomena described in Section 3.3 lead to internal overpotentials during charge and discharge processes which result in heat generation or absorption. In 1985, Newman et al. [BER85] published a general energy balance of a battery system based on the first law of thermodynamics:

$$\frac{dH_{tot}}{dt} = \dot{Q} - i \cdot v \tag{3.30}$$

where H_{tot} is the sum of the enthalpies of every existing phases and $\dot{Q}$ is the rate of heat transfer out of the battery. The authors of this paper assume an average composition of each phase and obtain Equation 3.31 by applying the Gibbs-Helmholtz relation. The rate of enthalpy change associated with the

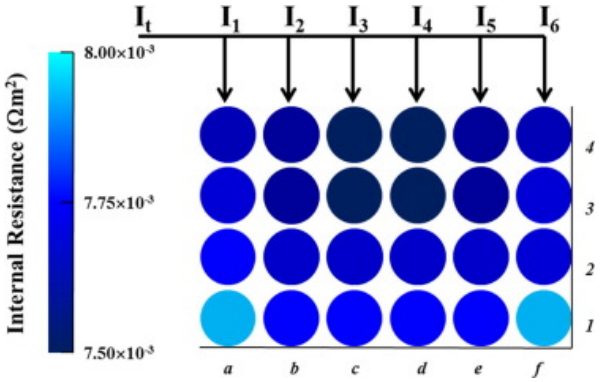

Figure 3.3: Distributions of the internal resistance of individual cells within the pack after 1600 s discharge based on simulations. Reprinted from [HUA17], with permission from Elsevier.

electrode reactions, mixing effects, and phase change processes can be written as:

$$\begin{aligned}\dot{Q} - i \cdot v = &\sum_{l} \left[i_l \cdot T^2 \frac{d\frac{v_{eq,l}}{T}}{dT} \right] \\ &- \sum_{j} \frac{d}{dt} \left[\int_{v_j} \sum_{k} c_{k,j} \cdot R \cdot T^2 \cdot \frac{\partial}{\partial T} \ln \left(\frac{\gamma_{k,j}}{\gamma_{k,j}^{avg}} \right) \cdot dv_j \right] \\ &- \sum_{j,j \neq m} \sum_{k} \left[\Delta H^0_{k_j \rightarrow m} - R \cdot T^2 \cdot \frac{d}{dT} \ln \left(\frac{\gamma_{k,m}^{avg}}{\gamma_{k,j}^{avg}} \right) \frac{dn_{k,j}}{dt} \right] \\ &+ \frac{dT}{dt} \left[\sum_{j} \sum_{k} n^0_{k,j} \cdot cp^{avg}_{k,j} + \sum_{l} \frac{\int_0^t i_l \cdot dt}{n_l \cdot F} \Delta cp_l \right. \\ &\left. + \sum_{j,j \neq m} \sum_{k} \left(cp^{avg}_{k,j} - cp^{avg}_{k,m} \right) \cdot \left(n_{k,j} - n^0_{k,j} \right) \right] \end{aligned} \tag{3.31}$$

The right-hand part of this equation has four terms which are the sources of energy obtained form thermodynamic principles. The first and second terms are related with enthalpy, representing the first of them the enthalpy of the electrochemical reactions and the second the enthalpy of mixing, which is the heat generated when the battery current is interrupted and the concentration gradients in the electrode particles are relaxed. The third term is the energy associated with phase changes in the battery, such as precipitation. Finally, the fourth term, which is written in the fourth and fifth lines of Equation 3.31, accounts for the heat accumulation of the different components by means of

their heat capacity.

This equation is usually simplified for easier applicability to engineering problems [EDO16, GRE16] by assuming an average heat capacity and isothermal cells, which are reasonable assumption for typical battery applications. Moreover, Newman et al. published a study [THO03b] where the contribution of the heat of mixing is compared with the other sources of heat and is considered negligible. Therefore, the heat generation rate is rewritten as a simple function of the battery current and voltage, operating temperature and open circuit voltage as follows:

$$\dot{Q} = \frac{1}{v} \cdot \left(i \cdot (v - v_{OC}) + i \cdot T \cdot \frac{\partial v_{OC}}{\partial T} \right) \tag{3.32}$$

The first term of this equation is called *irreversible* or *polarization* heat. It is due to all the irreversible processes that take place in the battery. This term in always positive, since the working potential is higher than v_{OC} only when the battery is charging ($i > 0 \Leftrightarrow (v - v_{OC}) > 0$). The second term is the *reversible* or *entropic* heat, given that it is the consequence of reversible electrochemical processes. The entropic heat can have positive sign (heat dissipation) or negative (heat absorption) depending on the values of current and entropic factor $\frac{\partial v_{OC}}{\partial T}$. The value of the entropic factor depends on the specific Li-ion battery technology and temperature, but has a typical shape with minimum, negative values at low SOC, maximum, positive values for medium SOC and average values for high SOC that have been published to be negative [BAZ14, MAR14a] or positive [VER14] depending on ther referred study.

3.4.3 Heat dissipation

The heat generation in a battery as a consequence of the processes explained in Subsection 3.4.2 takes place in the whole bulk volume of the cell, leading to a temperature increase due to the absorption of this heat during the initial transient period. As the cell temperature increases, the heat transfer process from the inside to the ambient is also increased, until the steady state operation conditions are reached, matching the amount of heat generated and evacuated [CEN07]. The assumption of uniform heat generation along the volume is reasonable for Li-ion batteries, given the uniform manufacturing method consisting of the stacking of thin, uniform electrodes, current collectors and separators. Under this assumption, the maximum temperature (T_{max}) is reached in the regions that are most separated from the outside of the cell, which are the central axis of a cylindrical cell (Figure 3.4 (a)), the symmetry plane of a pouch cell (Figure 3.4 (b)) and the central point of a

prismatic cell (Figure 3.4 (c)). T_{max} has a main importance for the analysis of lithium-ion batteries, given that, as explained in Subsection 3.4.1, high temperatures have a negative influence on battery performance and lifetime. Moreover, if this maximum temperatures triggers the thermal runaway, the chain reaction will start, leading to catastrophic failure of the cell.

The three fundamental mechanisms of heat transmission are conduction, convection and radiation [CEN07]. Given the small temperature difference between the batteries and the ambient, the radiated heat can be disregarded [GAM15]. Therefore, the generated heat is basically dissipated by means of conduction and convection. The fundamental equation describing the heat conduction, considering a constant an uniform thermal conductivity λ is the Fourier–Biot equation:

$$\frac{\partial^2 T}{\partial x^2} + \frac{\partial^2 T}{\partial y^2} + \frac{\partial^2 T}{\partial z^2} + \frac{\dot{q}}{\lambda} = \frac{\rho \cdot cp}{\lambda} \cdot \frac{\partial T}{\partial t} \tag{3.33}$$

where x, y and z are the rectangular coordinates, $\dot{q}$ is the volumetric heat generation rate and cp is the specific heat of the material.

The equations that describe convection heat transmission are more complicated than Equation 3.33, given that the fluid movement is involved in this process. The conservation of mass, conservation of energy and conservation of momentum are taken into account to describe convection [CEN07]. Even though, it is known that the rate of heat transfer is proportional to the difference between the surface temperature (T_{sur}) and the ambient temperature (T_{amb}). Therefore, the Newton's law of cooling represents a convection process:

$$\dot{Q}_{conv} = h \cdot S \left(T_{sur} - T_{amb}\right) \tag{3.34}$$

The resolution of conduction and convection equations in complex environments is an arduous undertaking which concerns to Heat Transfer discipline. Some simplifications to this process, which are reasonable for common use of

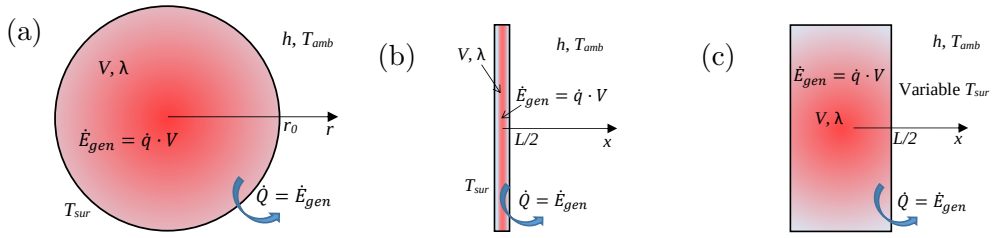

Figure 3.4: Schematic of thermal phenomena in different lithium-ion cells: cylindrical cell (a), pouch cell (b) and prismatic cell (c). The hottest areas are coloured in brightest red.

Li-ion batteries, are proposed hereinafter in order to provide a simplified solution of this engineering problem. With this purpose, an homogeneous and invariant heat conductivity λ and a uniform heat generation through the whole cell volume $\dot{q}$ are usually assumed. Let S be the external surface area of the cell, which is in contact with the ambient air, V the cell volume and T_{sur} the surface temperature. The generated heat is transferred to the ambient through a convection process with a heat transfer coefficient h.

3.4.3.1 Steady state

If the system has reached the steady state, the heat transfer rate from the cell to the ambient equals the total heat energy generated inside the cell, as represented in Figure 3.4:

$$\dot{Q} = \dot{q} \cdot V \tag{3.35}$$

Using the Newton's law of cooling shown in Equation 3.34:

$$T_{sur} = T_{amb} + \frac{\dot{q} \cdot V}{h \cdot S} \tag{3.36}$$

Equation 3.36 has a straight solution if unidirectional heat flow can be assumed, which is realistic for cylindrical cells whose radius r_0 is much shorter than their length (radial flow, as represented in Figure 3.4 (a)) and pouch cells whose thickness L is much lower than their length and width (transversal flow, as represented in Figure 3.4 (b)). This 1D approximation provides worse results for prismatic cells, given than their width is long enough for the heat transferred through the top and bottom faces not to be negligible. The result of a pouch-type cell is:

$$T_{sur,pouch} = T_{amb} + \frac{\dot{q} \cdot L}{2 \cdot h} \tag{3.37}$$

and for the cylindrical case:

$$T_{sur,cyl} = T_{amb} + \frac{\dot{q} \cdot r_0}{2 \cdot h} \tag{3.38}$$

Given the spacial symmetry and the uniform generation, the T_{sur} is constant for cylindrical and pouch cells. However, due to the 3D heat transmission, it is not the case for prismatic cells, as represented in Figure 3.4.

The maximum temperature, which takes place in the centre of the cell, can be calculated considering an internal, imaginary surface. The ideal surface for a pouch cell is a plane located at a distance x of the symmetry plane or a cylinder with a radius r for the cylindrical cell. Since steady state is analysed, the heat generated in the interior of this surface must match the evacuated

heat, therefore, if the height an length of the pouch cell are l_1 and l_2, and the heigh of the cylinder is l_3:

$$-\lambda \cdot (l_1 \cdot l_2)\frac{dT}{dx} = \dot{q} \cdot (l_1 \cdot l_2 \cdot x) \qquad \longrightarrow dT = -\frac{\dot{q}}{\lambda} \cdot x \cdot dx \tag{3.39}$$

$$-\lambda \cdot (2 \cdot \pi \cdot r \cdot l_3)\frac{dT}{dr} = \dot{q} \cdot (\pi \cdot r^2 \cdot l_3) \qquad \longrightarrow dT = -\frac{\dot{q}}{2 \cdot \lambda} \cdot r \cdot dr \tag{3.40}$$

for pouch and cylindrical cells respectively. If an integration from $x = 0$ to $x = \frac{L}{2}$ (pouch cells) and from $r = 0$ to $r = r_0$ (cylindrical cells) is performed, the following expressions are obtainde for T_{max}:

$$T_{max,pouch} = T_{sur} + \frac{\dot{q} \cdot L^2}{8 \cdot \lambda} \tag{3.41}$$

$$T_{max,cyl} = T_{sur} + \frac{\dot{q} \cdot r_0^2}{4 \cdot \lambda} \tag{3.42}$$

Note that these results are valid only under the above-mentioned assumptions and once the steady state is reached.

3.4.3.2 Transient state

The formulation of the problems to calculate the transient, unidimensional temperature distribution of a pouch or cylindrical cell (topologies in which the 1D analysis can be applied) leads to a partial differential equation, which can be solved by means of advanced mathematical techniques [CEN07]. However, these solutions often contain infinite series, which are not convenient due to their slow evaluation process. Therefore, tabular or graphical resolutions ar often preferred. Aimed at the reduction and standardisation of the parameters involved in this problem, four dimensionless variables are used: dimensionless temperature, dimensionless distance from the centre, dimensionless heat transfer coefficient (Biot number) and dimensionless time (Fourier number).

Given the complexity of the mathematical analysis required to solve this problem, it is usually not feasible to use these equations to solve transient heat dissipation in batteries. Therefore, different techniques are proposed to obtain an approximate solution. Depending on the available computational power and on the desired results accuracy, some simplifications are made in the resolution process. With this aim, the cell can be considered as a compact system, finite differences methods can be applied to discretise the system, finite elements software can be applied, etc. A review of the most used thermal dissipation models is provided in Section 4.5.

3.5 Ageing

3.5.1 Significance of battery ageing

The battery performance, based on the combination of two redox semi-reactions, seems straightforward at a first glance. However, there is an intrinsically complex system behind this simplicity. Besides the electrode active materials and the electrolyte that allow the ion flow, several "inactive" components are required for the practical performance of a battery. Some of these components are separators to avoid short circuits between both electrodes, current collectors to gather or distribute the electrons along the electrodes, a polymeric film in which the electrolyte is embedded, conductive additives to enhance the conductivity of the electrodes, etc. All these contribute to battery function by maintaining its electrochemical characteristics and structure integrity [PAL16].

The electrochemical reactions that are the basis of battery performance should ideally involve only the active materials, which are reversible and highly efficient. However, in a real system, all battery components can interact with one another, and many of these interactions are irreversible. Given this irreversibility, these interactions are considered *ageing mechanisms*, since they entail an irretrievable reduction of battery capacity. Some of these processes are related to environmental variables, such as temperature, and conditions of use (discharge rate, charge protocol, DOD, etc.).

Therefore, the understanding and analysis of the ageing phenomena have a main importance for the design of suitable battery management and control strategies, as well as for an optimal manufacturing process that achieves long-lasting batteries. Actually, Niehoff et al. [NIE13] compared the ageing of hand-assembled 40 mAh cells with automatically manufactured 40 Ah cells with the same materials. They concluded that the manufacturing process has measurable effects on the battery ageing mechanisms.

Given the complexity of these mechanisms and the requirements of longer lifetime of Li-ion batteries, plentiful research work concerning this topic is available in the literature. An early review on battery degradation mechanisms was published by White et al. [ARO98], in which the influence of overcharge phenomena, electrolyte decomposition, SEI and interfacial film formation, battery self discharge, current collector and electrode phenomena in capacity fade mechanisms were analysed. Eight years later, in 2005, Vetter et al. published a review paper in which the physical reasons for lithium battery ageing are explained and the effect on each battery component is separated [VET05]. Despite the accomplished effort, lithium battery ageing processes

still need a deeper understanding in order to achieve longer battery lifetimes, and many papers are published analysing the influence of different parameters, thereby proposing various approaches for the study of battery ageing [JAL15, SCH17, DE 17, GAO17].

As already covered in Section 2.5, there are different types of Li-ion batteries, with a number of different cathode and anode materials. Depending on these materials, particular parasitic reactions are induced and distinct ageing mechanisms take place in the battery [JAL15]. These reactions have macroscopic effects, being the battery capacity fade and impedance rise the most remarkable of them. The ageing effects that are associated with the simple storage of the battery are grouped in the so-called *calendar ageing* phenomena, while those related with the battery charge–discharge processes are named *cycle ageing*.

The most remarkable ageing mechanisms occurring in each battery material and their macroscopic implications on the battery performance are summarized through the following subsections.

3.5.2 Ageing mechanisms

Ageing of Li-ion cells consists of different mechanisms, including both chemical and mechanical factors. Given the similar construction of both electrodes (active material, conductive additives, polymeric binder, current collector and a passivating surface layer), ageing phenomena are classified through the following subsections in accordance with the affected material. Two schematics that represent the anode ageing phenomena (Figure 3.5) and cathode ageing phenomena (Figure 3.6) are reproduced from a review paper published by Vetter et al. [VET05]. The focus of this section is put on carbonaceous anodes and metal oxide cathodes with layered structure (such as NMC or LNO), given that they are the most currently-used options for stationary applications.

3.5.2.1 Anode solid–electrolyte interface

As introduced in Subsection 3.2.2, the SEI should be a stable layer of a perfect electron insulator material during the whole lifetime of the battery. However, this is not the case in real batteries, mainly because of its parasitic electronic conductivity and, to a lesser extent, because of its ionic conductivity [VET05]. The SEI formation and decomposition reactions are irreversible and produce the so-called passive compounds, which do not take part in subsequent electrochemical reactions. Furthermore, these reactions consume lithium and electrolyte, leading to an irreversible loss of active material [XU04]. Figure 3.5

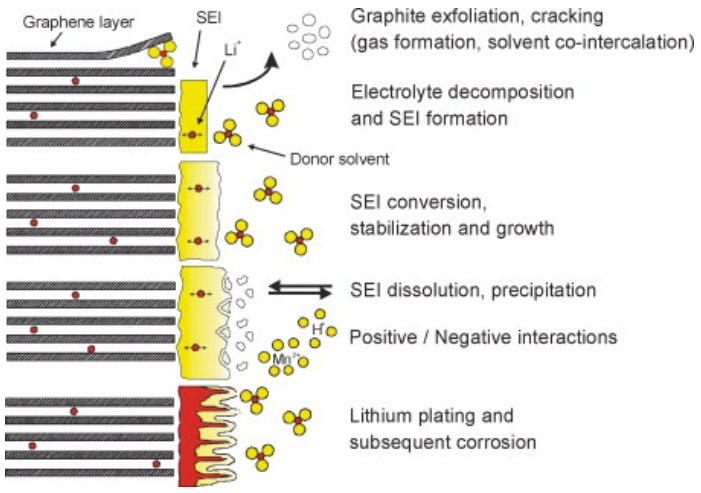

Figure 3.5: Changes at the anode/electrolyte interface. Reprinted from [VET05], with permission from Elsevier.

is a schematic representation of the main phenomena that drive the ageing of the SEI layer and the carbonaceous anodes.

Five mechanisms can be highlighted as the main grounds for ageing phenomena related with SEI:

SEI conversion and stabilisation The metastable organic SEI components, such as lithium alkyl carbonates, are slowly converted into more stable inorganic products, such as lithium salts through chemical reaction that are accelerated with higher temperatures. Even though inorganic SEI products are more stable and, therefore, less easily penetrated by solvent molecules, the growth of inorganic components may result in a lower ionic conductivity of the SEI for lithium [ZHE99].

Reactions with impurities Semicarbonates have been reported to be removed from the surface of the electrodes, specially with high temperatures [AND01]. These semicarbonates are decomposed provoking a morphology change of the SEI, as represented by the third schematic of Figure 3.5. This change let some parts of the anode surface uncovered form the SEI and exposed to the electrolyte, which leads to additional SEI formation and capacity loss [VET05].

Lithium plating The intercalation potential of carbonaceous anode materials is close to the potential of lithium metal. In the case of slow lithium ion diffusion into carbon and in the electrolyte, metallic lithium is plated on the anode material. This process is triggered by high charging rates and by low temperature [PAL16]. This lithium plating gives rise to the risk of dendrite formation, which can pierce the separator and short circuit the battery. Besides, deposited Li reacts to form its own SEI, as represented by the last schematic of Figure 3.5, consuming electrolyte and lowering the interface porosity, thereby creating inhomogeneities in the electrode.

Reactions with metal ions High-voltage oxide materials used to build the battery cathode are at the upper end of the electrolyte stability window at their charged state (around 4 V vs. Li^+/Li). Therefore, some metal ions from the positive electrode are dissolved in the electrolyte and migrate towards the negative electrode, being incorporated into the SEI [JAL15]. This increases the layer's electrical conductivity and leads to enhanced electrolyte reduction and layer growth, resulting in battery resistance increase and capacity fade [VET05, SAR04, BRO05].

Instability due to acidic compounds The formation of acidic compounds like HF has been reported to have a negative influence on the stability of the SEI [KAW02].

3.5.2.2 Anode active material

The most important ageing phenomena affecting the active anode material take place at its surface, but there are also some bulk effects that can also affect its performance [VET05]:

Surface of active material

- Graphite exfoliation and particle cracking due to solvent co-intercalation, electrolyte reduction inside graphite and gas evolution inside graphite, as represented in the top part of Figure 3.5, are considered to have the strogest impact on active material changes, which contribute to cell ageing [WIN03].
- Ion exchange at the surface groups with lithium ions and redox reactions of surface groups are ageing mechanisms that occur at the electrode

surface but are considered to have much lower effect than the previous phenomena.

Bulk of active material

- The volume changes of the graphite during the ion intercalation and deintercalation have a negative impact on the reversibility of this process. However, volume changes are considered to be in the order or 10% of the active material volume, which limits its impact on the battery ageing.
- During Li intercalation and deintercalation, the graphite undergoes a number of phase transitions (changes in its crystalline structure). These structural changes can cause mechanical stress on defects and on C–C bonds. This effect may lead to cracking or mechanical damage of the anode.

3.5.2.3 Anode conductive additives and polymeric binder

Isolated anode particles The anode carbon is part of the battery active material as long as it is electrically connected to the current collector. The volume changes of the active material change the size of the anode particles leading to contact loss between carbon particles, current collector and carbon, binder and carbon, and binder and current collector. This effect reduces the available anode capacity, given that these isolated areas are not able to store lithium [YAZ99].

Binder decomposition Fluorine-containing polymers and copolymers used as binder materials in composite electrodes have been detected to react with the charged anode to form LiF [SPO03]. This degradation reduces the amount of binder available in the electrode and can contribute to the degradation of the mechanical electrode properties in the long run.

3.5.2.4 Anode copper current collector

Some electrolyte components can react with the copper oxidizing the anode current collector. Therefore, the electronic and mechanical contact between the active material and the current collector is lost. Furthermore, these corrosion products have poor electronic conductivity and cause overpotentials and inhomogeneous current distribution along the anode, which facilitate the lithium plating [BRA99].

3.5.2.5 Cathode surface layer

The metal oxide cathode has been considered as a main contributor to the increase of interfacial impedance in high-power lithium-ion batteries [LI01, CHO02]. This increase is accelerated by higher temperature and by high end-of-charge voltages (4.2 V vs. Li/Li^+). Moreover, the oxygen contained in the metal oxide cathode can accelerate these oxidation reactions [VEN03] and be a source of gaseous species [BER16a].

3.5.2.6 Cathode active material

The phase transitions during insertion and extraction of lithium ions in layered metal oxides lead to large and anisotropic volume jumps [VET05]. They are usually minimised by adding some cobalt to the active anode material (about 20%). Besides, aluminium or magesium doped metal oxides exhibit better cycle life compared to undoped materials, given that these elements stabilise the layered structure [BRO03].

3.5.2.7 Cathode conductive additives, polymeric binder and aluminium current collector

As explained for the anode components, the mechanical stress caused by the variations in the cathode volume and the corrosion of aluminium can lead to loss of contact between some particles of the cathode material or with some parts of the current collector, as represented in Figure 3.6.

3.5.3 Ageing effects on battery performance

All the phenomena described above have two measurable effects on the performance of Li-ion batteries, which are capacity fade and impedance rise (or power fade). The capacity fade is mainly due to the blocking of some electrode porous, or the lack of active material provoked by some of the factors described above. On the other hand, power fade is a consequence of a decrease in the electrical or ionic conductivity of any material present in the battery (especially the SEI layer), or a reduced surface area of the electrodes, which reduces the region at which the intercalation electrochemical reaction takes place.

The ageing phenomena, which result into battery capacity and power fade, are usually divided into two components for easier understanding and applicability. These two components are named *cycle* ageing and *calendar* ageing,

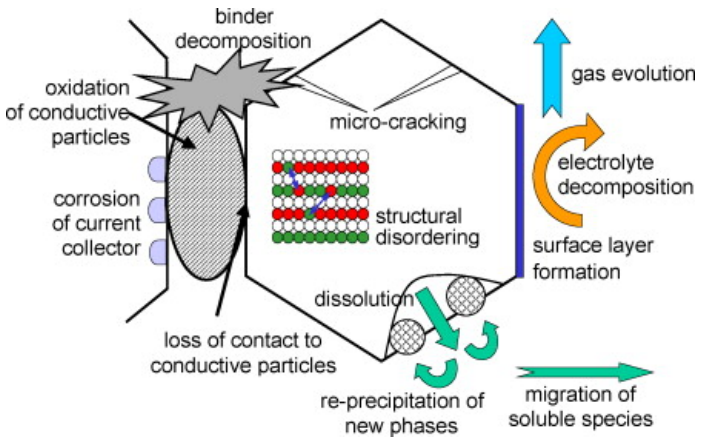

Figure 3.6: Overview on basic ageing mechanisms of cathode materials. Reprinted from [VET05], with permission from Elsevier.

and are assumed to be independent of each other, i.e. the total capacity and power fade is a superposition of calendar and cycle ageing phenomena [SCH14]. Calendar ageing refers to the performance loss due only to the passing of time. This is the ageing that a battery would suffer it it is stored at open circuit conditions, i.e. with no use. Cycle ageing denotes the changes suffered by the battery due exclusively to charge–discharge cycles [KÄB13]. Given that time goes by while the battery is cycled, the measurement of cycle ageing is a challenging task, since it is always superimposed with calendar effects. Likewise, the measurement of the ageing effects require the charging and discharging of the battery, which makes it difficult to measure the calendar effect avoiding the influence of measurement cycles. It has been already proven that the influence of cycle ageing on battery capacity and power fade is much lower than that of cycle ageing for normal battery operation [SCH17]. There are different test protocols and measurement techniques proposed to properly separate both ageing effects, like standard capacity and impedance measurement techniques [VET05], careful design of checkups for calendar ageing characterization [SCH17], standard charge-discharge cycles for cycle ageing phenomena [WAN14b, PUR14, SCH15], ageing acceleration techniques to shorten the required test time [GU14a, STR14, GUA14], etc.

Chapter 4

Modelling of lithium-ion batteries

The purpose of getting power is to be able to give it away.

– Aneurin Bevan

4.1 Introduction

This chapter concerns the Li-ion battery modelling from different approached from different perspectives. A large proportion of the working load of this thesis is summarised along the following sections, as well as many research contribution of the work. Modelling of electrochemical systems has a capital value, given its suitability to improve the battery material design and engineering, the manufacturing process, management strategies, control algorithms, power converter design, optimal dimensioning aimed at maximising the battery capability while minimising its cost, the on-line battery monitoring and control, etc.

Firstly, in Section 4.2, the Energy Storage Laboratory, located at the Public University of Navarre (UPNA), is detailed. The experimental work reported in this thesis has been done in this laboratory. Besides the laboratory equipment description, the 5.3 kWh Li-ion battery used for the application of the methodology proposed through the thesis and for results validation is described in this section.

The SOC estimation in Li-ion batteries is covered in Section 4.3. This

is one of the main parameters concerning battery performance, and its measurement cannot be directly done. The three most relevant trends for SOC estimation are compared in this section in order to identify their advantages and disadvantages through their practical application. The most interesting SOC-estimation method for each application is identified. The conclusions reached in this section were published as a conference in an international conference.

Then, the modelling of Li-ion batteries electrical performance is covered in Section 4.4. Firstly, we describe an equivalent-circuit simple model that was presented as a poster in an international conference. This kind of models are often used in engineering applications. After this, an electrochemical model based on the operation principles explained in Chapter 3 is developed. With this aim, reasonable simplifications of the physical equations are made in order to reach a relatively simple current–voltage relationship that can be expressed as an equivalent circuit. This work is waiting for its acceptance for publication in an international journal.

Subsequently, in Section 4.5, we presetn a thermal model for the Li-ion battery, which was designed and developed in a research collaboration with the group ITF(thermal and fluids engineering), from UPNA. On the one hand, the heat generation inside the battery cells is modelled based on the physical principles explained in Chapter 3. On the other hand, heat dissipation to the ambient air is modelled by means of the finite differences method detailed in Appendix A. The aim of this section is not to reach an accurate estimation of battery temperature, but to build a complementary thermal model that can feed the electrochemical model with a temperature estimation, thereby increasing its accuracy and robustness against changing operational conditions. This electro-thermal combined model is shown at the end of this chapter to provide accurate results for battery modelling.

Finally, in Section 4.6 an ageing model for the Li-ion battery is proposed. These phenomena are separated into calendar and cycle ageing for easier analysis. The ageing model proposed in this section is validated by means of computer simulation of different battery operating conditions. The results obtained through this model are compared with a lithium-ion battery guarantee, providing a good match between the model and the expected battery lifetime for all the simulated conditions.

4.2 Experimental setup

The experimental work presented in this thesis has been performed on a commercial entire battery pack in the Energy Storage Laboratory located at the Public University of Navarre (UPNA). Realistic battery performance has also been analysed by means of an experimental domestic microgrid installed at UPNA. An analysis of the most relevant features of the laboratory equipment employed for this experimental work, the characteristics of the battery pack and a brief summary of the experimental microgrid are presented along the following subsections.

4.2.1 The Energy Storage Laboratory

The Energy Storage Laboratory is one of the sections of the Renewable Energy Laboratory, located in *Los Pinos* Building, at UPNA. The equipment available in this laboratory is versatile and able to handle considerable power (several kilowatts) and current (hundreds of Amps), making form this facility an ideal place to experimentally test commercial ESS. Figure 4.1 shows an experimental setup assembled in this laboratory. The versatility offered by the laboratory allows for the testing of different ESS (supercapacitors and Pb–acid batteries in the figure). Depending on the planned experiment, the required laboratory equipment can be interconnected, providing a wide range of feasible test designs. The specific equipment used for the experimental work presented in this thesis is described through the following paragraphs.

The power management is performed through power sources and loads. The power source used in this thesis is the SPS400X75, from AMREL, whose maximum power is 30 kW, voltage of 400 V and current of 75 A (see Figure 4.2 (a)). It can be manually controlled by means of its frontal panel, or externally programmed. In this work an external analog signal is used to control this power source. Three different power loads were used to discharge the battery, depending on the requirements of the specific experiment. Two of them are linear electronic loads, specifically PLA7.5K–600–400–I (Figure 4.2 (b)) and PLA4K–400–360–I (Figure 4.2 (c)), from AMREL, with rated power, maximum voltage and maximum current of 7.5 kW, 600 V, 400 A and 4 kW, 400 V, 360 A respectively. These electronic loads can also be controlled with their frontal panels or by an external signal. An external control by means of analog signals allows better flexibility in the experiments, and is equivalent to that used for the power source control. The third load is the resistive load shown in Figure 4.2 (d), built ad hoc for the high-power requirements of the studied battery. This load can drain up to 55 kW, with a maximum voltage of

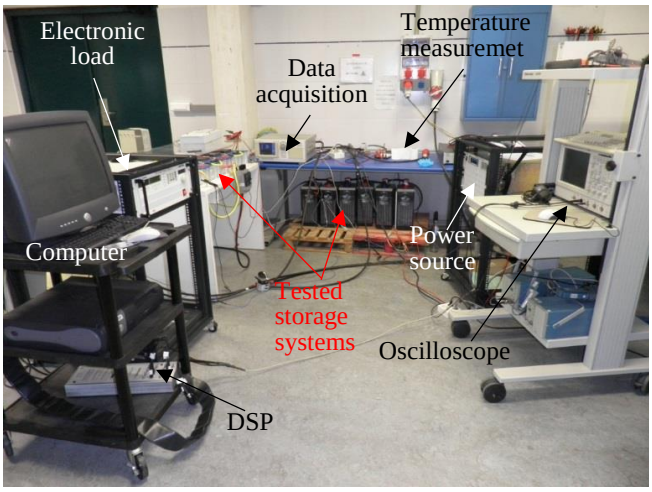

Figure 4.1: Experimental setup assembled in the Energy Storage Laboratory, at UPNA. Reproduced from [SAN13] with permission from the author.

160 V. Since the resistive load cannot be externally controlled, an electronic load is always connected in series, allowing the current control (and therefore also the power control).

Two options have been used for the control of these power systems depending on the required battery power profile. On the one hand, for experiments where standard charge-discharges are required or a pre-defined power has to be managed by the battery, a computer connected to a digital signal processor (DSP, DS 1104, from dSpace) is used, as shown in Figure 4.2 (e). The desired power profile is programmed into the computer using C++, and voltage and current can be measured to provide a closed-loop battery control. On the other hand, for electrochemical impedance spectroscopy (EIS) tests, the Frequency Response Analyser (FRA, from Amrel) shown in Figure 4.2 (f) was used. In these tests an AC current with different frequencies is superimposed to a DC current and the voltage response is measured. Using the generalised Ohm's Law the impedance of the battery can be calculated. The FRA used for these tests can make frequency sweeps from 0.1 Hz to 20 kHz measuring the battery response at each frequency, and providing the complex impedance of the system at each frequency.

The equipment used for data measurement and acquisition depends on the measured variables and the required time scale (sampling frequency and duration of the test). Voltage and current data are always measured and stored by the data logger WT1800, from Yokogawa (Figure 4.2 (g)). This

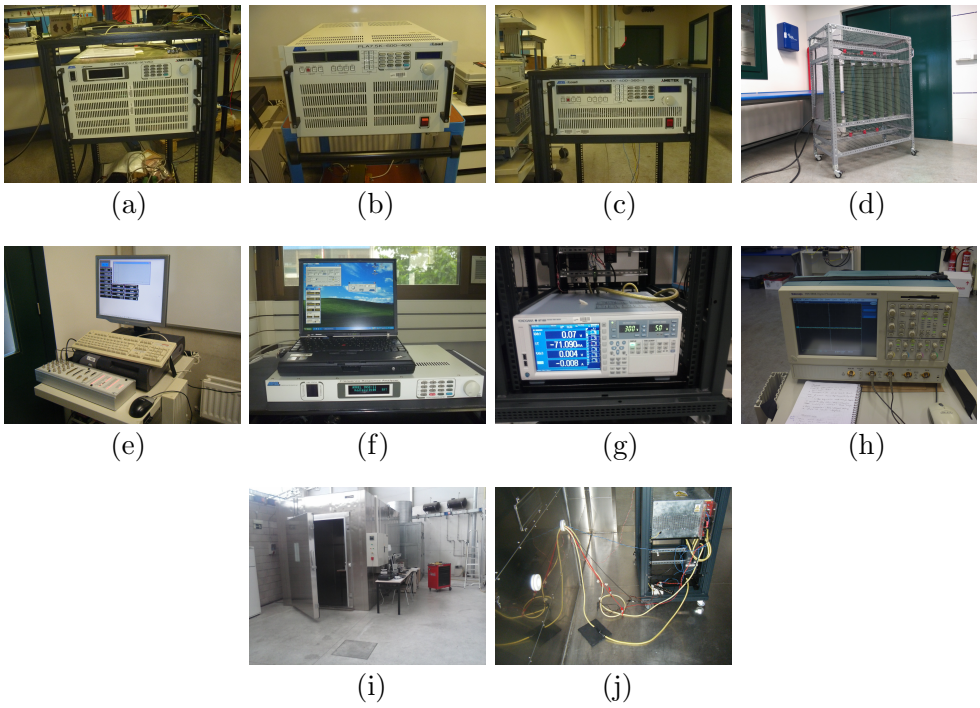

Figure 4.2: Main laboratory equipment used for the experimental work presented in this thesis. Power management equipment in the first row: power source (a), electronic loads (b), (c) and resistive load (d). Control and measurement equipment in the second row: computer with DSP (e), FRA and its controlling computer (f), data logger (g) and oscilloscope (h). In the third row climatic chamber (i) and battery rear view with some safety devices (j).

data logger has enough memory to store the data of any experiment required for this thesis. The maximum sampling frequency is 20 Hz an the accuracy is around 0.1% of the measurement + 0.05% of the range. When high frequency signals need to be measured or higher sampling frequency is required, an oscilloscope TDS 5054 (Figure 4.2 (h)), from Tektronix is used. Its bandwidth is 500 MHz and its highest sampling frequency is 5 GHz. For temperature measurement, PT-100 sensor driven by transductors were connected to the data logger and the measured voltages were latter converted into temperatures based on the transductor and PT-100 characteristics. Internal variables of the battery, such as cell voltages and temperatures taken by the battery control system are transferred from the battery microprocessor to a computer through an RS–232 communication protocol and stored by the computer.

The climate chamber shown in Figure 4.2 (i), located in the Energy Technology Laboratory (also at Public University of Navarre) is made available for the tests requiring a temperature control. The climate chamber is a CCK–

40/22B44, from Dycometal, which allows a temperature control from -40 °C to 150 °C with an error lower than 1 °C. Besides, the relative humidity can be controlled if the temperature is between 0 and 60 °C. The capacity of the chamber is 22 m^3 and can handle thermal gradients of –1 °C min^{-1} (cooling) and +2 °C min^{-1} (heating).

Typical protection systems are installed in order to minimize the risks of damaged equipment and electroshock. Ground connection of the system cases, automatic switches with overcurrent protection and battery monitoring concerning safety limits are some of the protection measurements adopted for the experimental work. Figure 3.4 (j) shows a rear view of the tested battery with some safety devices using during the experiments.

4.2.2 Battery description

A commercial Li-ion battery pack with graphite anode and NMC cathode was used to apply the experimental procedure proposed in this thesis and to validate the results. The rated voltage of this battery pack is 133 V and its capacity is 40 Ah, being able to store 5.3 kWh of energy. It is built by the series connection of 36 pouch-type cells, with a maximum current of 200 A during discharging (5 C) and 80 A during charging (2 C). The temperature which guarantees the safe operation of the battery ranges from 0 °C to 60 °C.

The cells of this battery are grouped into 6 modules, each comprising 6 cells, as can be seen in Figure 4.3 (a). Moreover, the battery has measurement and communication circuits to be controlled by a BMS, even though a BMS has not been used for the experiments conducted in this thesis. We are therefore able to make experiments under extreme operating conditions and to equalize the cells whenever needed. Figure 4.3 (a) shows the battery with the cover case removed. The green electronic boards on top of each module are the measurement and communication circuits. In Figure 4.3 (b) the battery is mounted on its laboratory rack and placed inside the climatic chamber. The cables shown on the right side of the battery are for power management, battery control and measurement through the equipment located outside of the chamber.

The three images on the right side of Figure 4.3 were taken during a battery disassembly process tackled during the thesis. In Figure 4.3 (c) one of the six modules (each containing six pouch cells) with its aluminium heat exchangers is shown. After the removal of the heat exchanges this module looks like the picture shown in Figure 4.3 (d), with the six cells packed in a black, plastic polymer. Finally, one of the battery pouch cells which are inside the plastic is

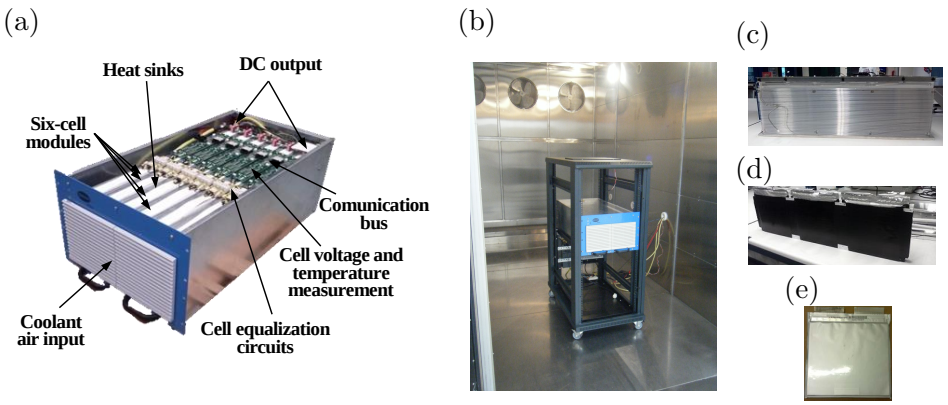

Figure 4.3: Li-ion battery pack analysed in this thesis. Battery without cover (a), installed on the laboratory rack and inside the climatic chamber (b), battery module with heat exchanges (c), battery module without heat exchanges (d) and battery pouch cell (e).

shown in Figure 4.3 (e).

With the study of the whole battery pack, all the components of the battery (connections, safety elements, etc.) are included in the analysis, which increases the pertinence of the conclusions to be applicable to a real entire system. Figure 4.4 shows the battery test bench installed around the climatic chamber. The battery is the only element placed inside the chamber and the required equipment is placed close to the battery for easier handling and higher measurement accuracy, but outside the chamber.

4.2.3 Experimental domestic microgrid

The real-life performance of the Li-ion battery is studied by means of an electrical microgrid located at UPNA [PAS15]. Two sources of electricity are installed in this microgrid, which are a 4 kWp PV system and a 6 kW wind microturbine. Given that the microgrid is installed in research facilities instead of in a private home, the home electricity consumption is emulated following the consumption pattern measured in a family home located in the vicinity of the university. Likewise, the microgrid also allows for the energy exchange with the electricity grid. Figure 4.5 shows a schematic representation of this microgrid, where the power conditioning stage, located in the central part of the figure enables the power flows between the different elements, represented in the figure with red, thick arrows. The power management system comprises a PC and a communication bus. It is communicated with each of the microgrid power system (as represented in Figure 4.5 by means of red, thin lines) and its

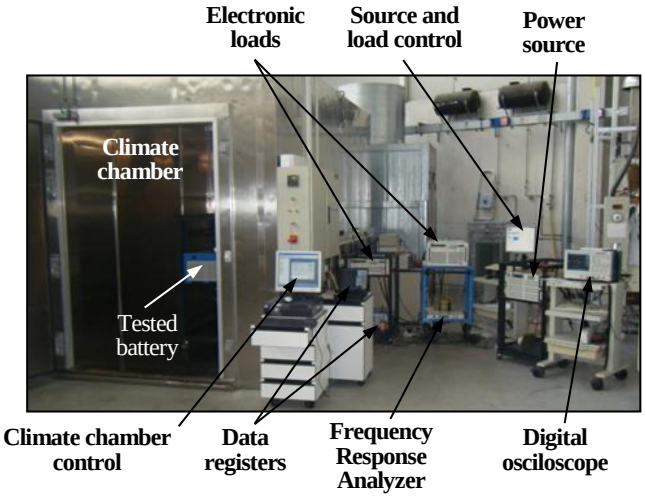

Figure 4.4: Battery test bench with temperature control.

function is the real time acquisition and control of the microgrid energy flows. In turn, the microgrid has a number of monitoring and measuring devices for electrical and meteorological variables. These variables are stored in a database with a one second frequency.

A number of energy storage systems (ESS) are available in the Energy Storage Laboratory, whose performance in this real microgrid can be experimentally analysed. Specifically a hydrogen-based system, lead–acid batteries, lithium-ion batteries and SCs are the storage systems currently available in our research facilities. The main characteristics of these ESS are described below:

- The hydrogen based system comprises four series-connected proton exchange membrane fuel cells (PEM FCs) with a total rated power of 4.8 kW and four hydrogen tanks with a total capacity of 35.2 Nm^3.
- The SC bank comprises three series connected BMOD0083 SCs which, in turn, are connected in parallel directly to the FCs.
- The lead–acid battery bank consists in 120 cells OPzV (FIAMM) connected in series, which provide a capacity of 72 kWh.
- The lithium-ion battery is described in Subsection 4.2.2. It is a commercial module from Cegasa which capacity is 5.3 kWh.

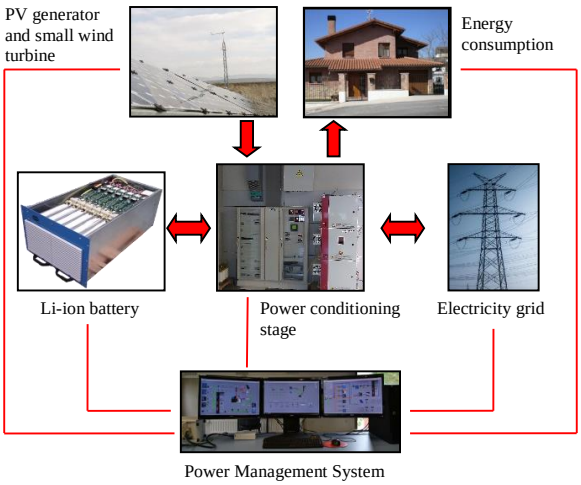

Figure 4.5: Schematic diagram of the electrical microgrid located at UPNA.

The ESS utilised for regular microgrid operation is the lead–acid battery bank, while the other systems are still being researched. The aim of including an ESS in this grid-connected electrical microgrid depends on the designed management strategy. Some typical objectives are increasing the renewable energy self-consumption, soften the power exchange between the microgrid and the electricity grid or provide some grid services such as voltage or frequency regulation. These grid services should be properly remunerated to make them attractive for ESS owners, and thereby improve the overall grid performance. The most suitable microgrid management strategy depends on the analysed scenario and is an on-going research topic [ARC17, ARC16, PAS15] which is out of the scope of this thesis.

The ESS management strategy used for the analyses presented along this thesis is a coupling of the renewable generation with the daily home consumption, while the annual fluctuations are absorbed by the electricity grid. In this way, the storage system guarantees a minimum power exchange with the electricity grid, keeping any inconvenience related to renewable energy generation away from the grid. Moreover, the grid connection allows for a reduction of the ESS size, given that an annual energy balance is not required.

4.3 SOC estimation

Many battery state variables should be accurately monitored in order to allow wise control decisions intended to optimize the performance of the storage

system. If the monitoring of the battery is not rigorous, a bigger (and more expensive) battery is needed to meet the same operational requirements. Moreover, unexpected blackouts and battery lifespan shortening can be undesirable penalties of an improper monitoring algorithm. There are several variables to be monitored, such as battery impedance or capacity, State of Health, State of Function, etc. Among them, one of the most important variables is the battery SOC, given that it is a measure of the actual charge content of the ESS. A battery management system (BMS) is required for a safe operation of Li-ion batteries to control the voltage and temperature of each cell inside safe limits. Given that battery SOC cannot be directly measured from the battery (unlike variables such as voltage, current or temperature that can be measured), an important function of the BMS is to provide an estimation of the battery SOC.

There is a wide variety of SOC-estimation algorithms proposed on the bibliography, each of them with advantages and disadvantages. The used algorithm should depend on the particular application, the desired accuracy and the budget available. The most used SOC-estimation techniques can be classified into three main groups and are analysed below:

4.3.1 SOC estimation techniques

4.3.1.1 Integrating methods

These methods predict the SOC of the battery based on an Ampere-hour counting. They are widely used with Li-ion batteries because the required computational power is low, and their performance with this kind of batteries is better than with others due to the lower magnitude of side reactions. Some authors take into account the coulombic efficiency [SID15, CHA13], or the capacity shift along the lifetime of the battery [FLE14a] to get a more accurate SOC value. The expression for SOC is:

$$SOC(t) = SOC_0 + \frac{1}{C} \cdot \int_0^t \eta_c \cdot i(t) \cdot dt \tag{4.1}$$

Where the capacity of the battery C can depend on the state of health of the cell. The coulombic efficiency η_c is commonly assumed to be unitary for Li-ion batteries in low current and ambient temperature scenarios, since $\eta_c > 99.5\%$ [ZHE15, SMI10]. The main disadvantage of this method are that it requires the knowledge of the initial SOC and that the inaccuracy arising from current measurement errors are integrated ant therefore accumulated, producing a significant error when the system runs during long periods of time.

A widely-used strategy to get ride of this cumulative error is to measure the open circuit voltage (v_{OC}) of the battery and define some points to reset the SOC value. Typical reset points are resting periods during which the battery remains in open circuit for long periods of time and the open circuit voltage reaches te equilibrium ($v_{OC} = v_{eq}$, minimum battery voltage reached with low discharging current (when the battery SOC is known to be 0), battery maximum voltage with reduced charging current (when the SOC is 1), etc. The main disadvantage of these reset point is that the reset condition needs to be satisfied in order to have an error-free SOC estimation, and there are some battery applications in which these reset conditions are not as common as would be desired.

4.3.1.2 Model-based methods

The battery behaviour is modelled and the observable variables (battery voltage v and current i) are related with the SOC through mathematical expressions. These estimators are not affected by cumulative error; however, they have a high sensitivity to model inaccuracies. Most of the models used to estimate the SOC represent the impedance of the battery through an electric circuit and adopt a polynomial expression for the v_{OC}–SOC relationship [SZU08]. The problem with this methods is that accurate models taking into account all the phenomena occurring in a battery have high computational requirements and, therefore, are not suitable for on-line SOC prediction. Additionally, the model-based prediction strategies are sensitive to variation in model parameters, which occurs with the battery ageing and temperature changes.

4.3.1.3 Closed-loop methods

The combination of ampere-hour integration and model-based estimation is a good trade-off between computational simplicity, estimation accuracy and cumulative error mitigation. These methods get a SOC prediction through an Ampere-hour integration strategy, and use the voltage and current measurements to reduce the error through a battery model. The most typical algorithms used to combine these two information sources are the Kalman filters with some variations [SID15, HE11, CHE13], adaptive filters [ROS11, ZHO14] and Gauss-Hermite quadrature [LI12a]. They have a good robustness against model parameters variation and measurement noise, but their computational requirements are sometimes too high.

4.3.2 Experimental comparative study of SOC estimators

A representative method from each of the three families addressed in the previous subsection is chosen and its parameters are adjusted to represent the battery described in Subsection 4.2.2. An experiment is designed in order to analyse the performance of these three estimators when the battery is subject to realistic stationary operation, specifically the microgrid described in Subsection 4.2.3 is used. The influence of two particular effects on the SOC estimators is studied. On the one hand, an inaccurate current measurement and, on the other hand, the influence of battery ageing in the SOC estimation. Given that the integration error is a cumulative effect that is noticeable after several hours or days of operation, particular test conditions are designed in Subsubsection 4.3.2.2 in such a way that the strengths and weaknesses of the estimators can be detected in a reasonable time, allowing important reductions of test time. The results of this subsection have been presented as an oral session in the conference IECON–2016 [BER16b].

4.3.2.1 Particularization of SOC estimators

Integration method As mentioned above, the coulombic efficiency is usually assumed to be 1 for Li-ion batteries. This approximation is also adopted for this comparison. Therefore, the only parameter required for the Ampere-hour counting method (Equation 4.1) is C. Since the battery is at an early stage of its lifetime, it is concluded that the actual capacity equals the nominal capacity ($C = 40$ Ah).

Model-based method Given that the SOC estimation with model-based methods is based on battery performance measurement, it has to be performed online. Therefore, an electric circuit model requiring low computational power is usually preferred for faster calculations. For this study, an equivalent circuit proposed later in this thesis (Subsection 4.4.2 and shown in Figure 4.6) is selected to calculate the open-circuit voltage (v_{OC}) from the measured battery current and voltage. The battery impedance consists of a resistance R_{ohm} which stands for the ohmic losses explained in Subsection 3.3.1, and a parallel connection of R_{dyn} and C_{dyn} which represents other battery dynamic processes, being the activation of the electrochemical reaction Subsubsection 3.3.2.2 and the diffusion of lithium ions Subsection 3.3.3 the most important ones. The equation obtained form this circuit is:

$$v_{OC} = v - \left(i - C_{dyn} \cdot \frac{dv_{dyn}}{dt} \right) \cdot R_{dyn} - i \cdot R_{ohm} \tag{4.2}$$

A usual relationship between v_{OC} and SOC is an empirical polynomial expression, which can be easily fitted to measured data and rapidly calculated during the computer simulation. The procedure for the model parameters fitting is explained in Subsection 4.4.4, and the parameter values obtained for the Li-ion battery used in this work are summarised in Table 4.1. This fitting method has been published during this thesis as a conference contribution [BER15]. Moreover, the resulting $v_{OC}(SOC)$ relationship for this 133 V battery is expressed in Equation 4.3 as an eight-order polynomial:

$$v_{OC} = 100 + 384 \cdot SOC - 3785 \cdot SOC^2 + 19\,976 \cdot SOC^3 - 59\,274 \cdot SOC^4 + 102\,480 \cdot SOC^5 - 102\,331 \cdot SOC^6 + 54\,734 \cdot SOC^7 - 12\,147 \cdot SOC^8 \quad (4.3)$$

Closed-loop method As closed-loop representative SOC-estimation algorithm, a method based on observer and controller was chosen. It is a variation of an idea presented by M. A. Roscher and D. U. Sauer [ROS11] for SOC monitoring. These authors presented a model for lithium iron phosphate (LFP) batteries, whilst the battery analysed herein has a lithium-nickel-manganese-cobalt oxide (NMC) cathode. The most notorious difference between both technologies is the hysteresis eye of the open-circuit voltage, which exists only in LFP batteries. The block diagram of this estimation method is shown in Figure 4.7.

Firstly, the algorithm uses a two-step adaptive filter. This adaptive filter calculates a first estimation of v_{OC}, named $v_{OC}(1)$, which is based on the parameter vector (θ) from the previous iteration step. To do so, the actual battery voltage and current are measured. The first step of the adaptive filter predicts the voltage of the battery (v') based on the measured current. Then,

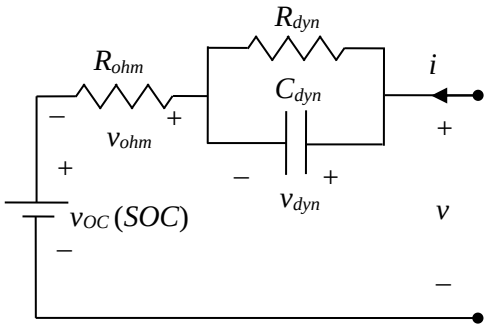

Figure 4.6: Electric circuit model used for SOC estimation.

Parameter	Value	Unit
R_{ohm}	70.2	mΩ
R_{dyn}	35.7	mΩ
C_{dyn}	714.6	F

Table 4.1: Value of each element of the model.

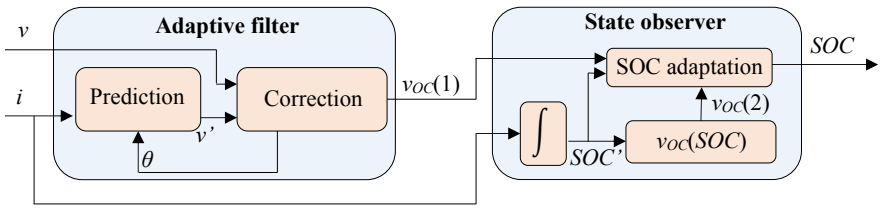

Figure 4.7: Block diagram of the observer and controller method for SOC estimation.

v' is compared with the actual measured voltage (v) in the correction step in order to adapt the circuit parameters to be used in the next iteration. By adapting the parameter vector θ, the prediction error ($|v' - v|$) is recursively minimized. Since the v_{OC} is one of the components of θ, the estimated v'_{OC} is extracted from the parameter vector and fed into the state observer block.

In the state observer, an SOC' is forecasted through Equation 4.1 by current integration. From this forecasted SOC', another estimation of v_{OC}, $v_{OC}(2)$ is calculated using the $v_{OC} - SOC$ relationship shown in Equation 4.3. A comparison between $v_{OC}(1)$ and $v_{OC}(2)$ leads to an SOC adaptation using a scaling factor characteristic from this method called voltage feedback gain. Hence, this method provides an SOC taking into account the results from current integration and model parameters, therefore compensating possible integral cumulative errors. Moreover the algorithm is able to adapt the model parameters in the correction step to keep its good performance under different operating conditions and ageing states of the battery.

4.3.2.2 Experiment description

The operation of the microgrid during eight hours at the afternoon and evening of the 11 April 2013 is used to test the SOC monitoring algorithms. Figure 4.8 (a) shows generated power (both from the wind turbine, P_{wind} and from the PV panels P_{PV}) and consumed power (P_{con}) from 15:00 h to 23:00 h. Note that P_{con} is pictured in Figure 4.8 (a) as positive for easier representation. However, its direction is the opposite of the wind and PV generation.

11 April 2013 was a sunny day, as can be inferred from the PV generation, while the wind power had the usual gusty pattern. The control algorithm was programmed to minimize the power exchange with the electricity grid, thus being the difference between generated and consumed power mainly assumed by the Li-ion battery. Using this management strategy, power flow between the microgrid and the electricity grid takes place only when the battery cannot

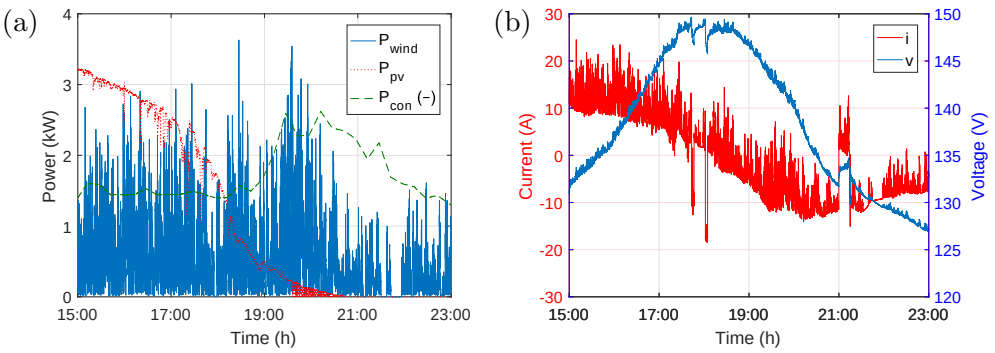

Figure 4.8: Main variables involved in the comparison experiment: generated and consumed power of the microgrid (a) and current and voltage managed by the battery (b).

assume more charge (17:45 h and 18:00 h).As shown in Figure 4.8 (b), the battery is charged during the afternoon, when the sun is shining and the domestic power consumption is low. The generated power decreases during the evening, and around 18:30 h the battery has to provide energy for the consumption. From this moment on, the battery SOC is reduced until the end of the test. The current shown in Figure 4.8 has a high variability caused by the wind power generation.

For the comparison of the SOC estimators, an ideal scenario with accurate knowledge of model parameters and current measurement is presented at first stage. However, a good monitoring method does not require the very accurate (and expensive) current sensor used in laboratory experiments, and keeps its accuracy during the whole lifetime of the battery. Therefore, after the ideal scenario, the performances of the methods are compared in two scenarios: (i) an inaccurate current sensor and (ii) an aged battery. An inaccurate sensor is simulated by an offset in the measured current, which is the most harmful effect of a sensor inaccuracy for SOC monitoring. In the 8 hour microgrid experiment shown in Figure 4.8, a measured current $i' = i + i_{offset}$, with $i_{offset} = 0.5$ A is considered. This offset represents around 10% of current measurement. The influence of this large offset in a short test is similar to that of a lower offset in a longer experiment, allowing for this analysis by means of a short laboratory test (8 hours). The battery ageing is considered to induce a capacity fade and a resistive rise, as explained in Subsection 3.5.3. Therefore, an aged battery is simulated by changing the algorithm input parameters to $C' = 1.1 \cdot C$, $R'_{ohm} = 0.9 \cdot R_{ohm}$ and $R'_{dyn} = 0.9 \cdot R_{dyn}$. Since an accurate current sensor is used during the test and the battery capacity has been measured beforehand, the real SOC is assumed to be the value estimated by the Ampere-

hour counting method using $C = 40$ Ah. The RMSE, calculated by means of Equation 4.4, and the maximum error of the methods during the experiment are calculated and compared.

$$RMSE = \sqrt{\frac{\sum_{k=1}^{n} \left(\hat{SOC}_k - SOC_k \right)}{n}} \tag{4.4}$$

where n is the number of measured and calculated SOC samples, SOC_j is the actual SOC of the sample j and $\hat{SOC}_j$ is the calculated SOC for the same sample.

4.3.2.3 Comparison results

Figure 4.9 shows a comparison between the performances of three SOC estimation methods during the above-described experiment in three scenarios analysed hereinafter. The RMSE and maximum error of each method are calculated and summarized in Table 4.2.

Accurate current and model parameters Figure 4.9 shows the evolution of the battery state of charge during the experiment. The initial SOC is around 0.3, increasing during the afternoon until it reaches a value close to 1 around 17:50 h. After one hour, it begins to decrease until the end of the test, where $SOC \approx 0.2$. The red line in this figure is called *real SOC*, given that it is calculated by the Amper-hour counting method and the laboratory current measurement equipment used for this experiment has a high accuracy. Moreover, the battery capacity is also known. The other two lines (green, dotted and blue, dashed lines) are the SOC evolution predicted by the electrical model method and by the observer and controller method respectively. The electrical model accuracy is a bit lower than that of the observer and controller method, as shown in Table 4.2, given that the battery model cannot take into account all the physical phenomena occurring in the battery.

Current measurement inaccuracy The robustness of the three methods to current measurement offset is studied at this point and the results are shown in Figure 4.9 (b). Given that the SOC evolution is the same as in Figure 4.9 (a), the errors between the calculated and the actual SOC are preferred to be shown in this graph, which allows a closer view of the inaccuracy of each method. The cumulative error of the Ampere-hour counting method is clearly seen in the red, solid line. This method is not suitable for the common scenario with an offset in the current measurement. Any current sensor has a larger

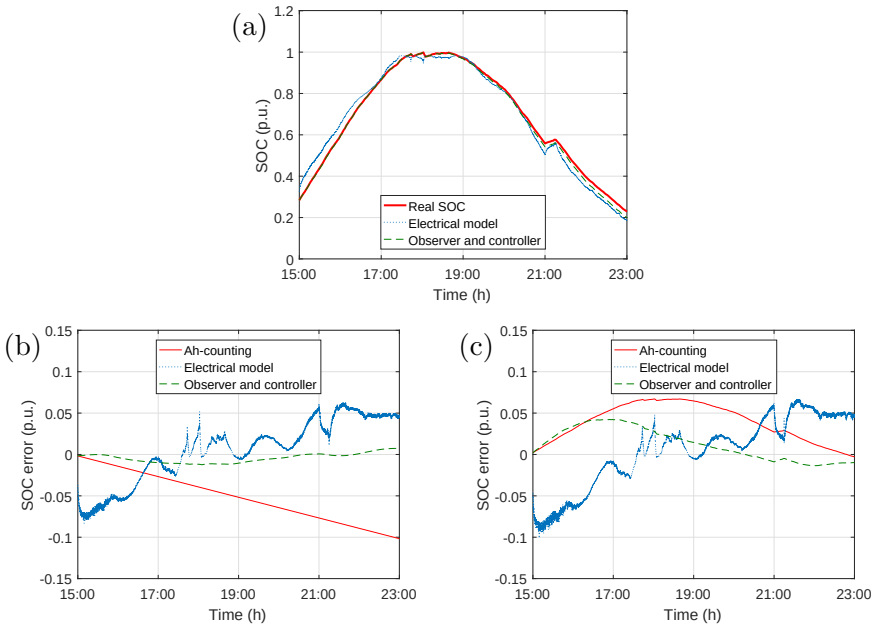

Figure 4.9: Performance of the three SOC estimation algorithms: with accurate current and model parameters (a), with inaccurate current measurement (b) and for an aged battery (c).

or smaller measurement offset that is usually affected by many parameters, such as measurement temperature, complicating its compensation. A small current offset integrated during a long time lapse has the same effect than the analysed large error integrated during a short time. As shown in Table 4.2 the maximum error of the ampere-hour counting method in this scenario is the largest of the performed tests. The results of the electrical model method are similar to the scenario where the current does not have measurement offset, which proves that the electrical model method is robust to measurement offset. However, this method is not highly accurate, as shown in Figure 4.9 (b). The observer and controller method keeps its high accuracy in this current offset scenario, as can be seen in the figure and the errors shown in Table 4.2, with an SOC prediction $RMSE = 5 \cdot 10^{-5}$ p.u. during the eight-hour experiment and a maximum error of $1.2 \cdot 10^{-2}$ p.u.

Aged battery The performance of the methods for an aged battery is simulated, as explained before, with different values of capacity and impedance. The results are shown in Figure 4.9 (c) and summarized in Table 4.2. The Ampere-hour counting method does not have a cumulative deviation, but the capacity fade triggers an error as high as $6.7 \cdot 10^{-2}$ p.u. when the battery

Table 4.2: SOC estimation errors of the three methods under different operational conditions. Ampere-hour counting (Ah-c), electrochemical model (EM) and observer and controller (OC) methods.

	Ah-c	EM	OC
		Accurate variables	
RMSE (p.u.)	—	$1.4 \cdot 10^{-3}$	$1.6 \cdot 10^{-4}$
Max error (p.u.)	—	$8.7 \cdot 10^{-2}$	$2.9 \cdot 10^{-2}$
		Current measurement offset	
RMSE (p.u.)	$3.6 \cdot 10^{-3}$	$1.5 \cdot 10^{-3}$	$5.0 \cdot 10^{-5}$
Max error (p.u.)	0.1	$8.3 \cdot 10^{-2}$	$1.2 \cdot 10^{-2}$
		Aged battery	
RMSE (p.u.)	$2.0 \cdot 10^{-3}$	$1.8 \cdot 10^{-3}$	$5.3 \cdot 10^{-4}$
Max error (p.u.)	$6.7 \cdot 10^{-2}$	0.1	$4.2 \cdot 10^{-2}$

is charged. The accuracy of the electrical model is slightly lower than in the previous scenarios. This method keeps its robustness, but its accuracy is low for the three scenarios, nonetheless. The observer and controller method keeps high accuracy and robustness under these conditions, with an error slightly higher than in the previous scenarios, as shown in Table 4.2. In Figure 4.9 (c), the observer and controller method is shown to behave in a similar manner to the Ampere-hour counting method at the beginning of the test. As the error increases, the observer and controller algorithm corrects its internal parameters and amends this miscalculation, achieving the most accurate results in the three scenarios.

4.3.3 Conclusion

This section has shown that each SOC estimation algorithm has its advantages and disadvantages. The ampere-hour counting method is easily programmable and requires low computational effort. Moreover, it is accurate if a trustworthy current measurement is available and the battery capacity is known. However, its cumulative error makes it unsuitable for online SOC calculation. The equivalent circuit method does not have this cumulative error and is robust to current measurement inaccuracies and battery parameter shift, keeping a reasonable error even when their inputs are not accurate. However, its error is usually relatively large. Meanwhile, the observer and controller estimator has outstanding performance, reaching the lowest estimation error and being able to adapt the circuit parameters to the actual state of the battery. The main disadvantages are that on-line current and voltage measurements are required and its higher computational requirements.

Therefore, a closed-loop SOC estimation method is the most reasonable for stationary applications, where the battery normally operates with an intermediate SOC and rarely has long resting period when the cumulative errors can be reset. On the other hand, the ampere-hour counting method provides good results for laboratory experiments, in which accurate current measurement and battery parameters are available, and which last no longer than several minutes or a few hours. Therefore, in the following sections, where SOC is used as an input variable for the presented models, the ampere-hour method is used to estimate this variable.

4.4 Electrochemical modelling: from physics to an equivalent circuit

4.4.1 Introduction

An electrochemical model is a conceptual, graphical or mathematical representation of the physical and chemical phenomena taking place during the battery operation. Its main purpose is to analyse, describe and explain these phenomena through computer simulation. Therefore, it is an essential tool to optimize the manufacture of the device, select the most suitable battery for each application and capitalise on its strengths during its working life, designing suitable management and control strategies. In this respect, a great deal of work devoted to the development of models for a wide range of applications is being carried out.

Battery models can be classified into physics-based models and equivalent-circuit models. Physics-based models use both the mathematical expressions of physical phenomena and the material microstructure to predict battery performance [TIP14, SAL15, GU15]. They are generally used to study a specific battery parameter and make it possible to analyse phenomena such as the relaxation of insertion cells [FUL94], phase change and the effect of the porous structure of electrodes [SRI04] and the optimization of electrode porosity and thickness [NEW95]. Although they are useful to improve battery design and manufacture, complex equations need to be solved, a high computational power is required and they fail to predict the performance of a whole battery system, given the infeasibility of taking each and every battery component and process into account.

On the other hand, equivalent-circuit models are generally comprehensive models that are able to predict the overall behaviour of the battery. These models are focused on estimating the SOC (with any of the approaches cov-

ered in Section 4.3) and having an accurate representation of the battery impedance. The accurate knowledge of this impedance enables the prediction of power losses inside the battery and available energy at any time. There are also two main approaches with regard to impedance calculation. On the one hand, a machine-learning algorithm can be used to figure out this parameter. These algorithms run for a training period in which they try to minimize the error between predicted and measured battery performance. The most typical learning algorithms used in these models are based on artificial neural networks [WAN16b, DON15, HU12]. These models generally provide good results in terms of accuracy, which can be maintained throughout the battery lifetime by parameter correction. However, they often fail to associate the battery behaviour with the underlying physical phenomena, since they are not based on physics but on mathematical optimization. On the other hand, the battery impedance can be designed by simplifying the physical equations in order to speed up the computer simulation while keeping the accuracy as high as possible [FLE14a, FEN15, NEJ16]. In this case, the impedance parameters represent the main physical processes which determine the battery performance. There is a wide range of impedance designs based on physical battery operation. A straightforward representation of the battery impedance is a series connection of a resistance to an ideal voltage source. However, this representation is seldom used due to its poor accuracy. Instead, many authors use the Randles Model, in which a number of RC circuits are added to the series resistance in order to represent battery dynamic phenomena [LIA04, CHE06a, KAR08, HE11, ZHA16b]. Although these models can achieve better accuracy in the prediction of high-dynamic performance, this accuracy is generally lower when the slow relaxation processes need to be taken into account.

Given that each modelling technique has its advantages and disadvantages, the best battery model depends on the purpose for what it is designed and on the application. Therefore, two modelling approaches are presented hereinafter. On the one hand, in Subsection 4.4.2, a simple electric-circuit model is presented, its parameters are adjusted to the battery described in Subsection 4.2.2 and its performance is experimentally validated. The results of this section have been presented in the 17th European Conference on Power Electronics and Applications (EPE'15 ECCE Europe). This model is useful for typical applications where the battery performance needs to be simulated using low computational effort, such as the study presented in Chapter 5, later in this thesis. On the other hand, a more detailed model based on physicochemical principles is designed in Subsection 4.4.3. The equations describing the most important phenomena taking place in the battery are simplified in

order to reach an equivalent circuit representation. After this, a parameter fitting method is proposed and particularised to the commercial battery studied in this thesis. Finally, the model is validated by means of different laboratory experiments. The results of this section are waiting for acceptance of publication in a scientific journal. This model can have different applications, such as achieving better simulation accuracies than simple models in a wider range of working conditions, understanding the relationship between physical phenomena and electrical characteristics of the battery, achieve more convenient control strategies for the power converter, design of improvements in the manufacturing process to achieve batteries with the most suitable electrical characteristics, etc.

4.4.2 Simple electric circuit model

4.4.2.1 Proposed model

The simple equivalent circuit shown in Figure 4.6 is proposed to be used as battery model. This is the same model adopted in Section 4.3 for SOC estimation. The output voltage (v) is calculated as the aggregation of the open-circuit voltage (v_{OC}) and two voltage drops v_{ohm} and v_{dyn} representing energy losses. The resistive element R_{ohm} stands for ohmic losses taking place in both electrodes, in the electrolyte and in the solid–electrolyte interface (SEI). Meanwhile, the R_{dyn} C_{dyn} network represents the activation losses, inherent to the electrochemical reaction, and diffusion losses, resulting from ion concentration gradient in the electrolyte. This method of grouping phenomena results in a straightforward model, which able to predict the evolution of the battery voltage. The model is a useful tool for the sizing of an ESS and for the design of the power electronics converter connected to it.

4.4.2.2 Parameter fitting

As explained in Section 4.3, the ampere-hour counting method is suitable for SOC estimation during short laboratory tests. Therefore, this is the method chosen along this subsection, using Equation 4.1 to calculate SOC, assuming $\eta_c \approx 1$. The single parameter required for this calculation is the battery capacity C, which is measured by a low current discharge experiment. This experiment starts with the battery totally charged, and consists in a battery discharge at a current $i = \frac{1}{10}C$, which means 4 A for the 40 Ah battery used along this thesis. The time required for the battery to reach the fully-discharged state is measured to be 10.25 h, which implies a battery capacity

of 41 Ah.

For the purpose of characterizing the v_{OC} of the battery, a discharge–charge experiment with a current $i = 0.025$C ($i = 1$ A for the battery used in this thesis) was performed. The voltage measured during this test is plotted versus SOC with blue, solid line in Figure 4.10 (a). The difference between charge and discharge curves is small because of the low current driven during the test. This small voltage difference is mainly due to ohmic and activation phenomena (see Subsection 3.3.1 and Subsubsection 3.3.2.2), since the v_{OC} curve has imperceptible hysteresis loop in NMC lithium-ion technology [WU12]. A very accurate characterization of v_{OC} is obtained from this test. For $SOC \approx 0.08$, a knee in the v_{OC} curve is precisely seen and slope changes are also perceptible for $SOC \approx 0.4$ and $SOC \approx 0.65$. The accurate characterization of these effects is a major issue from electrochemical point of view, given that slope changes are the result of the evolution of ions taking part in the electrochemical reaction [SAI01, XU11]. The average value between charge and discharge voltage is also plotted in Figure 4.10 (a) with black, dotted line. This line correlates each value of SOC with a voltage v_{OC}, which is especially interesting because it does not present significant modifications during the lifetime of the battery [WAA13].

The coefficients of a polynomial expression are fitted to model v_{OV}, as many authors have proposed in previous jobs [SZU08, YAN14]. The eight-grade polynomial showed in Equation 4.5, which provides an accurate approximation to the experimental data and has a low computational complexity.

$$\begin{aligned} v_{OC} =& 100 + 384 \cdot SOC - 3785 \cdot SOC^2 + 19\,976 \cdot SOC^3 - 59\,274 \cdot SOC^4 \\ &+ 102\,480 \cdot SOC^5 - 102\,331 \cdot SOC^6 + 54\,734 \cdot SOC^7 - 12\,147 \cdot SOC^8 \end{aligned} \tag{4.5}$$

Several charging and discharging step-current experiments were performed with different SOC levels in order to calculate the impedance parameters R_{ohm}, R_{dyn} and C_{dyn}, one of which is shown in Figure 4.10 (b). The parameters were fitted to measured data using Equation 4.6 and Equation 4.7.

$$v_{ohm} = i \cdot R_{ohm} \tag{4.6}$$

$$v_{dyn} = i \cdot R_{dyn} - R_{dyn} \cdot C_{dyn} \cdot \frac{dv_{dyn}}{dt} \tag{4.7}$$

Given that $v_{dyn} = v_{OC} – v_{ohm} – v$, Equation 4.7 can be rewritten as:

$$v_{dyn} = i \cdot R_{dyn} - R_{dyn} \cdot C_{dyn} \cdot \left(\frac{dv_{OC}}{dt} - \frac{dv_{ohm}}{dt} - \frac{dv}{dt} \right) \tag{4.8}$$

And since the current is constant during each step, ($\frac{dv_{ohm}}{dt} = 0$. Therefore,

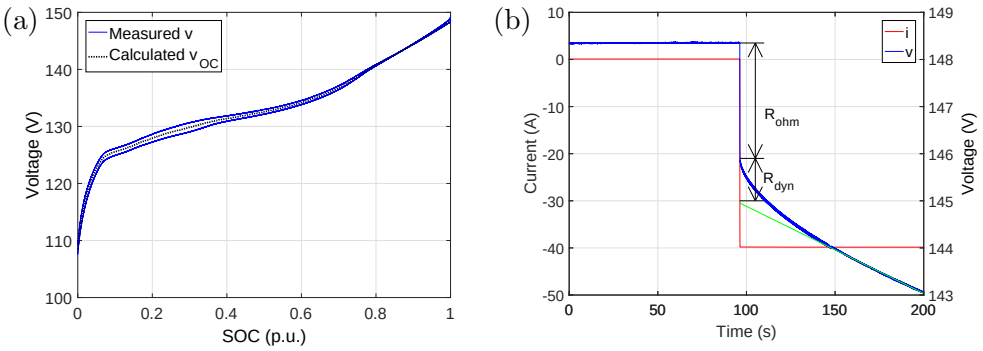

Figure 4.10: Experiments performed for parameter fitting: open-circuit voltage measurement (a) and current step test (b).

Equation 4.9 describes the terminal voltage of the battery after each current step:

$$v = v_{OC} - i \cdot (R_{ohm} + R_{dyn}) + R_{dyn} \cdot C_{dyn} \cdot \left(\frac{dv_{OC}}{dt} - \frac{dv}{dt} \right) \tag{4.9}$$

The experimental fits, which are carried out using the method of least squares for several SOC values, are shown in Figure 4.11. No substantial difference between charge and discharge behaviour is appreciated in these plots. Furthermore, since the points represented in these figures do not have a clear trend, no SOC dependency of the parameters has been included into the model. The fitted parameters are $R_{ohm} = 70.2$ mΩ, $R_{dyn} = 35.7$ mΩ and $C_{dyn} = 714.6$ F.

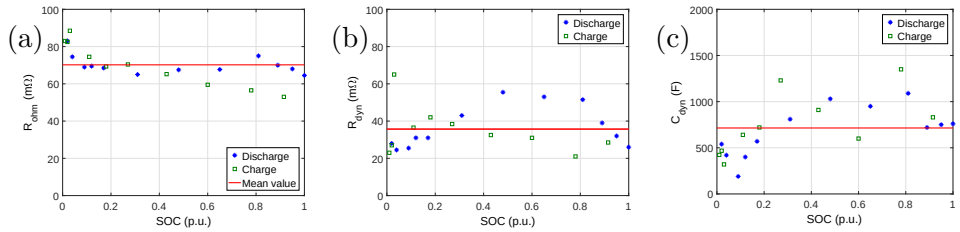

Figure 4.11: Impedance parameters calculated by means of step-current tests for different state of charges, both charging and discharging, and average values used for the model: R_{ohm} (a), R_{dyn} (b) and C_{dyn} (c).

4.4.2.3 Model experimental validation

The validation of the proposed model consists of three experiments in which the current and voltage of the battery are measured. These measurements are compared with the evolution predicted by the model presented in Figure 4.6. With this purpose, a vector with the current driven by the battery is fed into the model, which is used to calculate the terminal voltage of the battery. The RMSE is used, as defined in Equation 4.4, as standard measurement of the model precision.

Figure 4.12 (a) shows the first validation experiment consisting on a step-sized current. During the first half of the test, the battery is discharged and charged with various current levels, whilst random charging and discharging current steps are applied during the second half of the test. It is observed in Figure 4.12 (a) that the model accurately predicts the behaviour of the battery during both halves of the test. The obtained RMSE= 0.747 V is considered a small error compared with the voltage operation range of the battery (45 V).

The validation of the R_{dyn} C_{dyn} network which models the activation and concentration losses is shown in Figure 4.12 (b). Three sinusoidal-current experiments with an amplitude of 40 A were carried out. The frequencies were 10 mHz, 100 mHz and 1 Hz, which are lower and greater than the cut-off frequency of the R_{dyn} C_{dyn} circuit (40 mHz). Figure 4.12 (b) shows two portions of these six-minute tests, at frequencies of 10 mHz (top) and 1 Hz (bottom). The obtained RMSE values are 0.2 V for 10 mHz, 0.17 V for 100 mHz and 0.25 V for 1 Hz. These small RMSE values prove the suitability of the model to predict the behaviour of the battery in a wide range of frequencies, both higher and lower than the R_{dyn} C_{dyn} circuit cut-off frequency.

4.4.3 Physics-based model

The starting point of this model are the physical laws described in Section 3.3. Assumptions and simplifications are proposed in order to represent these laws as an equivalent-circuit model. Finally, all the parts are grouped and the comprehensive model is built.

4.4.3.1 Capacity, efficiency and state of charge

The capacity of a battery is defined as the maximum charge which can be drawn from the battery when it is totally charged [IEC15, FAR15b]. Meanwhile, there are two parameters which refer to efficiency, which are energy efficiency (η_e) and coulombic efficiency (η_c). The importance of η_c lies in the

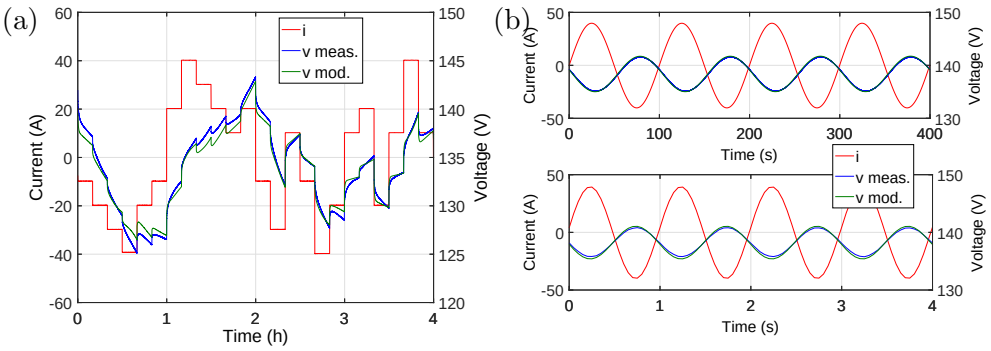

Figure 4.12: Validation experiments of the model performance, showing measured battery current and voltage, as well as voltage calculated by the model. Stepped current test (a) and sinusoidal current test with different frequencies (b).

irreversibility of the side reactions. These reactions involve coulombic inefficiency, irreversible loss of active material and formation of passive compounds, leading to battery ageing. This parameter is also important for the battery modelling, since it is part of the SOC calculation through the ampere-hour counting method, as shown in Equation 4.1.

The most significant physical phenomena that provokes a decrease in η_c is the SEI formation, which occurs during the battery charging [XU04]. However, the amount of SEI that has to be rebuilt depends on the SEI decomposition happened during the previous discharge by means of the physical mechanisms explained in Subsubsection 3.5.2.1. Therefore, η_c is assumed to be driven by the discharging process in this model. As covered in Subsubsection 3.5.2.1, the SEI decomposition during regular battery operation mainly depends on the its current and temperature, decreasing for reduced T, given that the SEI elasticity is lower, which leads to increased rupture. Even though the relationship between side reactions rate and temperature is known to follow Arrhenius law, taking into account that the battery temperature range is limited, the relationship between η_c and T is modelled as a linear function, as shown in Equation 4.10. With this assumption, a simplification in the model is achieved while maintaining its high accuracy. On the other hand, the relationship between η_c and current has not been widely characterized and modelled in the literature. Given that η_c is related with cycle ageing, we take into account a result obtained in [WAN11b]. The authors of this paper conclude that lithium-ion batteries age faster for higher currents. Therefore, η_c is expected to decrease for increasing current and, for the sake of simplicity, a linear trend is also assumed, as shown inEquation 4.10. Finally, there are a few studies about the relationship between η_c and SOC. In one of the most recent and

reliable papers concerning this issue [ZHE15] an experimental method is developed to obtain a measurement error in η_c lower than 10 ppm. Using this experimental procedure, the authors are not able to measure any SOC dependency. Therefore, no dependency of η_c with SOC is considered in the following equation:

$$\eta_c = \eta_{c,0} + \eta_{c,T} \cdot T + \eta_{c,i} \cdot i \tag{4.10}$$

4.4.3.2 Equilibrium voltage

The equilibrium voltage, also known as open circuit voltage (v_{OC}) of a lithium-ion battery is the voltage acquired by the battery after all the dynamic processes reach the steady state. It is determined by the equilibrium voltage of each of its electrodes, which, as stated in Equation 3.8, depends on the quantity of intercalated lithium ions. The fraction of intercalated ions in a lithium battery with carbon anion and nickel–manganese–cobalt oxide cathode was studied in [AUR99]. Based on this paper, a charged battery has a LiC_6 anode ($x_{\zeta,a} = 1$) and a $Li_{0.3}(Ni_{1/3}Mn_{1/3}Co_{1/3})O_2$ cathode ($x_{\zeta,c} = 0.3$). Meanwhile, a discharged battery has a LiC_{72} anode ($x_{\zeta,a} = 0.083$) and a $Li(Ni_{1/3}Mn_{1/3}Co_{1/3})O_2$ cathode ($x_{\zeta,c} = 1$). Taking into account that the SOC is the relationship between the charge stored in the battery and the maximum storable charge, a linear relationship between molar fraction and SOC can be inferred. The above-mentioned limits correspond to $SOC = 1$ and $SOC = 0$ respectively. Thus, these relationships can be written as:

$$x_{\zeta,a} = 0.083 + 0.917 \cdot SOC \tag{4.11}$$

$$x_{\zeta,c} = 1 - 0.7 \cdot SOC \tag{4.12}$$

Since measurement of anode and cathode voltage in a full operating cell cannot be achieved, some simplifications of Equation 3.8 are needed in order to calculate v_{OC}. The equivalent terms of this equation are grouped together, making it possible to fit the parameters of the expression from experimental data. For this purpose, the reference potential is defined as $v^0_{eq} = v^0_{eq,c} - v^0_{eq,a}$. Besides, non-ideal interactions $v_{INT,c}$ and $v_{INT,a}$ are assumed to be similar and grouped together in a single term, and interactions with an order higher than 7 are disregarded. Therefore, the following equation is obtained:

$$v_{OC} = v^0_{eq} + \frac{R \cdot T}{F} \cdot \ln\left(\frac{(1 - x_{\zeta,c}) \cdot x_{\zeta,a}}{x_{\zeta,c} \cdot (1 - x_{\zeta,a})}\right) + v_{INT} \tag{4.13}$$

where v^0_{eq} is the battery equilibrium potential at reference conditions and v_{INT} is the seven-order polynomial function introduced in Subsection 3.2.1, with the

parameters $b_0 ... b_7$ to be calculated, as shown below:

$$v_{INT} = \sum_{k=0}^{7} b_k \cdot \left[\left((2 \cdot x_{\zeta,a} - 1)^{k+1} - \frac{2 \cdot x_{\zeta,a} \cdot k\,(1 - x_{\zeta,a})}{(2 \cdot x_{\zeta,a} - 1)^{1-k}} \right) + \left((2 \cdot x_{\zeta,c} - 1)^{k+1} - \frac{2 \cdot x_{\zeta,c} \cdot k\,(1 - x_{\zeta,c})}{(2 \cdot x_{\zeta,c} - 1)^{1-k}} \right) \right] \tag{4.14}$$

4.4.3.3 Fast-dynamic processes

Ohmic phenomena The ohmic phenomena detailed in Subsection 3.3.1 are typically represented by an SOC- and temperature-dependent series resistance (R_{ohm}) because of their proportionality to the square of the battery current:

$$R_{ohm} = R_{ohm,0} + R_{ohm,T} \cdot T + R_{ohm,SOC} \cdot SOC \tag{4.15}$$

Since the lithium ion concentration in the electrodes is linearly related to SOC (Equation 4.11 and Equation 4.12), the relationship between R_{ohm} and SOC is also assumed to be linear, as shown in Equation 4.15. Even though R_{ohm} is known to follow Arrhenius law with temperature, a linear relationship is assumed to model this effect, which leads to a fairly small deviation for the operation temperature range (0 °C–60 °C). This simplification has two main advantages for the battery modelling. On the one hand, a faster computation is achieved and, on the other hand, the thermal coefficient $R_{ohm,T}$ can be calculated with a smaller test map.

Polarizable electrode The most remarkable phenomenon related with the polarization of Li-ion battery electrodes is the charge transfer through their SEI layer, which is the reason of the activation polarization losses (v_{act}). For the modelling of these phenomena, the battery current is usually divided into its faradaic and a capacitive components, as shown in Equation 3.9. For the capacitive current, the double-layer capacitor expressed in Equation 3.11 could be used. However, this ideal element is not able to accurately represent real systems distributed over a finite region. Instead, a constant phase element (CPE_{dl}) has been herein chosen, as shown in Figure 4.13. The admittance of a constant-phase element can be expressed by two frequency-independent coefficients Y_0 and Ψ as shown in Equation 4.16 [BAR05]:

$$Y_{CPE} = Y_0 \cdot (j \cdot \omega)^{\Psi} \tag{4.16}$$

This element behaves as an ideal capacitor when $\Psi = 1$ and as an ideal resistor when $\Psi = 0$. It is generally thought to arise, when $\Psi \neq 0$ or 1, from the presence of inhomogeneity in the electrode–material system [SCH57].

Its impedance, which is named in this thesis CPE_{dl}, is the inverse of the admittance:

$$CPE_{dl} = \frac{1}{Y_{CPE}} = \frac{1}{Y_0 \cdot (j \cdot \omega)^{\Psi}} \tag{4.17}$$

The faradaic current i_F is determined by the reaction kinetics at the electrodes and represented in the model by a current source, as shown in Figure 4.13 (a). The Butler–Volmer equation, Equation 3.26, is valid to calculate faradaic current produced by insertion reactions [DRE16, JIA16]. Some minor modifications are required in order to use the molar fraction x_ζ instead of concentrations c_O and c_R as independent variable. Two distinct scenarios for i_F are analysed in order to get simplifications of the Butler–Volmer equation. On the one hand, the widely-used simplification for large current shown in Equation 4.18 is the expression implemented in the final model:

$$i_F = F \cdot S \cdot k_0^0 \cdot \exp -\frac{E_A}{R \cdot T} \cdot \exp\left(\frac{n \cdot F}{2 \cdot R \cdot T} \cdot v_{act}\right) \cdot (x_{\zeta,a} \cdot x_{\zeta,c})^{0.5} \tag{4.18}$$

On the other hand, Equation 3.26 is linearised to get the small-signal model shown in Figure 4.13 (b), which will be useful for the parameter fitting process explained in Subsection 4.4.4. For small v_{act}, the Butler–Volmer Equation can be approximated as [BAR01]:

$$i_F = i_0 \cdot [1 - \alpha \cdot f \cdot v_{act} - 1 - (1 - \alpha) \cdot f \cdot v_{act}] \tag{4.19}$$

$$i_F = i_0 \cdot f \cdot v_{act} \tag{4.20}$$

being

$$i_0 = S \cdot F \cdot k^0 \cdot x_{\zeta,a}^{(1-\alpha)} \cdot x_{\zeta,c}^{\alpha} \tag{4.21}$$

Thus, the relationship between i_F and v_{act} can be considered linear if the current is not too high. The linearisation is valid if $n \cdot F \cdot |v_{act}| << R \cdot T$, which

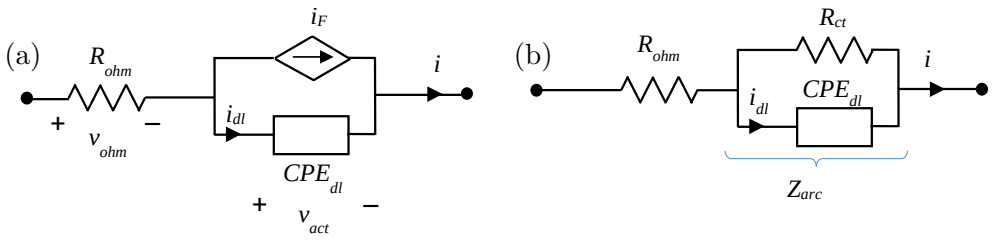

Figure 4.13: Equivalent-circuit representation for the fast-dynamic processes of a Li-ion battery (a). For small-signal model, the current source i_F is substituted by a resistance R_{ct} (b).

some authors take as $|v_{act}| < 5$ mV [TRA09]. This relationship is expressed by the so-called charge-transfer resistance R_{ct}:

$$R_{ct} = \frac{v_{act}}{i_F} = \frac{R \cdot T}{n \cdot F \cdot i_0} \tag{4.22}$$

Assuming $\alpha = 0.5$ and an Arrhenius trend in k^0, the following expression for R_{ct} is obtained:

$$R_{ct} = \frac{1}{(x_{\zeta,a} \cdot x_{\zeta,c})^{0.5}} \cdot \frac{R}{n \cdot F^2 \cdot S \cdot k_0^0} \cdot T \cdot \exp \frac{E_A}{R \cdot T} \tag{4.23}$$

In this small-signal scenario, the charge transfer process through the SEI is characterized by parameters CPE_{dl} and R_{ct}. Z_{arc} is the name given to the impedance of the parallel connection of these two parameters, as represented in Figure 4.13 (b). Z_{arc} can be expressed as:

$$Z_{arc} = \frac{R_{ct}}{1 + (j \cdot \omega \cdot \tau)^{\Psi}} \tag{4.24}$$

being

$$\tau = (Y_0 \cdot R_{ct})^{1/\Psi} \tag{4.25}$$

Given that R_{ct} depends on SOC and T, τ has also dependency of these two variables. An exponential relationship between τ and SOC and a quadratic expression to relate τ and T are empirically proposed for the temperature range analysed in this model. Therefore, τ is defined as:

$$\tau = \tau_T + \tau_0 \cdot \exp(\tau_{exp} \cdot SOC) \tag{4.26}$$

being τ_0 and τ_{exp} constant coefficients and τ_T a temperature-dependent coefficient as follows:

$$\tau_T = \tau_{T,0} + \tau_{T,1} \cdot T + \tau_{T,2} \cdot T^2 \tag{4.27}$$

4.4.3.4 Diffusion of lithium ion

The mass transport (lithium ion movement) through the crystal lattice of the electrodes, electrolyte and membrane is governed by diffusion processes. These processes are based on concentration gradients, and are therefore named concentration processes. They are responsible of the so-called concentration polarization losses (v_{con}).

Membrane diffusion The diffusion of lithium ions through the membrane, described by Fick's laws (Equation 3.27 and Equation 3.28), is a distributed process. Several simplifications have been proposed in the literature for this process to be included in a computational model, most of which consist on a

distributed RC network [TSI13]. With the aim of enhancing the functionality of the model, we use a single RC branch to model the membrane diffusion process, as represented in Figure 4.14 (a). While $C_{dif,mem}$ can be assumed to have a constant value, Fick's laws state an Arrhenius-type behaviour for $R_{dif,mem}$, as shown in Equation 4.28:

$$R_{dif,mem} = K_{dif,mem} \cdot \exp \frac{b_{dif,mem}}{T - T_{0,dif,mem}} \tag{4.28}$$

This diffusion process is SOC independent, since the properties of the electrolyte and membrane are unchanged with variable SOC because these battery components do not take part on the electrochemical reaction.

Electrode diffusion In a similar way, electrode diffusion is modelled by an RC branch with parameters $R_{dif,elec}$ and $C_{dif,elec}$, as shown in Figure 4.14 (b). The SOC calculation shown in this figure is consistent with Equation 4.1. The variable SOC_{sur} is the state of charge corresponding to the lithium molar fraction at the electrode surface. This difference between SOC and SOC_{sur} results in a battery voltage drop. In order to propose an expression for $R_{dif,elec}$ and $C_{dif,elec}$, spherical electrode particles with radius R_p and radial diffusion, as shown in Figure 4.15, are assumptions that allow an important reduction of model complexity while keeping a high level of accuracy. This leads to the so-called single particle model, which is widely used in the literature with different modifications [ZHE16, FAN16, RAM16]. Let D_s be the diffusion coefficient and r the radial coordinate of electrode particles. Equation 3.28 can be reduced to one dimension:

$$\frac{\partial x_{Li}}{\partial t} = \frac{D_s}{r^2} \cdot \frac{\partial}{\partial r} \left(r^2 \cdot \frac{\partial x_{Li}}{\partial r} \right) \tag{4.29}$$

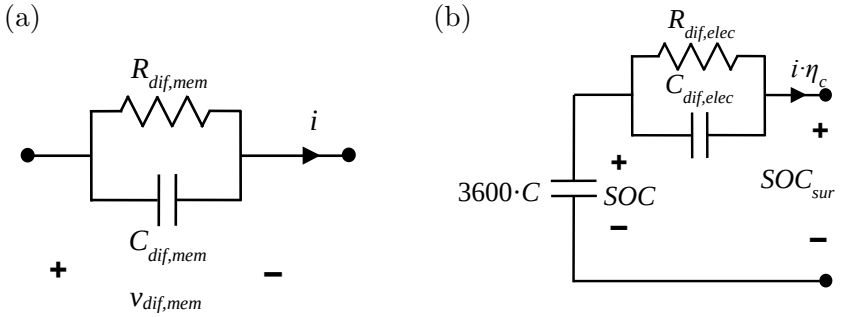

Figure 4.14: Equivalent-circuit representation for the diffusion processes of a Li-ion battery. Membrane diffusion (a) and electrode diffusion (b).

The average volumetric lithium concentration, which is determined by SOC, can be obtained from:

$$\bar{x_{Li}} = \frac{\int_0^{R_p} 4 \cdot \pi \cdot r^2 \cdot x_{Li}(r) \cdot dr}{\frac{4}{3} \cdot \pi \cdot R_p^3} \tag{4.30}$$

The current density over the particle surface can be assumed to be uniform [YAN14]. Besides, x_{Li} during a constant-current discharge have a parabolic profile for the radial coordinate as shown in Figure 4.15 [YAN14], and can be parametrized as follows:

$$x_{Li}(r) = b_0 + b_1 \cdot r + b_2 \cdot r^2 \tag{4.31}$$

The boundary conditions are:

$$\left.\frac{\partial x_{Li}}{\partial r}\right|_{r=0} = 0 \qquad \Longrightarrow \qquad b_1 = 0 \tag{4.32}$$

$$D_s \cdot \left.\frac{\partial x_{Li}}{\partial r}\right|_{r=R_p} = -\bar{j}_{Li} \qquad \Longrightarrow \qquad b_2 = -\frac{\bar{j}_{Li}}{2 \cdot D_s \cdot R_p} \tag{4.33}$$

In this context, when the steady state has been reached, Equation 4.30 and Equation 4.31 can be combined to provide the following expression:

$$\bar{x_{Li}} \cdot \frac{4}{3} \cdot \pi \cdot R_p^3 = 4 \cdot \pi \cdot \left(\frac{b_0}{3} \cdot r_p^3 + \frac{b_2}{5} \cdot R_p^5 \right) \tag{4.34}$$

$$x_{Li}(R_p) = b_0 + b_2 \cdot R_p^2 \tag{4.35}$$

From the combination of Equation 4.33, 4.34 and 4.35, the value of surface Li-ion concentration for a constant current and temperature discharge is inferred:

$$x_{Li}(R_p) = \bar{x_{Li}} + \frac{R_p}{5 \cdot F \cdot S_{SEI} \cdot D_0} \cdot \exp \frac{E_A}{T - T_0} \tag{4.36}$$

Considering that $\bar{x_{Li}}$ and $x_{Li}(R_p)$ are related to SOC and SOC_{sur} respectively, Equation 4.37 can be fitted to $R_{dif,elec}$:

$$\frac{SOC - SOC_{sur}}{i \cdot \eta_c} = R_{dif,elec} = K_{dif,elec} \cdot \exp\left(\frac{b_{dif,elec}}{T - T_{0,dif,elec}} \right) \tag{4.37}$$

Finally, an empirical expression is proposed for the temperature dependency of $C_{dif,elec}$. Given that polynomial expressions are easy to handle in a computer simulation, a second order polynomial is chosen, as shown in Equation 4.38:

$$C_{dif,elec} = b_{0,Cdif,elec} + b_{1,Cdif,elec} \cdot T + b_{2,Cdif,elec} \cdot T^2 \tag{4.38}$$

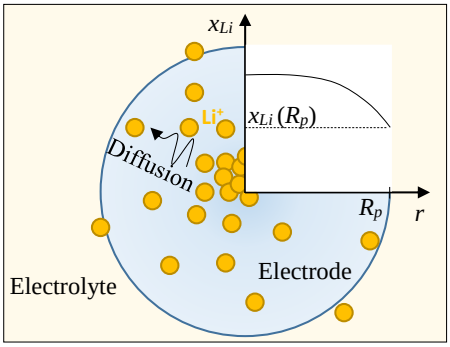

Figure 4.15: Single-particle model used for the electrode diffusion.

4.4.3.5 Final configuration of the model

The above-modelled phenomena are grouped, and the complete electric model of the Li-ion battery is configured as shown in Figure 4.16. This equivalent-circuit model has three main components: a voltage source for the equilibrium voltage v_{OC} as described in Equation 4.13, the representation of the fast-dynamic processes shown in Figure 4.13 and the representation of membrane diffusion process shown in Figure 4.14 (a). Besides, the circuit presented in Figure 4.14 (b) is used for the calculation of the parameter SOC_{sur}.

In this model, η_c is calculated through Equation 4.10 and used to figure out the value of SOC as stated in Equation 4.1. This data is included in the electrical circuit shown in Figure 4.14 (b), thereby obtaining the value of SOC_{sur} by means of circuit simulation. Besides, the value of x_ζ on both electrode surfaces is calculated trough Equation 4.11 and Equation 4.12 using SOC_{sur} as state of charge. Finally, Equation 4.13 is used to figure out the value of v_{OC}.

The dynamic phenomena included in the model are ohmic and charge-transfer behaviour, as detailed in Subsubsection 4.4.3.3. The ohmic phenomena, represented by R_{ohm}, depend on SOC and T, as stated in Equation 4.15. The faradaic current i_F is calculated as a function of $x_{Li}(R_p)$ and T, as described by the Butler–Volmer equation, particularised by means of Equation 4.18. Moreover, CPE_{dl} is, as shown in Equation 4.16 and Equation 4.26, a function of T and SOC. Concerning membrane diffusion, represented in Figure 4.16 by $R_{dif,mem}$ and $C_{dif,mem}$, the temperature dependency is confined to the parameter $R_{dif,mem}$, as explained in Subsubsection 4.4.3.4, see Equation 4.28.

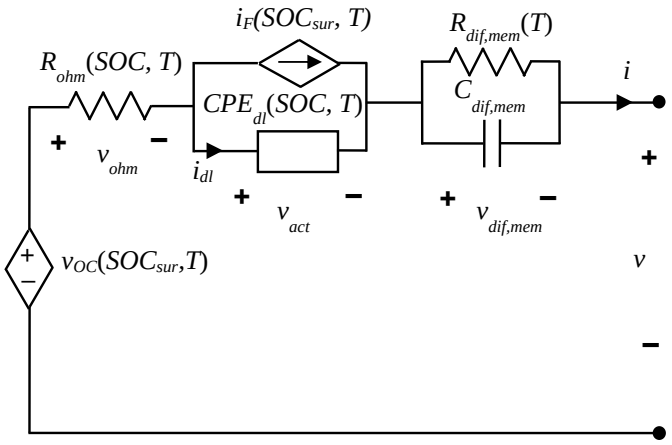

Figure 4.16: Battery equivalent-circuit model.

A compilation of all the equations required for the model simulation is presented in Table 4.3 for the sake of clarity. Each of the elements of the electric circuit is placed in the first column of the table. Columns 2 and 3 contain the equations used to express the circuit element as a function of physical constants, other variables of the model and parameters that need to be fitted (see the following subsection). Given that all of the compiled equations has been obtained along Chapter 4, their equation numbers are provided for better traceability. In the three last columns, the symbols used in each of the equations are classified as *parameters to be fitted*, with a total of 32 parameters which value is calculated in Subsection 4.4.4 and summarised in Table 4.4; *physical constants*, with a fixed and known value; and *model variables*, which are either input variables to the model or variables defined in a previous row of the table.

4.4.4 Experimental design to obtain the model parameters

4.4.4.1 Test procedure

The process to obtain the 32 parameters required for the battery model shown in Figure 4.16 (see fourth column of Table 4.3) is detailed in this subsection. For the purpose of ensuring test uniformity of the experiments, the following initialization protocol is followed. Prior to each experiment, the battery is kept in idle state for 12 hours with a SOC of around 80%. The cells are subsequently equalized to obtain a voltage dispersion of less than 20 mV. Then, the battery

Symbol	Calculation	Expression	Parameters to be fitted	Physical constants	Model variables
		Variables			
SOC	Equation 4.1	$SOC = SOC_0 + \frac{1}{C} \cdot \int_0^t \eta_c \cdot i \cdot dt$	C	—	SOC_0, i
	Equation 4.10	$\eta_c = \eta_{c,0} + \eta_{c,T} \cdot T + \eta_{c,i} \cdot i$	$\eta_{c,0}$, $\eta_{c,T}$, $\eta_{c,i}$	—	T, i
SOC_{sur}	Figure 4.14 (b)	Circuit simulation	—	—	—
	Equation 4.37	$R_{dif,elec} = K_{dif,elec} \cdot \exp\left(\frac{b_{dif,elec}}{T - T_{0,dif,elec}}\right)$	$K_{dif,elec}$ $b_{dif,elec}$ $T_{0,dif,elec}$	—	T
	Equation 4.38	$C_{dif,elec} = b_{0,Cdif,elec} + b_{1,Cdif,elec} \cdot T + b_{2,Cdif,elec} \cdot T^2$	$b_{0,Cdif,elec}$ $b_{1,Cdif,elec}$ $b_{2,Cdif,elec}$	—	T
		Voltages and currents			
v_{OC}	Equation 4.13	$v_{OC} = v_{eq}^0 + \frac{R \cdot T}{F} \cdot \ln\left(\frac{(1-x_{\zeta,c}) \cdot x_{\zeta,a}}{x_{\zeta,c} \cdot (1-x_{\zeta,a})}\right) + v_{INT}$	v_{eq}^0	R, F	T
	Equation 4.14	$v_{INT} = \sum_0^7 b_k \left[(2x_{\zeta,a} - 1)^{k+1} - \frac{2x_{\zeta,a} k (1-x_{\zeta,a})}{(2x_{\zeta,a}-1)^{1-k}} + (2x_{\zeta,c} - 1)^{k+1} - \frac{2x_{\zeta,c} k (1-x_{\zeta,c})}{(2x_{\zeta,c}-1)^{1-k}} \right]$	b_0, b_1, b_2, b_3, b_4, b_5, b_6, b_7	—	—
	Equation 4.11	$x_{\zeta,a} = 0.083 + 0.917 \cdot SOC_{sur}$	—	—	SOC_{sur}
	Equation 4.12	$x_{\zeta,c} = 1 - 0.7 \cdot SOC_{sur}$	—	—	SOC_{sur}
i_F	Equation 4.18	$i_F = F S k_0^0 \exp\left(-\frac{E_A}{RT}\right) \exp\left(\frac{nF}{2RT} v_{act}\right) (x_{\zeta,a} x_{\zeta,c})^{0.5}$	Sk_0^0, E_A	F, R, n	T, $x_{\zeta,a}$, $x_{\zeta,c}$

Model parameters

R_{ohm}	Equation 4.15	$R_{ohm} = R_{ohm,0} + R_{ohm,T}T + R_{ohm,SOC}SOC$	$R_{ohm,0}$, $R_{ohm,T}$, $R_{ohm,SOC}$	—	T, SOC
CPE_{dl}	Equation 4.17	$CPE_{dl} = \frac{1}{Y_0 \cdot (j \cdot \omega)^{\Psi}}$	Ψ	j, ω	—
	Equation 4.25	$Y_0 = \frac{\tau^{\Psi}}{R_{ct}}$	—	—	—
	Equation 4.26	$\tau = \tau_T + \tau_0 \exp(\tau_{exp} SOC)$	τ_0, τ_{exp}	—	SOC
	Equation 4.27	$\tau_T = \tau_{T,0} + \tau_{T,1}T + \tau_{T,2}T^2$	$\tau_{T,0}$, $\tau_{T,1}$, $\tau_{T,2}$	—	T
	Equation 4.23[1]	$R_{ct} = \frac{1}{(x_{\zeta,a} \cdot x_{\zeta,c})^{0.5}} \frac{R}{nF^2 Sk_0^0} T \exp \frac{E_A}{RT}$	Sk_0^0, E_A	F, R, n	T, $x_{\zeta,a}$, $x_{\zeta,c}$
$R_{dif,mem}$	Equation 4.28	$R_{dif,mem} = K_{dif,mem} \exp \frac{b_{dif,mem}}{T - T_{0,dif,mem}}$	$K_{dif,mem}$, $b_{dif,mem}$, $T_{0,dif,mem}$	—	T
$C_{dif,mem}$	—	Constant value	$C_{dif,mem}$	—	—

Table 4.3: Summary of the equations, parameters, physical constants and variables required for the simulation of the Li-ion battery electrochemical model.

[1]Note that the three last columns of R_{ct} (parameters to be fitted, physical constants and model variables) are exactly the same as for i_F, given that R_{ct} is the small-signal model representation of i_F.

is charged following a CC–CV protocol with $i = 1$C until the current decreased in the CV zone to $i = 0.05$C. This is considered the beginning of the test.

Three types of experiments are conducted in to fit the model parameters: type a, b and c. Type a experiments consist in a full constant-current discharge followed by a CC–CV standard charge in which $i = 1$C. Type b experiments consist in a stepped charge and discharge, with current steps of a few minutes and $i = 1$C. Between the current steps, there are resting periods with a duration of 60 minutes. Finally, type c experiments comprise electrochemical impedance spectroscopy (EIS). The above-mentioned tests are conducted with different ambient temperatures covering the whole range of the battery operating temperatures (0 °C–60 °C).

Based on these experiments, a five-stage fitting method is developed for the purpose of calculating the parameters of the equivalent circuit. The first stage concerns the calculation of the battery capacity (Subsubsection 4.4.4.2). Secondly, $v_{OC}(SOC_{sur})$ is fitted in Subsubsection 4.4.4.2. The parameters characterizing the battery impedance are then calculated in Subsubsection 4.4.4.3. In Subsubsection 4.4.4.4, the diffusion parameters of the membrane are fit to experimental data and, finally, the diffusion process in the electrodes is studied in Subsubsection 4.4.4.4.

4.4.4.2 Capacity, efficiency and equilibrium voltage

The first variable to be measured is battery capacity C. For this purpose, a type a experiment with negligible influence of the battery impedance is used. The influence of the impedance is minimized for low currents and high temperatures. Therefore, for the test used for capacity measurement, $i = 0.5$C and $T = 47.5 \pm 0.5$ °C. A value of $C = 41$ Ah is obtained. η_c is the second parameter to be fitted. To do so, all the tests of type a are used, with different values of i and T. The result is shown in Figure 4.17 (a). The values for the parameters of Equation 4.10 are summarized in Table 4.4.

Type b experiments are then used to obtain the coefficients of Equation 4.13, in which v_{OC} is defined. The slow diffusion phenomena are stabilized during the resting periods, allowing the accurate measurement of v_{OC}, as shown in Figure 4.17 (b). The charging and discharging measurements are almost superimposed, proving that the v_{OC} curve has no hysteresis in NMC batteries. The fitted parameters are shown in Table 4.4.

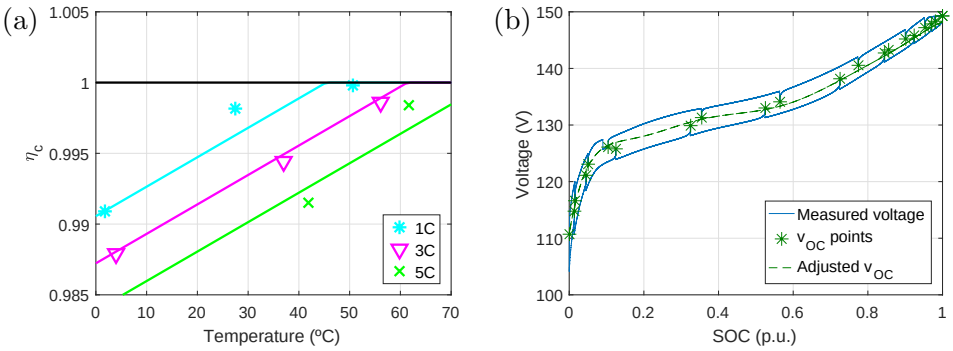

Figure 4.17: Experimental data and curve fitting. η_c obtained from experiments of type *a* (a) and voltage during a type *b* experiment (b).

4.4.4.3 Battery impedance

The impedance of a battery is characterized by R_{ohm} and Z_{arc}, defined in Equation 4.24. For the purpose of determining its value, type *c* experiments (EIS) were carried out on a number of values of SOC and T. The frequency analysed in the EIS experiments ranges from 100 mHz to 10 kHz. Since ohmic and charge transfer phenomena are measurable in this frequency range, the electric circuit shown in Figure 4.13 (b) can be fitted to the measured data.

Figure 4.18 (a) shows the Nyquist diagram of the battery at $T = 24.1$ ºC and $SOC = 0.6$. For the parameter fitting, R_{ohm} is firstly calculated, which is the impedance of the battery at high frequency (around 600 Hz) and corresponds to the x-intercept of its impedance arc. In the example shown in Figure 4.18 (b) $R_{ohm} = 33.13$ mΩ. The relationship between the real and imaginary part of the admittance in a depressed arc (Y_{arc}) is linear, as presented by Barsoukov and Macdonald [BAR05]. A value for Ψ, Equation 4.24, can be obtained from the linear fit shown in Figure 4.18 (b). Moreover, R_{ct} can be obtained from the x-intercept of this fitted line, since $\mathrm{Im}(Y_{arc}) = 0$ and $\mathrm{Re}(Y_{arc}) = \frac{1}{R_{ct}}$ when $\omega \to 0$ ($s \to 0$). τ is the last parameter to be calculated. Its value can be obtained from the relationship proposed in [BAR05] between vectors $u = \overrightarrow{BP}$ and $v = \overrightarrow{PQ}$, where point $B = (R_{ohm}, 0)$, $Q = (R_{ohm} + R_{ct}, 0)$ and P is a generic point in the Nyquist diagram:

$$\ln\left|\frac{v}{u}\right| = \Psi \cdot [\ln(\omega) + \ln(\tau)] \tag{4.39}$$

Therefore, if a linear polynomial is fitted to the relationship between $\ln\left|\frac{v}{u}\right|$ and $\ln(\omega)$, as shown in Figure 4.18 (c), the y-intercept is an estimator of τ.

This fitting process is repeated for all the type *c* experiments. R_{ohm} values

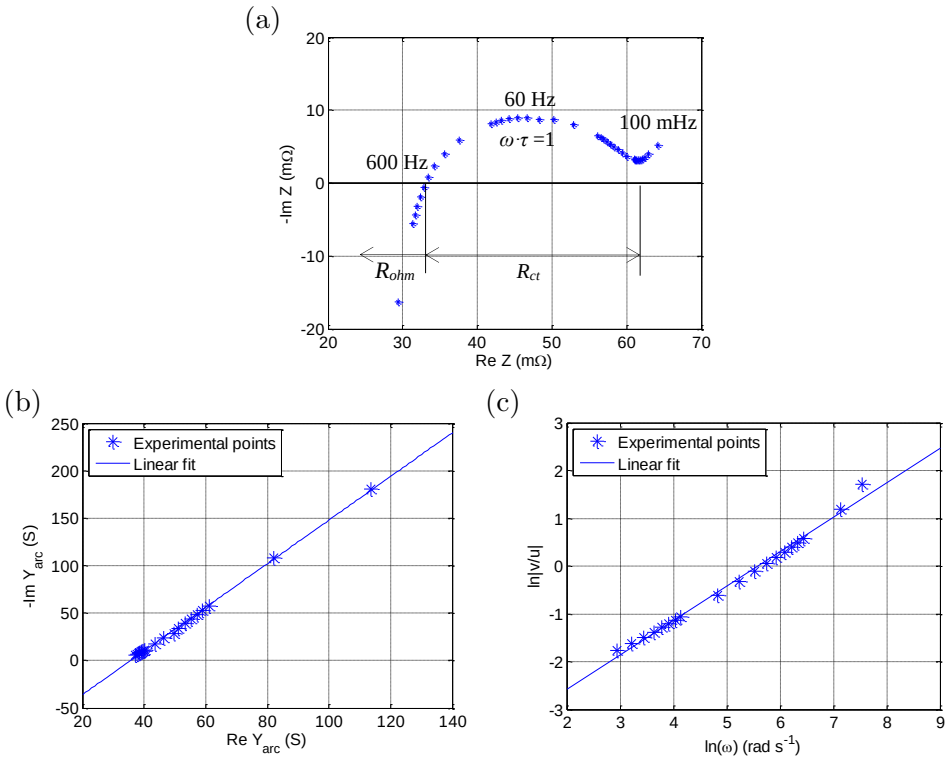

Figure 4.18: Fitting of EIS experiments with $T = 24.1$ °C and $SOC = 0.6$: equivalent circuit (a), Nyquist diagram (b), linear fit to Y_{arc} (c) and linear fit of $\ln\left|\frac{v}{u}\right|$ vs. $\ln(\omega)$ (d).

obtained from the individual EIS experiments and a fitting of Equation 4.15 are shown in Figure 4.19 (a). The parameter values, summarized in Table 4.4, are the result of this fitting. On the other hand, the parameters from Equation 4.23 are fitted to the data shown in Figure 4.19 (b). Thereby, the value of $E_A = 77$ kJ mol^{-1} is obtained, consistent with previous studies which propose $E_A = 41$ kJ mol^{-1} for a graphite electrode [SMA07] or $E_A \approx 40$ kJ mol^{-1} for 18650 Li-ion batteries [LIA03]. These parameters are represented in the model by i_F, defined in Equation 4.18.

The element CPE_{dl} is defined by parameters τ and Ψ, as detailed in Equation 4.24 and Equation 4.26. Its measured values and the fitting of Equation 4.26 are shown in Figure 4.19 (c). Likewise, calculated Ψ and average value are represented in Figure 4.19 (d). The values of the parameters are summarized in Table 4.4.

Table 4.4: Model parameters.

Phenomena	**Eq.**	**Parameter**	**Value**	**Unit**
Capacity		C	41	Ah
Coulombic efficiency	4.10	$\eta_{c,0}$	0.9922	—
		$\eta_{c,T}$	$2.08 \cdot 10^{-4}$	$^{\circ}\mathrm{C}^{-1}$
		$\eta_{c,i}$	$-4.2 \cdot 10^{-5}$	A^{-1}
Equilibrium voltage	4.13	v_{eq}^{0}	108.4	V
	4.14	b_0	54.96	—
		b_1	−9.33	—
		b_2	15.6	—
		b_3	−4.732	—
		b_4	−7.13	—
		b_5	−8.117	—
		b_6	33.19	—
		b_7	−20.19	—
Faradaic current	4.18	E_A	41	$\mathrm{kJ\,mol}^{-1}$
		$S \cdot k_0^0$	$1.95 \cdot 10^{-9}$	$\mathrm{m^2\,s}^{-1}$
Ohmic phenomena	4.15	$R_{ohm,0}$	73.58	mΩ
		$R_{ohm,T}$	−0.1292	$\mathrm{m\Omega\,K}^{-1}$
		$R_{ohm,SOC}$	−2.849	mΩ
Charge transfer	4.17	Ψ	0.673	—
	4.27	$\tau_{T,0}$	0.0174	s
		$\tau_{T,1}$	$-8.7 \cdot 10^{-4}$	$\mathrm{s\,^{\circ}C}^{-1}$
		$\tau_{T,2}$	$1.23 \cdot 10^{-5}$	$\mathrm{s\,^{\circ}C}^{-2}$
	4.26	τ_0	0.00994	s
		τ_{exp}	−7.18	—
Membrane diffusion	4.28	$K_{dif,mem}$	0.021	A^{-1}
		$b_{dif,mem}$	19.7	$^{\circ}\mathrm{C}$
		$T_{0,dif,mem}$	−13	$^{\circ}\mathrm{C}$
		$C_{dif,mem}$	3466	F
Electrode diffusion	4.37	$K_{dif,elec}$	$1.37 \cdot 10^{-5}$	A^{-1}
		$b_{dif,elec}$	468.2	$^{\circ}\mathrm{C}$
		$T_{0,dif,elec}$	−74.9	$^{\circ}\mathrm{C}$
	4.38	$b_{0,Cdif,elec}$	$7.67 \cdot 10^{6}$	A s
		$b_{1,Cdif,elec}$	$-6 \cdot 10^{-4}$	$\mathrm{A\,s\,K}^{-1}$
		$b_{2,Cdif,elec}$	119.3	$\mathrm{A\,s\,K}^{-2}$

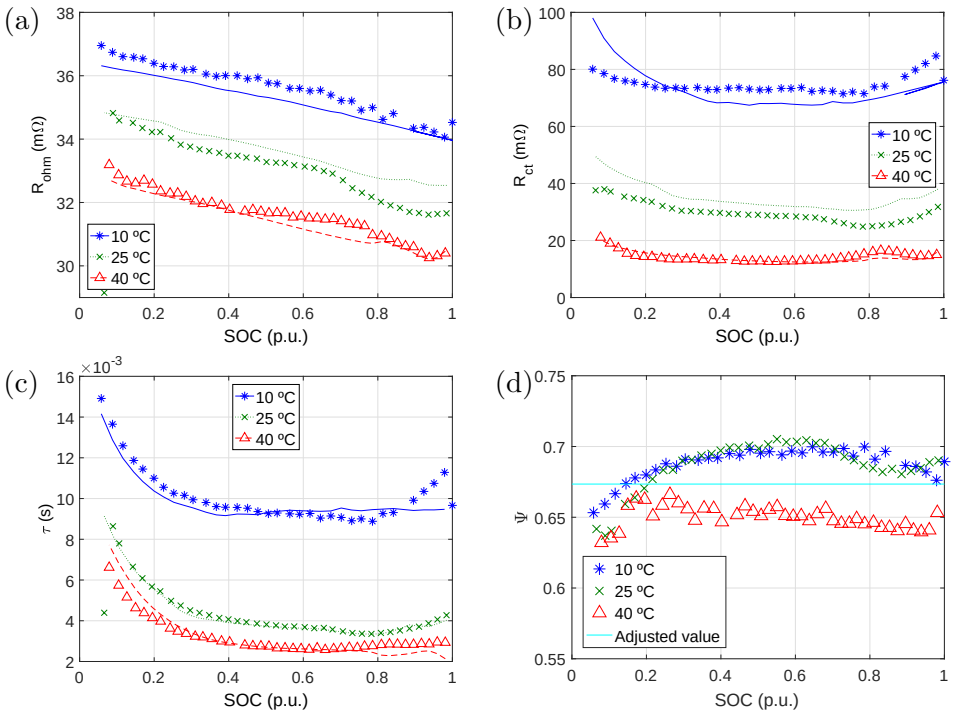

Figure 4.19: Calculated parameters (markers) and fitting curves (solid lines): R_{ohm} (a), R_{ct} (b), τ (c) and Ψ (d).

4.4.4.4 Diffusion phenomena

The two battery components with greatest influence in diffusion process are the membrane and the electrodes, as explained in Subsubsection 4.4.3.4. The vertical voltage shift arising from diffusion phenomena, shown in Figure 4.20, is proposed to be attributed to diffusion in the membrane, while the horizontal shift is attributed to diffusion in electrodes. This differentiation is due to the fact that electrode diffusion provokes a concentration gradient in electrodes and therefore the difference between the actual battery SOC and the variable SOC_{sur}.

The diffusion resistances ($R_{dif,mem}$ and $R_{dif,elec}$) are the first parameters adjusted with the iterative fitting process explained hereinafter. Only the part of the tests where all the studied phenomena are stabilised is used in order to achieve a good fitting of these resistances. Type a experiments include discharge curves with different values of i and T, which will be used to fit $R_{dif,mem}$. Since v_{OC}, R_{ohm} and R_{ct} are already known; the dotted curve from

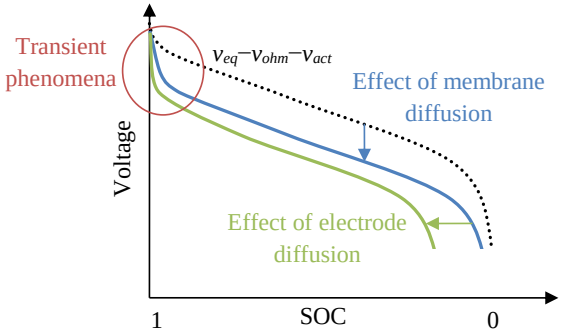

Figure 4.20: Schematic representation of the voltage drops arising from each diffusion phenomena during a constant-current battery discharge.

Figure 4.20 can be calculated. As the first iteration step, the whole voltage drop measured in the central part of the discharge process will be assumed to be caused by $R_{dif,mem}$. As next step of the fitting process, the first approximate value of $R_{dif,elec}$ is calculated using the last part of the discharge process, where this resistance has its largest effect due to the shape of the discharge curve. This diffusion process in the electrodes is described by Equation 4.36. At the end of the constant-current discharges from type a experiments diffusion phenomena are stabilized, the value of SOC at these points is known and, therefore, SOC_{sur} can be calculated using the equivalent circuit shown in Figure 4.14. The first approximate value of $R_{dif,elec}$ is obtained, and the process can be repeated taking the calculated parameters into account until accurate values for $R_{dif,mem}$ and $R_{dif,elec}$ are obtained. The values obtained for these variables after three iterations are shown in Figure 4.21 (a) and (c). The expression of $R_{dif,mem}$ as a function of T, defined in Equation 4.29, is fitted to these data as shown in Figure 4.21 (a). In a similar way, Equation 4.37 is fitted to the values of $R_{dif,elec}$ as shown in Figure 4.21 (c). The values obtained for the parameters are summarized in Table 4.4.

After the fitting of both diffusion resistances, the fitting of their associated capacitances is tackled. Capacitance $C_{dif,mem}$ can be studied with the stabilization process after each charge and discharge pulse in type b experiments. The diffusion time constant is calculated for different SOC and T, the values for $C_{dif,mem}$ shown in Figure 4.21 (b) are obtained and the independency of $C_{dif,mem}$ in relation to the SOC is confirmed. Neither has operating temperature (T) a noticeable effect on the value of $C_{dif,mem}$. Therefore, $C_{dif,mem}$ is assumed to have the constant value shown in Table 4.4.

The last parameter to be fitted is $C_{dif,elec}$, which governs the slowest phe-

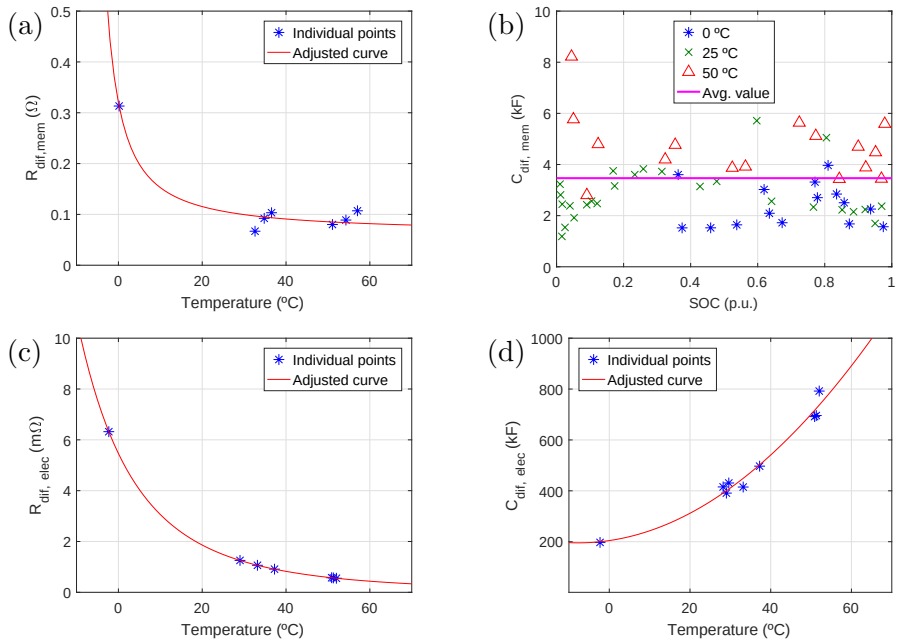

Figure 4.21: Calculated parameters (markers) and fitting curves (solid lines) obtained for the diffusion processes: $R_{dif,mem}$ (a), $C_{dif,mem}$ (b), $R_{dif,elec}$ (c) and $C_{dif,elec}$ (d).

nomenon taken into account in this model. The final parts of the type *a* experiments (the constant voltage part of CC-CV charges) are used to characterize its time constant. Considering that the electrode diffusion is in steady state when the charge is changed from CC to CV, its time constant can be measured during the CV phase. The value of $C_{dif,elec}$ for each test can be calculated, as shown in Figure 4.21 (d). The fitting of Equation 4.38 to these data provide the parameters shown in Table 4.4.

4.4.5 Model experimental validation

4.4.5.1 Full charge and discharge cycles

The first set of experiments proposed to validate the good performance of the battery model consists in full charge–discharge cycles with different current and temperature values through the entire operation range (10 ºC, 35 ºC and 55 ºC). Discharge currents of 1C, 3C and 5C are analysed, as shown in Figure 4.22 (a), (b) and (c) respectively. The battery is charged following the standard CC–CV procedure advised by the manufacturer, with a CC current of 1C, as shown in Figure 4.22 (d). Measured voltage is represented in this

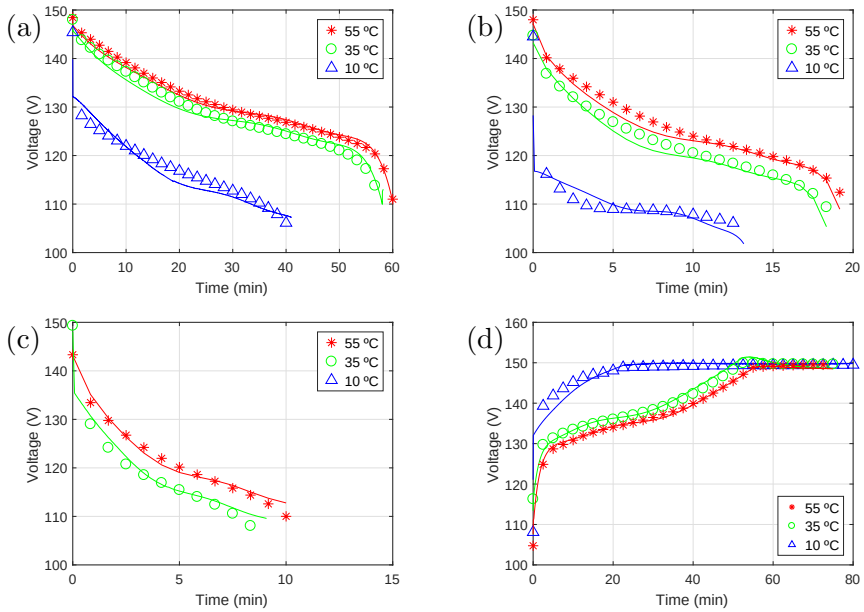

Figure 4.22: Full cycle experiments: experimental measurements (markers) and model prediction (solid lines). Discharges with current 40 A (a),120 A (b) and 200 A (c) and charges with 40 A (d).

figures with markers, while the solid lines represent the voltage predicted by the model. In the discharge tests (Figure 4.22 (a), (b) and (c)) the battery voltage is revealed to decrease for decreasing temperatures, given that ohmic and charge transfer losses are increased. Especially remarkable is the voltage decrease measured with $T = 10\,^{\circ}\mathrm{C}$. It limits the maximum battery discharge to around 65% of its nominal charge when $i = 1\mathrm{C}$ or $i = 3\mathrm{C}$ (Figure 4.22 (a) and (b)). Likewise, the charge experiments shown in Figure 4.22 (d) demonstrate a reduced CC charge provoked by a low temperature, which means an increase in time required for the battery charge. It is also provoked by an increase in the ohmic and activation losses.

The model herein proposed accurately predicts the battery performance facing any of these constant-current requirements at any of the studied operation temperatures. A visual analysis of the graphs presented in Figure 4.22 reveals that the model fails to predict the exact shape of the voltage curves for the most extreme situations ($T = 10\,^{\circ}\mathrm{C}$ or $i = 5\mathrm{C}$). However, each of the RMSE values obtained with the model simulations (see Table 4.5) is lower than 3 V, which is considered a reasonable accuracy for the modelling of a battery with a rated voltage of 133 V.

Table 4.5: RMSE of the model during full charge and discharge experiments.

RMSE	10 °C	35 °C	55 °C
Discharge 40 A	2.77	1.40	0.48
Discharge 120 A	2.63	2.94	2.69
Discharge 200 A	—	2.46	2.18
Charge 40 A	1.47	1.12	0.22

4.4.5.2 Dynamic performance

The battery was subjected to sinusoidal currents with amplitude of 25 A and frequencies of 1 Hz and 100 Hz. Furthermore, a sinusoidal current with an amplitude of 12.5 A and a frequency of 500 Hz is included. The ambient temperature is 23 ± 1 °C and the experiments are repeated with $SOC = 0.8$ and $SOC = 0.25$. The current–voltage $(i - v)$ relationships at each frequency are shown in Figure 4.23 for $SOC = 0.8$ (a) and $SOC = 0.25$ (b). The effect of the double-layer is noted on these graphs, specifically for the $i - v$ relationship with a frequency of 100 Hz, since this is the frequency where charge-transfer phenomena are noticeable. Furthermore, the slope of the $i - v$ curves decreases with increasing frequency due to the reduction of the equivalent battery resistance. A slightly higher slope of the curves with $SOC = 0.25$ is also appreciated when compared to $SOC = 0.8$. This effect is due to the increase in R_{ohm} and R_{ct} for lower values of SOC, as measured in Subsubsection 4.4.4.3. The validation for this dynamic operation is considered satisfactory, since RMSE values are lower than 90 mV for $SOC = 0.8$ and lower than 100 mV for $SOC = 0.25$.

4.4.5.3 Operation of the battery in a real microgrid

The battery model is validated herein while working in a real-life operating environment consisting the electrical microgrid described in Subsection 4.2.3. The proposed model is validated for the battery working as the storage system for this microgrid. For this purpose, an experimental validation with data from 7th of May, 2014, between 15:00 h and 23:00 h is presented herein. The generated and consumed energy durign this afternoon and evening were similar to the day used for the SOC estimation analysis (11 April 2013, see Figure 4.8). Similarly to the operation described for, Figure 4.8, there was no energy exchange with the grid during this time span.

The power profile that needs to be assumed by the battery is equivalent to the values of v and i shown in Figure 4.24. The top graph in Figure 4.24 shows

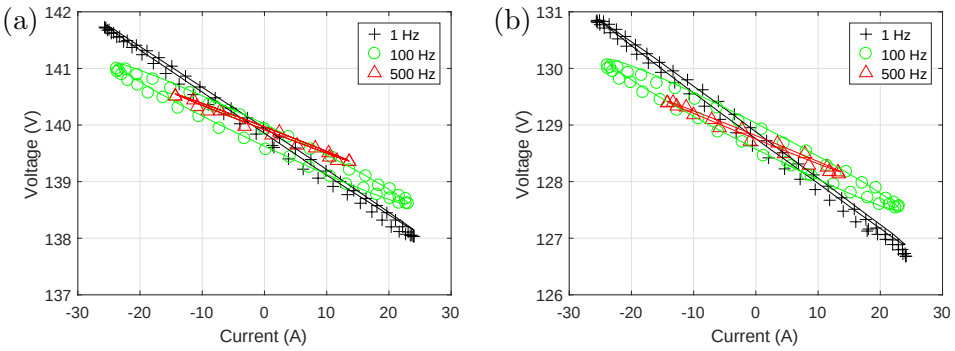

Figure 4.23: $i-v$ relationships: experimental measurements (markers) and model prediction (solid lines) with $SOC = 0.8$ (a) and $SOC = 0.25$ (b).

the battery current (i), while the bottom graph shows the battery voltage (v), with a maximum value of 150 V and a minimum of 126 V. The results obtained with the model show an adequate and reliable behaviour compared to the voltage measured during the experiment, with an RMSE in the voltage prediction of 0.627 V. Therefore, it can be concluded that the model is accurate when simulating real-time operating environments.

4.5 Thermal modelling

4.5.1 Introduction

As highlighted in Section 3.4, a thermal model capable of predicting the heat generation in a Li-ion battery and its evacuation has high interest during both its design process and its management in order to avoid eventual damages or premature degradation. Moreover, many important parameters of a battery model, such as the diffusion coefficient, ionic conductivity, etc. depend on the operation temperature. Therefore, a suitable thermal model enables better accuracy in the modelling of the battery electrical performance [KUM08].

Most of the thermal models recently published are aimed at their application in electric vehicles, given the outstanding thermal management systems required for the reduced-sized batteries used in the transport sector [BAH17, AL 17, LOP17]. An increased number of batteries used in stationary systems is predicted for the upcoming years. Given the high power of some of the stationary applications and the continuous working conditions fo this kind of batteries, the evacuation of relatively high thermal power may be required. Therefore, thermal models such as the one presented in this section,

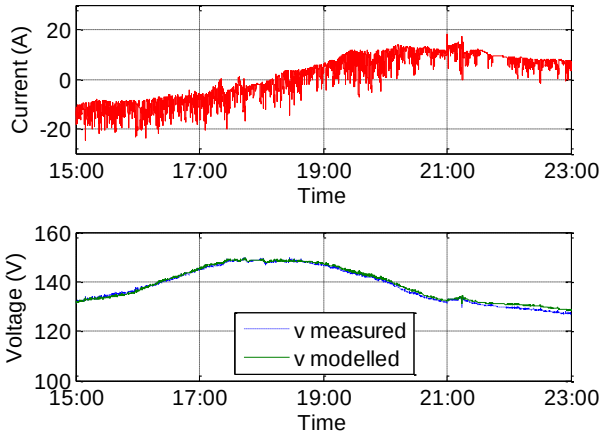

Figure 4.24: Experiment and simulation of the Li-ion battery integration into the microgrid with data from 11th of April, 2014. Battery current, on the top graph, and voltage, on the bottom.

focused on stationary Li-ion batteries, are expected to play a main role in the optimisation of this kind of batteries.

An overall thermal model includes, on the one hand, the heat generation mechanisms and, on the other hand, the heat evacuation ot the ambient. Concerning heat generation, according to a review paper published by Wang et al. [WAN12], there are two ways to face the heat generation modelling of a Li-ion battery. There is, on the one hand, the chemical reaction approach, which consists of the identification and modelling of the main electrochemical reaction that cause thermal events. These chemical figures are combined with the cell constructive parameters to simulate its thermal performance [NAG99, DOU02, ROT04, SPO07]. On the other hand, the calorimetry approach is based on global cell properties, experimentally measured, and on SOC-dependent variables to simulate the cell thermal performance. The first approach generates detailed models, of high utility during battery design. However, their complexity is usually too high for on-line applications and do not significantly contribute to an increased accuracy of the results [LI15].

In terms of energy dissipation to the ambient, one-, two- or three-dimensional model have been used in the literature. One-dimensional models assume some simplifications in the cell performance, such a uniform heat generation through the whole cell volume, a heat conduction inside the cell in a single direction or a constant convection rate to the external air uniform along the whole area of the cell [BIZ15]. Pals and Newman [PAL95a, PAL95b] presented a model in

which electrochemical equations are combined with an energy balance in the cells, based on the physico-chemical processes taking place during the battery operation. The influence of temperature in the battery parameters is disregarded in this model, and the electrochemical model equations are combined with a general energy balance in order to emulate, with this unidimensional model, the behaviour of a cell and that of the whole stack. Therefore, they are able to represent the temperature distribution along the whole battery pack. Conversely, two-dimensional models consider two coordinates for the heat distribution in a cell (radial and azimuthal for cylindrical cells [CHE06b] or length and width if they are prismatic [SON00]). The temperature distribution of a cylindrical, 10 Ah Li-ion battery at the end of 3 C discharge was obtained in [CHE06b]. The temperature at the angular direction is found to be fairly uniform and heat is mainly transferred along the radial direction. The two-dimensional model in Cartesian coordinates was proposed in [SON00], where the diffusion coefficient, ionic conductivity and transference number of lithium ions were characterized for the thermal behaviour of a Li polymer system. Finally, three-dimensional models have more flexibility in the simulation of the cells thermal performance. However, a typical assumption which is also kept in three-dimensional models is the constant heat generation through the whole cell volume. Using this simplification, Chen and Evans published two models that precisely consider the layered-structure of the cell stacks, the case of a battery pack, and the gap between both elements to achieve a comprehensive analysis [CHE94, CHE96]. Besides, a three-dimensional thermal abuse model on lithium-ion batteries was developed by Guo et al. [GUO10] with the aim of studying in detail the temperature field distribution and evolution inside a lithium cell.

Many researchers are focussing their interest during recent years in the development of electrochemical-thermal coupled models, most of which are unidirectional given their greater simplicity. In this sense, Guo et al. [GUO11a] extended the single-particle model presented by Santhanagopalan et al. [SAN06] to an electrochemical thermal model which including an energy balance. Meanwhile, Cai and White [CAI11] extended the existing lithium ion battery model in multiphysics software (COMSOL) to include the thermal effects. Moreover, the authors of this paper propose an orthogonal decomposition method devoted to develop this kind of reduced order models, which is used also in [CAI10].

Most of the models described above have been developed for single lithium-ion cells. However, real applications involve several cells packed in a commercial battery. In this concern, some authors utilise the software Modelica to implement an electrical model that they use for the calculation of the heat

generation in each cell of the battery pack [DVO14]. Subsequently, a thermal model for each of the cells is presented and the work is completed with a thermal model of the whole stack, able to simulate the airflow along the battery pack. As highlighted by the authors, this kind of models is useful for the designing of the battery cooling system, but are not suitable for online running, given their high level of details that requires the resolution of complex equations.

A thermal model is proposed in the following subsections. This model is designed to be coupled with an electrochemical model, such as the one presented in Section 4.4. The model parameters are adjusted to the performance of the commercial battery analysed along this thesis and the model is experimentally validated at the end of this section. The model is an extension of the work accomplished by Vertiz et al. [VER14], who present rigorous experiments to obtain the thermal capacity and conductivity of the pouch cells used to build the battery pack herein analysed. They design a unidimensional thermal model able to emulate the internal temperature of these cells. The model proposed in this section is focused on the battery stack. Thus, the heat generated in each cell is calculated using the electrochemical model presented in Section 4.4, using the thermal model proposed in [VER14] the temperature on the cell surface can be calculated and a model for the heat dissipation is proposed. The arrangement of the cells in the battery pack and the cooling air forced through the stack are taken into account with the aim of increasing model pertinence and accuracy.

4.5.2 Thermal model

4.5.2.1 Heat generation

The basic heat generation mechanisms of Li-ion batteries detailed in Subsection 3.4.2 can be re-arranged into five terms that ease the modelling process. The first source of heat are the resistive phenomena, which are not related with any electrochemical reaction. Related with the electrochemical reaction are the activation energy required for the reaction to take place, as well as the term representing its entropy variation, which is reversible. The parasitic reactions that take place in the cell are the fourth source of heat, and the fifth contribution is the so-called *heat of mixing*. This heat of mixing is the consequence of the concentration gradient relaxation in the electrode particles when the electrical current is interrupted. Its relative importance for battery normal operation regimes was studied by Thomas et al. [THO03b], who concluded that its contribution to the total generated heat is negligible.

Parasitic reactions take place at a extremely low rate compared with the main electrochemical reaction, thus, its generated heat is also disregarded. Therefore, three heat generation mechanisms are taken into account in this thermal model:

- Ohmic heat ($\dot{Q}_{ohm}$) due to the ohmic losses arising from electron movement in the electrode and ion transport in the electrolyte and across the membrane. It is proportional to the square of the current (i^2), as shown in Equation 4.40. The proportionality constant is the ohmic resistance, which value depends on temperature T as explained in Subsection 3.4.1 and modelled in Subsection 4.4.3.

$$\dot{Q}_{ohm} = i^2 \cdot R_{ohm} \tag{4.40}$$

- Polarization heat ($\dot{Q}_{act}$) is due to the electrochemical reaction polarization potential established on the surface of the active material particles.

$$\dot{Q}_{act} = i_F \cdot v_{act} \tag{4.41}$$

- Reversible or entropic heat ($\dot{Q}_{rea}$) is due to the entropy variation of the electrochemical reaction, and can be generated or absorbed depending on the reaction direction and on the sign of the entropic factor defined in Subsection 3.4.2.

$$\dot{Q}_{rea} = i_F \cdot T \frac{\partial v_{OC}}{\partial T} \tag{4.42}$$

Therefore, there are two irreversible components of the heat generation ($\dot{Q}_{act}$ and $\dot{Q}_{ohm}$) and a reversible component ($\dot{Q}_{rea}$). The heat generated per unit volume is denoted by lower-case $\dot{q}$, and the following equation can be used to relate the volumetric heat generation with the total heat:

$$\dot{Q}_k = \iiint_{V_{cell}} \dot{q}_k \cdot dV \tag{4.43}$$

where V_{cell} denotes the volume of the battery cell and the subscript $_j$ stands for $_{rea}$, $_{act}$ and $_{ohm}$.

The value of $\dot{Q}_{ohm}$ and $\dot{Q}_{act}$ can be directly calculated from the electrochemical model parameters and variables proposed in Section 4.4. However, the entropic factor needs to be known for the computation of the reversible heat. At a first glance, the dependency of v_{OC} with T presented in Equation 4.13 could be derived as follows:

$$\frac{\partial v_{OC}}{\partial T} = \frac{\partial}{\partial T}\left[v_{eq}^0 + \frac{R \cdot T}{F} \cdot \ln\left(\frac{(1 - x_{\zeta,c}) \cdot x_{\zeta,a}}{x_{\zeta,c} \cdot (1 - x_{\zeta,a})}\right) + v_{INT}\right] \tag{4.44}$$

And taking into account that none of the involved parameters are considered as temperature dependent:

$$\frac{\partial v_{OC}}{\partial T} = \frac{R}{F} \cdot \ln\left(\frac{(1 - x_{\zeta,c}) \cdot x_{\zeta,a}}{x_{\zeta,c} \cdot (1 - x_{\zeta,a})}\right) \tag{4.45}$$

However, this is an indirect approach to the entropic factor that uses an expression for v_{OC} in which an important assumption is done. The grouping of all the electrostatic interaction between the crystal lattice and the intercalated ions in the term named v_{INT} is a suitable simplification for the v_{OC} calculation, but introduces an important disturbance in the entropic factor. Even though no dependency on temperature is considered for the polynomial expression that fits v_{INT}, this term actually represents changes in the electrodes entropy, which is in fact composed of a configurational part (arrangement of species in the system) and a thermal part (energy distribution over the energy states in the system) [ABD14]. Therefore, the disturbance that this simplification implies in the computation of the entropic factor cannot be disregarded.

This is the reason why the majority of the approaches to the calculation of the entropic factor imply its direct measurement with different states of the battery. These measure data are used, by means of interpolation or polynomial fit, to calculate the reversible heat. This kind of measurements have been published for a number for Li-ion battery types, such as LFP [MIL17], LCO [AL 00], LMO [ZHA14b], $LiMn_{1.8}Al_{0.2}O$ [THO01], and the particular battery type analysed in this thesis, NMC [ABD14]. In accordance with this bibliography, the measured data presented in [ABD14], and shown in Table 4.6, are used for the computation of the entropic factor.

Figure 4.25 shows a comparison between the values of the entropic factor calculated from Equation 4.45 and the measurements presented in [ABD14]. Both approaches result in values of the same order of magnitude (lower than 0.5 $\mathrm{mV\,^{o}C^{-1}}$). Their similarity is more remarkable for low and intermediate battery state of charge. The more realistic measured results show that $\dot{q}_{rea}$ is endothermic during charge at $SOC \leq 0.2$, exothermic between 40% and

Table 4.6: Entropic factor $\left(\frac{\partial v_{OC}}{\partial T}\right)$, in $\mathrm{mV\,^{o}C^{-1}}$, for three different temperature changes. Reprinted from [ABD14], with permission from John Wiley & Sons, Inc.

Temperature/ SOC	1	0.8	0.6	0.4	0.2	0
25–35 °C	–0.13	–0.03	0.06	0.02	–0.07	–0.44
25–35 °C	–0.20	–0.05	0.15	0.14	–0.08	–0.47
25–35 °C	–0.38	–0.08	0.14	0.15	–0.09	–0.48

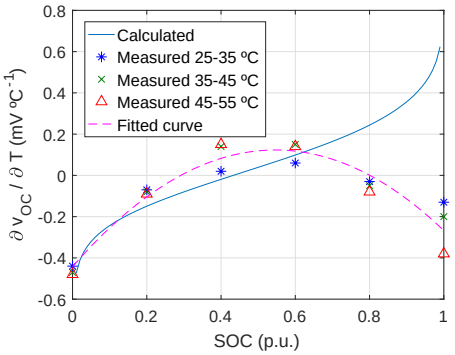

Figure 4.25: Comparative graph of the entropic factor calculated with Equation 4.45 and measured in [ABD14].

60% SOC and endothermic again for $SOC > 0.8$. For the sake of physical interpretation of this entropic factor, it is noticeable that the negative to positive change in entropy indicates a stage structure change in the graphite anode or phase transition in the cathode. Meanwhile, a negative variation typically indicates the ordering of the structure.

The entropic factor has been reported to have a slight dependency on temperature. Nonetheless, the weight of reversible heat in the total NMC battery heat generation is relatively low, and the effect that operation temperature has on this term is disregarded in this thesis. Therefore, a second-grade polynomial expression is fitted to the measured data, as shown in Figure 4.25, obtaining the following expression for the entropic factor as a function of SOC $\frac{\partial v_{OC}}{\partial T}(SOC)$:

$$\frac{\partial v_{OC}}{\partial T} = \left(-0.8958 \cdot SOC^2 + 2.0711 \cdot SOC - 0.4426\right) \cdot 10^{-3} \tag{4.46}$$

Adding this expression to the terms described above, the required parameters for the total heat generation by each cell are known:

$$\dot{Q}_{cell} = \dot{Q}_{ohm} + \dot{Q}_{act} + \dot{Q}_{rea} \tag{4.47}$$

4.5.2.2 Heat dissipation

Even though the fundamental unit concerning the electrical battery performance is a cell, its thermal phenomena are determined by modules such as the one shown in Figure 4.26. Figure 4.26 (a) shows a module consisting in six cells, three of them facing the other three in a symmetrical structure, with an aluminium heat sink on each side of the block. Taking into account that

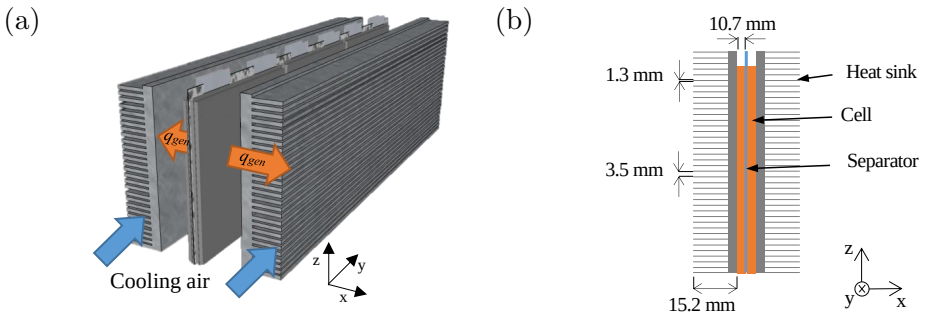

Figure 4.26: Schematic representation of the thermal performance of a battery module: perspective view of the module and the heat sinks (a) and frontal view of the assembly (b).

the dimension of the used pouch cells in the x axis (see Figure 4.26) is much smaller than the dimensions y y z (see Table 4.7 for accurate values), the heat flow is considered to be unidimensional in the x direction, as represented by means of red arrows in the figure. Figure 4.26 (b) shows a frontal view of the module with its characteristic dimensions. Given its geometrical symmetry and uniform heat generation (also symmetric), and considering that the thermal characteristics of each module are independent of their location inside the battery pack due to the cooling airflow that refrigerates the heat sinks, the thermal model of the battery is reduced to the analysis of half of a module.

Thanks to this unidimensional simplification, a thermal model based on the finite differences method can be proposed. This kind of models is based on the representation, as a voltage of an equivalent-circuit node, of each remarkable temperature of the system, as detailed in Appendix A. Therefore, the temperature at each node is related with its own temperature at the previously-analysed time and with the temperature of the adjacent nodes by means of the heat transfer equations explained in Section 3.4. Figure 4.27 (a) represents the electrical analogy of this finite differences thermal model for a generic node, which corresponds with the graphical representation of Equation A.20.

Table 4.7: Dimensional characteristics of the battery cells.

Variable	Value	Unit
Weight	892	g
Length (y)	222	mm
Hehgth (z)	214	mm
Width (x)	10.7	mm

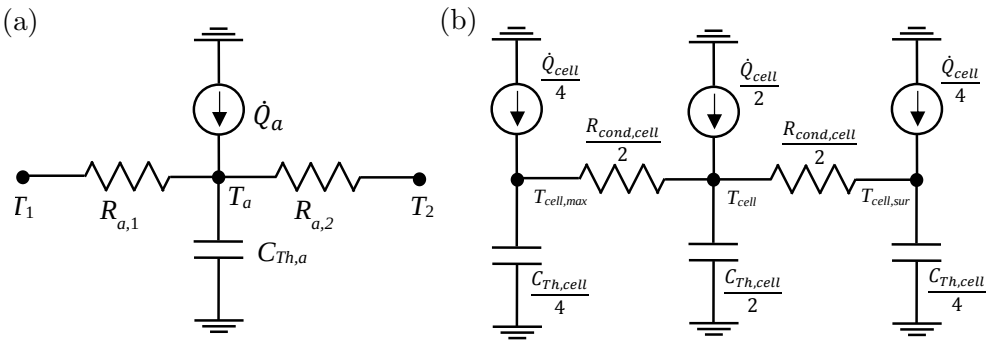

Figure 4.27: Finite difference model of a generic node a (a) and of the battery cell (b).

The most relevant cell temperatures are the maximum temperature $T_{max,cell}$, which can trigger a thermal runaway process and takes place in the volume of the cell which is closest to the centre of the module; the average cell temperature (T_{cell}), which takes place in the central part of the cell and determines the electric model parameters; and the temperature reached on the surface of the cell ($T_{cell,sur}$), given that this contact temperature between the cell and the heat sink determines the heat exchange rate between both components and, therefore, the evacuated heat flow. In order for the model to calculate each of these temperatures, the cell thermal model consists in three nodes, one representing each of these temperatures, as shown in Figure 4.27 (b).

The aluminium heat sink placed in each battery module to improve the heat transition between the cells and the cooling air needs to be modelled as part of the heat disputation process. As shown in Figure 4.26 (a), each heat sink manages the heat generated in three of the battery cells (its length is 721 mm). Taking into account the inconvenience of a non-homogeneous thermal distribution in a cell reported in Subsubsection 3.4.1.3, the cooling air flow through the heat sinks is controlled during regular battery operation in order to achieve enough heat flow dissipation so the cell temperature is almost constant. Therefore, and taking the unidirectionality assumed for the heat flow, the heat generated by a single cell can be considered to be transferred by its correspondent heat sink area (a third of the total heat sink) extrapolating the obtained results to the 36 cells that build the battery. The overall thermal model, in which the cell model shown in Figure 4.27 is complemented with the parameter $R_{Th,dis}$ modelling the conduction process in the heat sink and its convection to the cooling air is shown in Figure 4.28. Moreover, given that the node $cell, s$ is equivalent to the node $sink, 1$, the heat sink thermal capacitance $C_{Th,sink}$ is added to the model, representing one third of the total heat sinks,

which is the part corresponding to each cell.

4.5.3 Experimental design to obtain the model parameters

4.5.3.1 Cell parameters

A combination of experimental tests, finite-element simulations and theoretical calculus are presented in this section with the aim of obtaining the values of the battery thermal model parameters shown in Figure 4.28. On the one hand, the heat generation phenomena are represented by the variable $\dot{Q}_{cell}$, whose value depends on the electrical cell performance and is calculated by means of Equation 4.47, whose parameters are part of the electrochemical model proposed in Section 4.4. The only distinct parameter is the entropic factor $(\frac{\partial v_{OC}}{\partial T})$, which is taken, as explained in Subsubsection 4.5.2.1, from published measurements performed in cells similar to the ones studied in this thesis.

On the other hand, the parameters required for the modelling of the heat conduction through the cell are $R_{cond,cell}$ and $C_{Th,cell}$, which are proposed to be measured by means of two experiments. Firstly, the test proposed for the measurement of $R_{cond,cell}$ consists of driving a known heat power across the cell measuring the temperatures on both sides of the cell as schematically shown in Figure 4.29 (a). Figure 4.29 (b) is a photograph of the experimental setup built in the Energy Technology Laboratory, at UPNA (note that the battery cell and the plate resistors cannot be seen for being located inside the thermal isolator). The measurement of the resistor current and voltage (v_{PR} and i_{PR}) allows the calculation of the generated heat power and, given that the system is thermally isolated, the total heat flow is evacuated across the cell. Once the temperatures, both on the cold and hot sides of the cell, reach the steady state,

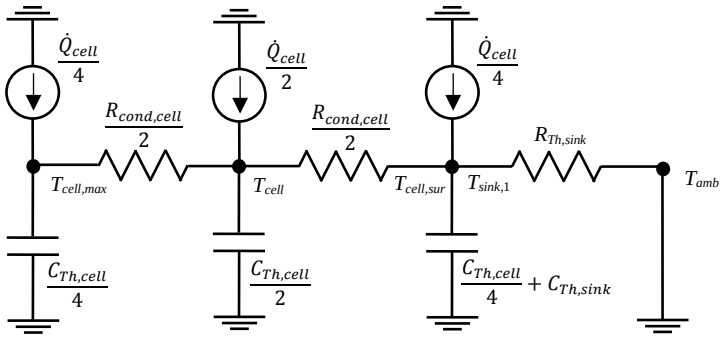

Figure 4.28: Thermal model of the battery pack for forced convection conditions.

the thermal resistance is calculated by means of the following expression:

$$R_{cond,cell} = \frac{T_{hot} - T_{cold}}{v_{PR} \cdot i_{PR}} \tag{4.48}$$

Figure 4.29 (c) shows an example of such a test, in which both T_{hot} and T_{cold} are measured on two different points of the cell surface. Te experiment lasts until stable temperatures are reached (around 200 minutes) and the temperature difference between the hot and the cold sides is recorded. In this particular test $v_{PR} = 8$ V and $i_{PR} = 4.4$ A, therefore:

$$R_{cond,cell} = \frac{79.7 - 54.78}{8 \cdot 4.4} = 0.708 \text{ K W}^{-1} \tag{4.49}$$

Given that the Li-ion battery electrochemical reactions involve the electrode materials, the thermal properties of these electrodes depend on the battery SOC. Specifically, a variation of its thermal resistance has been reported in previous research papers. Therefore, the previously-described experiment has been performed in cells charged at different values of SOC, repeating each of them a number of times with different heat flow crossing the cell, as shown in Figure 4.30. These measurements corroborate the SOC dependency of $R_{cond,cell}$ and allows the fitting of the following empirical expression:

$$R_{cond,cell} = -0.3054 \cdot SOC^3 + 0.42 \cdot SOC^2 - 0.0951 \cdot SOC + 0.7205 \tag{4.50}$$

For the sake of comparability of the cell characteristics with the published bibliography, the thermal resistance is expressed as average thermal conductivity of the material, which is a characteristic of each material, therefore independent on cell shape and size. The expression shown in Equation 4.51 is used to perform this transformation, leading to the results shown in Figure 4.30.

$$\lambda = R_{cond,cell} \frac{S_{cell}}{L} \tag{4.51}$$

These results agree with previously-published research works, such as [VER14], where LFP cells manufactured with a similar process than the NMC cells herein studies are reported to have a thermal conductivity of $\lambda \approx 0.26$, which is close to the values measured and presented in Figure 4.30 (b). Even though most of the materials used for the manufacturing of both cells are similar, the cathodes of LFP and NMC cells are different. Therefore, no better agreement between both results can be expected.

Besides $R_{cond,cell}$, its thermal capacitance $C_{Th,cell}$ is the other cell parameter needed for the battery thermal model shown in Figure 4.28. The experiment takes place in an adiabatic vessel, consisting of a properly isolated container. The container is sealed with an isolating cap with two holes used to introduce two thermometers into the container. A measured amount of water

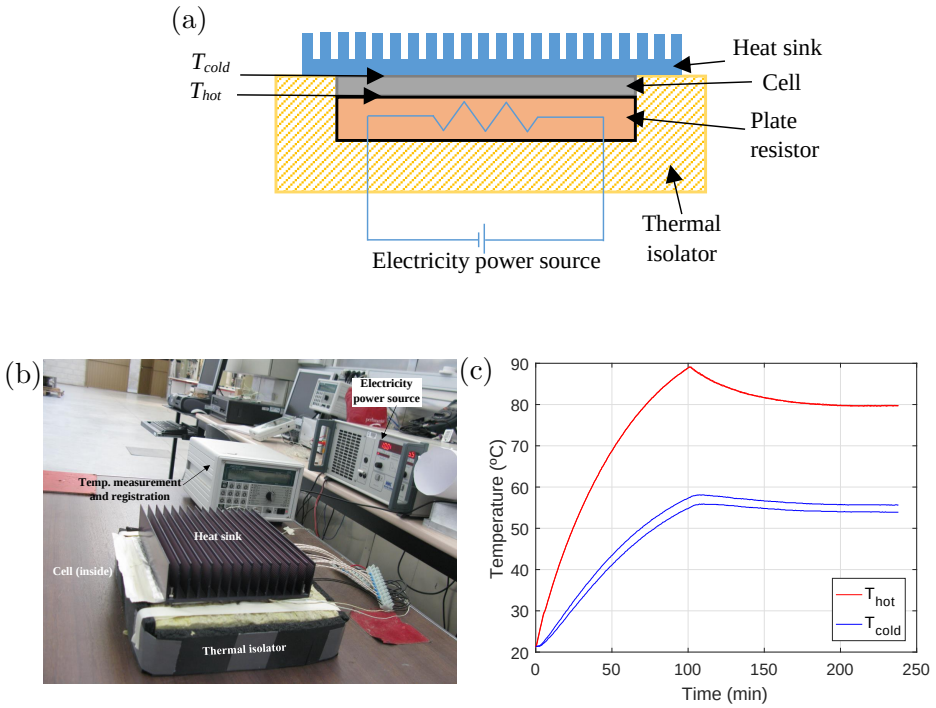

Figure 4.29: Experimental test for thermal conductivity measurement: schematic layout (a), photograph of the experimental setup (b) and measured temperatures (c).

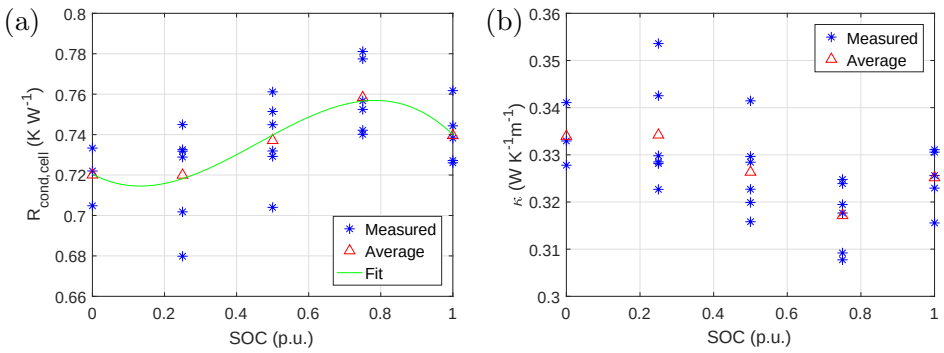

Figure 4.30: Thermal conductivity parameters as function of SOC: thermal resistance $R_{cond,cell}$ (a) and thermal conductivity λ (b).

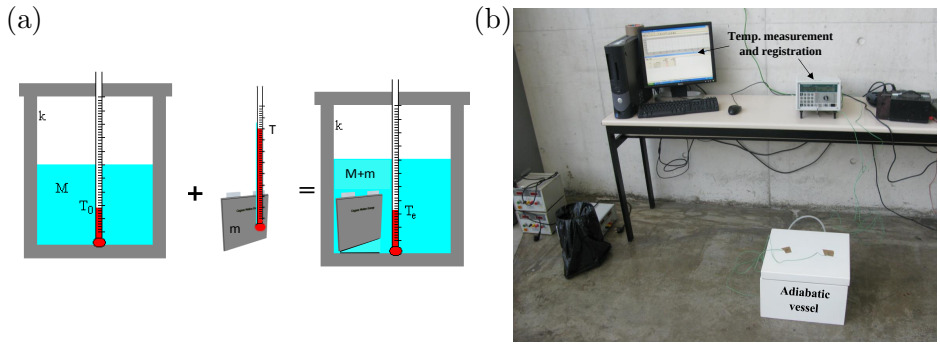

Figure 4.31: Experiment proposed to measure thermal capacitance $C_{Th,cell}$: schematic representation (a) and photograph of the experimental setup (b).

at a known temperature is placed inside the container, where the experiment takes place under adiabatic conditions. The studied cell is heated up to a temperature hotter than the water and subsequently submerged in the water. The container is sealed and the cell and water temperatures are allowed to equalise. Figure 4.31 (a) shows a schematic of the experiment, where a mass of water M at a temperature T_0 is place inside the container. When the cell (mass m) is submerged into the adiabatic container, the total mass is $M + m$, and after the required time lapse, an equilibrium temperature T_{eq} is reached. Analogously, Figure 4.31 (b) shows a picture of the experimental setup assembled in the Energy Technology Laboratory, at UPNA.

Given that the process is adiabatic (no heat is exchanged with the surroundings), the heat exchanged between the system components must be balanced. The involved components are the the studied cell, the water and the own adiabatic vessel. The heat capacitance of the vessel ($C_{Th,av}$) needs to be experimentally measured before the real experiment. To do so, a quantity of water with a mass m_1 is placed inside the vessel and the temperature evolution is allowed to reach a steady state of T_1. After this, an extra mass of water m_2 at a different temperature T_2 is added to the adiabatic vessel, waiting again for the steady state. The equilibrium temperature T_{eq} is measured. The energy balance of the described process can be expressed as follows:

$$m_1 \cdot cp_{H_2O} \cdot (T_{eq} - T_1) + m_{av} \cdot cp_{av} \cdot (T_{eq} - T_1) + m_2 \cdot cp_{H_2O} \cdot (T_{eq} - T_2) = 0 \quad (4.52)$$

The parameter $m_{av} \cdot cp_{av}$ is the thermal capacitance of the adiabatic vessel, that can be calculated substituting in Equation 4.52 the measured variables. The thermal capacitance of the particular vessel used for this experiment was measured to be 2.44 $\mathrm{J\,K^{-1}}$, as summarised in Table 4.8.

Once the vessel is characterised, the actual experiment can be performed. To do so, the parameters shown in Table 4.8 need to be used. Figure 4.32 shows two simultaneous temperature measurements performed in two regions of the adiabatic vessel. Given the lack of temperature gradients during the steady state, both measurements coincide at the end of the test. It can be inferred from this figure that the cell is introduced in the adiabatic vessel at $t = 50$ min. The thermal capacitance of the cell can be calculated by means of the following expression:

$$(M \cdot cp_{H_2O} + m_{av} \cdot cp_{av}) \cdot (T_{eq} - T_0) + m \cdot cp_{cell} \cdot (T_{eq} - T) = 0 \tag{4.53}$$

$$C_{Th,cell} = m \cdot cp_{cell} = -\frac{(M \cdot cp_{H_2O} + m_{av} \cdot cp_{av}) \cdot (T_{eq} - T_0)}{T_{eq} - T} \tag{4.54}$$

Substituting the values shown in Table 4.8, $C_{Th,cell} = 796\ \mathrm{J\,K^{-1}}$.

4.5.3.2 Cooling air and heat sink

The evacuation of the heat generated inside the cells is done by means of aluminium heat sinks, which transfer this heat to a flow of cooling air as represented in Figure 4.26. The heat mechanisms that determine this process are the heat conduction across the heat sinks and the convection to the cooling air, which are grouped, based on the model shown in Figure 4.28 in the parameters $R_{Th,sink}$ and $C_{Th,sink}$. Taking into account that the heat sink is totally made of aluminium, a theoretical expression can be used to calculate the parameter $C_{Th,sink}$, as shown in Equation 4.55. The division by 3 is due to the fact that the heat generated in each of the cells is evacuated through a third of the heat sink. The values of the parameters involved in this calculation are shown in Table 4.9.

$$C_{Th,sink} = \frac{1}{3} \cdot m_{sink} \cdot cp_{Al} = 806.7\ \mathrm{J\,K^{-1}} \tag{4.55}$$

For the calculation of the conduction and convection thermal resistance, a simulation of these processes by a finite-element based software is faced. Given

Table 4.9: Value of the parameters required for the modelling of the thermal performance of the heat sink.

Parameter	Value	Unit
m_{sink}	2.698	kg
cp_{Al}	897	$\mathrm{J\,kg^{-1}\,K^{-1}}$
S_{wt}	0.01131	$\mathrm{m^3}$
ρ_{air}	1.19	$\mathrm{kg\,m^{-3}}$

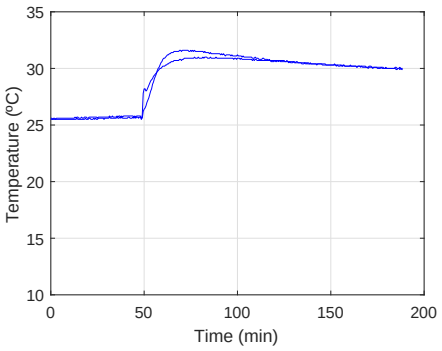

Figure 4.32: Temperature measurement for $C_{Th,cell}$ calculation.

Parameter	Value	Unit
$(m \cdot cp)_{av}$	2440	$\mathrm{J\,K^{-1}}$
M	1.13	kg
m	0.892	kg
cp_{H_2O}	4184	$\mathrm{J\,kg^{-1}K^{-1}}$
T_0	25.7	ºC
T	68.7	ºC
T_{eq}	30	ºC

Table 4.8: Value of the required parameters for $C_{Th,cell}$ calculation.

the substantial influence of the cooling air velocity in the convection process, this velocity needs to be characterised in advance. With this purpose, a 1 m long wind tunnel is built (see Figure 4.33 (a)), in which the air flow is totally developed. The velocity is measured in the central section of the tunnel with the aim of avoiding turbulences formed at the input and output of the flow. As schematically shown on the right side of Figure 4.33 (b), the wind speed is measured in seven equidistant points along the tunnel diameter, thereby obtaining the spacial velocity profile shown in this figure. Taking into account that the tunnel area (S_{wt}) coincides with the area covered by each of the battery fans and, taking the air density shown in Table 4.9 into account, the air flow at each operating point is calculated.

This test has been repeated for different fan operation points, thereby characterising the air flow for any working conditions. Using these data, and

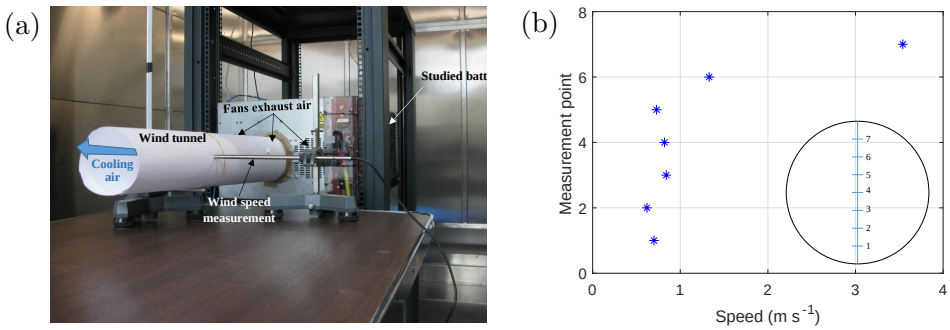

Figure 4.33: Experimental measurement of the cooling air flow: experimental setup (a) and measurement results (b).

taking into account the available area inside the battery for air circulation through the heat sinks, the air speed is computed as a function of the electric power fed to the battery fans. Finally, by means of the finite element analysis performed using the software Ansys, as shown in Figure 4.34 (a) the thermal resistance associated to the heat sink ($R_{Th,sink}$) for each fan operation regime is calculated. This resistance represents the heat conduction through the aluminium and the convection to the cooling air. The obtained results for this resistance are shown in Figure 4.34 (b), and fitted to a second order polynomial expression getting the following expression:

$$R_{Th,sink} = 1.31 \cdot P_{fan}^2 - 2.185 \cdot P_{fan} + 1.06 \tag{4.56}$$

where P_{fan} is the per-unit power fed into the fan, which ranges from 0 when the fan is off to 1 when the rated power is fed. Note that $R_{Th,sink}$ was calculated also for natural convection (red triangle in Figure 4.34 (a). However, natural convection was not included in this model, given that

4.5.4 Model experimental validation

Once the values of the thermal model parameters are known, the experimental validation of the model is accomplished to quantify its performance. With this aim, the electrical and thermal models are assembled together in Matlab® in order to calculate the battery operation variables $T_{cell,max}$, $T_{cell,sur}$ and v using T_{amb}, P_{fan} and i as input variables. As mentioned above, $T_{cell,max}$ has a main importance for the prevention of the thermal runaway of the battery, while $T_{cell,sur}$ is the measurable temperature at the surface of the cell and the variable used for the model validation. This interaction between both models is based on the calculation of battery voltage by means of the electric models, whose parameters (resistances, SOC, etc.) are used for the calculation, by means of the thermal model, of the heat generated by each cell. Moreover, the thermal model calculates the average cell temperature (T_{cell}), which is fed into the electric model to allow the update of its parameters, as shown in Figure 4.35.

Two experiments are herein presented, in which the battery is subjected to different working regimes. The voltage v and temperature $T_{cell,sur}$ are measured for comparison with the model prediction. The first experiment, shown in Figure 4.36, is a stepped current profile with low power requirements (both charging and discharging currents are lower than 1C), and is performed in a mild ambient with a temperature of 26±1.5 ºC. These conservative conditions allow for the battery operation without cooling system, being the convection process form the heat sinks to the air a natural convection. Figure 4.36 (a) shows the measured and predicted thermal evolution of the battery.

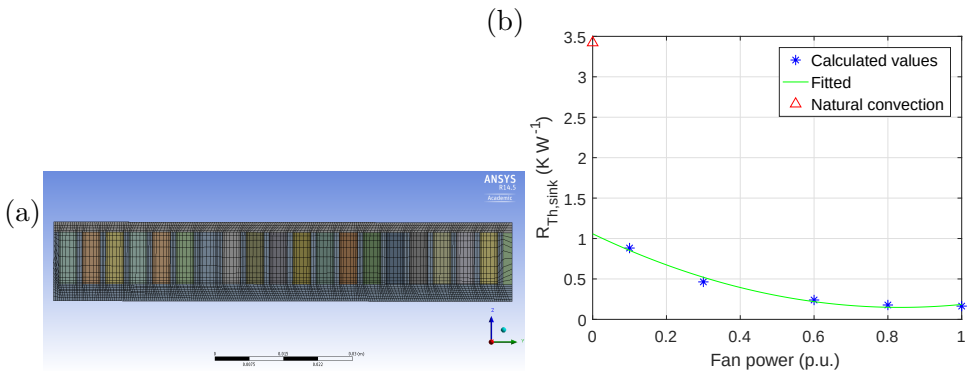

Figure 4.34: Finite element calculations to obtain $R_{Th,sink}$: Software results (a) and calculated $R_{Th,sink}$ as a function of the fan power (b).

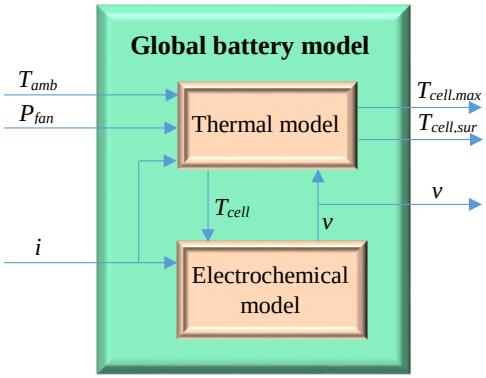

Figure 4.35: Flow diagram of the electrochemical-thermal model of the Li-ion battery with input and output variables of each model.

The measured value of $T_{cell,sur}$ is represented by the blue line and the model prediction by the red line. The thermal model is not able to accurately predict each variation of $T_{cell,sur}$, but the global temperature evolution is modelled, providing temperature values that are close to the real measurements. Actually, the battery range of battery temperature variation along the experiment is 8 °C, and the thermal model achieves an RMSE on its prediction of 0.31 °C, as shown in Table 4.10. The electric model is used in turn to predict the battery voltage during the experiment, as shown in Figure 4.36 (b). This is a typical Li-ion battery operation regime, given that the battery is neither fully charged (which would mean $v = 150$ V) nor fully discharged (which would mean $v = 105$ V). The electrothermal model is able to calculate the value of v during the whole test with an $RMSE = 0.39$ V, as summarised

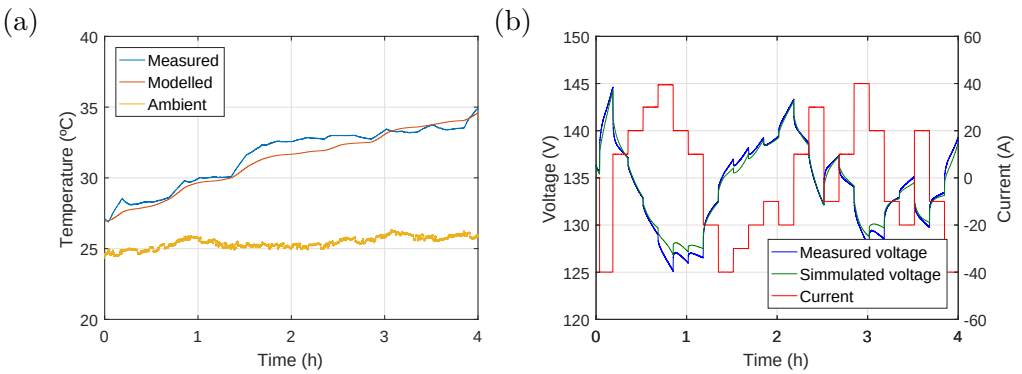

Figure 4.36: Experimental validation of the electrothermal model for low battery current, room ambient temperature and natural convection on the heat sinks: thermal (a) and electrical (b) variables.

in Table 4.10.

Moreover, a comparison of the prediction accuracy obtained by the single use of the electric model and the combination of the electric and thermal models is presented. With this aim, the same experiment is simulated considering that $T_{cell,sur} = T_{amb}$, thereby putting the thermal model aside. The accuracy obtained by the single use of the electric model to predict this experiment is the same as the one reported below for the combination of both models ($RMSE = 0.39$ V). This is due to the fact that the small power managed by the battery entails a reduced thermal generation, thereby reducing the difference between the cell and the ambient temperature, and therefore its effect on the battery electrical performance.

The second experiment presented to validate the usefulness of the combined electro-thermal model is shown in Figure 4.37. It consists of three battery discharges with a relatively high current (3C) each of them followed

Table 4.10: Influence of temperature modelling in the accuracy of the battery model for the two validation experiments.

Test	Variable	Electic model RMSE	Electrothermal model RMSE
Low	v	0.39 V	0.39 V
current	$T_{cell,sur}$	—	0.31 ºC
High	v	2.8 V	1.8 V
current	$T_{cell,sur}$	—	3.6 ºC

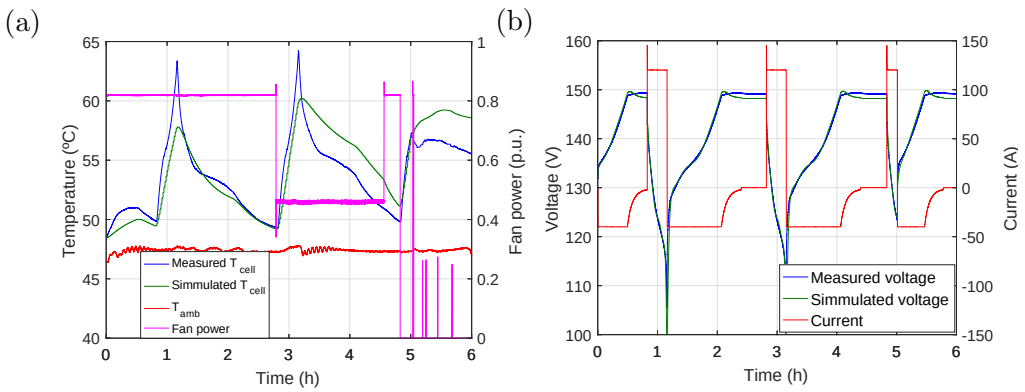

Figure 4.37: Experimental validation of the electrothermal model for high battery current, high ambient temperature and forced convection on the heat sinks: thermal (a) and electrical (b) variables.

by a standard (CC–CV) charging with a current in the CC region of 1C. The temperature during these charge–discharge cycles is 47 ºC, representing aggressive conditions for the battery performance. Given the high power losses entailed by these operating regime, the forced cooling is activated at different levels in order to widen the comparison scenario. Specifically, the first charge–discharge cycle is done with the cooling at 82% of its maximum capability, 48% is set during the second cycle followed by an idle period with the cooling set at 82%, and a third cycle (which is not finished, given that the battery voltage is not allowed below 122 V, and its minimum value is 105 V) with no forced cooling.

The performance of the model in this experiment is similar to the results reported above, given that the thermal model is able to predict the global increasing or decreasing trend of T_{cell}, but does not accurately reproduce each detail of its evolution. Due to the larger temperature variation of this experiment (around 15 ºC from the minimum to the maximum cell temperature) and to the successive heating and cooling cycles, the thermal model prediction error is larger than the previous results, increasing to an RMSE of 3.6 ºC. The comparative analysis of the voltage prediction accuracy obtained by the electrical and electrothermal model reveals that, in this situation with larger temperature variation, the model RMSE for the voltage prediction is reduced from 2.8 V obtained if $T_{cell,sur}$ is assumed to equal T_{amb} to 1.8 V achieved by the electrothermal model, as summarised in Table 4.10.

Even though the accuracy of $T_{cell,sur}$ reached by the thermal model decreases as the battery power is increased, as shown in Table 4.10, the global performance of the electrothermal model is increased when the temperature is

predicted by the thermal model. As covered in the previous paragraphs, the improvement brought by the thermal model is priceless when the battery manages a low power and, therefore, $T_{cell,sur} \approx T_{amb}$. However, when the battery power losses are relevant, the modelling of the generated heat and the thermal gradients established inside the battery means a noticeable contribution for a sustained Li-ion battery model accuracy, even subjected to extreme operation conditions.

4.6 Ageing modelling

4.6.1 Capacity fade and impedance rise model

As explained in Subsection 3.5.3, battery ageing is divided into calendar and cycle ageing. These ageing phenomena are normally assumed to be independent and their effects are added up [SCH14]. Based on the conclusion of the calendar ageing study published by researchers from Fraunhofer ISE [SCH17], a linear time dependency of capacity fade and resistance rise is assumed, as shown in Equation 4.57 and Equation 4.58. For the cycle ageing modelling, the conclusion of [WAN14b, PUR14, SCH13] are applied and the dependency of capacity fade and impedance rise with the number of equivalent cycles (Q, concept described in Section 2.3) is assumed to be also linear:

$$\frac{\Delta C(t,Q)}{C(t)} = -\left(\alpha_C \cdot t + \beta_C \cdot Q\right) \tag{4.57}$$

$$\frac{\Delta R_i(t,Q)}{R_i(t)} = \alpha_{R_i} \cdot t + \beta_{R_i} \cdot Q \tag{4.58}$$

where t is expressed in years and Q in equivalent full cycles. These expressions represent the capacity fade ($\Delta C = C(t) - C(t-\Delta t)$) and impedance rise ($\Delta R_i = R_i(t) - R_i(t-\Delta t)$) suffered by the battery during the analysed time lapse Δt. Therefore, battery ageing has a linear dependency on time and equivalent full cycles, which reduces the computational power required to run the model.

The parameters α_j (j representing C and R_i) determine the calendar ageing, while β_j govern the cycle ageing. These four parameters are not constant, since calendar ageing is faster for increasing SOC and temperature [SCH17] and cycle ageing is faster for higher current [WAN14b], average voltage and depth of discharge (DOD) [SCH13]. These dependencies of α_j and β_j are

modelled using the following expressions:

$$\alpha_j = a_{v,j} \cdot (v_{cell} - a_{0,j}) \cdot exp\left(-\frac{a_{T,j}}{T}\right) \tag{4.59}$$

$$\beta_i = b_{0,j} + b_{v,j} \cdot (v_{cyc} - b_{v0,j}).^2 + b_{DOD,j} \cdot \Delta DOD + b_{I,j} \cdot exp(b_{exp} \cdot \frac{|i_{bat}|}{C}) \tag{4.60}$$

With these expressions, calendar ageing has a linear dependency on the cell voltage and the temperature effect is modelled by an Arrhenius expression, as proposed in [SCH13]. The cycle ageing has a quadratic dependency on average cycle voltage (v_{cyc}), a linear relationship with DOD [SCH13] and an exponential trend with current, as modelled in [WAN14b]. These are the main variables reported to drive Li-ion battery calendar and cycle ageing, which are taken into account in this model bay means of the parameters shown in Table 4.11.

It is noteworthy that the proposed ageing model is valid for the linear region of battery lifetime, which takes place for capacity fade and impedance raise lower than 20% of their nominal values [SCH15]. After that, both ageing processes are accelerated, due to non-linear ageing phenomena, and the battery lifetime is usually considered to be over.

4.6.2 Validation of the battery ageing model

This subsection is devoted to check that the ageing phenomena are consistent with current Li-ion batteries available in the market. With this aim, three scenarios are designed and the proposed ageing model is used to predict the lifetime of a Li-ion battery in these three situations. For the three scenarios,

Table 4.11: Battery ageing model parameters for ΔC (first column) and ΔR_i (second column) calculation.

	Parameter	Unit	ΔC	ΔR_i
Calend.	a_v	–	$2.716 \cdot 10^5$	$9.486 \cdot 10^3$
	a_0	V	3.1482	3.096
	a_T	K	6976	5986
Cycle	b_0	–	$2.71 \cdot 10^{-5}$	$2.28 \cdot 10^{-5}$
	b_v	V^{-1}	$3.14 \cdot 10^{-4}$	$3.208 \cdot 10^{-4}$
	b_{v0}	V	3.683	3.741
	b_{DOD}	–	$1.61 \cdot 10^{-6}$	$3.404 \cdot 10^{-6}$
	b_I	–	$1.56 \cdot 10^{-5}$	$1.56 \cdot 10^{-5}$
	b_{exp}	h	1.8	1.8

a constant battery temperature of 30 °C is considered, and the daily electrical profiles are:

- Non-used battery: The battery is stored at 40% SOC with no use, as shown in Figure 4.38 (a).
- Intensive self-consumption: The battery is charged and discharged every day following a typical PV self-consumption pattern, as shown in Figure 4.38 (c).
- Extreme battery use: The battery is continuously charged and discharged at the maximum power limit, as shown in Figure 4.38 (e).

The ageing of a commercial Li-ion battery is simulated in these three scenarios and the resulting lifetime and equivalent full cycles are compared with the warranty offered by the manufacturer. The battery Tesla Powerwall 2 is chosen because of its recent market release, the simplicity of its warranty and its advantageous price (around € 500 kWh^{-1} including the power converter). The main parameters of this battery are summarized in Table 4.12. The warranty certificated by the manufacturer is ten years if the battery is used exclusively for PV self-consumption (with some limitations) or to 37.8 MWh of energy throughput otherwise, which means 2800 equivalent full cycles. Even though the end of life (EOL) criteria defined by Tesla is a capacity fade of 30%, the battery will be considered aged when the capacity fade reaches 20% in the simulation. This consideration is due to the reported nonlinear ageing phenomena for batteries with a capacity fade larger than 20% [SCH15].

The ageing model described in Subsection 4.6.1 is used to calculate the lifetime of the Powerwall 2 battery under these three scenarios and the results are calculated with the performance guaranteed by the manufacturer. For the first limit scenario, which consists on storing the battery at 40% SOC with no use, the model predicts a lifetime of 44 years. The capacity fade during the first 20 years is shown in Figure 4.38 (b). The single sensible comparison of

Table 4.12: Main characteristics of the battery Tesla Powerwall 2 based on the manufacturer's website.

Parameter	Value	Unit
Rated capacity	14	kWh
Maximum power	5	kW
Price	6200	$
Installation cost	800–2000	$

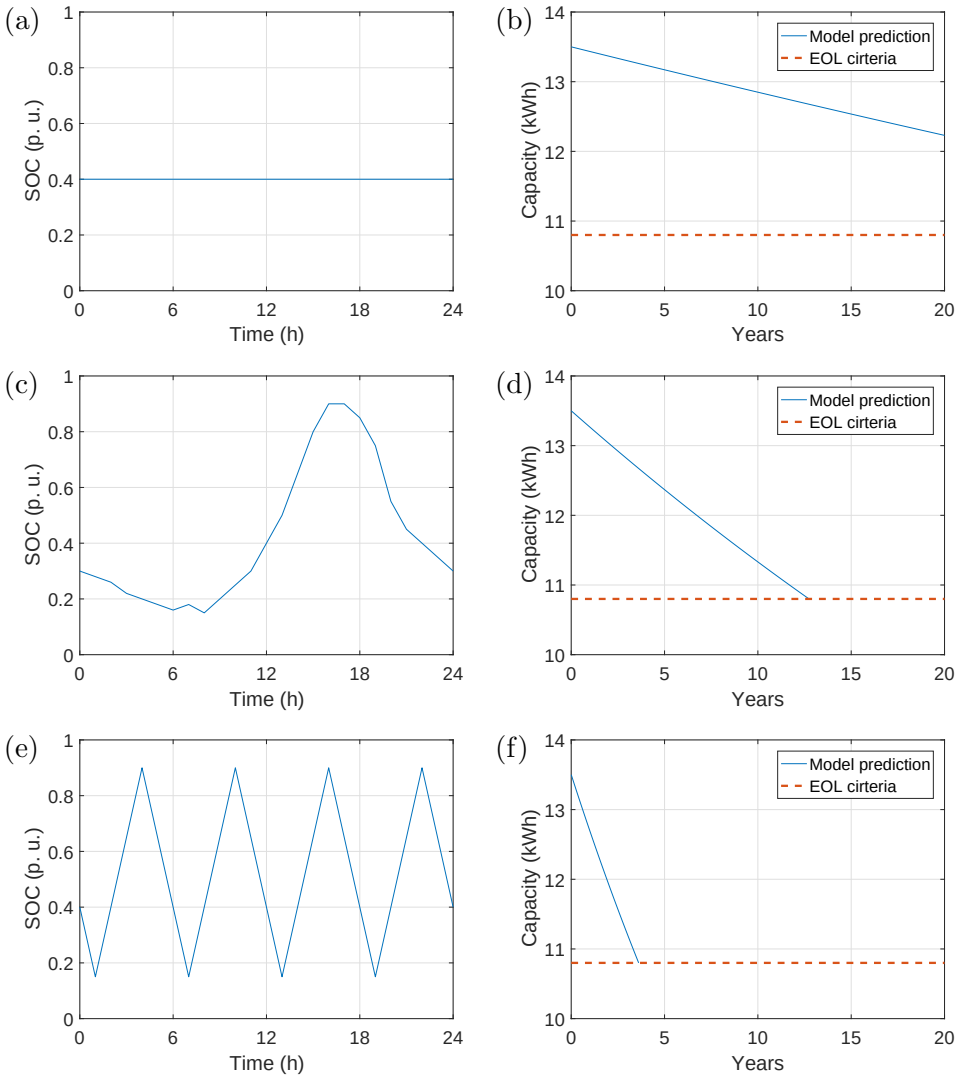

Figure 4.38: Validation of the Li-ion battery ageing model: daily battery SOC for the three designed scenarios (a, c and e) and modelled capacity fade for each of them (b, d and f).

this prediction to the guaranteed lifetime is to check that the model predicts a much longer lifetime than 10 years, which is true. For the second scenario, an intensive PV profile, the model predicts a battery lifetime of 13 years, which is equivalent for the proposed scenario to 46 MWh of energy throughput, as shown in Figure 4.38 (d). This is 30% longer that the guaranteed life, which is reasonable for a commercial product. Finally, for the extreme scenario of continuous battery charging and discharging at the maximum power rate, a lifetime of 3.6 years is predicted, as shown in Figure 4.38 (f), which means 51 MWh of energy throughput. The predicted lifetime is shorter than 10 years, but, given that the battery is not used for PV self-consumption, the limiting parameter is the energy throughput, which is 35% larger than the guaranteed 37.8 MWh. The comparison of the ageing model results with the guaranteed performance is summarised in Table 4.13.

Table 4.13: Comparison of the Li-ion battery ageing model results and the performance guaranteed by Tesla.

Scenario	Life time (years)		Energy throughput (MWh)	
	Model	% of warranty	Model	% of warranty
Idle battery	46	460%	0	—
PV self-consumption	13	130%	46	122%
PV self-consumption	3.6	36%	51	135%

Chapter 5

Integration of Li-ion batteries in renewable energy plants

When Henry Ford made cheap, reliable cars,
people said, 'Nah, what's wrong with a horse?'
That was a huge bet he made, and it worked.

– Elon Musk

5.1 Introduction

The energy sources used to produce electricity undergo a fast change from traditional fossil fuels to renewable energy in most of the countries, in both developed and developing areas [ZER16]. Electricity grids are complex systems composed by a wide range of elements. Therefore, the substitution of traditional generators by renewable energy power plants has to be carefully tackled, since they entail some risks that could eventually provoke undesirable effects in the performance of the grid. A main particularity of renewable energy is the unpredictability of its resource, which is a handicap when contributing to the frequency and voltage regulation of the grid [STE17a, KÖH17]. Due to the persistent installation of new renewable plants, updated regulations and grid codes are needed for a safe integration of renewable energy, ensuring the proper performance of the grid. There are two main problems that are being studied, which are fast fluctuations and grid overload.

On the one hand, new grid codes are published in order to regulate the fast fluctuations. These fluctuations, which can be caused by clouds move-

ment or gusty wind, endanger the stability of the electricity grid [LAM14]. Therefore, some of the most recently-published grid codes impose some kind of limitation concerning the maximum power change rate. For example, in Puerto Rico, no more than 10% power variation per minute is allowed for PV installations [GRI13], regulation that has been positively evaluated by the NREL [GEV13]. This maximum power variation is relaxed in Mexico to 20% per minute [GRI14] and is also addressed in the grid code from South Africa, where no general restriction is specified but power facilities receive information about this changing limitation depending on the state of the grid at each time [MAG14]. Batteries have been proposed in many research papers as a solution to deal with this restriction [PAR15, LEE12, MAR14b], but this issue is not analysed in this chapter.

On the other hand, some problems related with grid overload have been detected during the highest irradiance period in areas with high PV production, while this grid remains underused during the rest of the day. Power curtailment has been studied as a solution for this problem in the European Research project Insight_E [STE14]. The conclusion of this project is that curtailment is an option to solve grid overload, but some drawbacks were detected, like the greater consumption of fossil fuels. Energy storage is an alternative solution to curtailment, which has increasing interest as renewable energy generation is expanded and battery price is reduced. In this concern, the International Energy Agency (IEA) published a report in 2016 [PÉR16], where the synergies of combining centralized and decentralized energy storage for electricity grids are highlighted. Meanwhile, the MIT published a report where the design of updated market rules is suggested in order to trigger the installation of currently-improving technologies like batteries [IEA16]. Concerning the economical aspect of batteries, the main distributed energy storage system, the Rocky Mountain Institute published a report in 2015 concluding that multi-use, customer-sited batteries are the best option to maximize their advantages for customers and the grid [FIT15]. The German Energy Agency (dena) indicates that the investment on distribution grid extension in Germany to the year 2030 could decrease by 30% if the maximum generated power from variable renewable plants is set to 70% of their nominal power. For this reason, some energy policies are being developed in this country in order to accelerate the installation of grid-connected batteries to shave the PV generation peaks. The most remarkable example of these policies is a subsidy plan for home PV systems in Germany called *KfW-Programm Erneuerbare Energien "Speicher"*, which was launched for the first time in 2013 [SAU13]. The main requirements to apply for this funding is that a power limitation down to 60% of its original value is achieved and that the battery proper performance is warranted

by the manufacturer. The first part of this program (2013-2016) induced the establishment of more than 30 000 PV storage units. During the first months (2013) lead–acid batteries were the preferred technology for almost 70% of the participants, but a constant decrease in this type of batteries towards lithium-ion was registered and almost 90% of the storage systems installed during the last quarter of 2016 were Li-ion batteries [KAI16].

In order to get the most out of the batteries installed in these renewable plants, the optimal sizing and management of the storage system needs to be studied. Several research works concerning this topic have been recently published. Microgrids are particular systems where renewable generation and energy storage are also combined with consumption. The optimisation of their management strategy is an important research topic, as covered by Minchala–Avila et al. in their review [MIN15]. The uncertainty of the power generation and consumption is taken into account in some of the research works which analyse the management strategy design [HAN14], and linear programming methods are a common tool used to determine the optimal energy dispatch [HOK13]. Energy storage systems are also used for wind power integration support, as reviewed by Zhao et al. [ZHA15c], but the application herein addressed is a PV plant. These generation plants are usually connected to the low voltage distribution grid, whose constraints limit the further installation of PV power [WAF14].

A cost benefit analysis of photovoltaic–battery plants (PV+ plants) published in 2013 [NOT13] concluded that the addition of a battery to a PV system would be profitable if the battery cost were between $ 400 and $ 500 per kWh, which is nowadays realistic. Actually, the price for the small-scale, stationary battery Tesla Powerwall 2 (14 kWh) with its bidirectional power converter is already $ 490 per kWh excluding taxes [TES]. Prices for large-scale battery systems are not that easy to access, and therefore there are reports analysing fabrication costs and market trends, specially focused on the electric mobility, which is currently the most important sector for Li-ion batteries. In this concern, as already mentioned in Chapter 2, the U.S. Department Of Energy (DOE) monitored the cost of Li-ion batteries for electric vehicles and detected a fall from about $ 1000 kWh^{-1} in 2008 to $ 268 kWh^{-1} in 2015, which means a 73% reduction in battery cost in seven years, as summarized by the IEA in a report published in 2016 [CAZ16] (see Figure 2.3 (b), in Chapter 2). Moreover, the DOE set a target of $ 125 kWh^{-1} by 2022, which is an additional 10.3% annual cost decrease during the following seven years. The IEA considers this target as a realistic value and some vehicle manufactures announced more drastic price decrease. General Motors expects a cost below $ 100 kWh^{-1} by 2022 [ARI15] and Tesla aims to break the $ 100 kWh^{-1} by 2020 [HYB].

Given the similar manufacturing processes for electric vehicles and stationary batteries, these results can be extended to stationary systems.

The optimisation problems concerning battery sizing and management can be tackled from different points of view, either as an economic analysis, focusing the attention on the implications of the ESS to the electricity grid, analysing the implications of the management strategy into the battery performance, etc. A number of studies proposing advanced economical models aimed at optimal sizing of the storage system [MUL13] are useful for an overall study of investment profitability, but they usually entail the use of simple battery models and assumptions (such as battery life longer than 20 years independently of its use) that reduce the reliability of the results. Other authors centre their attention on the effect that the battery has on the electricity grid [WAF14, MÉG15]. They discuss different grid situations (rural areas, suburbs, multistorey building) and grid services (peak shaving, infrastructure deferral, etc.) based on advanced grid models. Given that the battery performance is not the aim of these researches, it is modelled based on a constant efficiency and its ageing is not accurately studied. Some of the published papers that propose an optimisation method for the battery management are based on linear programming [LI14, NOT13, WEN14]. Linear optimisation is computationally efficient, but the battery model needs to be linearised, which can be a source of inaccuracy in the results. Moreover, no special attention is paid to the battery ageing in this papers, which is a main issue for the sizing and management of an ESS. Finally, there are recent research works proposing neural networks [OLA17] and nonn-linear optimisation techniques [BAR17] to optimise the battery energy dispatch. The authors of [OLA17] use high-quality measured data to achieve a realistic optimal battery size. However, not much attention is paid to the battery management, since it is devoted to cover the load requirements. On the other hand, the authors of [BAR17] study the battery management of a large PV plant with no special concern of achieving an optimal size and no ageing considerations.

We present in this chapter an integrated optimisation method for battery sizing and management developed in a collaborative research project between the Ingeper research group (UPNA) and the Team Battery Engineering (Fraunhofer ISE). The method is then particularised to a medium-size PV plant (100 kWp). The reason of this optimisation method combining battery sizing and management is that battery management determines its lifetime, which needs to be taken into account to size the ESS. Meanwhile, depending on the size of the battery, more or less aggressive management strategy can be designed to obtain a trade-off between battery functionality and lifetime. A non-linear, dynamic program algorithm is used for the energy dispatch op-

timisation, while a hill climbing algorithm is proposed for the battery sizing, as detailed in the following sections. These non-linear methods allow the use of advanced battery performance and ageing models, increasing the reliability and robustness of the conclusions. Even though the uncertainty of the resource availability for renewable plants is an interesting topic of study and improvement, it is not tackled in this thesis. Actually, intensive and productive research efforts on weather prediction algorithms made during the last decade have significantly reduced the effect that this inaccuracy has in real systems, and values for RMSE lower than 12% of nominal PV power for a day-ahead prediction are not surprising [PIE16]. Moreover, it is a regular case that a single company manages several renewable energy plants. It has been proven that the output power of several distributed plants has an even lower uncertainty due to prediction inaccuracy than single plants, given that the errors compensate each other when the distance between plants is big enough [MAR12, MAR16]. Therefore, the analysis presented herein, with no study of forecast errors has a high interest for current systems, even though weather forecasting is a stimulating research topic.

The chapter is organized in eight sections. After this introduction, the studied PV+ plant is explained along with the models of each system. In Section 5.3, the energy dispatch optimiser used to design the battery management is exposed while the details about the sizing optimisation are given in Section 5.4. The simulation set-up, proposed scenario and used data are detailed in Section 5.5. In Section 5.6 we show the simulation results and emphasise the usefulness of this combined optimisation. An application of this optimisation method is presented in Section 5.7, which is a sensitivity analysis to quantify the influence of different parameters in battery profitability. Finally, Section 5.8 is the conclusion of the chapter.

5.2 System architecture and modelling

The optimisation method proposed in this chapter is applied to a medium-size PV plant. These plants are usually connected to distribution grids, in which grid overload is already a problem in areas with high penetration of renewable energy, as covered in Section 5.1. As shown in Figure 5.1, the PV system is built by the PV field, which makes the actual conversion of solar power to electricity, and the PV inverter. The peak power of the PV field (P_{peak}) is the DC power generated with optimal solar radiation and standard ambient temperature, which is achieved only during a few hours along the year. A usual design strategy is to oversize the PV field in relation to the

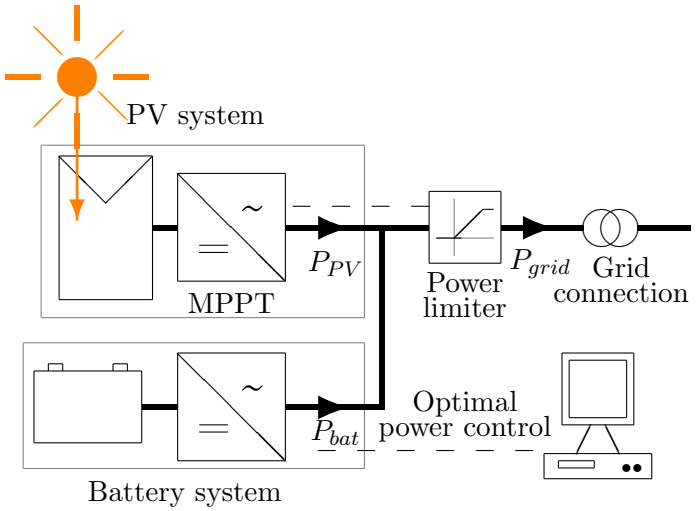

Figure 5.1: System diagram of the PV+ plant.

PV inverter, thus not being able to generate the whole P_{peak} during the few hours with maximum irradiance. As advantage, the price of the inverter is lower and its efficiency at more common, lower irradiance is enhanced. Using an accepted design rule, $P_{PV,inv} = 0.85 \cdot P_{peak}$. The control algorithm of the PV inverter is the maximum power point tracker (MPPT) devoted to maximize the power generated by the PV modules. P^*_{PV} is the maximum power that could be generated by the PV field with a given irradiance and ambient temperature. In a normal situation, the MPPT achieves this PV power, and $P_{PV} = P^*_{PV}$. However, when there is a power higher than the maximum fed-in power ($P_{grid,max}$) injected into the grid, the PV inverter power is limited, as represented in Figure 5.1 and the extra available power is not generated, therefore $P_{PV} < P^*_{PV}$. P_{grid} is assumed to be unidirectional from the plant to the grid, since regulations in most countries do not allow to feed grid power to a generation plant.

A schematic of the battery system analysed in this chapter is shown in Figure 5.1. It consists of a lithium-ion battery pack, whose size needs to be determined, and a bidirectional battery power converter used to connect it to the AC grid. The management strategy of the battery system is optimised and an external controller feeds the converter with its power setpoint. Two services are provided by the battery in this scenario. On the one hand, the energy generated by the PV modules can be increased, since the shaved peaks are stored and delivered in other moments, when the grid is not overcharged, which is a service to the utility grid manager. On the other hand, the stored

electricity is sold when the price is at its highest value, providing greater economical revenue to the PV plant owner.

The optimisation method proposed in this chapter is based on system modelling. Given the importance of model accuracy to obtain representative results, robust and reliable models are used for the PV field, PV and battery inverters and lithium-ion battery pack. These utilized models are detailed through the following subsections.

5.2.1 PV system modelling

The conversion of solar irradiance to DC electricity and later to AC, takes place in the PV system. The amount of the DC energy that can be generated during the simulated time is strongly influenced by the solar irradiance. This process is modelled using the PVLIB toolbox, which is a set of open-source modelling functions for simulating the performance of photovoltaic energy systems provided by Sandia National Laboratories [LAB]. The inputs for this toolbox are the PV plant location, global horizontal irradiance, temperature, size of the PV field and orientation of the modules. To perform the simulation, PVLIB calculates the position of the Sun and, using horizontal irradiance data and an atmosphere model, divides this global irradiance into its direct and diffuse components. With these variables and the ambient temperature, the module orientation and field size, the PV cell temperature and DC generated current are calculated.

The DC to AC conversion is modelled through the Driesse model [DRI08], which takes into account power and input voltage in the calculation of inverter efficiency, as shown below:

$$P_{PV} = P_{PV,DC} - P_{PV,loss} \tag{5.1}$$

$$P_{PV,loss} = b_0 + b_1 \cdot P_{PV,DC} + b_2 \cdot P_{PV,DC}^2 \tag{5.2}$$

where $P_{PV,loss}$ are the power losses in the PV power converter (labelled as "MPPT" in Figure 5.1), and b_0, b_1 and b_2 are empirical, voltage-dependent coefficients.

PVLIB includes databases with characteristics of several commercial panels and inverters. These are realistic and trustworthy features required by the models. These databases increase the reliability of the simulation results.

5.2.2 Battery system modelling

The two components of the battery system (power converter and battery pack) need to be modelled. On the one hand, the bi-directional battery converter is modelled using the same modelling technique described above for the PV inverter. Based on Driesse model, the performance of the battery converter is modelled through Equation 5.1 and Equation 5.2. This approach takes into account self-consumption, voltage and resistive losses.

On the other hand, the accuracy of the battery pack model has special importance in this study, since it has a big influence in the conclusion extracted from the work. Therefore, an ageing-dependent lithium-ion battery model is suggested (see Figure 5.2 (a)). This model is built from the simple electric circuit model presented in Subsection 4.4.2 (see Figure 4.6). Given that this section concerns an energy analysis, and no dynamic phenomena are taken into account, the capacitance C_{dyn} is disregarded, and the series connection of R_{ohm} and R_{dyn} is named R_{int} (internal resistance). Given that Li-ion batteries require the monitoring and control of their temperature in most of the outdoors applications, battery temperature variations are disregarded and not taken into account in this model. The state of charge (SOC) is the main state variable of a battery, and is calculated using the ampere-hour counting method presented in Equation 4.1, disregarding the effect of coulombic inefficiencies $\eta_c \approx 1$ and a time-dependent capacitance due to the ageing effects. Therefore, the final equation used for the SOC estimation is:

$$SOC(t) = SOC(t_0) - \int_{t_0}^{t} \frac{i_{bat}(t)}{C(SOH)} \tag{5.3}$$

where SOH is the state of health of the battery, calculated by means of its ageing model. Note that the negative sign before the integral term is due to the sign of the current i_{bat} defined as battery discharging current to be consistent with the sign of P_{bat}.

The relationship between SOC and v_{OC} has been analysed and experimentally measured in Subsection 4.4.3. A characterization experiment similar to the one shown in Figure 4.10 was performed with an NMC Li-ion cell in the ServiceLab Batteries Laboratory, at Fraunhofer ISE, whose data are shown in Figure 5.2 (b). This characteristic curve remains almost constant for the whole battery lifetime [WAA14] and is included in the model as a lookup table. The internal resistance R_i also depends on SOC, and can be measured by means of a stepped-current test such as the one reported in Figure 4.10 (b). The measurements of the studied NMC fresh cell obtained by Frauhofer ISE are shown in Figure 5.2 (c). As long as the battery is aged, this parameter is scaled up, as a consequence of the battery ageing phenomena explained in

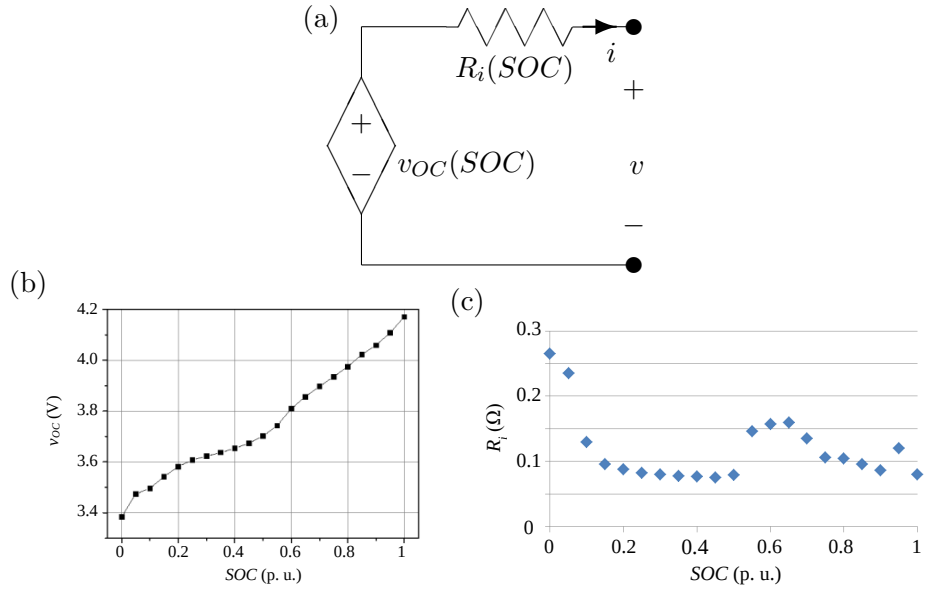

Figure 5.2: Cell electrical model: Equivalent circuit (a), v_{OC}–SOC relationship (b) and R_i–SOC relationship (c).

Section 3.5 and modelled in Section 4.6.

The battery ageing model is a key tool for this optimiser, since the size of the battery is calculated for the device to be useful during its whole lifetime, and the power managed by the battery is also calculated with the aim of enlarging its lifetime. The battery ageing model presented in Section 4.6 is used to calculate the loss of battery state of health ($\Delta SOH = SOH(t) - SOH(t - \Delta t)$) during each analysed time lapse Δt. In this context, ΔSOH is defined, accordingly with Equation 2.9 and Equation 2.10, by means of the battery ageing parameters presented in Equation 4.57 and Equation 4.58 as follows:

$$\Delta SOH = -max\left[\left|\frac{\Delta C}{C}\right|, \left|\frac{\Delta R_i}{R_i}\right|\right] \tag{5.4}$$

5.3 Energy dispatch optimisation

The energy dispatch optimisation problem consists of determining the battery power dispatch plan that maximizes or minimizes the value of an objective function. With this aim, an optimiser based on a dynamic program algorithm

is proposed as shown in Figure 5.3.

5.3.1 Involved variables

On the one hand, the input variables for this Energy Dispatch Optimiser (EDO) are the weather conditions, the electricity price and the system characteristics.

- Weather conditions:
  - ⋆ Global horizontal irradiance.
  - ⋆ Ambient temperature.
- Electricity price (PC_{elec}): it can be a constant rate, as is usually the case for domestic contracts, or dependent on time, which is common in electricity markets.
- System characteristics
  - ⋆ Location: latitude, longitude and attitude.
  - ⋆ PV field: peak power and orientation of the modules.
  - ⋆ Power converters: nominal power of the PV inverter and the battery bidirectional converter.
  - ⋆ Battery energy capacity.

On the other hand, the output variables are:

- Power profile (P_{bat}) that achieves an optimal value for the objective function.
- Optimal value of the objective function J.

It is remarkable to note that the maximum power that can be generated from the PV field (P^*_{PV}) depends on its peak power and on weather conditions. However, given that P_{grid} must be limited, P_{PV} may be lower than the maximum available power if the whole surplus energy is not stored in the battery. This is not a problem for PV systems, since they can generate lower power by simply driving the modules out of their maximum power point (MPP).

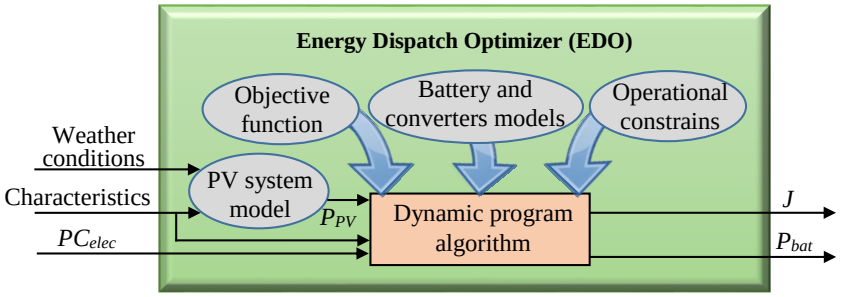

Figure 5.3: Schematic of the energy dispatch optimiser (EDO). Input variables (weather conditions, electricity price and system characteristics), internal tools (objective function, operational constraints and models of the PV system, battery and power converters) and output variables (battery power P_{bat} and value of the objective function J).

5.3.2 Objective function and constraints

As shown in Figure 5.3, the EDO combines the models explained in Section 5.2 with an objective function and several operational constraints and solves the problem by means of a dynamic programming algorithm. The objective function (J) is defined as the extra economical revenue obtained with the battery, taking battery ageing into account. The battery ageing costs are accounted by deducting, from the total profit of a time interval, the percentage of the battery cost corresponding to the life reduction during that time. The proposed expression is shown in the following equation:

$$J = \int_{t_0}^{t} \left[(P_{grid,\mathrm{PV+}} - P_{grid,\mathrm{PV}}) \cdot PC_{elec} + \Delta SOH \cdot PC_{bat} \right] dt \tag{5.5}$$

where $P_{grid,\mathrm{PV+}}$ is the power output of a PV+ plant and $P_{grid,\mathrm{PV}}$ is the power output of the PV plant with no battery. The economical variables involved in this expression are PC_{elec}, which is the price of electricity (in €kWh^{-1}), and PC_{bat}, which is the acquisition price of the Li-ion battery (in €).

The operational constraints can be classified into four groups:

- PV availability:
  - ⋆ $P_{PV} \leq P^*_{PV}$
- Fed-in power limitation:
  - ⋆ $P_{grid,min} \leq P_{grid} \leq P^*_{grid}$
- Battery performance:

  - ⋆ $v_{bat,min} \leq v_{bat} \leq v_{bat,max}$
  - ⋆ $SOC_{min} \leq SOC \leq SOC_{max}$
  - ⋆ $i_{bat,min} \leq i_{bat} \leq i_{bat,max}$

- Battery pwer converter:
  - ⋆ $P_{bat} \leq P_{R,conv}$, where $P_{R,conv}$ is the rated power of the battery power converter.

5.3.3 Optimization algorithm

Using these variables, objective function and constraints, a dynamic program (DP) optimisation is performed. This technique is based on the principle of optimality, which was described by R. Bellman [BEL57]: an optimal policy has the property that whatever the initial state and initial decisions are, the remaining decisions must constitute an optimal policy with regard to the state resulting from the first decision. DP was chosen as optimisation method because it can handle non-linear systems and it does not converge to local optimums. The main drawback is the large time needed to solve complex problems, which limits its applicability in on-line applications. In our case, which is a simulation study, optimisation time is not a constraint.

Some assumptions are needed in order to optimise the problem using a DP algorithm. The whole system is assumed to be a deterministic process, i.e. the initial state and decisions uniquely describe the outcome. Therefore, the influence of weather forecast accuracy, model uncertainty, measurement deviations and other sources of error is not analysed in this work. Moreover, the system needs to be discretised in order to have a finite number of paths. This means that decision variables cannot take an arbitrary value, but have to belong to a discrete set. The number of discrete classes is chosen to be sufficiently high to achieve good quality in the solution. The objective function (Equation 5.5) also needs to be time-discretised. Therefore, the time interval analysed on a single problem and the time resolution are to be decided. The number of time steps that are tackled by an optimisation problem (N) is an important parameter to define the size of the problem, since this is the number of decision variables $[P_{bat,1}...P_{bat,N}]$. Taking into account the daily pattern of PV generation and the suitability of Li-ion batteries for charge–discharge cycles of a few hours, the optimisation problem is reduced to 24 h, which means that the battery SOC at the beginning and end of each day needs to be determined. Besides, time steps of one hour ($\Delta t = 1$ h) were chosen, since the electricity price has an hourly pattern in most of the markets. With

this time step, high power peaks or battery dynamics cannot be analysed, but it is suitable for the energy study presented in this work. With this time restrictions, Equation 5.5 can be rewritten as:

$$J = \sum_{t=1}^{24} [(P_{grid,\mathrm{PV+}}[t] - P_{grid,\mathrm{PV}}[t]) \cdot \Delta t \cdot PC_{elec}[t] - \Delta SOH[t] \cdot PC_{bat}] \quad (5.6)$$

Therefore, 24 decision variables need to be calculated by the EDO ($P_{bat,i}$, with i=1...24). Actually, they are 48 variables if $P_{PV,i}$ are accounted. However, given that $P_{PV,i}$ is the input parameter $P^*_{PV,i}$ limited by the grid fed-in cap, these 24 variables are easily handled by the EDO. As shown in Figure 5.1, P_{grid} can be calculated from P_{PV} and P_{bat} taking the power fed-in limit into account. Therefore, the optimisation variables are the battery power to be managed during each hour of the day [$P_{bat,1}$...$P_{bat,24}$]. For the application of a DP algorithm to this problem, initial and final states for the system must be defined (which are battery SOC), and the decision variables must be able to drive the system from one state to others. The operation principle of the algorithm, which is shown in Figure 5.4, is based on four phases. In the first phase (Figure 5.4 (a)), all the feasible paths (which violate no constraints) starting from the initial state are identified. After this (Figure 5.4 (b)) the paths that do not conclude in the final state are eliminated from the study. The third phase is the calculation of the objective function for each path, as shown in Figure 5.4 (c), with the particularity that steps that are repeated for several paths (such as the grey steps in the figure, which are repeated for 2 and 3 paths) need to be calculated only once because their results are stored the first time and looked up when needed. The final phase is based on the Bellman's principle of optimality, and consists on the search of an optimal path, based on the calculations done during the third phase, starting from the final state, as represented in Figure 5.4 (d).

The performance of the EDO is shown in Figure 5.5 during two four-day periods, in two different seasons. The main system variables from 26 May to 29 May 2016 (Thursday to Sunday) ar shown in Figure 5.5 (a). During the central hours of each day, the available solar power (P^*_{PV}) is higher than the grid fed-in limit, as represented by the yellow solid line. Meanwhile, the electricity price during the two weekdays (26 and 27 May) is around € 0.13 kWh^{-1}, as shown with a blue, dotted line. However, it has a lower value during the weekend due to the lower electricity demanded on holidays.

Therefore, during the central part of the 26 and 27 May, the actual power generated by the PV system (P_{PV}, dashed green line) is close to P^*_{PV}, using the power that cannot be fed into the grid to charge the battery, as shown in the magenta dot-dash line. During the evening, when P^*_{PV} decreases below

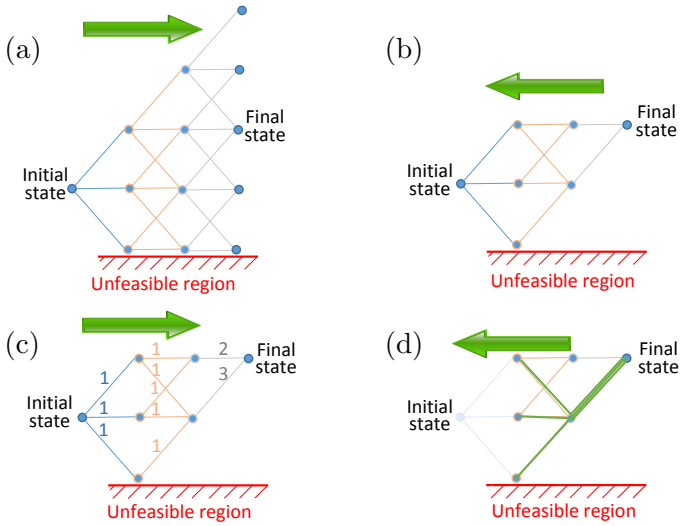

Figure 5.4: Optimization with an algorithm based on Dynamic Programming with its typical four steps: Calculation of the feasible paths starting from the initial state (a), elimination of the paths that do not reach the required final state (b), calculation of the objective function for each path avoiding repeated calculus (c) and calculation of the optimal path based on the Bellman's principle of optimality (d).

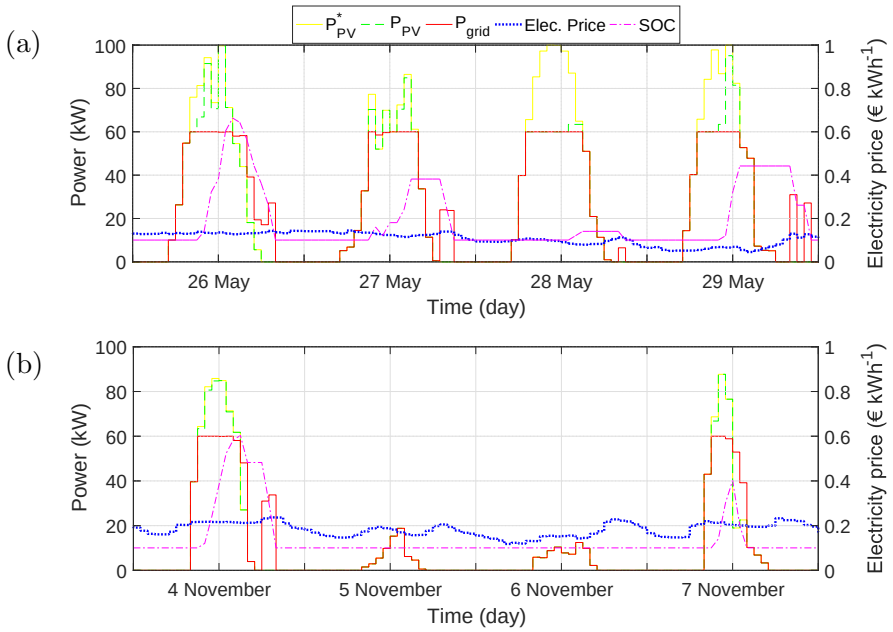

Figure 5.5: Performance of the EDO during four days in May (a) and four days in November (b).

the grid fed-in limit and the electricity price is high enough to produce an interesting economic profit, the battery is slowly discharged, avoiding high-power intervals that accelerate the ageing phenomena. The discharging process is stopped when a SOC of 0.1 is reached, since lower SOC are avoided in order to enlarge the battery lifetime.

Due to the low electricity price during the whole Saturday, the energy that cannot be directly fed into the grid is discarded and not stored in the battery, given that the profit made with the energy sold at such a reduced price does not make up for the extra ageing phenomena induced by a charge–discharge battery cycle. Finally, there is a fast increase of the electricity price on Sunday evening. Therefore, a portion of the surplus energy is stored in the battery and then fed into the grid during the two evening hours at which the electricity price reaches its maximum. Thus the EDO calculates the best battery management strategy to maximize the achieved revenue taking into account climatological and market conditions of every day.

During the days shown in Figure 5.5 (b), which are from Friday 4 to Monday 7 November 2106, the electricity price is higher than in May. Therefore, the profit obtained with a charge–discharge battery cycle is also higher. This is the reason why, on 4 and 7 November, all of the surplus energy that cannot be directly fed into the grid during the central hours of the day due to the fed-in power limit is stored in the battery and discharged in the evening. However, the 5 and 6 November were cloudy days and the generated power $P^*_{PV} = P_{PV}$ does not reach the grid fed-in limit. Therefore, the battery remains discharged during these two days, even though the electricity price is fairly high.

5.4 Battery size optimisation

The battery size optimisation problem consists of the selection of the battery size that allows for an optimal performance of the overall system. This is a main part of the PV+ plant design process, given that the profitability of the battery is affected by its size. On the one hand, if the battery is too small, it does not allow for the storage and management of the surplus PV energy, thereby limiting the achieved revenue. On the other hand, if its size is too large, its cost is also higher. Therefore, the battery size must be chosen in order to find a trade-off between the battery capabilities and price.

A schematic of the Battery Size Optimiser (BSO) is shown in Figure 5.6. The best size of the battery depends on the functionality required for the ESS and, therefore, on the algorithm that will be used for the battery management. Given that the EDO described in Section 5.3 will manage the ESS, a run of

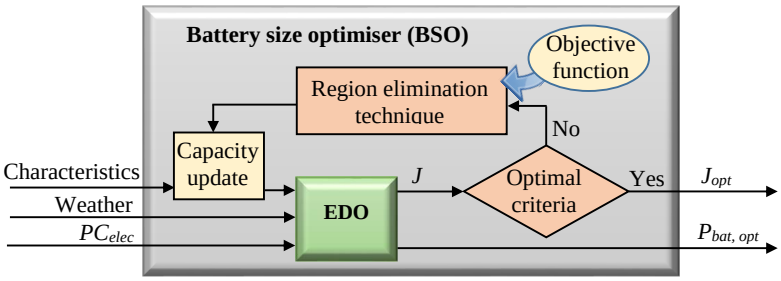

Figure 5.6: Schematic of the battery size optimiser (BSO). Input variables (weather conditions, electricity price and system characteristics), internal tools (EDO, objective function, capacity updater, and the optimisation algorithm consisting on a region elimination technique and a decision algorithm to detect the optimal solution) and output variables (optimal battery power $P_{bat,opt}$ and value of the objective function J_{opt}).

this algorithm is required for each BSO iteration step, as shown in the figure. The objective of the ESS designer must be the same as that of the battery management in order to achieve a rational design. Therefore, the EDO and BSO must have the same objective function (Equation 5.6). The complexity of this optimisation problem is much lower than that of the EDO explained in Section 5.3 because the BSO has only one decision variable (the size of the battery), while the EDO has 24. Therefore, taking into account that the objective function for the BSO is a unimodal function, the Dynamic Program algorithm used for the EDO can be substituted by the straightforward Region Elimination technique and an optimal criteria to detect the iteration at which the optimal value is reached.

Unimodality means that there is only a single highest value. the Region Elimination technique is based on this characteristic of the economical revenue written as a function of battery size, which is concave in the studied interval. This algorithm evaluates the objective function for different values of the independent variable and eliminates regions that cannot host the optimal solution, thereby narrowing the area in which the optimal value for the objective function is reached, as shown in Figure 5.7.

There are several options for the detection of the optimal value, which has to stop the algorithm. Three of the most commonly-used approaches are (i) a given number of iterations is reached, (ii) the difference between the value of J in two successive iterations is lower than a predefined value, and (iii) the optimal area is narrower than a value. Given that simulation time is not a limiting variable for this study, approach (i) was chosen and 10 iterations were calculated for each optimisation problem.

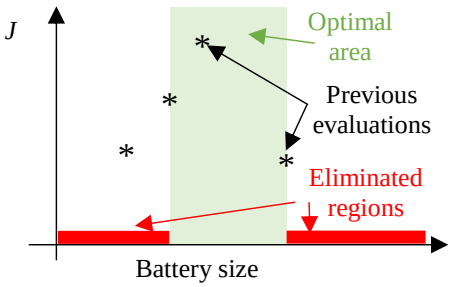

Figure 5.7: Schematic of the optimisation process carried out by a Region Elimination technique. New battery size values are chosen from the optimal area (asterisks in the figure), the objective function is evaluated and this area is narrowed.

5.5 Analysed scenario

Our aim with this section is to establish a realistic and fair scenario that allows us to show the potential of the optimisation techniques described in this chapter. As covered in Section 6.1, lithium-ion batteries are currently experiencing a fast price decrease due to technology learning, RD&D and mass production mainly for the electric vehicle market. Current prices of about \$ 220 kWh^{-1} are realistic, and prices between \$ 100 kWh^{-1} and \$ 125 kWh^{-1} are also expected for 2020 or 2022 [CAZ16, BRA16].

Therefore, given the current market prices, Li-ion batteries already have the potential to reduce the cost of the electricity grid [NOT13]. Moreover, taking into account the expected development of the technology for the near future, their benefits will be greater during the following years. However, not many Li-ion battery systems are connected nowadays to the grid. This fact is due to outdated market regulations and incentive plans, which do not allow interesting business models based on energy storage systems or fail to suitably remunerate some grid services such as frequency regulation, voltage support, resource adequacy, grid investment deferral, etc. [LEH16, LOM17]. There are nowadays a few incentive plans aimed at increasing the amount of distributed electricity storage connected to the grid, such as the German *KfW-Programm Erneuerbare Energien "Speicher"* [SAU13].

The key parameters of the proposed fair, near-future scenario are described below. It is remarkable to note that the sole purpose of this scenario is to set the required conditions to show the functionalities of the battery optimisation technique. Our aim is not to predict the future market trends nor to state whether the installation of a Li-ion battery is profitable or not.

- PV field size: As already mentioned in the introduction, a 100 kWp PV plant was chosen as the studied scenario. Therefore, because of the slight oversize of the PV field compared to the inverter, a 115 kWp PV field is considered to be connected to a 100 kW PV inverter.

- Type of installation: 100 kWp is the typical size of a PV plant mounted on the roof of a factory, which is usually connected to the distribution grid. Industrial areas are electricity consumers and distributed generation in these grids is desirable to reduce the grid power requirements and transport losses. However, during low-consumption periods, such as weekends or holidays, this grids can suffer from generation overload. In this context, a PV+ plant can bring important benefits.

- Grid power limitation: Based on the conclusions of the research works mentioned in Section 6.1 [STE14, PÉR16], a fed-in power limitation for the PV+ plant is considered for this scenario. Following the guidelines established by the German *KfW-Programm Erneuerbare Energien "Speicher"*, this limitation is set to 60% of the peak power ($P_{grid} \leq 0.6 \cdot P_{PV,\ peak}$, or $P_{grid} \leq 60$ kW), as shown in Figure 5.8 (a). As can be seen in this plot, there is part of the available PV energy (P^*_{PV}) from 10:00 to 15:00 that cannot be directly fed into the grid. Moreover, the grid power usually has also a lower limit. Given that PV plants are generators, typical grid codes prevent them for taking power from the grid, therefore, $P_{grid} \geq 0$.

- Meteorological data: With the aim of increasing the veracity of the scenario, measured meteorological data from year 2016 were used. Specifically, the online free-access database called Meteonavarra [AEM] was used. The data were recorded by a weather station named *Bardenas*, which is located in the north of Spain (42.2º N, 1.58º W), in a region with an annual irradiance of around 1700 kWh m^{-2}. This location was chosen because of its average climate conditions and annual irradiance. The available PV power on 2 October 2016 is plot in Figure 5.8 (a). It was a mostly-clear day, as can be deduced from the characteristic bell-size PV availability. The nominal power (100 kW) is not reached even during the central hours of the day. This is due to the time of the year, given that the Sun does not reach high elevation at the studied latitude in October.

- Electricity price: In most of the electricity markets, the price of energy varies along the day following the supply–demand rule. It is interesting to analyse the optimisation tool under realistic, variable electricity

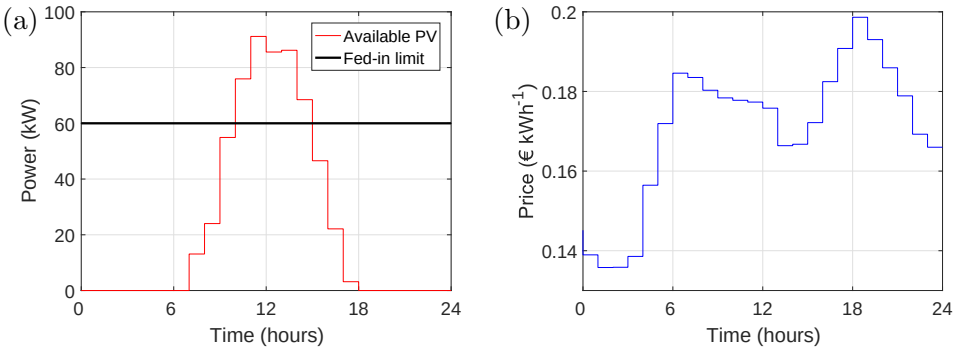

Figure 5.8: Most remarkable scenario variables on 2 October 2016: PV available power and grid fed-in power limit (a), and market electricity price along the day (b).

price. However, as mentioned above, there are grid services that are not properly remunerated with the current market rules. Therefore, the real electricity price in Spain during the year 2016 was scaled to an average price of € 0.14 kWh^{-1} keeping the actual variability of the market prices, as shown in Figure 5.8 (b) for 2 October 2016. The price followed a typical daily pattern this day, in which the price during night time is lower than during the day, and it reaches two peak values, one in the morning and the highest one in the evening, due to increased electricity demand. It is noticeable that the electricity price during this day was higher than the average annual price, which is € 0.14 kWh^{-1}.

- Battery price: A price of € 250 kWh^{-1} for the battery system (including battery bidirectional power converter) is considered. This price is lower than the system cost in the current market, but, based on the market evolution expectancies, can be a realistic approach for the near future.

- Figure of merit: For the sake of comparability between different results, a figure of merit needs to be defined. The higher the figure of merit of an scenario, the more attractive the scenario is. Given that the objective of the proposed method is to maximize the economical revenue, and that the required investment to acquire the battery and the savings achieved take place in different time spots, the Net Present Value (NPV) is chosen as the figure of merit. This magnitude is defined by the equation proposed by [DUF15]:

$$NPV = -Cost_{bat} + \sum_{k=1}^{Life} Rev \cdot \frac{(1+g_{elec})^k}{(1+IR)^k} - Cost_{O\&M} \frac{(1+g_{O\&M})^k}{(1+IR)^k} \quad (5.7)$$

where $Life$ is the life time of the battery expressed in years, Rev is the

annual profit achieved by the inclusion of the battery system, $Cost_{bat}$ is the battery cost and $Cost_{O\&M}$= € 1 kWh^{-1} year^{-1} is the annual operation and maintenance cost, all of which depend on the system design and management. The other variables from Equation 5.7 are economical magnitudes, which values are suggested by [DUF15] as follows: g_{elec}=3% is the inflation for electricity prices, $g_{O\&M}$=2% inflation for O&M costs and IR=4% is the interest rate.

5.6 Usefulness of the optimisation tool

As mentioned in Section 6.1, some research works that analyse the optimisation of battery systems are focused either on the battery size optimisation [MUL13], not paying special attention to the management strategy, while others analyse the best strategy to achieve an optimal energy management [KIM15b] but the studied battery is not optimally sized to achieve the best results. However, both optimisation processes are the two sides of the same coin and need to be faced accordingly. A comparison is presented along the following subsections, where the usefulness of the battery size optimisation and that of the energy dispatch optimisation are separately analysed based on the NPV, figure of merit described in Section 5.5 by means of Equation 5.7. Besides, the battery lifetime and the investment payback are provided to support the comparison of different options. The economical terms used in this section are defined in the following lines for the reader's convenience.

- **Profit**: is the difference between the money earned with the PV+ plant and that earned with a simple PV plan (no ESS) during the analysed period of time:

$$\text{Profit} = \sum_{t=0}^{t_{max}} (P_{grid,PV+} - P_{grid,PV}) \cdot PC_{elec} \tag{5.8}$$

- **Payback**: is the time (years) required to pay for the battery investment using the obtained profit.

$$\text{Payback} = \frac{\text{Battery price}}{\text{Annual profit}} \tag{5.9}$$

- **Revenue**: is the net income money resulting from an investment which can be given as an annual quantity or the total amount during the lifetime of the investment.

$$\text{Total revenue} = \text{Total profit} - \text{Battery price} \tag{5.10}$$

- **NPV**: As defined in Section 5.5, it has similarities with the revenue, but takes into account the time value of money.

5.6.1 Energy dispatch optimiser

The energy management of an already-existing PV+ plant is tackled in this subsection. The analysed PV plant is the one described in Section 5.2, with a peak power of 100 kWp, installed in the scenario proposed in Section 5.5. The battery of the PV+ plant needs to be sized in order to perform this comparison. Since the battery size optimiser is not analysed in this subsection, an arbitrary size is chosen for the analysis. The obtained results are compared in Subsection 5.6.2 with an optimally sized ESS. In order to have a reasonable battery, the size proposed in [KIM15b] (1 kWh per kWp) is taken, which means a 100 kWh battery pack. The results obtained by the following two management strategies are compared through a simulation of the PV+ plant performance during the whole lifetime of the battery.

- **Intuitive algorithm**:
  The battery is charged when there is a PV energy surplus, and discharged during the hour with highest electricity price. If one hour is not enough to fully discharge the battery because of system constraints, the discharging process will also take place during the hour with second highest electricity price, as shown in Figure 5.9 (a) and (b).

- **Energy Dispatch Optimizer**:
  The EDO method proposed in Section 5.3 which optimises the objective function expressed in Equation 5.6, as shown in Figure 5.9 (c) and (d).

Actually, the difference between both energy management strategies can be appreciated in Figure 5.9, in which the energy dispatches calculated by both algorithms and the resulting battery SOC on 2 October 2016 are shown. The battery SOC limits are set to 10% and 95%, which is a common practice to reduce battery ageing while using the majority of its energy capacity. The intuitive algorithm (Figure 5.9 (a) and (b)) charges the battery when the available PV power surpasses the maximum grid fed-in limit, and keeps the charging mode until the battery is fully charged (10:00 h.–14:00 h.), as can be seen in the SOC plot shown in Figure 5.9 (b). Between 13:00 h. and 15:00 h. there is an amount of energy that is available from the solar radiation, but cannot be generated, since it cannot be fed into the grid (because of power limit) nor stored in the battery (because it is already full). The battery remains fully charged from 14:00 h. to 18:00 h. and then, the battery discharging takes

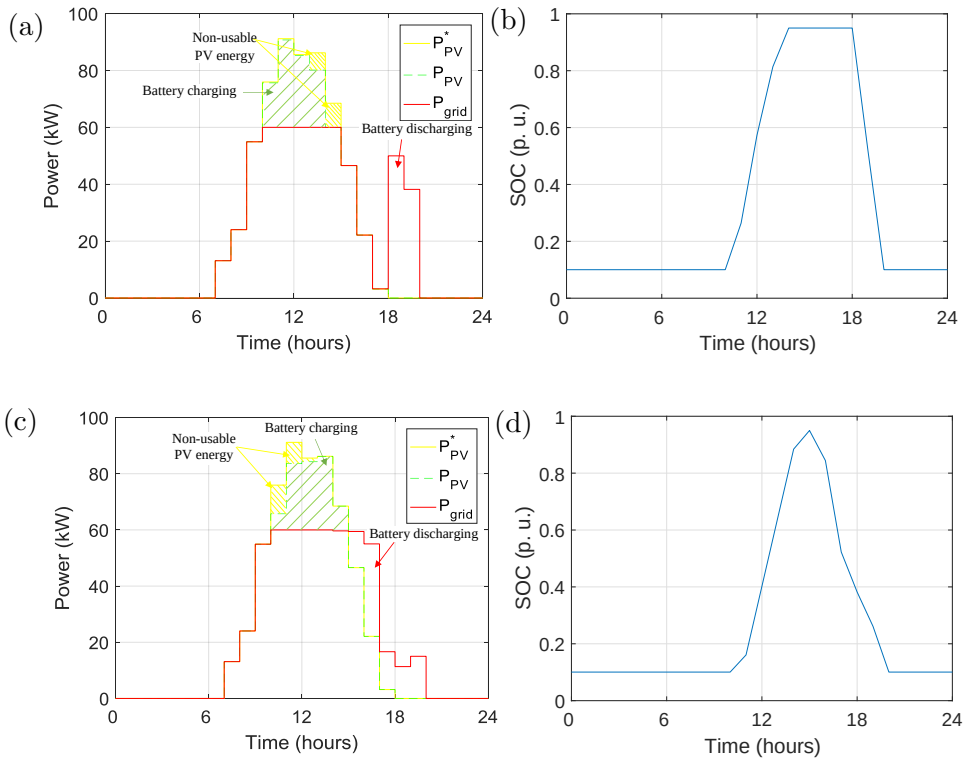

Figure 5.9: Energy dispatch and battery SOC on 2 October 2016 calculated with two algorithms: Intuitive charging and discharging (a) and (b) and proposed EDO (c) and (d).

place in just two hours, from 18:00 h. to 20:00 h., which are the two hours with highest electricity price, as shown in Figure 5.8 (b). Analogously, the EDO algorithm, whose power dispatch plan and battery SOC are shown in Figure 5.9 (c) and (d) respectively, also charges the battery when there is extra PV power available, and there is also an amount of the available PV energy that has to be discarded because of a lack of battery capacity and grid fed-in maximum power. However, the charging process programmed by this method is slower than the one designed by the intuitive algorithm, lasting from 10:00 h. to 15:00 h., which allows for a lower battery charging current, thereby limiting the battery ageing mechanisms. Moreover, the surplus energy is discarded during the first three hours of extra PV power (10:00 h.–13:00 h.), reducing the time at which the battery is kept at maximum SOC (and voltage), which also limits the ageing reactions. Finally, the battery is discharged from 15:00 h. to 20:00 h. at variable current rate. Even though the revenue obtained with this electricity is lower than the one achieved by the intuitive algorithm

(because of lower electricity prices, see Figure 5.8 (b)), the battery is kept at maximum SOC during a shorter time and it manages a lower discharging current, thereby enlarging its lifetime and reducing the battery ageing costs.

The PV+ plant was simulated with both energy dispatch strategies until battery end of life (EOL). Given that the amount of available PV energy does not have significant year-to-year variations, the conditions of the year 2016 were repeated the required number of times to analyse the complete ageing process of the battery. The battery EOL is assumed to happen when either the battery capacity fades to 80% of the initial value or its impedance rises to 120% of the initial value. The results of these simulations are summarized in Table 5.1. As it was expected, the intuitive algorithm reaches the highest annual profit (€ 3435 vs. € 2874 of the EDO), since the battery is charged when there is available energy, and discharged when the electricity price has its maximum value. Therefore, given that the battery size (and price) are the same for both cases, the payback period is shorter for the intuitive algorithm (7.2 vs. 8.7 years). However, while the battery ageing mechanisms are taken into account in the objective function of the EDO (Equation 5.6), it is not the case for the intuitive strategy. Therefore, based in the battery ageing model proposed in Section 5.2, the battery lifetime is sensibly longer when managed by the EDO (13.7 years) than with the intuitive algorithm (6.9 years). For this reason, higher total revenue can be obtained if the battery is managed by the EDO and the Net Present Value of the system is higher. Actually, if NPV is the chosen figure of merit, the investment in this battery system is profitable when managed by the EDO (NPV= € 10 448) and not when managed by the intuitive strategy (deficit of € 1090). As in most investment analyses, the NPV, which takes into account the time value of money, is lower than the total revenue given that the acquisition expenses are done at the beginning of the lifetime of the system and annual profit take place during the following years.

Table 5.1: Figures of merit for two energy management strategies for a 100 kWh battery (battery cost of 25 000 €).

Strategy	Intuitive	EDO
Average annual profit (€)	3335	2774
Payback (years)	7.2	8.7
Battery lifetime (years)	6.9	13.7
Total revenue (€)	–1000	13 870
NPV (€)	**–1090**	**10 448**

5.6.2 Battery size optimisation

The EDO algorithm analysed in the previous subsection is proposed to be combined with a battery size optimiser (BSO) whose performance will be quantified through this subsection. We proved in the previous subsection that the results obtained when the EDO is used to manage a PV+ plant are better than if it is managed by an intuitive algorithm. However, if the size of the battery is chosen according to the objective function (as explained in Section 5.4), there is a further improvement potential in the NPV of the investment. In order to quantify this improvement, two designs of the PV+ plant, with different battery sizes, are simulated. On the one hand, the dispatch plan for a 1 $\mathrm{kWh\,kWp^{-1}}$ battery pack is calculated using the EDO, which is the optimisation already presented in Subsection 5.6.1. It is compared, on the other hand, with the performance of a battery with its optimal size calculated by means of the BSO method previously proposed in this chapter. The optimisation process of this BSO algorithm, with its ten iterations, is shown in Figure 5.10. The value of the objective function for the ten battery sizes are represented by markers. The Region Elimination technique explained in Section 5.4 achieves a relatively fast approach to the optimal battery size, which is 1.785 $\mathrm{kWh\,kWp^{-1}}$.

The optimal energy dispatch and battery SOC for the 2 October 2016 calculated by the EDO for the PV+ system with a battery size of 1.785 $\mathrm{kWh\,kWp^{-1}}$ is shown in Figure 5.11 for its comparison with Figure 5.9. The power dispatch (Figure 5.11 (a)) shows that almost the whole available PV energy is used either to be fed into the grid or to charge the battery. Given that the battery is larger than the one analysed in Figure 5.9 (c) and (d), there is enough capacity to store the surplus energy from 10:00 to 15:00 reaching a battery maximum SOC of 66%. After this charging, the battery discharge is programmed to take place during the afternoon (from 15:00 to 20:00). This slow discharging process results in lower battery current and, therefore, reduced ageing effects.

The figures of merit for the PV+ plant optimally managed with both battery sizes are shown in Table 5.2. The first column, corresponding with the battery size of 1 $\mathrm{kWh\,kWp^{-1}}$ coincides with the second column of Table 5.1, since both are the same scenario. Both results summarized in Table 5.2 are profitable based in the proposed models, since they have positive NPV. The result obtained by the BSO algorithm is a battery size almost 80% larger than the previously analysed 1 $\mathrm{kWh\,kWp^{-1}}$. The result is that the required investment (battery price) is also 80% larger, which allows a less intensive use of the battery, prolonging its lifetime from 13.7 to 16.42 years. Besides, given that more battery capacity is available, a lower amount of PV energy

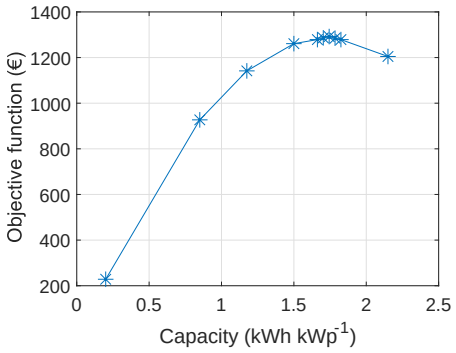

Figure 5.10: Optimization process of the proposed BSO with a Region Elimination technique. The objective function, which is the average annual revenue, is shown in Equation 5.6.

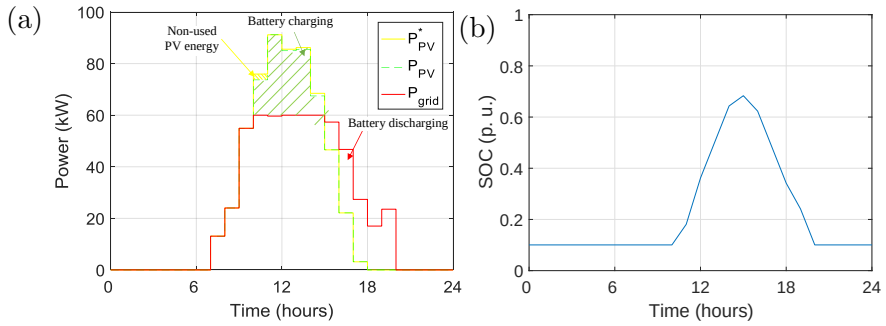

Figure 5.11: Energy dispatch plan (a) and battery SOC (b) on 2 October 2016 calculated with the EDO algorithm for a PV+ system with a battery sized by means of the BSO algorithm.

must be discarded, thereby increasing the annual profit of the system. As it was expected, the total revenue, which is the objective function of the BSO, increases from 13 870 € to 20 178 € when this algorithm is used to size the battery, resulting in an increase of 28% in the NPV.

Depending on the investor's interest, the second option can look less attractive than the first one, as an increment of 80% in the investment brings only an increase of 28% in NPV. However, as explained in Section 5.3 and Section 5.4, the objective function for this study is the total revenue of the investment, and the best result is obtained by the combined use of the BSO and EDO, as reported in the second column of Table 5.2. The customization of this optimisation method for the interest of each individual investor can be easily done by modifying the objective function (Equation 5.6), but this

Table 5.2: Figures of merit for two battery sizes for a 100 kWp PV plant managed by the proposed EDO.

Battery size ($kWh\,kWp^{-1}$)	1	1.785
Battery price (€)	25 000	44 625
Average annual profit (€)	2774	3822
Payback (years)	8.7	11.14
Battery lifetime (years)	13.7	16.42
Total revenue (€)	13 870	20 178
NPV (€)	**10 448**	**13 400**

analysis is out of the scope of this work.

5.7 Sensitivity analysis

As an application of the battery optimisation method proposed in this chapter, a sensitivity analysis is presented in this section. In this context, a sensitivity analysis provides information about the most critical variables that need a close analysis for the calculation of PV+ plat profitability. It can help answering questions such as: is a 10% reduction in battery price more or less profitable than a 10% increase in electricity prices for a PV+ plant?, or which variable should I look more carefully for the design of my system, average electricity price during the year or the difference between maximum and minimum daily price?

The chosen sensitivity method is the variation of one factor at a time, which consists of setting a standard scenario (the one described in Section 5.5 and used in Section 5.6), defining the studied variables and moving the value of one input variable, while the others are kept at their nominal point. After that, the variable is returned to its rated value and the process is repeated for the next input variable. Sensitivity is then measured by monitoring changes in the output, as any observed change will unambiguously be due to the single variable changed. Three magnitudes are chosen as input variables for the sensitivity analysis: (*i*) average electricity price, whose variation is shown in Figure 5.12 with green, dash-dot line, (*ii*) electricity price range, shown in Figure 5.12 with red, dashed line, and (*iii*) battery price. The variation interval around their rated values (defined in Section 5.5) is set to ±20% with a total of seven points (0.8, 0.9, 0.95, 1, 1.05, 1.1 and 1.2 times the nominal value). The output variable, whose changes are analysed, is the NPV.

The results of a sensitivity analysis are usually displayed in graphs with the input parameter, whose influence in the system is being studied, represented

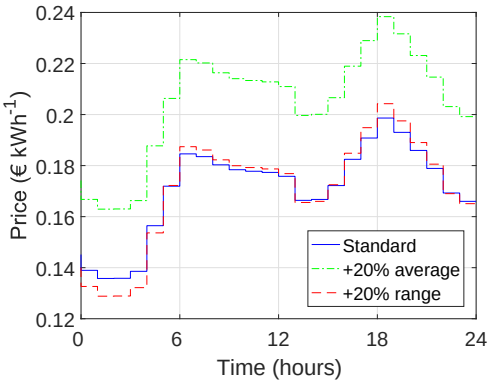

Figure 5.12: Electricity price variables during the 2nd of October, 2016 studied in the sensitivity analysis: Standard electricity price, increase of 20% on the average price and increase of 20% in the price range.

in the horizontal axis and the output variable in the vertical axis. For the sake of comparability, both values are usually normalised, being (1, 1) the central point of each plot. Besides this plot, a numerical value of the average sensitivity is also useful for easy and accurate comparison of different analyses.

The results of the sensitivity analysis for the PV+ plant are shown in Figure 5.13. The circles are the NPV of the simulated system sized by the proposed BSO and managed by the EDO considering different scenarios. A straight line is fitted to these markers, whose slope is the average sensitivity of NPV to each parameter. The nominal point (1, 1) in the three figures corresponds with a NPV of € 13 400, as already reported in Table 5.2, in which the standard scenario is analysed. The absolute value for each input variable in this point are defined in Section 5.5, which are an average electricity price of € 0.14 kWh^{-1}, electricity price range of € 0.23 kWh^{-1} and a battery price of € 250 kWh^{-1}.

A variation in the average electricity price is studied in Figure 5.13 (a). As it is expected, an increase in this input variable results in a greater NPV of the investment. Moreover, the variation in the NPV is more drastic than the one made in the average electricity price. Actually, a 20% increase in the electricity price entails an NPV more than 2 times higher, which means a sensitivity of 5.31, as reported in Table 5.3. Therefore, the average electricity price needs to be closely studied during the design and management of such a PV+ plant, since the variation produced in the NPV of the investment is five times larger than its motivating change in electricity price. Figure 5.13 (b) shows the sensitivity of NPV to the electricity price range. The points

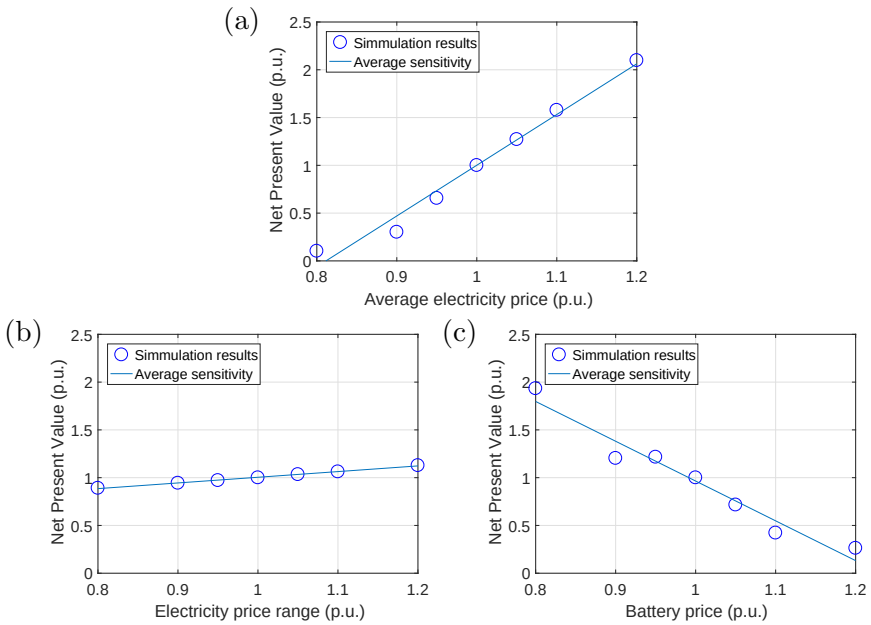

Figure 5.13: Sensitivity analysis of the NPV to three input variables: average electricity price (a), electricity price range (b), and battery price (c).

are much closer to 1 and, therefore, the slope of the line is lower than in the previous case. Actually, a variation of 20% in the electricity price range only brings a change of 12% in the NPV, i.e., the sensitivity is 0.59. Finally, Figure 5.13 (c) shows the sensitivity of NPV to battery price. As expected, it has a decreasing trend, since an increasing battery price entails a decreasingly interesting investment. The slope of the line is –4.16, which is a sensitivity almost as high as that to the average electricity price.

After this analysis, the questions asked before can be answered. A 10% reduction in battery price is actually a bit less profitable than a 10% increase in electricity prices based on this analysis (1.15% less profitable). And for the comparison between average electricity price and electricity price range, more

Table 5.3: Average sensitivity of the NPV in a ±20% interval to three characteristic parameters.

Input parameter	Sensitivity of NPV
Average electricity price	5.31
Electricity price range	0.59
Battery price	–4.16

care should be taken in the analysis of average price, because it actually has a 9 times higher influence on the NPV for the application analysed in this study.

5.8 Conclusion

The optimisation method for the ESS of a PV+ plant proposed in this chapter combines the battery sizing based on an objective function, using a BSO method, with the battery management aimed at optimising the same objective function using the EDO. Both BSO and EDO have been explained with the required level of detail for other researchers to be able to reproduce them, explaining the mathematical optimisation methods, the system operation constraints and the proposed objective function. This objective function has an economical perspective (annual profit of the ESS) and it needs to be the same for the BSO and EDO.

The improvement that the use of the BSO and EDO brings to the PV+ plant is quantified, proving that both of them improve the value of the defined objective function, and their combined use, as proposed through the chapter, maximizes the value of the ESS. Actually, if a reasonable but not optimal battery size is installed (55% of the size calculated by the BSO) and an intuitive algorithm is used to manage it, the value of the objective function is below zero, which means that the set-up of an ESS is not convenient for the involved stakeholders. If the EDO is used to manage this non-optimal battery, the result of the objective function turns into positive, which means that the investment in the same system can acquire interest by a consistent management of the ESS. Moreover, if the BSO is used for an optimal battery sizing, the above-mentioned value of the objective function undergoes a 45% growth.

In order to apply the proposed optimisation method to a realistic case, a reasonable scenario for the PV+ plant in the near future has been proposed. The current evolution of the electricity grids, the development of Li-ion battery technology and the published future perspectives are taken into account in this scenario. A mathematical model is used for each of the component of the PV+ plant, with special care and detail given to the electrical performance and ageing model of the Li-ion battery, whose optimisation is studied in this chapter. Models that have been already published and whose good performance has been validated are used with this purpose.

Besides, a sensitivity analysis is presented in order to analyse the influence that three input variables have in the defined figure of merit of the system, which is the Net Present Value (NPV) of the investment. The three studied variables are average electricity price, electricity price range and battery price.

A variation of the average electricity price has the highest influence on the NPV, given that the NPV deviation is five times bigger than the causing shift in the electricity price (average sensitivity of 5.31). The NPV is also sensible to battery price, even though it has obviously the opposite sign, since an increasing battery price entails a four-times reduced NPV. Finally, the electricity price range has a low influence in the NPV, given that its sensitivity to this variable is only 0.59.

Chapter 6

Extension to supercapacitors: state of the art and modelling

Synergy – the bonus that is achieved
when things work together harmoniously.

– Mark Twain

6.1 Introduction

As covered in previous chapters, Li-ion batteries are currently the most commonly-used ESS for applications requiring a run time of several hours and a moderate power consumption, such as mobile phones, electric vehicles, standalone PV installations and the requirements that electricity grid regulators are placing regarding stability and other grid services. Besides, there are also systems requiring shorter storage times and more peak power, such as a photo camera flash. In these cases, capacitors are usually the most suitable ESS technology. Capacitors use an electric field to store energy and consist in two conductive materials, separated by a dielectric, which are charged with opposite polarities. Given that the electricity is not converted into another form of energy, capacitors have an extremely fast response. This high power capability is also used to improve the integration of electrical systems in the electricity grid. Some examples of this use are the capacitors built into many electronic systems to reduce the current harmonic content fed into the grid, or the capacitors installed in many factories to manage the required reactive power. Although their energy density is low compared with batteries, capacitors are more efficient due to the fact that no energy conversion takes place during

operation. Moreover, given the non-ideal electrochemical reactions, batteries perform fewer charge–discharge cycles than capacitors during their lifetime [SHA10].

Supercapacitors (SCs) are ESSs that bridge the gap between batteries and conventional capacitors with regard to energy and power densities. As shown in the Ragone Plot (Figure 6.1), their specific energy is far higher than conventional capacitors and their specific power is greater than existing batteries. Li-ion batteries are suitable for applications requiring charge–discharge cycles of a few hours (for instance PV self-consumption) and traditional capacitors have optimal performance with cycle times in the order of ms or μs (e. g. power converters). In this context SCs arise as the best option for several applications in which charge–discharge cycle times ranging from a few seconds to several minutes are required, as detailed along this chapter.

SCs can be combined with Li-ion batteries in a hybrid ESS in which synergies between both storage systems are established. Specifically, the long cycle life, fast dynamics and high efficiency of SCs can be exploited in combination with Li-ion batteries to achieve the same performance with a lower inversion or to improve the overall performance of the ESS. This chapter of the thesis is devoted to the analysis of SCs as an advantageous technology to be hybridised with Li-ion batteries. With this purpose, the current state of this technology with an emphasis on its applicability is covered in Section 6.2. Inside this section, the principles of SC performance are covered in Subsection 6.2.2, along with a summary of the most important material characteristics, a classification of SCs based on this information and guidelines for the most suitable SC type based on application requirements. In Subsection 6.2.3, the basic electrical phenomena that can be measured in an SC are explained based on the previously-described principles. This is followed in Subsection 6.2.4 by a description of the main trends in SC modelling, as suitable tools to relate electrochemical principles with electrical performance. This subsection also includes a critical analysis of the suitability of each type of model from different points of view (SC design, manufacturing, design of an energy system, storage system control strategy, etc.). Furthermore, the most commonly-used experiments to characterise the parameters of each type of model are covered, with an emphasis on their strengths and weaknesses in identifying each phenomenon. After this, Subsection 6.2.5 goes on to analyse the key features of currently available SCs and their suitability for each type of energy system. Then, we present a critical analysis of successful and recently-emerged energy applications in which SCs play a primary role as an ESS, with particular emphasis on future trends. The documentation work presented in this section has given rise to a review paper on supercapacitors application that is cur-

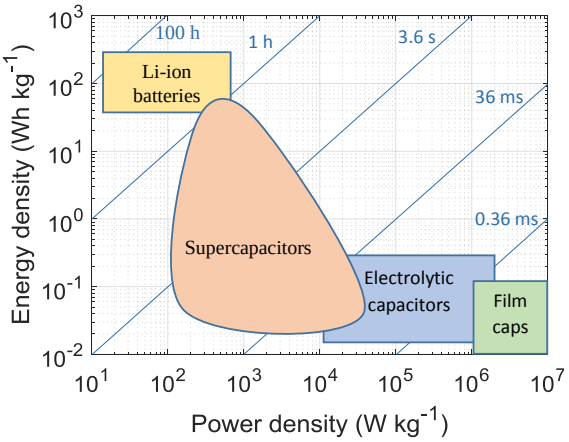

Figure 6.1: Ragone Plot of electrical energy storage systems. Characteristic times correspond to lines with unity slope.

rently under the peer review process needed to be published in an international journal.

After this, in Section 6.3, a SC model is proposed. Following the same criteria used for the Li-ion battery model in Chapter 4, an electrochemical model is built based on physical principles, along with a thermal model able to calculate the SC operation temperature. Each model is represented by an electrical equivalent circuit, making the models easier to understand and allowing them to be readily incorporated into simulation software. This model and the parameter fitting procedure are particularised to a SC model BMOD0083, manufactured by Maxwell [MAXa] with a rated capacitance of 83 F and rated voltage of 48 V. A number of experiments served to validate the electric and thermal models developed for a wide range of operating currents, frequencies and temperatures. The work presented in this section has been published as a research paper in the Journal of Power Sources [BER14].

6.2 Current state of supercapacitors, engineering applications, and future trends

6.2.1 Introduction

A number of terms are used by researchers, manufacturers and users to refer to SCs. Some authors call them electrochemical capacitors (ECs) [LI17d] or electric double-layer capacitors (EDLC) [PAR17], given that an electric field

created in the double layer between the electrodes and the electrolyte is the primary energy-storage mechanism. Since SCs behave similarly to capacitors and are often used to manage high power peaks, other authors call them pseudocapacitors or power capacitors. Ultracapacitors [ZHA15a] and gold capacitors are also names used to refer to SCs. This terminology has its origin in the first commercially available SCs, launched in the late 70s and early 80s by companies such as the Nippon Electric Company (under the name "super capacitor"), Panasonic (commercial name "gold capacitor") and the Pinnacle Research Institute ("PRI Ultracapacitor") [SHA10]. A simple bibliographic search reveals that *supercapacitors* is the most common name.

In recent years, numerous research papers have been published on different SC-related topics, given the evident current need for such a technology, the year-on-year market growth, the growth expectations for the future and the predicted impressive improvement potential [FAR15a]. Many review papers have been published directed at meeting the need to organise and summarise new published research findings. A study focused on SC testing, voltage management and applications was released in 2010 by Sharma and Bhatti [SHA10]. Given the rapid technological development and market expansion experienced since then, updated reviews on complementary perspectives about SCs have been made public. In 2014, Münchgesang et al. [MÜN14] published a brief technology review summarising the physical principles governing the SC performance. One year later, in 2015, Zhong et al. published an extensive review with a particular focus on electrolyte materials for SCs [ZHO15]. In 2015, Zhang and Pan published a review analysing the methods used to evaluate the SC electrical performance, identifying a number of inconsistencies between such methods and proposing the use of comparable and clearly-defined parameters in order to eliminate these inconsistencies [ZHA15b]. In 2016, Wang et al. [WAN16a] analysed the SC storage mechanisms and briefly discussed the characterization process and applications in a review specially focused on SC electrode and electrolyte materials. Meanwhile, also in 2016, González et al. [GON16] published a review paper explaining the basic physics governing the performance of SCs, providing a wealth of information on electrode and electrolyte materials and, finally, briefly describing the most common SC cell configurations and the leading manufacturers.

The aim of this section is to complement these SC reviews from an energy application point of view. For this purpose, the relationship between the SC material properties and their electrical performance is explained using electrochemical principles. After this, the applications where SCs can play a significant role are identified and the main electrical characteristics that need to be analysed for the successful design, selection and control of SCs in these

energy systems are addressed. This chapter can be used as a reference for SC experts, since it summarises the most promising current research trends and publications. Furthermore, researchers working on different topics may also find it useful to read this overview of the current state of SC technology and the possibilities offered by these ESSs.

6.2.2 Fundamentals and types of supercapacitors

The aim of this subsection is to explain the electrochemical mechanisms and the materials involved in SC energy storage process. Furthermore, since the energy is stored on the electrode-electrolyte interfaces, the storage mechanism on each SC electrode needs to be addressed separately. A combined analysis can lead to misinterpretations when the two electrodes in a device are made of different materials. With this aim in mind, the operation principle of SCs is briefly covered in Subsubsection 6.2.2.1 and the energy storage mechanisms used on each of the electrode–electrolyte interfaces are addressed in Subsubsection 6.2.2.2. Subsequently, in Subsubsection 6.2.2.3, a classification of the SCs based on *both* electrodes is presented; and a classification based on electrolyte materials is addressed in Subsubsection 6.2.2.4. Finally, the interaction between the electrodes and the electrolyte of an SC is analysed in Subsubsection 6.2.2.5, summarising the most noteworthy theoretical and experimental studies on this topic.

6.2.2.1 Operation principle

SCs consist in two porous electrodes immersed in an electrolyte. The energy is stored using the electric field created between the electrodes and the electrolyte, as shown in Figure 6.2. Positive charges are coloured in blue and negative charges, in yellow. Ionic charges are represented bigger than electronic ones, since their size is important for the SC performance, as detailed below. Both electrodes are separated by an ion-conductive membrane, which is the central part of the schematic shown in the figure, that allows ion throughput while preventing short circuits between the electrodes.

6.2.2.2 Energy storage mechanisms

A wide range of materials are used to manufacture SC electrodes and electrolytes, thereby determining the energy storage mechanisms occurring in the SC. A knowledge of these processes is critical for the understanding and optimal utilisation of SCs. Two main experiments are performed to characterise an

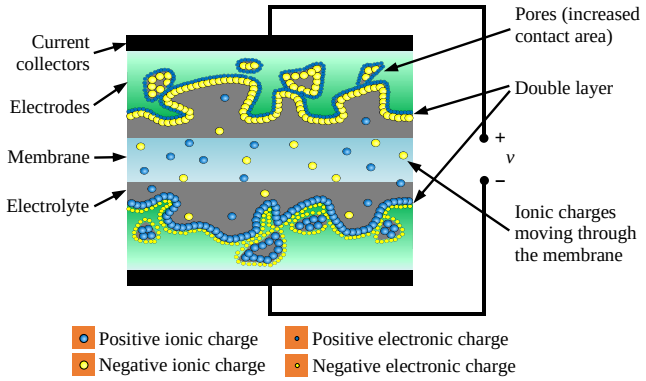

Figure 6.2: Operation principle of a SC cell.

SC electrode, and these are convenient tools to understand the different energy storage mechanisms. On the one hand, cyclic voltammetry (see Figure 6.3 (a) and (b)) is an experiment in which the electrode potential is ramped linearly versus time. When a set potential is reached, it is ramped in the opposite direction to return to the initial potential. The current is measured and plotted against the applied voltage to give the cyclic voltammogram trace. On the other hand, a galvanostatic discharge consists in a constant-current discharge of an electrode. The voltage is measured and plotted against the electrode charge (see Figure 6.3 (c) and (d)). The three basic types of behaviour that SC electrodes can exhibit are explained hereafter. Their properties are compared and contrasted, and the electrical performance of each type of electrode is described based on their cyclic voltammetry and galvanostatic discharge.

Double-layer behaviour The double layer effect consists in an accumulation of two types of charge on the electrode–electrolyte interface, and is the primary storage mechanism in electrodes made of carbon powders, fibres or felts. On the one hand, an excess or a deficit of conduction-band electrons in the electrode, at or in the near-surface region of the interface. On the other hand, counterbalancing charge densities of accumulated cations or anions of the electrolyte on the solution side of the double layers at the electrode interfaces [CON99]. Given that the surface density of these charges, *electrostatically stored* at the electrodes interfaces, depends on the applied voltage, the double-layer capacitance varies with the electrode voltage. The only electrochemical reaction involved in double-layer behaviour takes place at the surface of the electrode and consists in the adsorption and desorption of cations and anions [WAN16a]. Therefore, double-layer capacitance is characterised by rectangu-

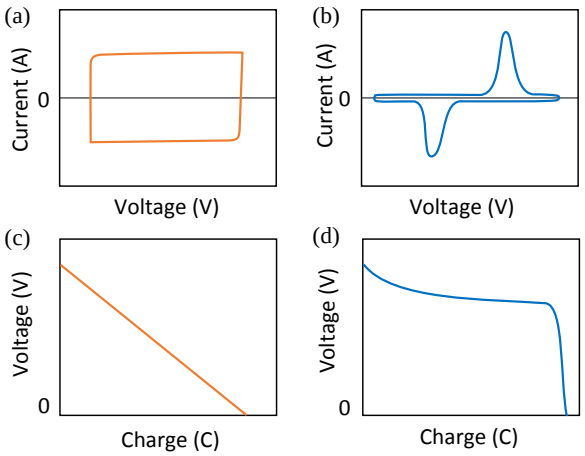

Figure 6.3: Schematic representation of cyclic voltammograms (a and b) and galvanostatic discharges (c and d). Both tests show the difference between capacitor-like behaviour, typical of double-layer and pseudocapacitive mechanisms (represented in orange in graphs a and c) and battery-like (or faradaic) behaviour (represented in blue in graphs b and d).

lar cyclic voltammograms, as shown in Figure 6.3 (a), since the response to a linear change in voltage is a constant current. Moreover, the galvanostatic discharge for this kind of material is linear (Figure 6.3 (c)) [SIM14].

The double layer effect takes place on every interface between electronic-conductor and ionic-conductor materials, which is a typical scenario in most electrochemical ESSs. It is, however, a parasitic effect instead of the primary energy storage mechanism in systems such as electrolysers, fuel cells and batteries [URS12, SAN14, BER15, PIL16]. Conversely, the SC operating principle is based on this property, and its electrodes are designed with the aim of maximising this effect.

Pseudocapacitive behaviour Pseudocapacitance is the result of fast and reversible faradaic charge-storage mechanisms [BRO15]. Although there are similarities between these reactions and battery behaviour since they involve the passage of charge across the double layer, unlike normal batteries, the capacitance is the result of a particular thermodynamic relationship between the extent of charge acceptance and the change of voltage [CON99]. Pseudocapacitive electrodes present a capacitor-like behaviour, since their cyclic voltammogram is similar to the double layer rectangular shape (Figure 6.3 (a)) and they have a linear galvanostatic discharge (Figure 6.3 (c)). In comparison with double-layer electrodes, pseudocapacitive electrodes can deliver a significantly higher specific capacitance, which makes them attractive for

applications requiring high energy density. However, they suffer from two main drawbacks associated with the electrochemical reactions involved: lower power density and weaker cyclability. The reasons for these drawbacks are irreversibility and the dynamics of the electrochemical reactions involved. The irreversibilities induce a faster ageing of the electrode while the reaction dynamics limit its power capability.

The birth of pseudocapacitive electrodes is due to the discovery of the unusual electrochemical behaviour of RuO_2 [TRA71]. Since then, various cheap metal oxides have been studied as potential electroactive materials for pseudocapacitors [CON99, GHO12]. Among the currently-researched metal-oxide materials, iron based oxides and hydroxides are receiving tremendous interest due to their abundance, high specific capacitance and low toxicity [ZEN16]. Both single oxides/hydroxides such as Fe_2O_3 or FeOOH and binary metal oxides such as MFe_2O_4 (with M=Ni, Co, Sn, Mn, Cu, etc.) are currently being researched [XU15, ZEN15] with the aim of obtaining cheap materials with suitable pseudocapacitive properties.

In addition to metal oxides, metal carbides [LI17c] and conducting polymers [KUR16] intrinsically display pseudocapacitive behaviour. The main drawback of conducting polymers compared to inorganic materials is that, even though both have void volume to allow for the intercalation of ions, the spaces of conducting polymers are not big enough to host the ions and the intercalation causes severe volume changes in the electrode. Polyaniline (PANI) is one of the pioneering conductive materials. PANI SCs were first manufactured several decades ago, but no further research was developed due to the problems caused by volume change. Greater attention has been paid to this material over the last few years due to technology advances that have made it possible to combine PANI with other electroactive materials to enhance the electrochemical performance of SCs [EFT17c, WAN14c].

It should be taken into account that the majority of SC electrodes available marginally fall within the pseudocapacitive category due to the presence of functional groups resulting in the occurrence of a pseudocapacitive secondary response [LI16b]. In fact, the electrochemical response of double layer capacitors composed of nanomaterials such as graphene, is partially due to the electrochemical redox systems of electrochemically active groups over the carbon chemical and structural irregularities [EFT17b].

Faradaic behaviour This storage mechanism is based on the redox reactions of metal ions *within* the crystalline structure of the electrode. Usually, metal cations are intercalated and deintercalated, and this process needs to

be coupled with redox reactions involving the electron gain or loss of the electrode material. It should be noted that this mechanism also involves phase transformation and/or alloying reactions, in addition to the passage of charge mentioned in the pseudocapacitive behaviour. The electrode voltage is determined by some singular value by the Gibbs energies of pure, well-defined phases, and usually also the composition and concentration of the solution. Therefore, these materials exhibit a voltage plateau in a galvanostatic discharge (Figure 6.3 (d)) and faradaic redox peaks in cyclic voltammograms (Figure 6.3 (b)). The capacity[1] achieved in Faradaic electrodes is several times (10–100 times) higher than that of capacitive electrodes.

Unfortunately, many battery-type electrodes, such as $Ni(OH)_2$ or other materials, that exhibit faradaic behaviour have been considered as pseudocapacitive materials in many reports, causing confusion for readers [WAN16a]. Even if the redox properties of battery materials are electrochemically reversible, they are much worse than those of pseudocapacitor materials and their charge and discharge power is limited by the ion diffusion within the crystalline framework.

It is noteworthy that the same electroactive materials can deliver either pseudocapacitive or battery-like behaviour. For example, by adjusting the current applied during the electrodeposition of manganese oxide, it is possible to prepare either a battery-like electrode [EFT15a] or a pseudocapacitive electrode [EFT15b]. The difference is due to the lattice structure and nano-architecture of the electroactive material controlling the electrochemical mechanism.

6.2.2.3 Types of SCs based on their electrodes

The most suitable supercapacitor for a system depends on the specific requirements of each application. A classification of SCs highlighting their characteristic properties is a useful tool to correctly select the best SC to be used in each application. This classification based on the electrode material is the one most commonly used to categorize SCs, and it is presented herein with the aim of clarifying the different options available, identifying their advantages and disadvantages, and addressing the critical parameters and characteristics to make a rational selection of SC.

It is important to highlight the fact that the macroscopic behaviour of a given device does not presume the processes that occur at each electrode

[1]Note that *capacity* (C or Ah) and not *capacitance* (F) is the most meaningful metric for the analysis of faradaic materials.

inside the device, and furthermore does not indicate whether individual electrodes are capacitive or faradaic in nature. For instance, an SC formed by a faradaic electrode and a complementary capacitive electrode results in a charge/discharge plot which looks capacitive because it is the combination of a capacitive electrode (triangular shape) and a faradaic one (plateau shape).

As detailed below, SCs can be classified into three main groups: symmetric, asymmetric and hybrid SCs. Confusion sometimes arises from this classification since some authors consider hybrid SCs to be a sub-category of asymmetric SCs. Given the significant difference between hybrid SCs and the other two types of SCs regarding characteristics and performance, and following the criteria established in previous papers [WAN16a, BRO15], three categories of SCs are presented herein. Typical characteristics of each type of SC are summarized in Table 6.1.

- Symmetric SCs: The same double-layer material is used for both electrodes. These are the most commonly used SCs, given the lower cost of the electrodes (typically activated carbon) and their higher maturity [HAD09]. Research in these SCs is aimed at taking advantage of carbon nanotubes [LEI10, EMM14], carbon aerogels [KWO16, SEO16] and graphene [YE16]. Their energy density is relatively low, around 5 $\mathrm{Wh\,kg^{-1}}$, and their power density is as high as 9 $\mathrm{kW\,kg^{-1}}$ [MAL14]. Symmetric SCs are the most suitable option for energy applications in which safety, low maintenance and long lifetime are essential requirements, high power density is also required, but energy density is not a limiting issue.

- Asymmetric SCs: This term is reserved for SCs that use two different *capacitor-like* materials to manufacture the electrodes and can achieve high energy and power densities [WAN16a, CON99]. 30.4 $\mathrm{Wh\,kg^{-1}}$ and 5 $\mathrm{kW\,kg^{-1}}$ were reported for a MnO_2 Nanowire/ Graphene and Graphene asymmetric SC [WU10]. However, these SCs are still relatively expensive and may suffer from lower efficiencies and rated voltage due to the need for aqueous electrolytes [HAD09], as well as from poor lifetime (79% of performance retention after 1000 cycles is reported in [WU10]). Therefore, asymmetric SCs could be suitable for applications in which the compromise between power and energy density is mandatory, and where cost is not a critical issue.

- Hybrid SCs: These devices are composed of a capacitor-like electrode and a faradaic electrode, achieving a higher energy density, reported to reach values of more than 100 $\mathrm{Wh\,kg^{-1}}$ [LIU17a, ZHA13]. By con-

trast, the power density is lower than the values achieved by symmetric SCs, and is around 4.5 $kW\,kg^{-1}$ [MAL14]. The development of this technology is currently much less advanced than that of symmetric and asymmetric SCs. Even though there are already hybrid SCs available in the market [VIN, YUN, MAXa], many papers have been published suggesting new materials and manufacturing processes [CHE15, O'N15]. Recently, many hybrid systems have been reported, such as AC// PbO_2 [ZHA12], graphene//PbO_2 [SOU15], AC//$Ni(OH)_2$ [SUN15], AC//$Li_4Ti_5O_{12}$ [ZHU14] and AC//$LiMn_2O_4$ [LI17b, LIU17b]. Manufacturing methods dedicated to using original raw materials, such as egg white, for the manufacture of hybrid supercapacitors were also suggested [LI16a], obtaining a hybrid SC which shows promising power and energy density characteristics. Only values at material level are given in this paper (only the weight of the electrodes and electrolyte is taken into account). 257 $Wh\,kg^{-1}$ and 867 $W\,kg^{-1}$ (material level) with a performance retention of 79.2% after 15 000 cycles is reported in this paper.

6.2.2.4 Types of SCs based on their electrolyte

- Organic electrolyte: An organic solvent, such as acetonitrile (ACN) or propylene carbonate (PC) is the basic component of these electrolytes. A salt such as Et_4NBF_4, whose organic ions are relatively large, is dissolved in the solvent. These ions should be able to access the electrode pores in order to contribute to the energy storage. Therefore, electrodes with micropores that are not able to host the ions are not suitable for organic electrolytes. Furthermore, the lack of micropores enhances the SC power performance. Their decomposition voltage can be as high as 2.2–3 V [GU14b], contributing to the high power and energy density of the device.

  The most commonly-used organic solvents are PC and ACN, due to their low viscosity, high conductivity and electrochemical stability, making it possible to manufacture high-energy SCs that are able to deliver high power and high cyclic stability [BAL16]. However, there are some safety concerns regarding the AN solvent, which is flammable and toxic [BUR14]. Even though organic electrolytes are widely used, research efforts are currently focusing on the development of new, safe solvents to provide higher energy densities [SCH16]. A solvent with a decomposition voltage of up to 4 V has already been presented [SOE13]. However, the trade-off for this increase in the voltage window is a considerable reduction in the maximum power managed by the SC.

Table 6.1: Key features of the main supercapacitor technologies.

	Symmetric	Asymmetric	Hybrid
Main storage mechanisms	Double layer	Double layer + pseudocapacitance	Double layer + faradaic
Energy density	5 $Wh\,kg^{-1}$	30 $Wh\,kg^{-1}$	100 $Wh\,kg^{-1}$
Power density	9 $kW\,kg^{-1}$	5 $kW\,kg^{-1}$	4 $kW\,kg^{-1}$
Operating temperature	–40 / 80 °C	–25 / 60 °C	–40 / 60 °C
Typical electrodes	Carbon materials	Carbon, metal oxides, conducting polymers	Carbon, intercalation materials
Typical electrolyte	Organic	Aqueous	Organic
Applicability	Commercial	Material research & early commercial	Manufacturing research & commercial
Advantages	Power density, mature, efficient	Trade-off between energy and power	Energy density
Disadvantages	Energy density	Price, efficiency, lifetime	Power density
Challenges	Upgrade carbon porosity and graphene	New materials and volume change in polymers	Manufacturing process

- Aqueous electrolyte: These electrolytes consist of small acid molecules, for instance, H_2SO_4, dissolved in water. Given the smallness of these inorganic ions, electrodes with micropores (diameter around 1 nm) such as T-carbons or carbide-derived carbons are preferred. The decomposition voltage limit of aqueous electrolytes is lower than that of organic electrolytes. Given that water dissociates in H_2 and O_2 at a voltage of 1.23 V, the stability of aqueous electrolytes is limited to a maximum voltage of 0.6–1.4 V [GU14b].

  Research efforts in aqueous electrolytes are focusing on improving their electrochemical properties. The most noteworthy research trends in this respect are, on the one hand, the increase in their decomposition voltage, which has already been reported to be up to 2.2 V [FIC12] by the use of an aqueous electrolyte with high solvation energy. On the other hand, the cycle stability of aqueous electrolytes needs to be improved, and a promising approach is to use a protic ionic liquid as a solute for aqueous electrolytes [HU16].

- Room-temperature ionic liquids: : These materials were initially considered as alternative solvents for aqueous electrolytes, thereby limiting their applicability. However, nowadays, they are known to be an alternative to solid electrolytes and are considered to be a promising

electrolyte due to their operating voltage window, which is even wider than that of organic electrolytes, leading to a very high energy density [EFT17a, COW14, LYU16]. Their components are also less toxic than organic electrolytes [BUZ04], while offering higher thermal stability [ZHA16a, HUD01] and lower volatility [APA10], which increases the maximum operating temperature.

The current high price of ionic liquids is not due to the material itself, but to the necessary purification cost. A better understanding of these materials as an SC electrolyte is expected to lead to less restrictive purity criteria and, therefore, to lower the price of ionic liquid SCs [EFT17a]. These materials are still at an early stage of development and, therefore, a significant research effort is being made to improve their properties. In this respect, two important research trends focussing on ionic liquids for SCs are, firstly, the design and characterization of additives to improve the performance of these devices [LIU16, POH15] and, secondly, the achievement of solvent-free (or solid-state) SCs, offering outstanding ionic transport properties [NEA16, OBE17].

6.2.2.5 Interaction between electrodes and electrolyte

The selection of the electrodes and electrolyte for a particular SC is not independent. There should be a match between the physical properties of both elements in order to maximise the SC capabilities. Regardless of the material or energy storage mechanism (covered above), SC electrodes are porous materials designed to maximise the usable interfacial area S. As shown in Equation 6.1, the larger the area the greater the capacitance and, therefore, the greater the storable energy E, as stated in Equation 6.2. Moreover, given that these devices have no isolating material between the positive and negative charges (contained on the electrode and in the electrolyte), d is a molecular-order distance called Debye length, determined by the size of the electrolyte anions [MIL11]. This small d, combined with the large S, boosts the capacity achieved by SCs compared with conventional capacitors.

$$C = \epsilon \cdot \frac{S}{d} \tag{6.1}$$

$$E = \frac{1}{2} C \cdot v^2 \tag{6.2}$$

where ϵ is the permittivity of the dielectric material and v the SC voltage.

Therefore, the porous structure of the electrode material deserves special attention. Nanopore materials with smaller pores lead to higher surface den-

sities. Currently, electrode materials with surface densities in the order of 1000 m^2g^{-1} can be manufactured [VAQ12]. However, in order to maximize the contact area between the electrodes and electrolyte, the nanopores should be large enough to host solved ions and to thereby actually contribute to the double layer capacitance. According to IUPAC recommendations [ROU94], nanopores are classified according to diameter (Φ) in micropores ($\Phi < 2$ nm), mesopores (2 nm$< \Phi <$ 50 nm) and macropores ($\Phi >$50 nm). When manufacturing SCs, the most suitable size depends on the electrolyte. When the electrolyte comprises small acid molecules (e. g. H_2SO_4) and water as a solvent, micropores with a diameter close to 1 nm, such as T-carbons or carbide-derived carbons, are desirable. On the other hand, when an organic electrolyte is used, whose ions are considerably larger, then mesoporous electrodes are preferred,enabling faster ion access and thereby increasing the SC capacitance for higher charge and discharge currents. In fact, a number of experimental studies confirm the better performance of mesoporous electrodes with organic electrolytes while microporous electrodes are more suitable for acid electrolytes [VAQ12]. Therefore, the usable double-layer surface of an SC with an aqueous electrolyte is higher than that of an organic SC, with the associated capacitance improvement. However, the decomposition voltage of aqueous electrolytes is lower than that of organic materials. Organic materials are typically chosen as SC electrolytes taking into account the fact that, while the energy stored in an SC (E) is linearly related to C, it has a quadratic correlation with v, as expressed in Equation 6.2 [BAL16].

Currently, intensive research is being conducted in materials science and engineering, focussed on achieving the highest uniformity and accuracy in pore size. The authors of a recently-published study [XIO16] propose a manufacturing method based on a nickel (hydro)oxide foam which, according to the reported results, achieves a good distribution in pore size. Other authors [TAN16] propose the use of salt, so that the electrode material crystallises around the salt ions, which are then removed using water. Surface areas as high as 1400–2100 $m^2\,cm^{-3}$ have been recently reported for different electrode materials and manufacturing processes [YAN16b, BHA15, KUN15]. Moreover, significant research efforts are devoted to achieving electrodes for organic and ionic liquid electrolytes with higher surface areas. Graphene-based electrodes with an active area of up to 3100 $m^2\,g^{-1}$ have been published [ZHU11].

6.2.3 Electrical performance of supercapacitors

Following the analysis of the main electrode and electrolyte material properties performed in Subsection 6.2.2, we will now go on to discuss the electrical

implications, disclosing the reasons for the most noteworthy electrical phenomena and analysing their impact on the SC performance, when it is part of an energy system. Greater attention should be paid to one aspect or another, depending on the particular requirements of each application, as covered in the following subsections.

6.2.3.1 Voltage-dependent capacitance

Variable capacitance is one of the characteristic features of SCs. Although it is usually not critical to the SC performance, since it does not represent a significant feature loss, it does need to be taken into account when the SC is part of an energy system. This is due to the fact that the capacitance variation through the entire voltage range has been reported to be between 15% and 20% of the rated capacitance [BER14], a figure that cannot be disregarded in most designs.

Capacitance is a magnitude that measures the amount of stored charge (q) for a given voltage difference (v):

$$C = \frac{q}{v} \tag{6.3}$$

This magnitude is of particular interest in traditional capacitors given that, as shown in Equation 6.3, it is a characteristic property that relates charge stored in a device to its terminal voltage. However, the distance between charges in the double layer of an SC, d, lies on the atomic scale, and an increase in the voltage applied to this double layer intensifies the electric field in this zone, thereby increasing the force of attraction. This effect induces an increase in the density of stored charge, which means that the SC capacitance increases in line with the applied voltage. As a result, since C is a voltage-dependent parameter, Equation 6.3 does not offer the same advantages as when working with conventional capacitors. This is the reason why differential capacitance C_{dif} is a preferred parameter when studying SCs. C_{dif} is defined as the ratio between the increase in the stored charge dQ and the induced voltage variation dv:

$$C_{dif} = \frac{dq}{dv} = \frac{i \cdot dt}{dv} \tag{6.4}$$

Capacitance C and differential capacitance C_{dif} refer to the same property of an SC: the relationship between stored charge and voltage. Even though C is the parameter used to define conventional capacitors, C_{dif} is often chosen to describe SCs. The mathematical correlation between C and C_{dif} depends on the expression used to relate C to voltage v. If a linear dependency is assumed ($C = C_0 + kv$) — which is a typical approach in the literature [ZUB00, LAJ07,

BER14] — then the correlation between C and C_{dif} can be deduced from the following expression of current i:

$$i = \frac{dq}{dt} = \frac{d\,(C \cdot v)}{dt} \tag{6.5}$$

Substituting the linear expression for C_{dif}:

$$i = \frac{d\,((C_0 + k \cdot v) \cdot v)}{dt} = (C_0 + 2 \cdot k \cdot v) \cdot \frac{dv}{dt} \tag{6.6}$$

and using the relationship shown in Equation 6.4:

$$C_{dif} = C_0 + 2 \cdot k \cdot v \tag{6.7}$$

Therefore,

$$C_{dif} = C + k \cdot v \tag{6.8}$$

In addition to voltage dependency, temperature is a factor that may affect the capacitance of an SC. One of the main advantages of SCs is their good performance in extreme temperatures. However, the variation in the capacitance value produced by such large temperature fluctuations may require attention for the proper design of the energy system. Given the fact that a temperature increase causes a growth in the Brownian motion of the ions forming the double layer, there is a larger gap between the positive and negative charges in this double layer with increasing temperature, which leads to a decrease in capacitance [BRA07, GUA03, MIC06]. In fact, a capacitance loss of around $0.1\%\,{}^{o}C^{-1}$ has been reported [BER14]. Assuming a temperature variation of 80 °C, this means an 8% of divergence in C. Temperature usually has a lower impact than voltage on the value of C but may require attention for a system designed to operate outdoors.

6.2.3.2 Charge distribution along the electrode surface

The importance of a match between the size of the electrode pores and electrolyte ions has already been highlighted in Subsubsection 6.2.2.5. Nonetheless, it is important to point out that the solvents used in most electrolytes are polar (usually water as an inorganic liquid or an organic solvent such as acetonitrile). This polarity leads to molecular interactions with the solved ions and therefore ion solvation, which is an association process between solvent molecules and solute ions, as represented in Figure 6.4 [HAD09]. This process takes place in solvents with polar molecules since their partial charges are oriented towards ions, as a result of electrostatic attraction, thereby stabilising the system. The importance of the match between pore size and ion diameter is also shown in Figure 6.4. Pores with a Φ that is less than that of

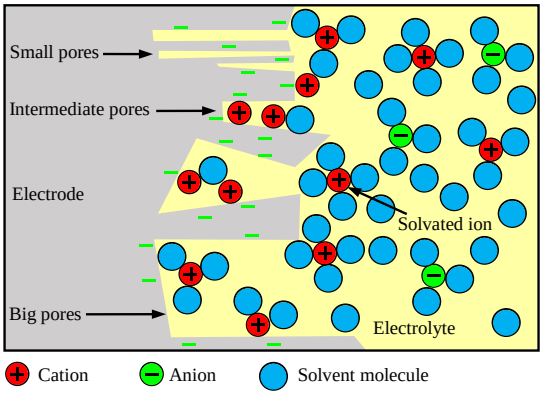

Figure 6.4: Desolvation of ions to access small electrode pores [BER14].

the electrolyte ions are too small to allow access and make no contribution to total capacitance. While those pores with a Φ that is greater than that of the solvated ions are totally accessible to the ions, and intermediate pores with a Φ between that of the solvated and non-solvated ions are available to the electrolyte ions that have undergone a desolvation process [DAF10]. In this respect, in order to allow the ions to penetrate these intermediate pores, there is a need to break down the intermolecular forces established between the ions and the solvent molecules, a process which has its own dynamic behaviour and requires energy.

Charge distribution processes have special relevance in applications requiring fast and deep charge–discharge cycles. In these situations, the SC provides its full power capability; however, the effect of these solvation dynamics is that it is not possible to fully charge or fully discharge at this high-current rate. The proportion of surface area that requires some degree of ion solvation and desolvation in a typical SC has been reported to be around 20% of the total electrode–electrolyte interface area [BER14].

6.2.3.3 Ohmic phenomena

Electronic and ionic charge transport occurs during the SC charging and discharging process [GUA03]. On the one hand, the Joule effect takes place in the electron conductors, whereby part of the electron kinetic energy is converted into heat due to friction with the conductor material. On the other hand, during the ionic charge transport process taking place in the electrolyte, part of the ion kinetic energy is converted into heat due to friction with the other atoms in the dilution. The voltage required to overcome both dissipative phe-

nomena is proportional to the number of charges transported and, therefore, to current. This proportionality results in both these effects being grouped together and called ohmic phenomena.

Temperature variation has opposite effects on these two phenomena. For the solid electrode, an increase in the operating temperature implies the greater vibration of the atoms which, in most cases, results in an increased Joule effect with temperature. While, in the liquid electrolyte, it provokes an increase in the molecule mobility, resulting in a decrease in viscosity, implying a reduction in dissipated energy [FLE10]. Some studies show that the weight of the ionic charge transport is considerably higher than that of the electric charges in the SCs [MIL11], therefore, a temperature increase results in decreased ohmic phenomena.

Ohmic phenomena have a minor impact on SCs when compared to other electrochemical ESSs such as batteries. However, given the high power managed by SCs in typical applications, attention should be paid to this issue. On the one hand, ohmic phenomena provoke a voltage drop, which means a decline in SC energy efficiency. Since a significant advantage of SCs is their high efficiency, ohmic losses can take on a primary role in applications in which this parameter has the utmost importance. On the other hand, the dissipated heat needs to be evacuated in order to avoid danger due to overtemperature, which may require particular attention with regard to outdoor applications or SCs placed close to other heat sources.

6.2.3.4 Electrical self-discharge

Self-discharge is one of the main drawbacks preventing SCs from being used to store energy for times of more than 30 minutes. In fact, the authors of [RIC00] quantify the energy lost during the first two hours of storage as 36% of the useful energy stored in the SC. The main self-discharge mechanism in SCs is current leakage through the ion-conductive membrane separating both electrodes. The self-discharge effect is shown by a linear decrease in the SC voltage over time.

The SC self-discharge is one of the aspects that need to be improved and a number of research works have been published on this topic. In the same paper, some authors study self-discharge behaviour, and ionic charge distribution in electrode pores [HAO16, SHE16, SPE14]. Note that charge redistribution is measured as a nonlinear evolution of SC voltage over time during the first minutes or hours of voltage stabilisation. However, this process does not provoke a discharge in the SC, since the electrical charge is still available in

the SC even though the voltage is lower because more electrode surface area is used to build the double layer [FLE14b]. The authors of [RIC00] rule out the self-discharge faradaic reactions as the reason for the nonlinear voltage change in SCs for two main reasons: (*i*) the v–$\ln t$ relationship does not have the characteristic linear trend of a faradaic reaction and (*ii*) the voltage at which this trend is measured is well below the decomposition voltage of the electrolyte.

Research works have also been published in which SC performance is enhanced by reducing self-discharge, proposing a 1.5 nm polyphenylene oxide (PPO) coating for the electrodes which is able to reduce the leakage current by 78% [TEV13, TEV15]. The drawback of this proposal is that the specific capacitance and energy storage density is also reduced by 56%. Other authors [YAN16a] assume this limitation imposed by self-discharge and propose management strategies in order to minimise the wasted energy.

6.2.3.5 High-frequency behaviour

Supercapacitors are usually used for fast charge–discharge cycles, given their outstanding performance in these applications. Cycles lasting from tens of seconds to ten minutes are harmful to other ESSs such as batteries and hydrogen based systems, while SCs show their best performance within these timeframes. However, given that the charge and discharge processes involve the movement of ions through the electrolyte (mass transport), they are not able to manage frequencies as high as those managed by conventional capacitors. The usable capacitance C_u (or equivalent capacitance) loss with increasing frequency has been studied in several papers [RAF07, BER14], reaching the conclusion that the usable capacitance of an SC has the behaviour shown in Figure 6.5. There is a cut-off frequency (which depends on the SC materials and manufacturing process, but it is usually around 1 Hz) where the device capacitance drastically decreases and no capacitive behaviour is measured for higher frequencies. This is the reason why SCs cannot be used to filter the harmonic components of an electronic converter (several kHz). However, there are applications where intermediate frequencies need to be filtered, for instance, the harmonics produced by diode rectifiers (hundreds of Hertz). The use of SCs in these applications has also been studied [MIL10], concluding that graphene electrodes are required in order to have a usable capacitance at this frequency range. Therefore, the cut-off frequency shown in Figure 6.5 for a graphene SC is in the order of hundreds of Hertz.

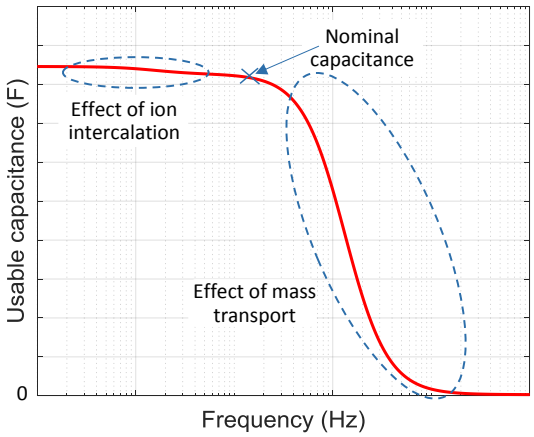

Figure 6.5: Equivalent capacitance as a function of frequency.

6.2.3.6 Efficiency

Two efficiencies are usually addressed when working with electrochemical energy storage systems, which are coulombic efficiency (η_c) and energy efficiency (η_e). Both magnitudes are usually given as round-trip efficiencies, given that the stored charge or energy cannot be measured until the device is discharged. η_c is the efficiency related to electrical charge (Ah), and is defined as shown in the following equation:

$$\eta_c = \frac{\text{Ah}_{\text{discharge}}}{\text{Ah}_{\text{charge}}} \tag{6.9}$$

A value of η_c lower than 1 means that the total amount of electrons that are pumped from the positive to the negative electrode during charge cannot be extracted during SC discharge. This is a main parameter for SC material design and manufacturing process, since improvements in these fields yield increased η_c. The main sources of coulombic inefficiency are electron crossover through the membrane and parasitic, non-reversible electrochemical reactions that provoke SC ageing besides reduced η_c.

Energy efficiency is related to energy (Wh), and is defined as follows:

$$\eta_e = \frac{\text{Wh}_{\text{discharge}}}{\text{Wh}_{\text{charge}}} \tag{6.10}$$

A high η_e, which means low power losses, is a desirable characteristic of any ESS for two main reasons. Firstly, because a high efficiency reduces the gap between charging and discharging energy, therefore increasing the profitability of the ESS. Secondly, devices with low energy losses require more

straightforward refrigeration system, simplifying their set up. Therefore, η_e is more useful than η_c for the application of SCs in energy systems and for the design of their control algorithms.

η_c and η_e are related through the SC voltage. Given the non-ideal SC characteristics explained above (being ohmic phenomena and charge distribution the most remarkable), the voltage required to charge the SC is higher than de discharging voltage. Therefore, η_e is always lower than η_c.

6.2.3.7 Energy and power density

Energy and power density are two magnitudes that are widely used to compare different ESSs, such as the Ragone Plot shown in Figure 6.1. They are the energy and power that can be stored, per unit of mass, and the most suitable units to express the typical SC characteristics are Wh kg^{-1} and kW kg^{-1} respectively. The calculation of these magnitudes needs to be standardised to make it possible to compare between different technologies. This standardisation is of particular importance to SCs, since, given the quasi-linear relationship between stored charge and voltage, only part of the total energy can be used in a real application. The total energy stored in an SC is calculated by means of Equation 6.2, using the rated voltage, V_R, as the voltage value. However, due to the usual requirement of a minimum operating voltage that does not allow for a total SC discharge, remaining energy (E_{min}) is stored in the SC but cannot be used. A usual approach is to set a minimum voltage $V_{min} = \frac{1}{2}V_R$, which reduces the voltage variation to 50% of the total range while allowing an energy usage (E_u) as high as 75% of E_{max}:

$$E_u = E_{max} - E_{min} = \frac{1}{2} \cdot C \cdot V_R^2 - \frac{1}{2} \cdot C \cdot \left(\frac{V_R}{2}\right)^2 = \frac{3}{4} \cdot E_{max} \tag{6.11}$$

The energy density of an SC (ρ_e) is therefore calculated by means of the following equation, where m represents the mass of the device:

$$\rho_e = \frac{3}{4} \cdot \frac{1}{2} \cdot \frac{C \cdot V_R^2}{m} \tag{6.12}$$

On the other hand, the specific power describes the speed at which energy can be delivered or absorbed from the SC. The real power that an SC can handle depends on the current–voltage relationship, which is affected by the voltage drop. Standardisation of this variable is also necessary for the purpose of comparability. In this regard, standard IEC 62391–2 establishes Equation 6.13 as a practical maximum power for an SC as a function of its

rated voltage and its equivalent internal resistance R_i:

$$P_{max} = \frac{1}{8} \cdot \frac{V_R^2}{R_i} \tag{6.13}$$

Therefore, the power density of an SC can be expressed as:

$$\rho_p = \frac{1}{8} \cdot \frac{V_R^2}{m \cdot R_i} \tag{6.14}$$

6.2.4 Modelling and parameter characterisation

The model of a physical system is the mathematical representation of certain aspects of its behaviour. Given the complexity of processes governing the behaviour of any system and the considerable amount of variables having a greater or lesser influence on its performance, each model is designed with the aim of achieving particular objectives. The modelling of electrochemical systems, and SCs in particular, is an essential tool to exploit the electrochemical principles and optimise the integration and management of the SC in a complete electrical system. Moreover, this good interaction between material science and electrical engineering is useful for the improvement of SC materials and manufacturing processes, SC performance prediction, control strategy, lifetime prediction, cost calculations and future expectations.

A survey of the main modelling trends is presented in this subsection, identifying the major strengths and weaknesses of each one, and addressing the most reasonable functions of each model. The most-used characterisation techniques for each model trend are summarised and the results of some experimental tests are presented as illustrative examples to facilitate the understanding of models and characterisation processes. Given the system-integration focus of this review, more emphasis is placed on model trends focussed on supporting SC engineering applications.

6.2.4.1 Modelling the core principles of double layer behaviour

The double layer effect was initially described by the German physicist Hermann von Helmholtz [HEL79]. He realised that a charged electrode submerged in an electrolyte repelled ions with its same charge and attracted the ions with the opposite charge [WAN11a]. He modelled this phenomenon as a conventional capacitor with distance for charge separation d, which is approximately the radius of solvated ions, as shown in Figure 6.6 (a). The main weakness of this proposal is that capacitance has no dependence on voltage, which is not in line with real measurements [BAR01].

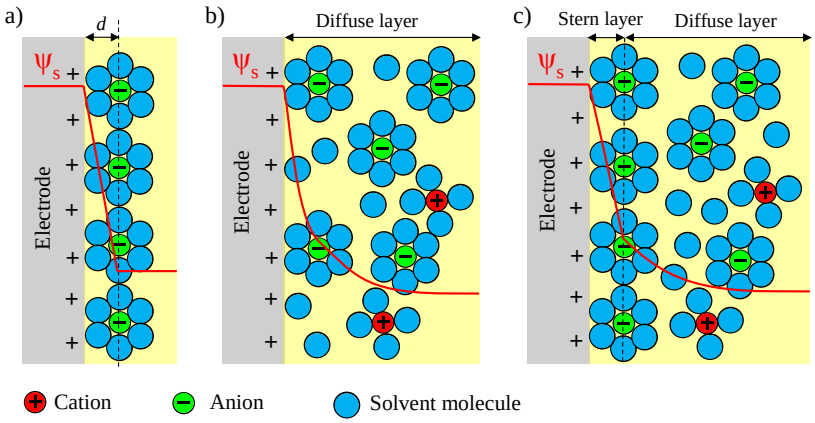

Figure 6.6: Schematics of the electric double layer structure showing the arrangement of solvated anions and cations close to the electrode–electrolyte interface in the Stern layer and the diffuse layer: Helmholtz model (a), Gouy-Chapman model (b) and Gouy-Chapman-Stern model (c) [WAN11a].

Subsequently, Guoy [GUO10] and Chapman [CHA13] independently developed a model for the double layer in which ion mobility is taken into account. Ions are threatened as point charges, and a combination of diffusion (statistical in nature) and electrostatic forces is proposed as the governing phenomena for ion mobility [WAN11a]. Therefore, a diffuse layer in the electrolyte region closest to the electrodes is proposed, as shown in Figure 6.6 (b). However, since ions are considered as point charges, the capacitance values predicted by Guoy and Chapman are larger than actual measurements because in reality ions have a finite size and they cannot approach arbitrarily close to the surface [BAR01].

Stern [STE24] combined the Helmholtz and Guoy–Chapman models and described the double layer as a combination of the two layers shown in Figure 6.6 (c). He proposed a compact layer of immobile ions strongly adsorbed to the electrode surface, similar to the Helmholtz layer, and a diffuse layer where ions have mobility and the Guoy–Chapman model is applied [WAN11a].

These are the original works in which the principles of the double layer behaviour were established and the fundamental equations were proposed. Even though these ideas are used to develop SC models, they are not used by themselves to model physical devices, since the influence of other phenomena must also be taken into account in a model in order to predict the actual behaviour of the SC.

6.2.4.2 Molecular models

Molecular modelling is a handy tool for the design of SCs and material properties analysis. Thanks to this technique, it is possible to predict phenomena that are not observable in any experimental set-up, such as the distribution and orientation of electrolyte ions, the change in the electrode morphology [BUR14], influence of the ionic resistance of the separator on the SC performance, and the ionic and electronic resistance of the porous electrode [SRI99].

Both the equilibrium state and dynamic phenomena which drive the SC behaviour can be modelled through molecular modelling. With this aim, the behaviour of the SC materials is studied at molecular level starting from the physicochemical laws governing the matter. Quite complex simulations need to be solved to run this kind of models, requiring the use of simulation techniques such as spectral element methods to discretise the model equations [DRU15] or Monte Carlo, based on statistical mechanics or molecular dynamics, which solve Newton's equation of motion for a many-bodied molecular system over a short period of time [ALL89, FRE01].

Both the accuracy and computational requirements of these models are mainly dependent on the modelling of electrodes and electrolyte. In this regard, a primitive model can be chosen, which considers ions as hard spheres and electrodes as simple walls, thereby reducing the simulation cost. However, the model accuracy is also reduced due to their unrealistic structural assumptions and its inability to calculate electrostatic properties. The other option for electrolyte modelling, which significantly increases the accuracy and computational cost of the model, is to consider the solvent molecules as uncharged hard spheres. The computational requirements of these all-atom electrolyte models limit their use, particularly in simulating large systems [WAN07]. With the aim of overcoming these limitations, reduced-order [MUN16], united-atom or coarse-grained models [BUR14] are proposed in the literature.

There are also two main options for the electrode models. On the one hand, the voltage on each electrode atom at each molecular dynamics step can be assumed to be equal to a specified value [VAT10, XIN12]. On the other hand, a simpler, computationally less expensive option is a simulation where fixed partial charges are assigned to each atom [LI12b, PAE13]. As concluded in [MER12], the use of constant charge simulations alters both the structure of the adsorbed fluid at the interface and the time scales over which relaxation phenomena occur.

There are experimental techniques devoted to analysing the material properties of an SC. The capability of these techniques for the characterization of

working devices are of special interest in order to understand the performance of these ESS. In this sense, the nuclear magnetic resonance and electrochemical quartz crystal microbalance techniques are used in [GRI15] to directly quantify the populations of anionic and cationic species within an SC electrode. However, the majority are specific techniques that do not allow for the testing of the SC as a whole, since access to the materials is required. The pore structure and its correlation with the size of electrolyte ions are of utmost importance in material characterisation. A number of studies also analyse the reason for SC failures under different abuse conditions with the aim of preventing hazards, maintaining the integrity of other systems and protecting persons. These abusive conditions usually include high or low temperatures, high voltages and short circuits. After the SC death, it is disassembled and the state of its materials at this point provides valuable information for life extension and catastrophic failure prevention. Therefore, the experiments used to characterise standard materials are also used for post-mortem analysis [TOR15].

These are the most salient approaches to the analysis of SC materials. The first material property that can be measured is the pore structure of the electrodes, whose diameters are in a nm or μm scale. The suitable size of these pores has a primary influence on the SC behaviour, and several techniques are proposed to characterise this parameter. Scanning electron microscopy [KUM15], volumetric gas adsorption or microwave measurement [YAN16b] are three of the most widely-used ones. A second property that is usually characterized is the lattice structure of these pores, which is several orders of magnitude smaller than the pore size (Å). The most-used experiments for lattice structure analysis are X-ray spectroscopy and nuclear magnetic resonance, [TOR15]. Finally, the third property that is usually of interest is the relationship between material properties and their electrical performance. This issue can be explored via electrochemical measurements for three-electrode systems with either a potentiostat or galvanostat [TOR15].

6.2.4.3 Transmission line models

A transmission line model, first introduced by de Levie [DE 63, DE 89], is a tool to model the electrical impedance of an SC. It is a useful approach to switch from the local pore scale to the macroscopic scale of an electrode. Instead of taking into account all the trajectories that each of the adsorbed species follows, the transmission line is a suitable electric circuit representation of the overall behaviour of an electrode. It consists of an infinite succession of electrode slices modelled as a resistance and a capacitance in order to simulate the progressive penetration of the charges into the electrode. Two transmission

lines are represented in Figure 6.7 to model both electrodes in an SC. These two transmission lines, as well as the bulk resistance of the electrolyte R_{bulk}, are put together in [PEA16] to represent the behaviour of a complete SC.

The number of branches included in a transmission line model is a decision that determines the accuracy of the model, the complexity of the parameter fitting procedure and the computational requirements. The higher the number of branches, the greater the number of time constants that can be taken into account and also the greater the computational requirements to perform the simulations. Depending on the application, more or less branches are preferable. Proposals for transmission lines with a variable number of branches, ranging from 5 [MOA13] to 15 branches [LOG15] can be found in the literature. Therefore, there are also authors that propose methods directed at reducing the simulation time in transmission line models, such as the authors of [MOA13] who suggest a waveform relaxation strategy to reduce the simulation time while maintaining a good accuracy.

Parameter fitting is also a key topic in models of this type, given the high number of resistors and capacitors forming part of them. [PEA16] propose a parameterization method for a transmission line model based solely on equilibrium molecular dynamics while recommending that quantitative comparisons should be made between molecular-scale simulations and electrochemical impedance experiments.

Given that the transmission line model is based on the physical structure of the interface, it is useful to study the relationship between the physical properties of the electrodes and the electrical behaviour of the SC. A transmission line model was combined with information on pore size distribution in [GHO13] to simulate the frequency response of the entire electrode and to investigate

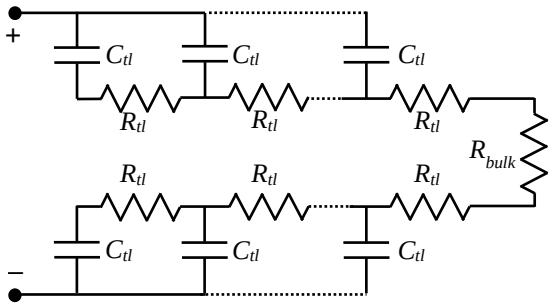

Figure 6.7: Equivalent circuit in the transmission line model. R_{bulk} is the resistance of the electrolyte in the bulk region, while R_{tl} and C_{tl} are the resistance and the capacitance inside the electrodes, respectively [PEA16].

the dependence of the relaxation time constant on several parameters. As a result, the authors determined a strategy to design the best mesoporous material for SCs with regard to energy and power density. The authors of [GON17] use a transmission line model combined with electrochemical impedance spectroscopy experiments and density functional theory to understand how redox reactions lead to the premature ageing of conducting polymers. In this way, they are able to propose new methods to increase the durability of these SCs and to improve their electrochemical properties.

Even though transmission-line models offer a number of advantages for the simulation of electrode impedance, one of their main drawbacks is that they are difficult to scale when several cells are connected in series or parallel [MIL11]. Therefore, when a real SC system needs to be analysed, analytical models, which are addressed in Subsubsection 6.2.4.4, are usually preferred.

The most common experiment for this analysis is electrochemical impedance spectroscopy (EIS), consisting in the application of a small sinusoidal current perturbation with varying frequencies around a steady-state operating point and the measurement of the voltage response. A small perturbation is required since the behaviour of the system is then linearised around the steady state. The complex impedance of the SC is determined using the generalised Ohm's law, and the result is represented in the Nyquist diagram, as shown in Figure 6.8 (a). Note that the imaginary axis is usually inverted to have the capacity behaviour plotted in the positive y-axis. From this graph, the impedance associated with the instantaneous phenomena can be calculated as the point at which the Nyquist plot intersects the real axis when there is neither capacitive nor inductive behaviour. This instantaneous impedance obtained from the test shown in Figure 6.8 (a) is 5.95 mΩ. A semicircle or semi-ellipse needs to be fitted to the central part of the Nyquist plot in order to calculate the influence of the dynamic phenomena associated with the double layer. Given the dynamic nature of the double layer, its impedance varies with frequency, as shown in the Nyquist plot.

From the impedance obtained with these experiments, the usable capacitance (C_u) of the SC for various frequencies can also be calculated, as shown in Figure 6.8 (b). As explained in Subsubsection 6.2.3.5, C_u decreases at a frequency around 1 Hz, and there is also a frequency limit above which no capacitive behaviour is measured. This frequency limit coincides with the point at which the Nyquist plot intersects the real axis in the EIS.

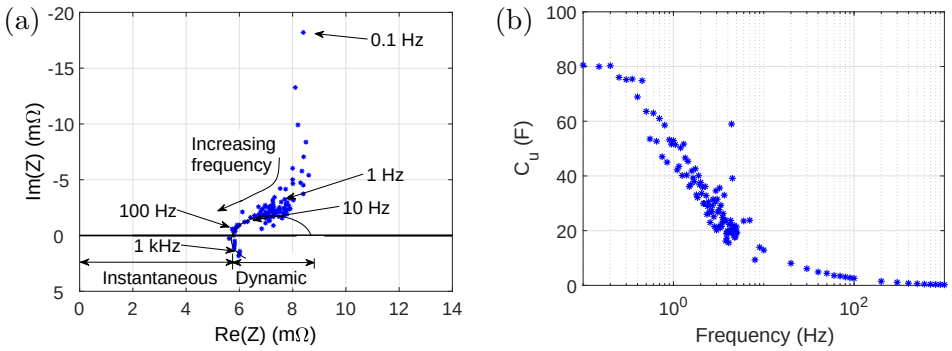

Figure 6.8: Dynamic performance of a Maxwell BMOD0083 SC: electrochemical impedance spectroscopy (EIS) (a) and usable capacitance calculated from the EIS (b).

6.2.4.4 Simplified analytical models

Simplified analytical models are the next step after the transmission line models in the representation of the electrical performance of a complete supercapacitor. While transmission line models represent the impedance of an SC, simplified analytical models include other concepts such as coulombic efficiency, self-discharge and parasitic inductances. They are usually represented as equivalent electric circuits and are a suitable tool for the estimation of the electrical performance of SCs. This equivalent circuit representation is of particular interest for the analysis of installations in which the SC is one of the many systems involved, and an interaction of all these models is needed in order to simulate the entire plant.

The strategy followed to simplify and represent the physical phenomena as an equivalent circuit is an important topic to be addressed during the design of a simplified analytical model [MEY00, DRU17]. The more the model is simplified, the lower its mathematical complexity and accuracy in the prediction of SC performance. The targeted accuracy and the frequency range of interest should be considered when selecting the most suitable model. The characterization of the SC behaviour and the process to calculate the values of the equivalent circuit parameters is another important topic in which intensive research is being conducted [DEV14a, MIN16].

One of the main parameters involved in the SC modelling process is capacitance. Most of the simplified analytical models take into account the voltage dependence of SC capacitance. Some authors propose a tangential expression

as shown in the following equation [MIL11]:

$$C = b_0 + b_1 \tanh\left(\frac{v}{v_x} - v_x\right) \tag{6.15}$$

where v_x is the voltage at the inflexion point of the hyperbolic tangent term, v is the supercapacitor voltage and b_0 and b_1 are fitting coefficients. Other authors use a linear expression to fit the voltage variability of capacitance [ZUB00, LAJ07, BER14]:

$$C = C_0 + k \cdot v \tag{6.16}$$

Besides this variable capacitance, simplified analytical models represent other phenomena that determine the supercapacitor electrical performance. The most commonly-used electric circuits used with this aim are:

- RC circuit: This model consists of an ideal capacitor and a series resistance which represents all non-ideal phenomena in the SC, as shown in Figure 6.9 (a). Its main advantages are simplicity in the fitting process of its two parameters, fast computer simulation and good accuracy for fast dynamics [GOH14]. It is generally used for the sizing of storage systems and the approximate calculation of system efficiency [SPY00]. With the aim of significantly improving the accuracy of simple RC circuit models, some online fitting methods have been proposed in the literature [EDD13].
- Multi-branch models: These model are built by the parallel connection of several RC branches with different time constants. These branches model the ion diffusion through the electrode pores. A suitable selection process for the time constant and the distribution of resistance and capacitance in these branches has been analysed in the literature [FLE17]. Three is the number of branches used by most authors [ZUB00]. A

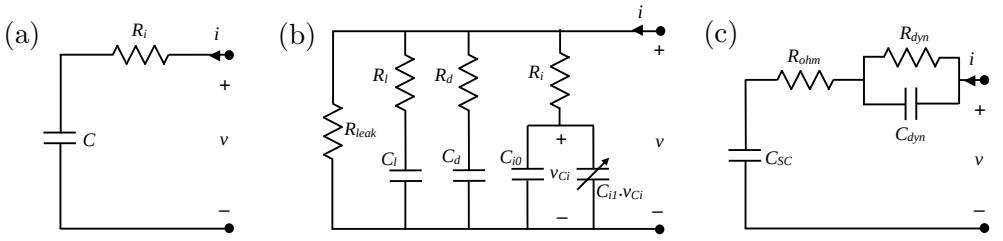

Figure 6.9: Basic electric circuits for SC modelling: simple RC circuit (a), multi-branch model (b) and dynamic model (c).

leakage resistance (R_{leak}) is also usually included to model the self-discharge of the SC, as shown in Figure 6.9 (b). Some authors propose only two parallel branches, but they need to include a time-dependent leakage resistance [SED15]. Slow dynamics (tens of seconds or more) and self-discharge behaviour are accurately predicted by these models. Several studies conclude that multiple-branch models achieve the best accuracy for the energy stored in an SC (state of charge) [NAD15] and self-discharge [SHE16].

- Dynamic models: These are built by the series connection of a capacitor representing the primary capacitance of the SC and some RC groups, as shown in Figure 6.9 (c), thereby improving the accuracy of the model for high-frequency applications. They are particularly suitable for modelling fast charge–discharge cycles or rapid fluctuation in the supercapacitor power [PAR16b]. The conclusion of [ZHA15a] is that the typical performance of the SC in an electric vehicle is best modelled by a dynamic model.

Ageing phenomena have particular relevance for SC simplified analytical models and their engineering applications. When the effect of ageing in SCs needs to be studied, the characterization of its electrical performance with the above-described tests is combined with methods directed at accelerating the ageing process in order to conclude the experimental work within a reasonable time frame. The temperature and operating voltage are usually increased, since the ageing rate doubles if either the cell voltage is increased by 100 mV, or the temperature is increased by 10 K [BOH07a]. It is noteworthy that a performance recovery phenomenon associated with cycle interruptions has recently been reported in a paper in which an empirical model for the state-of-health prediction is proposed [CHA14]. Moreover, the influence of high-frequency ripple currents in SC ageing has been experimentally studied [GER15], concluding that they have no effect on SC ageing. Torregrossa and Paolone studied SC ageing phenomena in closer detail in a two-part article. Experimental measurements of capacitance decline and resistance increase under high-pulsed current and high temperature are presented in Part I [TOR16a]. They conclude in this paper that, while the SC capacitance decline is enhanced with a pulsed current, this stress condition does not affect resistance increase. The measurements performed in the previous paper allow the authors to present an ageing model in Part II [TOR16b] whose good performance is experimentally validated.

6.2.4.5 Thermal models

The thermal modelling of SCs is a useful tool to calculate working temperature T. The inputs for these models are usually the electrical performance of the SC (v and i) and the ambient temperature T_{amb}. The knowledge of the SC internal temperature is necessary, given that it has several effects on the electrical properties of the device. Specifically, an increase in T provokes a decreasing series resistance of the SC and increasing capacitance [FLE10, KÖT06, GUI06, BOH07b]. Moreover, high values of T accelerate the self-discharge of the device and parasitic chemical reactions, such as oxidation, following Arrhenius law, which means a faster ageing of the SC [GUA16]. A thermal model consists in:

- Heat generation: Two kinds of processes generate heat during normal SC operation. On the one hand, there are ohmic losses due to the internal resistance which induce an overall increase in temperature. On the other hand, a reversible heat generation (or entropic term) is usually included in thermal models to model the entropy change in the double layer and to achieve better accuracy [PAR16b]. The most suitable model for this entropic term is still an open discussion in the literature. Most authors base their entropic heat generation on the approximate model proposed in [SCH06], in which a single-atom double layer is assumed. However, in a recent comparative paper [JAN17], the authors conclude that better results are obtained if the Poisson-Nernst-Planck equation is combined with heat equation, as suggested in [D'E14].

- Heat transmission: Besides heat generation, the SC temperature T depends on the ability of the device to transfer this heat to the surrounding air. There are three heat transmission mechanisms, namely conduction, convection and radiation. Heat is transferred inside the solid from high to low temperature zones based on conduction phenomena. Convection (either natural or forced) allows the heat to be transferred from the surface of the device to the surrounding air. A thermal model whose equations are the fundamental heat transfer laws is proposed in [GUA09] and has been used in the following research works like [GUA11]. Given the small temperature difference between the SC surface and the ambient air, many authors disregard the effect of radiation as a heat transfer mechanism [BER14, LYS15, VOI15]. Enclosed modules comprising several cells and cooled by natural convection are usually modelled as thermal equivalent circuits. Meanwhile, for the cases in which an airflow is forced around the cells to improve the heat dissipation, some authors propose modelling the process with an equivalent thermal circuit [LYS15] while

others prefer Fluid Dynamic Software to increase the accuracy of the model [VOI15].

A usual approach to experimentally characterise the thermal performance of an SC is by achieving an almost constant heat power generation in the device resulting from its normal operation. The accuracy of the results is increased if the thermal characterization is performed with a constant ambient temperature, which can be achieved by placing the SC inside a climate chamber. The interior and ambient temperatures need to be measured since the difference between these two variables is related to the heat dissipation phenomena.

6.2.5 Supercapacitor applications in energy systems

SCs are experiencing rapid market growth and catalogue diversification thanks to their high power density, fast electrical response, long maintenance-free lifetime and their ability to perform in a wider temperature range than other ESSs. This subsection starts with a summary of some issues about the SC manufacturing process, it then goes on to present a survey of the main characteristics of the products available in the market and, finally, a critical analysis of successful and recently-emerged SC applications is made, classifying them into the four top market sectors.

6.2.5.1 Supercapacitor manufacturing basics

As explained in Subsection 6.2.2, the main components of an SC are the electrodes and the electrolyte. However, they also have a separator, to prevent short circuits inside the SC and metal current collectors attached to each electrode to drive the current from the electrodes to the external circuit and vice versa. The thickness of each electrode layer deposited on the current collectors and the deposition technique are of central importance in achieving good electrochemical properties and a long device lifetime [KUM15].

Most commercial supercapacitor cells are cylindrical, such as the product shown in Figure 6.10 (b). This shape is achieved by rolling up a jelly roll consisting of two aluminium foil current collectors with the electrode active material deposited on both sides. The porous paper separator is located between both electrodes to prevent short circuits, as shown in Figure 6.10 (a). As can be seen in this figure, the positive and negative output terminals are on the top and bottom of the jelly roll. Once rolled-up, the jelly roll is impregnated with the electrolyte and enclosed into a hard case to prevent the

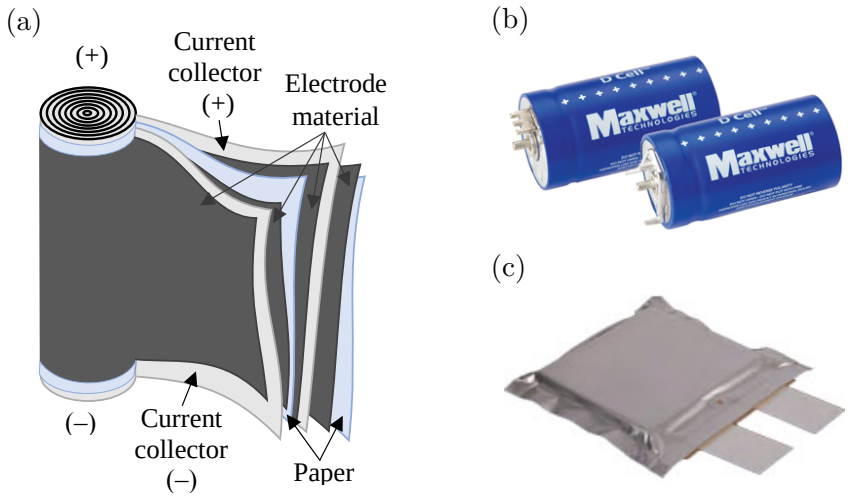

Figure 6.10: Jelly roll schematic (a) and two commercial SCs: Maxwell cylindrical SC (b) and Ioxus pouch SC (c).

evaporation of the electrolyte and the contamination of the active materials. Following the trend addressed by the world's leading manufacturer, Maxwell Technologies, the cell diameter has been standardised to 60 mm. The height of the can has the required size to achieve the desired capacitance.

Given the easy automation of this manufacturing technique, cylindrical SCs are cheaper to manufacture and, therefore, used in most applications. The main drawback of this circular shape is that the heat generated inside the cell must be conducted through a thick material layer in order to be evacuated. Even though SCs have a high efficiency and the power losses are proportionally low, temperature can be a limiting factor on the maximum manageable power.

Pouch supercapacitors, such as the Ioxus device shown in Figure 6.10 (c) have been designed to improve thermal conductivity. In this case, the manufacturing process consists of cutting and stacking current collectors, electrodes and separators. Electrodes with the same polarity are connected in parallel, and the whole device is sealed in a plastic bag. These devices are usually more expensive than cylindrical ones but are suitable for higher power densities.

Intensive research to reduce the price of SCs is currently being conducted. On the one hand, low-cost materials are being designed. A recent research work reports on a new electrode material which achieves a 90% price reduction by decrementing the SC capabilities by 50% [BLO17]. On the other hand, manufacturing processes and materials for flexible SCs are being investigated. These soft ESSs are expected to be a key component of next-generation elec-

tronics. Given that flexible SCs are still not commonly available in the market, their manufacturing technique is to be developed during the upcoming years. A number of review papers [KIM15a], progress reports [YOU16] and research papers [LI17a, GUO17, SCA17] have been published recently establishing the basics of this new market sector.

6.2.5.2 Supercapacitor manufacturers and products

The purpose of this subsubsection is to present a comparative analysis of the products offered by the main SC manufacturers. Therefore, eight representative manufacturers have been selected, as shown in Table 6.2. Maxwell Technologies, which leads the SC global market, is represented in the first row of the table. The key features of each product are stated in columns 5–9, which are capacitance (C), rated voltage (V_R), energy density (ρ_e), power density (ρ_p) and operating temperature (T).

As covered in Table 6.1, symmetric SCs (Sym. type in Table 6.2) are the most common option and are offered by all the manufacturers. Of the companies summarised herein, only Vinatech and Yunasko offer hybrid models, while Nesscap has asymmetric SCs (Asym. type in the table) in addition to their symmetric options. As part of their symmetric SC products, most of the companies complement their offer of cells with standard modules, built by a number of series connected cells, whose characteristics are also summarized in Table 6.2. Besides these standard modules, most companies offer the option of customised modules adapted to the power and energy requirements of each customer, which are manufactured by the series or parallel connection of the required number of cells. These modules can be connected in series or parallel to meet the energy and power requirements of any particular application. Panasonic is the only company which centres its whole product line on SC cells and coin SCs, which are the series connection of two cells.

The parameters covered in the table are useful decision tools for the selection of the most suitable SC for each application. Firstly, there is a high range of capacitance values since greater or lower capacitance is achieved by using a bigger or smaller electrode in each cell. Conversely, the cell voltage depends on the SC technology instead of on the size and, as explained in Subsection 6.2.2, its enhancement is a current research topic directed at achieving increased SC energy content. Although the rated voltage range offered by all manufacturers is tight (2.3–3 V), this difference has sensitive implications, given that the company that is able to provide the cell with the highest rated voltage (3 V) also has the highest energy density for a symmetric cell: 7.5 $\mathrm{Wh\,kg^{-1}}$. The voltage range offered for the standardised modules varies considerably and is

Table 6.2: Characteristics of the supercapacitors offered by the main naufacturers.

Company	Country	Type	Device	C (F)	V_R (V)	ρ_e ($\mathrm{Wh\,kg^{-1}}$)	ρ_p ($\mathrm{kW\,kg^{-1}}$)	T (°C)	Applications
Maxwell [MAXa]	U.S.A.	Sym.	Cell Module	1–3400 5.8–500	2.3–2.85 16–160	0.7–7.4 2.3–4	2.4–14 3.6–6.8	–40/65	Transport, energy
LS Mtron [LS]	Rep. Korea	Sym.	Cell Module	100–3400 2.5–500	2.7–3 16–381	3.3–7.5 2.3–5	0.9–2.4 0.3–0.6	–40/65	Industry, electronics, transp.
Nesscap Co., Ltd [NES]	Canada	Asym.	Cell	50–300	2.3	4.8–8.8	4.9–6.2	–25/60	Heavy vehicles, pitch control, solar tile
		Sym.	Cell Module	3–5000 1.5–500	2.3–2.7 5–125	2–5.7 1–3.7	6–17 2.5–6.8	–40/85	
Panasonic Corp[PAN]	Japan	Sym.	Cell Coin[a]	3.3–100 0.1–1.5	2.3–2.7 3.6–5.5	1.4–4.1 0.13–1.5	0.29–3.65 10^{-3}	–40/70 –40/85	Electronic devices
Vinatech [VIN]	Rep. Korea	Hybrid	Cell	10–800[b]	2.3	4–12	0.4–0.8	–25/60	Transport, UPS, wind turbines
		Sym.	Cell Module	1–3000 2.5–60	2.5–3 16–144	0.7–6.5 1.7–5.6	1–11.3 0.4–4	–40/70	
Yunasko [YUN]	Ukraine	Hybrid	Cell	1.3 Ah[b]	2.7	37	4	–40/60	Transport, industry, electronics
		Sym.	Cell Module	400–3000 13–500	2.7 16–90	4.7–6.2 3.9–2.1	7.1–41 3.3–11.3		
Ioxus Inc [IOX]	U.S.A.	Sym.	Cell Module	1250–3150 21–500	2.7 16–162	4.5–6.3 2.2–3.8	23–34 0.2–0.4	–40/85	Transport, ren. energy, backup
SPS Cap [SUP]	China	Sym.	Cell Module	1–5000 0.5–500	2.5–2.7 16–2300	0.9–6.5 1.4–3.6	0.5–8 0.3–0.7	–40/60	Transport, wind turbines, micro grids

[a] This SC is actually the serial connection of two symmetric cells.
[b] Given that the characteristics of hybrid SCs are a combination of typical properties from batteries and SCs, one of the manufacturers provides the capacitance value (F) while the other uses capacity (Ah) as a characteristic variable.

not as interesting as the cell voltage, given that modules are built by the series connection of many cells. Limiting factors for the series connection of SC cells are the requirements of voltage equalisation and the electrical isolation of the metal components, which are easier to overcome than the material properties determining the cell voltage.

The comparison between SC energy and power density is also interesting. As shown in the Ragone Plot (Figure 6.1), these devices can provide high power (several kW per kg), while the stored energy is not exceptionally high (a few Wh per kg). It is significant that the power and energy densities for modules are lower than those reported for individual cells, given that, apart from the actual cells, the manufacturing of a module requires, connections, safety devices and the module shield, making the module heavier than the sum of the weight of single cells. In a comparison of energy and power densities between different SC technologies (symmetric, asymmetric and hybrid devices), the data provided in Table 6.1 are supported herein. Regarding energy density, symmetric cells achieve a maximum of 7.5 $\mathrm{Wh\,kg^{-1}}$, while asymmetric cells reach 8.8 $\mathrm{Wh\,kg^{-1}}$ and hybrid cells 37 $\mathrm{Wh\,kg^{-1}}$. Conversely, power density presents the opposite trend, given that hybrid cells achieve only 4 $\mathrm{kW\,kg^{-1}}$, asymmetric cells 6.2 $\mathrm{kW\,kg^{-1}}$ and symmetric cells up to 41 $\mathrm{kW\,kg^{-1}}$.

The wide temperature range in which any of the cells can operate is one of the key features that make SCs an advantageous option compared to batteries. While lithium-ion batteries cannot perform below 0 °C and the minimum temperature for lead–acid batteries is –20 °C, SCs can safely and reversibly operate at –60 °C. Asymmetric and one of the two hybrid cells covered in Table 6.2 have the narrowest operating temperature range (–25 to 60 °C), which is still wider than the safe window of most batteries. The last column of the table summarises the applications suggested by each company for their products, providing a tentative approach to the selection of an SC. However, given the wide range of products offered by each manufacturer and the distinct requirements of each particular energy system, engineering applications of SCs are analysed in detail in the following subsubsection.

6.2.5.3 Engineering applications

As mentioned in Section 6.1, SCs are becoming a main ESS for an increasing number of applications. Several market outlooks were published in 2016 by independent agencies, coming to similar conclusions. Firstly, Grand View Research, Inc concluded that the SC market would reach $8.04 billion by 2024, which means a Compound Annual Growth Rate (CAGR) of 25% during the years 2017–2024 [GRA16]. Likewise, Accuracy Research LLP, published an

analysis of the decade 2016–2025, where a CAGR of 21.1% is expected, giving a market size of $9.88 billion in 2025 [ACC16]. Finally, Technavio focussed its study on the electric vehicle sector, which holds a key share of the global SC market. A CAGR of 19.24% is expected during years 2016–2020 [TEC16]. The four sectors in which SCs play a significant role as ESSs are summarised below.

Transport sector Supercapacitors provide substantial benefits to railway electricity systems. This technology has been used for many years to allow the regenerative braking of trains and to stabilise the catenary voltage. Two early examples are cities such as Cologne and Madrid, where trackside storage systems called SITRAS SES, built by Siemens using Maxwell's 1344 supercapacitors [SIE10], have been installed since 2001 and 2003 respectively. Another example of such an application is located in south-eastern Pennsylvania, where trains stop and accelerate several thousand times per day. These stop-and-go processes have a duration of between 15 to 20 seconds. The transport authority installed a hybrid SC-battery ESS which captures excess braking energy from the trains by detecting a rise in the line voltage on an overhead catenary system. As a result, a reduction of 10–20% in electricity consumption was achieved, as well as 800 kW of fast response load modulation support to the grid operator, which is a paid service that can provide more than $200,000 in annual revenues [MAXb]. The installation of systems of this kind is increasing year after year. As a current example, in 2016, the China Railway Rolling Stock Corporation installed Maxwell's 48-volt modules in two regenerative braking energy storage devices, enhancing the No. 8 line of the Beijing subway system, an urban rail network running north–south through China's capital, one of the most populous cities in the world [MAXa]. In addition to regenerative braking, SCs have been proposed as energy storage systems to avoid the electrification of remote train tracks. A high-efficient energy harvesting system is intended to convert track vibration into electricity. SCs were selected as the ESS given their ability to manage fast charge-–discharge cycles. The stored energy is subsequently used for cross lighting, track switching and maintenance work [ZHA16c].

Railways systems are also addressed in research and development projects. For instance, *Ferrolinera*® project was carried out in Spain by ADIF, the public entity that manages the railway infrastructure. In this project, a hybrid lithium battery–SC ESS is used not only to enhance the regenerative braking of trains and grid quality but also to allow for the fast charging of electric vehicles through a fast charger connected to the railway electricity grid, as shown in Figure 6.11 (a). Scientific papers proposing future SC applications to improve

the transport sector have also been published. In this line, a management strategy to improve the energy efficiency in light railway vehicles through SC-based ESS is proposed in [CIC14]. Some scientific papers propose installing SCs in trains [WAN14d] since onboard systems can have some performance advantages over trackside installations. However, trackside systems are more common in commercial applications due to the smaller size of the overall ESS and the lower installation cost.

Another important niche markets for SCs are urban buses. Due to their frequent stop-and-go driving conditions, SCs provide attractive characteristics for this application. There are proposals concerning hybrid battery–SC ESSs for electric buses [SON14b, CAP15], as well as commercial urban electric buses which rely only on SCs to store the required energy to reach the next stop. Buses of this kind, also known as *Capabuses*, are fitted with two roof-mounted pantographs for flash-charging the SC-based ESS at bus stops, as shown in Figure 6.11 (b), and SCs provide the energy needed during the driving time between two stops. Capabuses are booming nowadays, some companies such as Sinautec [SIN] are specialised in the manufacture of Capabuses while Maxwell Technologies, the SC market leader, opened a branch office in China in 2017 to increase its competitiveness in the Chinese electric bus market [MAXa]. New ideas about the best strategy to size and manage SCs in city buses are being investigated. In this line, Song et al. recently published a research work in which the influence of the driving cycle of city buses on ESS design and control is studied using fuzzy pattern recognition [SON17].

Apart from railway systems and buses, the use of SCs in passenger cars is also increasing [BUR15], in fuel, hybrid and electric vehicles alike. An example of SCs in a commercial fuel vehicle is the Mazda i-ELOOP, which has a combustion engine and supercapacitor-type regenerative braking, achieving

(a)  (b) 

Figure 6.11: Transport applications of SCs: Electric car charging station in the foreground and railway track in the background. Lithium batteries and supercapacitors are used for the regenerative braking of railways and fast charging of electric vehicles [ADI]. Reproduced by kind permission of Adif (a) and Capabus charging its ESS based on supercapacitors. Reproduced from Wikipedia (b).

fuel savings of 10% according to the manufacturer's website [MAZ11]. Moreover, supercapacitor companies such as Ioxus offer an SC product line directed at either supporting or replacing traditional batteries for combustion engine starting [IOX]. Regarding hybrid vehicles, supercapacitors are used in micro-hybrid (or stop-go hybrid) vehicles such as Peugeot e-HDI as well as in full hybrid vehicles such as the Toyota safety braking system [MAL15]. Research papers have also been published proposing the use of SCs in hybrid heavy-duty vehicles to achieve fuel savings [OUY15]. The power converter design for these applications is also an open discussion [CAM10]. In full electric vehicles, SCs provide faster acceleration, extended battery life and increased range. They exhibit the capability of absorbing regenerative braking energy, thereby limiting the high charging current to the battery. Therefore, recent studies propose management strategies [TRO15, CAS16] for dual SC–battery ESSs for electric vehicles. Specifically, two meta-heuristic methods are theoretically and experimentally compared in [TRO15], while an SC is added to the Tazzari Zero battery ESS in [CAS16] in order to lower the stress of the battery, thereby extending its lifetime. Two control strategies for the ESS are compared in this work: filtering-based strategy and λ-control strategy. As an alternative to batteries, fuel cell–supercapacitor hybridization is also a current research topic concerning the most suitable management and control strategies for such a system, given the fuel saving, increased efficiency and enlarged FC lifetime provided by the SC [WU14, REZ17, CAR17].

Additionally, the aerospace industry is focussing its development efforts on achieving a more-electric aircraft. An increasing number of electric devices are proposed, such as emergency power systems for aircraft. The high power peaks that are required from these ESS and the requirements for a long lifetime make SCs an attractive option to be installed along with batteries or FCs to create a hybrid ESS [GER16]. The management strategies of such a hybrid ESS is a key issue with regard to weight and volume minimization, as well as cost reduction [MOT14, DEV14b]. Finally, also worthy of mention is the proposal made in some recently-published research papers, in which SCs are put forward as the only ESS for an all-electric ferry. The authors of this study conclude that SCs are the best ESS to meet the particular requirements of vessel use [TRI15, HMA16].

Energy sector The energy sector is characterised by stationary applications in which SCs are chosen because of their outstanding power characteristics. Moreover, the extreme conditions that SCs are able to withstand and their low maintenance requirements make these systems especially attractive for renewable energy-related applications [BRA16]. This sector has shorter

time-to-market periods than transport applications, with time requirements of between one to three years [YUN].

One of the primary uses of SCs in renewable energy systems is the pitch control of wind turbines. According to the leading manufacturer Maxwell Technologies Inc. [WER15], 20 to 30% of wind turbines are equipped with SC pitch control systems, while 35 to 45% include a battery ESS instead. With regard to the conditioning of the actual wind power generated, many researchers propose SCs as a solution to deal with high-dynamic issues (faster than 1 minute). Power curtailment is a major concern associated with the increasing wind generation. Wind power intermittency has been detected as a remarkable cause of this curtailment, and SCs have been proposed to reduced this issue [REN17]. Some authors propose the sole use of SCs to deal with wind intermittency both with full converter [ABE08] and double fed induction turbines [QU11]. The hybridization of SCs with flow batteries has also been studied by means of simulation [LI10]. This hybrid system smooths the power output, lowering the battery cost and enhancing battery life and overall efficiency due to the inclusion of SCs. Besides wind energy, SCs are proposed to be installed in other types of renewable generation plants for fluctuation suppression [PEG15], low voltage ride through, voltage control support [BEN15] and oscillation damping, as summarised in a review of energy storage technologies for renewable applications [DÍA12]. Little growth is expected for this sector, given that more restrictions are expected to be imposed on renewable energy generation [PAR16a]. For the same purpose of dealing with high dynamics, SCs can be used as a solution for solar firming. This is evidenced at a plant located in California, where the increasing intermittent solar and wind energy installations threatened grid stability. Since only 20 to 30 seconds of energy storage were required, an SC storage system was designed to demonstrate the capability of smoothing short term solar power fluctuations and providing ramp rate control [MAXb]. Research papers have also been published in which different control strategies are proposed to address these problems [KAN11].

Electrical microgrids are usually equipped with renewable energy generators while the grid connection, when available, is often controlled to minimise the disturbance caused by the microgrid. Therefore, the selection of the most suitable ESS and its control strategy are of primary importance [PAS13, PAS15]. SCs have useful characteristics that can improve the microgrid ESS. For this reason, SCs are used in stand-alone microgrids to deal with fast load fluctuations [CAM16]. They are also useful in grid-connected microgrids [KOT17]. As an illustrative example, the role played by SCs in the experimental microgrid described in Subsection 4.2.3 is herein analysed.

For this analysis, instead of the previously described lithium-based ESS, the storage requirements of the microgrid are covered by a hydrogen-based system with a capacity of 40 kWh. In this context an SC bank is included with the aim of managing power fluctuations caused by renewable generation and consumption. Given that power demands with a frequency of a few hertz shorten the lifetime of fuel cells (FCs) and electrolysers [FER13, GER10, JUN11], in line with these results, some authors propose, for the above-mentioned microgrid , an SC bank that is able to manage frequencies of more than 3 mHz. These requirements were met with three Maxwell BMOD0083 SC modules that offer 82 Wh of storage. The SCs and FCs are directly connected in parallel, as shown in Figure 6.12 (a). This hybrid ESS makes it possible to achieve a higher overall efficiency and a longer lifetime of the hydrogen subsystem.

Figure 6.12 (b) shows the power of the FCs and SCs during 350 s of microgrid performance. The power of the ESS (P_{SS}) is the sum of the fuel cells power (P_{FC}) and the supercapacitors power (P_{SC}). The fast frequencies are managed by the SCs, allowing a better performance of the FCs. The fastest variation of P_{SC} takes place between t=257 s and t=262 s, when P_{SC} increases from 0 to 2.93 kW in only 5 s. Conversely, the fastest growth in P_{FC} takes place at the same time but has a much lower gradient, from 2.31 kW to 3.5 kW in 15 s.

There are also weak grids whose stability is threatened by voltage fluctuations. Such networks can be found, for instance, in small islands, such as La Palma (Canary archipelago, Spain). The DSO Endesa is using SCs for a double purpose on this island. Firstly, they provide a fast response which improves the spinning reserve of diesel units. Secondly, the SC system prevents load shedding, which is a protocol that disconnects electricity users from the grid in the event of frequency deviations. Specifically, an LS-Mtron SC system with a maximum power of 4 MW and an energy content of 5.5 kWh was installed in 2013. The outstanding power capacity of SCs is exploited in this project since they are completely discharged in just 5 seconds. This experience has reported good results, as shown in Figure 6.13 [FON16], where each power loss event is represented by blue bars. The effect of the SC bank can be appreciated since, before the commissioning of the ESS, any power losses of more than 4% of the total installed generation capacity would lead to load shedding. Conversely, no load was shed during the SC operation, even though significant generation losses were measured. Due to this excellent performance, the system is expected to be replicated in other markets [FON16]. Another example of a weak grid is the Yangshan Deep Water Port, near Shanghai, which is located at the end of a 20-mile bridge. The port's 23 quay cranes caused high voltage fluctuations in the grid, while an increase in the transmission line capacity

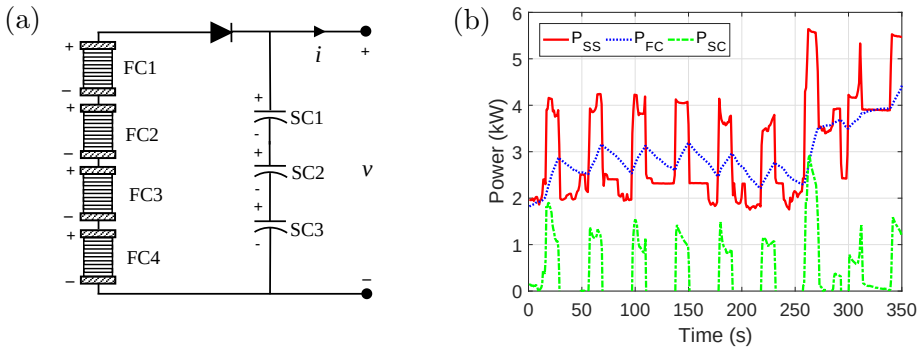

Figure 6.12: SCs as complementary ESS of a domestic microgrid: electrical connection of the ESS of a microgrid (a) and power measurements on the 12^{th} of December, 2012 at 20:00 h: Power required from the ESS (P_{SS}), which is shared between the SC subsystem (P_{SC}) and the FCs (P_{FC}) (b).

to correct this situation would have involved tremendous cost. A 3 MW, 17.2 kWh supercapacitor storage system was therefore installed to provide 20 seconds of reserve power. This system has been fully operational since 2013 and has led to a 38% reduction in the peak power demand from the grid with no need to upgrade the size of the transmission line [MAXb]. On the topic of grid stabilisation, particular mention should be made of the company Freqcon [FRE], focused on power electronics for the grid connection of renewable energy. In 2016, this company was awarded the German Renewables Award for its *UGS Ultracap Grid Stabilizer*, an IGBT power converter which uses SCs for active power support. In weaker grids with frequent outages, the use of SCs as ESSs in UPSs is proposed, like [ZHA14a], where a two-stage nitrogen expander is combined with an SCs bank to feed a 10 kW load due to the fast power capability of the SC.

In this context, it is also noteworthy that some authors have studied the suitability of SCs to be used as a filter in rectifiers [MIL10]. Their conclusion is that the time constant of traditional SCs is too long to be useful for this application (around 1 second). However, graphene SCs have a time constant of around 200 μs and can be used to filter the 120 Hz ripple arising from rectifiers connected to 60 Hz grids.

Industrial sector Those systems using SCs in the industrial sector include vehicles such as forklifts, shovel trucks, agricultural machinery, excavators, mining shovels, harbour cranes and industrial lasers. SC use in these machines is also stimulated by CO_2 emission regulations imposed in a number of

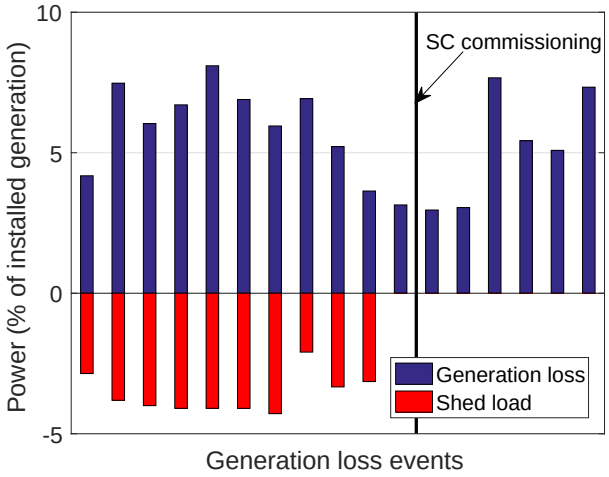

Figure 6.13: Performance improvement of the electricity grid of La Palma island due to a 4 MW, 5.5 kWh SC module installed by Endesa [FON16] (c).

countries. This sector is characterised by long design-in and testing periods since they are expensive devices with a small production volume.

Of the machines mentioned above, forklift trucks is the fastest growth segment, since the production volume is much larger than that of other heavier machines. Moreover, the dangers and health concerns related to the indoor use of fossil fuels make all-electric forklifts more common. This kind of vehicle can have either a battery or a fuel cell ESS, and SCs are usually added as a power source to support lifting operations and to recover braking energy [MIL11]. Forklifts of this type have been available on the market for several years. For example, the Komatsu forklift shown in Figure 6.14 (a) features a battery – SC storage system and was launched on the market in 2007, as reported in [YOS07]. This kind of system is a current research topic, especially its life cycle analysis [CON14].

In the harbour crane market, typical characteristics of the energy storage demands include deep discharge cycling. Port cranes equipped with SCs can recover energy from braking and drop manoeuvres, leading to savings on diesel consumption of up to 20% [MAXa]. Extra fuel savings are achieved by reducing the maximum engine power since the peak power is provided by the SC storage system. These systems have shown a 35% reduction in CO_2 emissions. Recent research works on the sizing of ESSs for these applications have been published [ZHA16d]. The authors of this study compare a battery ESS with an SC – battery hybrid ESS and conclude that the battery – SC

Figure 6.14: Industrial machines that use SCs. FB15HB-12 battery – SC hybrid forklift for Komatsu (a), PC200–8 Hybrid Excavator (b) and Rockster R1100DE Parallel Hybrid Crusher (c). Photos taken from the manufacturers websites.

hybrid crane shows great potential for regenerative energy recovery associated with a reduction in fuel costs and emissions.

Earth moving machinery is large sized and mobile, therefore requiring high power peaks. Supercapacitors come within those applications used in combination with diesel motors to meet the high power demand and to recover energy from regenerative movements [MIL11]. Three different hybrid machines are referred to herein as examples of the benefits achieved with SCs. In 2007, Komatsu launched the world's first hybrid excavator on the market [KOM08], the PC200–8 Hybrid Excavator shown in Figure 6.14 (b). Although a diesel engine is the primary energy source of the excavator, an electric motor is used for the turntable of the upper structure. An SC bank is connected to this motor, allowing for energy recovery when the turning slows down. Since the mass of the PC200–8 is 20 100 kg, the SCs allow for energy savings of 25% in standard tests. Real measurements were performed by the manufacturer in a sludge disposal application, where the cabin turns more frequently than in standard tests, and a fuel saving of 41% was recorded [KOM08]. Five years later, in 2012, Caterpillar presented a hybrid hydraulic shovel, the Cat® 6120B H FS, which recovers energy not only from cabin swing deceleration but also from boom-down movements. This energy is stored in SCs, and electric motors are used to assist the diesel engine when maximum power is required. Fuel savings of 25% were also reported [CAT12]. As a final example, the R1100DE Parallel Hybrid Crusher shown in Figure 6.14 (c) marketed by Rockster, has the diesel engine directly coupled to a generator. In this way, the engine always operates at its maximum efficiency. Electric motors are used to move the machine, and an SC bank smoothes the power peaks required to crush the rocks [REC].

Consumer electronics The consumer electronics segment has a lot of features that make it quite different from the above-mentioned cases. It is costly

and time-sensitive for SC manufacturers due to the very short design times and to the significant portion of volume required by the SC in the final device. Although consumer electronics is a very diverse market, the primary uses of SCs in these devices can be classified into four groups, as shown in Figure 6.15 [PAN]:

- Real-time clock or memory backup: for instance, solid-state drives have many advantages over hard-disk drives. However, the write speed is their main weakness, which can be enhanced using protected cache memory (SDRAM). This SDRAM needs a backup power, supplied in many cases by SCs [MAR09].
- Power failure backup: These systems provide emergency power to a load when the primary power source fails. An appropriate backup power supply should be able to provide instantaneous power without glitches. They are typically used to protect hardware such as telecommunication equipment, industrial or other electrical equipment, where an unexpected power disruption can cause malfunction or data loss. Texas Instruments published a report [HEL15] in which the performance of a backup power supply which uses SCs as an ESS is analysed in detail.
- Storage applications in which SCs are used instead of batteries: The fast charging capability, long lifetime and low maintenance requirements make SCs more advantageous than batteries as an ESS for some devices. For example, a flashlight with SC energy storage is reported in [MIL16].
- High load assist to the primary ESS: In some applications, such as the flash of a smartphone camera, the peak power load is significantly higher, albeit for a short time, than that of any other use case. SCs are selected as secondary power sources in order to use a low-power, cheaper battery as the primary source of energy. Several manufacturers have been using SCs for a number of years, such as the IC presented by STMicroelectronics in 2012, which is an integrated camera flash controller combining a supercapacitor, a discrete high-current MOSFET switch and high-power white LEDs [STM12].

6.3 Electro-thermal modelling of a supercapacitor and experimental validation

As mentioned above, a SC model is a handful tool to analyse hybridisation options between different ESSs. An electrochemical-thermal model for SCs

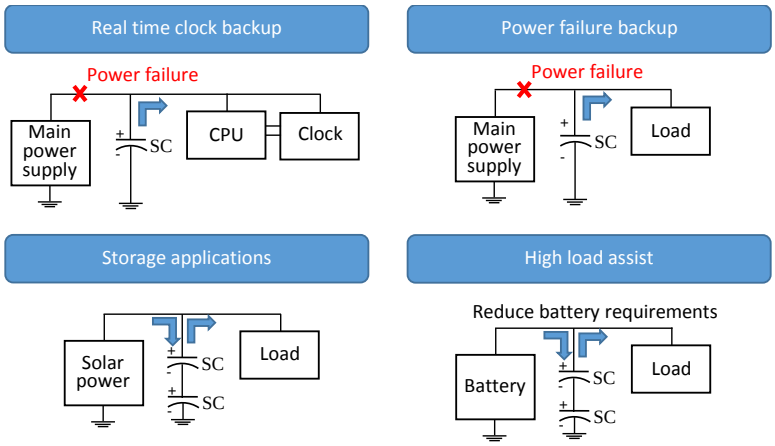

Figure 6.15: Schematic diagram of the use of SCs for different consumer electronic applications.

that follows the methodology used for the Li-ion battery model described in Chapter 4 is presented in this section. This model is designed to be integrated with the Li-ion battery model in order to analyse the synergies achieved by a hybrid ESS. Moreover, the model is a handful tool for the design of power converters, given its accuracy to represent dynamic phenomena, which allows a detailed analysis of the performance of SCs connected to power converters.

6.3.1 Electric model

In order to propose an electric model for SCs, the main physical phenomena that have an influence on their performance are analysed hereinafter. Each of the phenomena is explained, simplified and expressed as an equivalent circuit.

6.3.1.1 Double layer effect and charge distribution

As explained in Subsubsection 6.2.3.1, the double layer effect built by the alignment of charges of opposite polarity at the interface between each electrode and the electrolyte in the supercapacitor cells is dependent on voltage, and a number of expressions have been proposed to model the double layer effect. In this work, we opted for the proposal detailed in Subsubsection 6.2.4.4, which is a linear relationship between capacitance (C) and the voltage applied at the double layer (v_{dl}):

$$C = C_0 + k \cdot v_{dl} \tag{6.17}$$

where C_0 is the capacitance at 0 V (F) and k is a parameter which multiplies v_{dl} ($\mathrm{F\,V^{-1}}$). Therefore, taking into account the relationship between C and C_{dif} explained in Subsubsection 6.2.3.1, the differential capacitance is defined as follows:

$$C_{dif} = C + k \cdot v_{dl} \tag{6.18}$$

C_{dif} is the parameter obtained from experimental tests which is linearised as shown below:

$$C_{dif} = \frac{i_{dl} \cdot dt}{dv_{dl}} \approx i_{dl} \cdot \frac{\Delta t}{\Delta v_{dl}} \tag{6.19}$$

where Δv_{dl} is the double layer voltage variation occurring over time increment Δt. As well as dependence on voltage, the capacitance of an SC cell is affected by the operating temperature, given the fact that a temperature increase causes a growth in the Brownian motion of the ions forming the double layer. As a result, there is a larger separation between positive and negative charges in this double layer, which brings a decrease in the capacitance [BRA07, GUA03, MIC06].

The significance of the distribution of electric charges over the surface of the double layer is highlighted in Subsubsection 6.2.3.2, since it determines the area of contact between the electric and ionic charges and, therefore, the cell capacitance. This capacitance is largely determined by the ratio between the size of the electrolyte ions and the electrode pores [GRY05]. In order to model the charge distribution process, the different electrode pore sizes are taken into account. The pore sizes of the activated carbon used in the manufacture of the SC electrodes are shown in Figure 6.16 [QU98]. For its part, a typical electrolyte contains dissolved ions $[Et_4N]^+$ and $[BF_4]^-$. Given the fact that the number of electronic charges managed by both electrodes is the same, the number of cations that are either inserted or deinserted in the double layer of the negative electrode is the same as the number of anions in the positive electrode. The slowest ion type performing the insertion and deinsertion process is the one to limit this phenomenon in each SC cell. This behaviour is closely related to the size of the ions given the fact that, the bigger their diameter, the greater the difficulty in penetrating small pores. Given that the size of the cation $[Et_4N]^+$ is 6.7 Å and the anion $[BF_4]^-$ is 4.8 Å, the charge distribution process is considered to be limited by $[Et_4N]^+$. Figure 6.16 uses vertical lines to show its solvated Φ (solid line) with a size of 13 Å, and non-solvated Φ (dashed line) with a size of 6.7 Å. It can be seen that most of the pores have a diameter larger than 13 Å. These large pores are accessible to the electrolyte ions with no need for a prior desolvation process. Therefore ions penetrate into this pore type with no size-related impediment. Intermediate pores (6.7 Å $< \Phi <$ 13 Å) are accessible to the ions once these have undergone

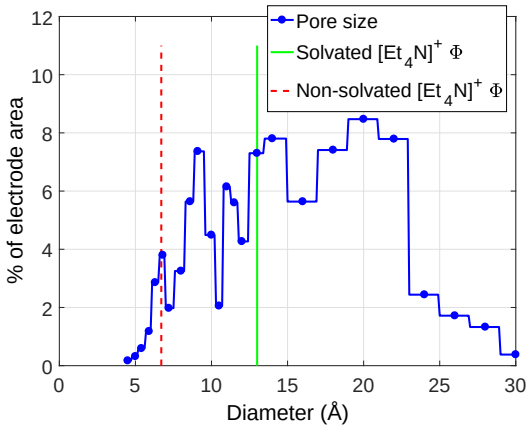

Figure 6.16: Pore diameter distribution in a typical SC electrode. With vertical lines solvated and non-solvated $[Et_4N]^+$. Data from [QU98].

a desolvation process. The smaller the pore size, the higher the number of intermolecular links to be broken down and the longer the time required for this process. Figure 6.16 also shows that there are two sizes of intermediate pores which represent the greatest percentage of the electrode area (9 Å and 12 Å). Taking this pore distribution into account, a model is proposed which characterises the concept of capacitance defined in Equation 6.17 to refer to the capacitance of a cell (C_{cell}), a parameter represented by capacitive terms C_i (immediate capacitance), C_d (delayed capacitance), and C_l (long term capacitance). Term C_i represents the large pores capacitance (Φ >13 Å), C_d that of the pores with sizes close to 12 Å and C_l that of the pores close to 9 Å.

Since capacitance is influenced by temperature only slightly [MIL11], a linear relationship between both magnitudes has been used, which produces an accurate result while maintaining reasonable level of mathematical complexity. Therefore, capacitance C_i was considered to be dependent on the double layer voltage (v_{dl}) and operating temperature (T) based on the following expression:

$$C_i = C_{i0} + C_{i1} \cdot v_{dl} = C_{i0,0} + C_{i0,1} \cdot T + C_{i1} \cdot v_{dl} \tag{6.20}$$

where $C_{i0,0}$ is a capacitance coefficient which is independent of voltage and temperature, $C_{i0,1}$ is a coefficient associated with the thermal dependence of the capacitance and C_{i1} is another coefficient reflecting the dependence of capacitance on voltage. Equation 6.20 is valid for temperature values between 0 and 70 °C. The lower limit is due to the increase in the viscosity of the electrolyte for lower temperatures, which prevents ions penetration into electrode pores and therefore results in a capacitance decrease. The higher limit

is the maximum operating temperature for the SC. Given the high proportion of pores bigger than 13 Å in relation to smaller pores in the SC cell electrode (see Figure 6.16), the model proposed considers that the dependency of their capacitance on voltage and temperature has a negligible influence on terms C_d and C_l.

Figure 6.17 depicts the physicochemical phenomena analysed in this subsection based on an electrical equivalent circuits. Three branches (i, d and l) are included in Figure 6.17 (a) with their corresponding capacitive terms making up the overall cell capacitance. In turn, the ion desolvation process required to penetrate the pores with Φ close to 12 Å is represented by resistor R_d, whilst resistor R_l represents the desolvation process to penetrate the pores whith Φ close to 9 Å. Branch i does not include a resistor, as no desolvation process is required.

6.3.1.2 Ohmic phenomena and electrical self-discharge

Electronic and ionic charge transport result in the ohmic phenomena covered in Subsubsection 6.2.3.3. This effect, caused by the losses associated with the ion and electron flow through the SC cells, is herein modelled by an electrical resistor (R_s) through which the same current crossing the cell double layer passes, namely i_{dl}, as shown in Figure 6.17 (b). The influence of temperature in this parameter is complex, since the movement of atoms and electrons needs to be modelled. In a trade-off between accuracy and simplicity, we have proposed the linear evolution of R_s with the operating temperature (T) based on the following expression:

$$R_s = R_{s0} + R_{s1} \cdot T \tag{6.21}$$

There are studies which show that the weight of the ionic charge transport is considerably higher than that of the electric charges in the SCs [MIL11]. Since the first effect decreases with increasing temperature, the coefficient R_{s1} must be less than zero. Equation 6.21 is valid for a temperature range from 0 to 70 °C, since the non-linearity of the system has significant effect for higher or lower temperatures [SAK09, GUA03].

Another phenomenon caused by the non-ideality of the SC materials, is the electrical self-discharge explained in Subsubsection 6.2.3.4, due to the fact that the ion conductive membrane separating both electrodes is not a perfect electrical insulator. The self-discharge effect is shown by a linear decrease in the SC voltage. It is represented by the electrical resistor (R_{leak}) through which leak current i_{leak} flows as a consequence of the voltage applied to the membrane v_{mem}, as shown in Figure 6.17 (c).

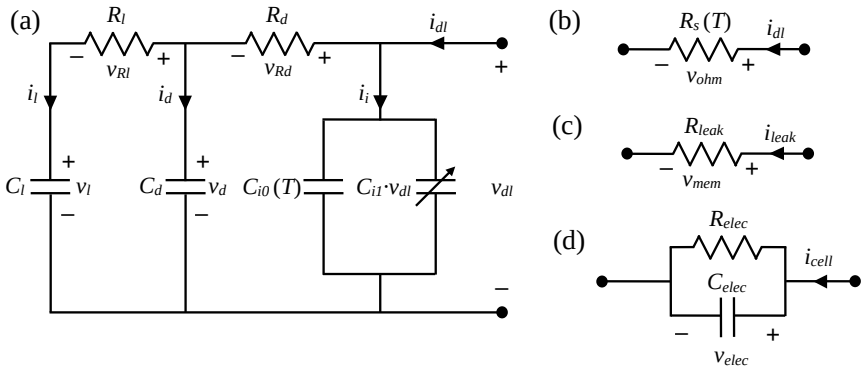

Figure 6.17: Equivalent circuit representations of the main SC phenomena: double layer effect and charge distribution in the electrode pores (a), ohmic losses (b), self-discharge (c) and ion penetration into the electrode pores (d).

6.3.1.3 Ion penetration into the electrode pores

The porous structure of the carbon electrodes explained in Subsubsection 6.2.3.5 means that, during the SC charging process, the electrolyte ions penetrate these pores to be distributed throughout the entire electrode contact surface. Likewise, during the discharge, the ions must leave the pores and return to the initial SC discharged situation. If the ions are solely located in the more accessible areas of the pores, then the effective capacitance of the SC decreases. The effects produced by the ion transport in the SC cell electrodes, is modelled by the RC network shown in Figure 6.17 (d). Resistor R_{elec} represents the losses associated with the ion transport from the pore exterior to the electrode–electrolyte interface, whilst the process dynamics are represented by capacitance C_{elec}.

6.3.1.4 Final configuration of the model

Following the analysis of the various phenomena taking place in a cell, the complete electric model of the SC was configured, based on the electric circuit shown in Figure 6.18. Given that the SC is formed by the series connection of a certain number of cells (n_{cell}), it is possible to relate the parameters for this model with the cell parameters, as shown in Equation 6.22 and Equation 6.23:

$$\begin{aligned} R_{l,SC} &= R_l \cdot n_{cell}, \quad R_{d,SC} = R_d \cdot n_{cell}, \quad R_{s,SC} = R_s \cdot n_{cell}, \\ R_{elec,SC} &= R_{elec} \cdot n_{cell}, \quad R_{leak,SC} = R_{leak} \cdot n_{cell} \end{aligned} \tag{6.22}$$

$$C_{l,SC} = \frac{C_l}{n_{cell}}, \quad C_{d,SC} = \frac{C_d}{n_{cell}}, \quad C_{i0,SC} = \frac{C_i 0}{n_{cell}},$$
$$C_{i1,SC} \cdot v_{dl,SC} = \frac{C_{i1} \cdot v_{dl}}{n_{cell}}, \quad C_{elec,SC} = \frac{C_{elec}}{n_{cell}} \tag{6.23}$$

Likewise, the voltages established in the various components of the electric circuit shown in Figure 6.18 are related to the analogue voltages of a cell, through factor n_{cell}. On the other hand, given that the cells are series connected, the current flowing through the cells is identical to that flowing through the supercapacitor's equivalent circuit. The series connection of the cells gives the SC a parasitic inductance which is included in the model through inductive parameter L_{SC} as shown in Figure 6.18.

6.3.2 Thermal model

The thermal energy generated in the SC interior during operation is dissipated into the environment as heat. This energy transfer can be expressed overall through a balance of heating powers [CEN07]:

$$\dot{Q}_{net} = \dot{Q}_{gen} - \dot{Q}_{ev} \tag{6.24}$$

In the expression above, $\dot{Q}_{gen}$ is the generated heat, in other words the electric power converted into heat. The term $\dot{Q}_{ev}$ is the dissipated heat from the SC into the environment. $\dot{Q}_{net}$ is the net heat, contributing to the SC heat energy variation. This heating power conditions the SC temperature variation through the term known as the thermal capacitance (C_{Th}):

$$\dot{Q}_{net} = C_{Th} \cdot \frac{dT}{dt} \tag{6.25}$$

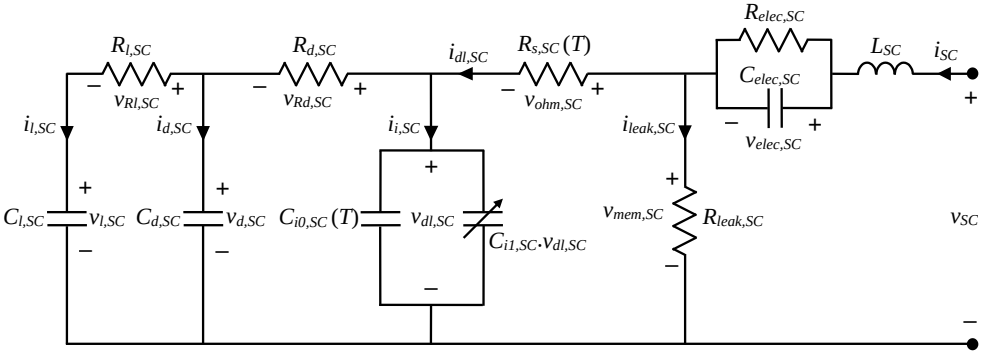

Figure 6.18: Electric model of the SC.

Physically, the heat transfer $\dot{Q}_{ev}$ to the environment occurs through a conduction phenomenon from the heat energy generating zone to the SC surface, and a convective phenomenon which transfers this energy to the surrounding air. The capacity of a material to conduct heat is measured by thermal conductivity (λ), which is defined as:

$$\lambda = -\frac{\dot{Q}_{cond}}{S_{cond} \cdot \frac{dT}{dx}} \tag{6.26}$$

whereby $\dot{Q}_{cond}$ is the heat transferred by conduction, S_{cond} is the transfer surface and $\frac{dT}{dx}$ the temperature gradient. In the case of composite materials, such as the SC, an equivalent thermal conductivity can be calculated for the materials as a whole.

Convection is the heat transfer mechanism occurring in a fluid as a result of the displacement of its molecules. In the case of heat transfer in an SC, this fluid is the air. Heat transfer by convection can be expressed by Newton's Law of Cooling:

$$\dot{Q}_{conv} = h \cdot S_{conv} \cdot (T_{sur} - T_{amb}) \tag{6.27}$$

where $\dot{Q}_{conv}$ is the heat transferred by convection, h is the convection heat transfer coefficient, S_{conv} is the surface area of the body in contact with the fluid, T_{sur} is the surface temperature of the body and T_{amb} is the ambient temperature.

In the SC thermal model design, the system was considered to be a compact, homogeneous body, bearing in mind that the heat generated is dissipated into the surrounding air, firstly through a conduction process and then through a thermal convection one. In this respect, the SC thermal model has been represented by the electrical equivalent circuit shown in Figure 6.19. Heat generation $\dot{Q}_{gen}$ is modelled as a current source dependent on the currents flowing through the resistors of the electric model shown in Figure 6.18. The natural conduction and convection processes are modelled as equivalent thermal resistance R_{Th} governed by the following expression:

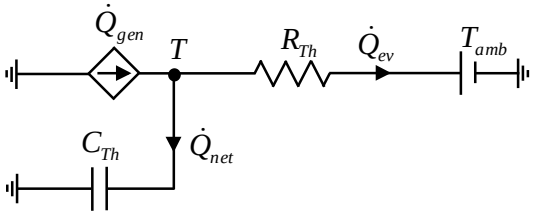

Figure 6.19: Thermal model of the SC.

$$R_{Th} = R_{cond} + R_{conv} = \frac{l_{cond}}{\lambda \cdot S_{cond}} + \frac{1}{h \cdot S_{conv}} \tag{6.28}$$

where l_{cond} is the mean length from the heat generating points up to the SC surface. This thermal resistance relates the dissipated heat flow with the difference between T and T_{amb}, as shown in the model in Figure 6.19. The analysis of this circuit gives the differential equation which makes it possible to calculate the SC operating temperature:

$$T = T_{amb} + R_{Th} \cdot \left[\dot{Q}_{gen} - C_{Th} \cdot \frac{dT}{dt}\right] \tag{6.29}$$

The SC dissipated power ($\dot{Q}_{gen}$) is calculated from the electric model shown in Figure 6.18, disregarding the entropic heat referred to in Subsubsection 6.2.4.5. The following expression is used:

$$\begin{aligned}\dot{Q}_{gen} =& \frac{v_{elec,SC}^2}{R_{elec,SC}} + R_{s,SC} \cdot i_{dl,SC}^2 + R_{d,SC} \cdot (i_{d,SC} + i_{l,SC})^2 \\ &+ R_{l,SC} \cdot i_{l,SC}^2 + R_{leak,SC} \cdot i_{leak,SC}^2\end{aligned} \tag{6.30}$$

6.3.3 Supercapacitor description and experimental setup

The experimental work reported through the following subsections was performed at the UPNA Energy Storage Laboratory described in Subsection 4.2.1 which is equipped with several Maxwell BMOD0083 supercapacitors [MAXa]. Each SC comprises 18 series-connected BCAP1500 P270 cells, each having a rated capacitance of 1500 F and a rated voltage of 2.7 V, giving the BMOD0083 supercapacitor a rated capacitance of 83 F and a rated voltage of 48 V. The SC cells comprise two activated porous carbon electrodes, separated by a cellulose membrane, and an organic electrolyte consisting of a quaternary salt tetraethylammonium tetrafluoroborate (TEATFB) solved in acetonitrile (AN). The SC housing is primarily aluminium, for high thermal conductivity, facilitating the dissipation of the heat generated during operation.

Figure 6.20 (a) shows the SC analysed herein whilst Figure 6.20 (b) shows the test bench developed to conduct the experimental tasks required. The SC is protected from cell overcurrents, overvoltages and overheating by a circuit breaker (compact NS 160 3P, Schneider Electric) coupled to a trip coil (TM100DC, Schneider Electric). The SC is connected, through this circuit breaker, to a programmable power source (SPS400x75K12D, Amrel) and a controllable electronic load (PLA4K-400-360-I, Amrel). The current profile supplied or drawn from the SC is externally programmed from a PC through a digital signal processor (DSP, DS 1104, dSpace). A frequency response analyser (FRA, Amrel) is also used in combination with the electronic load

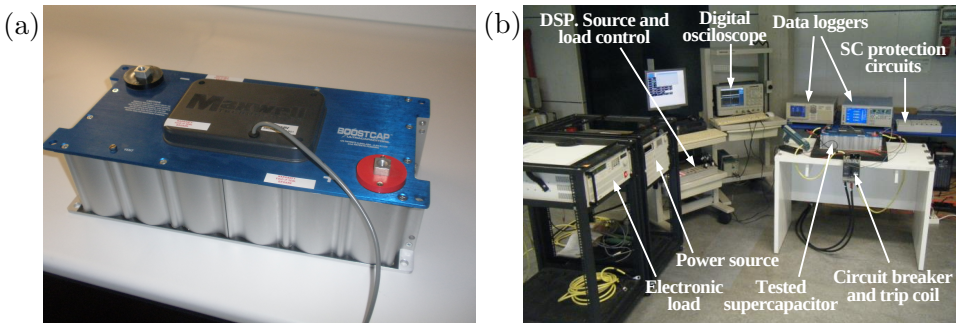

Figure 6.20: Supercapacitor experimental setup: photo of the Maxwell SC BMOD0083 (a) and SC test bench located in the UPNA Renewable Energies Laboratory (b).

in order to perform electrochemical impedance spectroscopy (EIS) test. The analysed physical variables are measured and recorded using a data loggers (WT 1800, Yokogawa) and a digital oscilloscope (TDS 5054, Tektronix). The characteristics of these equipment is detailed in Subsection 4.2.1, where the Energy Storage Laboratory (UPNA) is described.

6.3.4 Methodology and experimental design to obtain the model parameters

This subsection details the process to obtain the SC electric model (Figure 6.18) and thermal model (Figure 6.19) parameters implemented in Subsection 6.3.1 and Subsection 6.3.2 respectively. To do so, three experiment types are conducted: *a*, *b* and *c*. Experiment *a* consists in subjecting the SC to charge and discharge steps from 1 V up to 46 V and vice versa, with a value of $i_{SC} = \pm 75$ A for 10 hours, followed by a further 10 hours with the SC idle. In this way, operating temperature T increases during the first 10 hours and decreases again during the next 10 hours. Experiment *b* consists in providing the SC with a charge step of 40 A until it reaches 41 V, followed by a three-day open circuit period. Experiment *c* consists in conducting an EIS on the SC, maintaining T at 30 °C, v_{SC} at 30 V and a steady-state discharge current i_{SC} of 2 A. The amplitude of the sinusoidal perturbation of the small signal current is set at 5% of the steady-state value, and the frequency interval ranges from 10 mHz to 1 kHz.

Based on experiments *a*, *b* and *c*, a five stage method is developed to obtain the parameter values. The first stage consists in obtaining parameters $R_{s,SC}$, $R_{elec,SC}$ and $C_{elec,SC}$ through the analysis of the different points at which the charge and discharge steps occur in experiment *a*. Figure 6.21 (a)

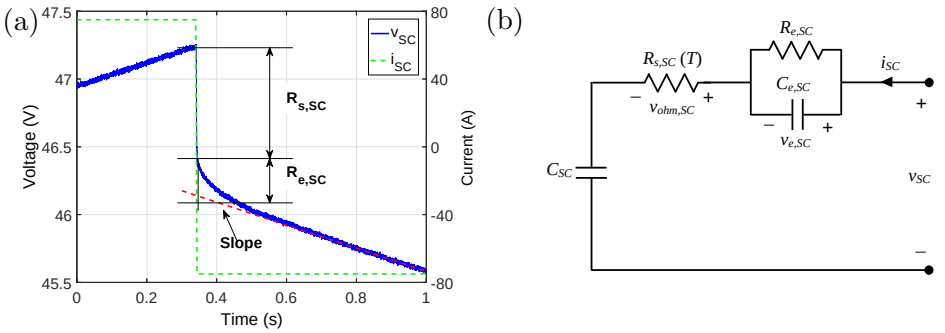

Figure 6.21: Fitting procedure for $R_{s,SC}(T)$ and $C_{elec,SC}$: SC voltage and current during an interval in experiment a (current step from 75 to –75 A at an operating temperature of 24.2 °C) (a) and simplified electric circuit considered for the fitting (b).

shows the evolution of v_{SC} in relation to the charge-to-discharge step in the experiment, where i_{SC} varies instantaneously from 75 to –75 A. In order to obtain the aforementioned parameters for experiment a, we use the simplified electric circuit shown in Figure 6.21 (b). The capacitance C_{SC} represents the SC capacitance at the operating point studied. This parameter needs to be calculated in order to obtain values $R_{s,SC}$, $R_{elec,SC}$ and $C_{elec,SC}$ for the SC electric model. To do so, we use the v_{SC} slope, as shown in Figure 6.21 (a) with a dashed line (slope). The value of C_{SC} is obtained from the following expression:

$$C_{SC} \approx i_{SC} \cdot \frac{\Delta t}{\Delta v_{SC}} \tag{6.31}$$

The MATLAB curve fitting toolbox is used to fit the equivalent circuit in Figure 6.21 (b) to v_{SC}, taking charge and discharge steps at 16 points with different T values. Figure 6.22 shows the parameter fits in relation to T. The fit of $R_{s,SC}$ has a negative slope with temperature whilst a constant evolution is shown for $R_{elec,SC}$ and $C_{elec,SC}$ as proposed in Subsection 6.3.1. In this way, parameter $R_{s,SC}$ is defined from its coefficients $R_{s0,SC} = 6.6253$ mΩ and $R_{s1,SC} = -2.57 \cdot 10^{-2}$ mΩ °C^{-1} through Equation 6.21 and parameters $R_{elec,SC}$ and $C_{elec,SC}$ take values of 2.4 mΩ and 28.4 F respectively as shown in Table 6.3.

In the second stage of the fitting method, an approximate value is obtained for parameters $C_{i,SC}$, $R_{d,SC}$, $C_{d,SC}$, $R_{l,SC}$ and $C_{l,SC}$, in addition to a definitive value for $R_{leak,SC}$, which serves as a starting point for the iterative fitting process explained in the third stage. To do so, we use the data of experiment b assuming a zero current flowing through certain model elements. Specifically, it is assumed that during the charge process shown in Figure 6.23 (a) (from 65

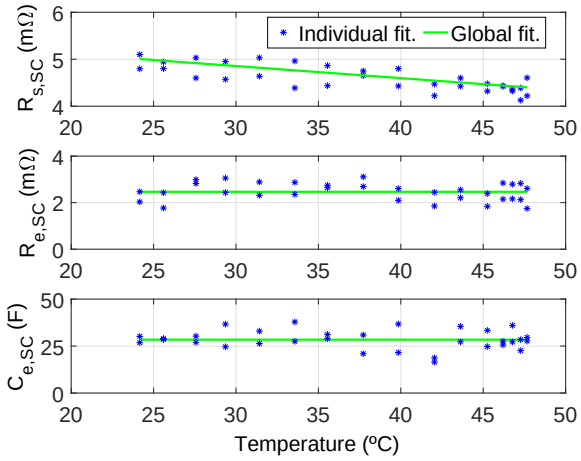

Figure 6.22: Fitting of parameters $R_{s,SC}$, $R_{elec,SC}$ and $C_{elec,SC}$ of the SC electric model in relation to its operating temperature.

to 150 s) $i_{SC} \approx i_{i,SC}$ given that delayed branch and long-term branch present time constants which are higher than that of the immediate branch by more than one order of magnitude. Using Equation 6.18 and Equation 6.19, through a fit to the corresponding first order circuit, we obtain an approximate value for $C_{i,SC}$ in relation to $v_{dl,SC}$ at a temperature of 27 °C whereby $C_{i,SC}(1) = 65.062 + 0.291 \cdot v_{dl,SC}$ F. On completion of the SC charging process and with the system left as an open circuit, an exponential voltage drop is observed. In this first iteration, it is also assumed that, for the period of time between 150 s and $3 \cdot R_{d,SC} \cdot C_{d,SC}$ the discharge of capacitance $C_{i,SC}$ is made through $C_{d,SC}$. In other words, in this time interval $i_{l,SC} \approx i_{leak,SC} \approx 0$ A, given that the time constant for the long-term branch is also higher than that of the delayed branch by more than one order of magnitude. We thus calculate the first approximation of values $R_{d,SC}(1) = 14.31\ \Omega$ and $C_{d,SC}(1) = 5.0383$ F through a fit with the MATLAB curve fitting toolbox. In the period of time from $3 \cdot R_{d,SC} \cdot C_{d,SC}$ to $3 \cdot R_{l,SC} \cdot C_{l,SC}$ it is assumed that the discharge incurred by $C_{i,SC}$ and $C_{d,SC}$, already established at the same voltage, occurs through $C_{l,SC}$, considering $i_{leak,SC} \approx 0$, given that $R_{leak} >> R_l$. In this way, through a fit similar to the previous ones, we obtain the values of $R_{l,SC}(1) = 150.23\ \Omega$ and $C_{l,SC}(1) = 6.1405$ F. Finally, once sufficient time has elapsed (approximately one day), the exponential trend of the voltage disappears. From that moment onwards, considering the leakage resistance to be the path for the SC discharges, we obtain a value of $R_{leak,SC} = 169.048$ kΩ.

In the third stage of the method, we use experiments a and b to develop

Table 6.3: Value of the parameters for the electric and thermal models of the SC for the Maxwell SC BMOD0083 (T in °C).

Param.	**Value**	**Unit**
$C_{i0,SC}$	$69.7527 - 0.079 \cdot T$	F
$C_{i1,SC}$	0.2543	$\mathrm{F\,V^{-1}}$
$C_{d,SC}$	8.92	F
$R_{d,SC}$	5.21	Ω
$C_{l,SC}$	9.68	F
$R_{l,SC}$	372.02	Ω
$R_{leak,SC}$	169.048	kΩ
$R_{s,SC}$	$6.63 - 2.79 \cdot 10^{-2}T$	mΩ
$C_{elec,SC}$	28.40	F
$R_{elec,SC}$	2.4	mΩ
L_{SC}	404	nH
R_{Th}	0.7086	$\mathrm{°C\,W^{-1}}$
C_{Th}	9670.81	$\mathrm{J\,°C^{-1}}$

an iterative process to allow us to firstly correct the error introduced in the parameters calculated in the previous stage, when ignoring currents $i_{d,SC}$, $i_{l,SC}$ and $i_{leak,SC}$ and, secondly, to study the variation of capacitance $C_{i,SC}$ with temperature. Firstly, we use a number of charge and discharge sections at 75 A from test a at different temperatures. Using the values of the parameters of the electric model calculated in the iteration above, it is possible to calculate the value of $i_{i,SC}$ based on the measurements of v_{SC}, and i_{SC}. Following the corresponding fit of a first order circuit to current $i_{i,SC}$ a value for $C_{i,SC}$ is obtained, being more accurate than the previous iteration. As shown in Figure 6.23 (b), for each iteration, data are available taken from different values for T, which makes it possible to add the thermal dependence to $C_{i,SC}$. Subsequently, with test b, we follow a similar process to that used in the first iteration, with the difference that, in the following iterations, we have an approximate value for the currents passing through each element of the model. In this way we calculate values $R_{d,SC}(k)$, $C_{d,SC}(k)$, $R_{l,SC}(k)$ and $C_{l,SC}(k)$ in the same way as for stage 2, obtaining increasingly more accurate values. After repeating this iterative process between 30 to 40 times, the parameter values converge into the following ones, as summarised in Table 6.3: $R_{d,SC} = 5.21$ Ω, $C_{d,SC} = 8.92$ F, $R_{l,SC} = 372.02$ Ω, $C_{l,SC} = 9.68$ F and term $C_{i,SC}$ is defined by coefficients $C_{i0,SC} = 69.7527$–$0.079 \cdot T$ F and $C_{i1,SC} = 0.2543\ \mathrm{F\,V^{-1}}$, as shown in Equation 6.20.

In the fourth stage of the method, we obtain the contact inductance L_{SC}, the only electrical parameter still required to complete the model in Figure 6.18. To do so, the c test was used, consisting in an EIS. The time

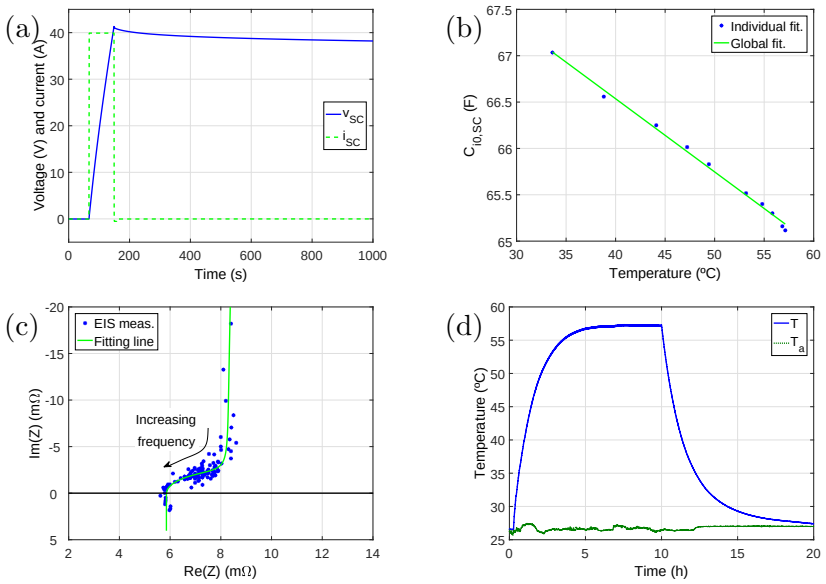

Figure 6.23: Measurements and fitted parameters for the proposed fitting method: 1000 seconds of experiment b (a), linear fitting of $C_{i0,SC}$ in relation to T with data from experiment a (b), Nyquist diagram obtained from an EIS experiment (c) and thermal evolution of the SC in experiment a (d).

required to go through the high frequencies of this EIS is very short ($\Delta t < 1$ s for a frequency interval from 10 Hz to 1 kHz). This ensures that there is little variation in the SC voltage and that the system is at a stable operating point. The equivalent impedance of the electric model is represented by the following expression:

$$Z = j\omega L_{SC} + \frac{1}{\frac{1}{R_{elec}} + j\omega C_{elec}} + \frac{1}{\frac{1}{R_{leak}} + \frac{1}{R_s + \frac{1}{j\omega C_i + \frac{1}{R_d + \frac{1}{j\omega C_d + \frac{1}{R_l + \frac{1}{j\omega C_l}}}}}}} = \mathrm{Re} + j \cdot \mathrm{Im} \tag{6.32}$$

All the parameters of the electrical equivalent circuit intervene in Equation 6.32, with inductance L_{SC} being the only unknown parameter. In order to obtain the value of L_{SC} the MATLAB curve fitting toolbox is used to fit Equation 6.32 to the data measured in the EIS conducted in experiment c as shown in Figure 6.23 (c). We therefore obtain a value of $L_{SC} = 404$ nH, as shown in Table 6.3.

In the fifth stage of the method, we obtain the parameters for the thermal model shown in Figure 6.19 based on the temperature data for test a. Fig-

ure 6.23 (d) shows the thermal evolution of the heating and cooling processes taking place in the SC during the 20 hour test. For the first 10 hours, the heating power generated by the SC ($\dot{Q}_{gen}$) is considered constant, given that $i_{SC} = \pm 75$ A, whilst in the last 10 hours it is assumed that $\dot{Q}_{gen} = 0$ W, given that $i_{SC} = 0$ A. The fitting of the heating circuit shown in Figure 6.19 is immediate, providing the values of parameters $R_{Th} = 0.7086$ °C W^{-1} and $C_{Th} = 9670.81$ J °C^{-1} as shown in Table 6.3.

6.3.5 Comparison of experimental and simulated results

6.3.5.1 Introduction to the validation of the electro-thermal modelling

The validation of the electro-thermal modelling is based on three experiments in which the SC is made to work in different operating modes. The experiments are programmed on the DSP controlling the electronic load and the power source. In turn, these experiments are reproduced in MATLAB-Simulink using the electric model (Figure 6.18) and thermal model (Figure 6.19) in order to compare the results obtained by simulation with the data measured in the said experiments. The input magnitudes for the models are current i_{SC} and temperature T_{amb}. The electric and thermal models interact to reciprocally provide information. While the electric model feeds the thermal model with the electric power loss, the thermal model provides the value of T, which allows the electric model to increase its accuracy. The results of the simulation are voltage v_{SC} and operating temperature T. Thus the operation of the SC is predicted and then compared with the measured results.

6.3.5.2 Validation of dynamic behaviour

To make a validation of the dynamic operating mode, the SC is subjected to sinusoidal currents with amplitudes ranging from 15 A to 60 A and at three different frequencies: 1 Hz, 10 Hz and 100 Hz. The mean value of v_{SC} and operating temperature T remained constant during the test (22.15 V and 25 °C respectively). Figure 6.24 shows the experimental and modelled current–voltage relationships ($i_{SC} - v_{SC}$) for each frequency with an amplitude of 15 A (a) and 60 A (b). The graphs show how an increase in the i_{SC} amplitude brings with it a greater variation in v_{SC}. On the other hand, it can be seen that, as the frequency increases the slope for the i_{SC}–v_{SC} relationships decreases due to the decrease in the SC equivalent resistance. The area formed in the interior of the i_{SC}–v_{SC} relationships, primarily reflects the SC capacitive behaviour.

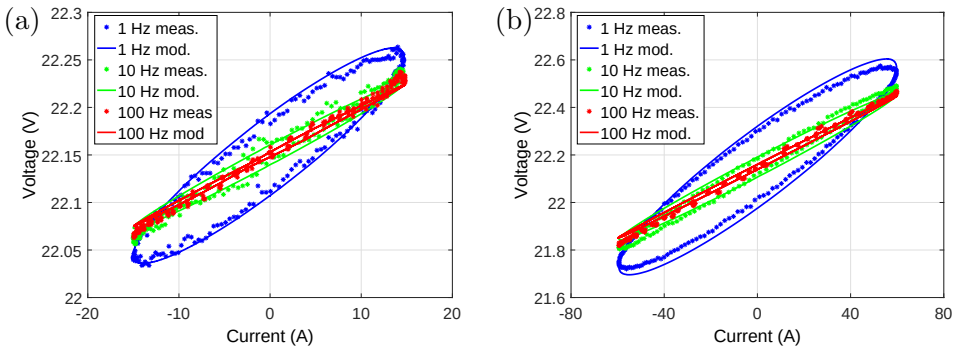

Figure 6.24: Validation test for the SC electric model in dynamic mode. Experimental $i_{SC} - v_{SC}$ relationships modelled for a T value of 25 °C and a mean v_{SC} value of 22.15 V. Sine wave currents with frequencies of 1, 10 and 100 Hz and amplitude 15 A (a) and 60 A (b).

However, as the frequency increases up to 100 Hz, the area of the i_{SC}–v_{SC} relationships decreases, given the fact that the SC gradually loses its capacitive nature.

For the various current frequencies and amplitudes shown in Figure 6.24, the results obtained from the electric model were suitably adjusted to the experimental ones. The validation of the model in this dynamic operating regime was considered to be satisfactory as it shows the capacity of the model to provide reliable results, without an increase in current frequency and amplitude involving significant losses of accuracy. The 15 A amplitude i_{SC}–v_{SC} shown in Figure 6.24 (a) obtained some RMSE values under 9 mV whilst the 60 A relationship shown in Figure 6.24 (b) provided RMSE values lower than 35 mV.

6.3.5.3 Validation of long term operation

Figure 6.25 shows the validation of the SC electric and thermal models through a long-term experiment, consisting in a two and a half hour stepped current mode (Figure 6.25 (a)), moving continuously from 75 A charging to 75 A discharging and vice versa, causing v_{SC} to oscillate between 2 V and 45 V. Figure 6.25 (b) shows the evolution of v_{SC} measured (v_{SC} *meas.*) and modelled (v_{SC} *mod.*) whilst Figure 6.25 (d), (e) and (f) show three 300 s zooms, each at different time points in the experiment. In general, high consistency can be observed between v_{SC} *mod.* and v_{SC} *meas.*, with an RMSE value in the test of 0.4323 V. The three zooms correspond to three different operating temperatures, that is 28 °C (Figure 6.25 (d)), 40 °C (Figure 6.25 (e)) and 54 °C

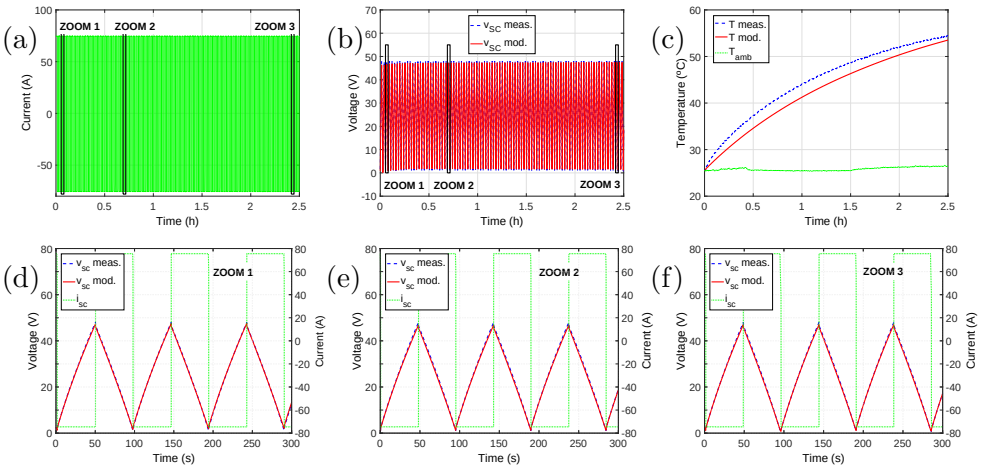

Figure 6.25: Endurance test for the SC electro-thermal modelling validation. Test variables: i_{SC} (a), v_{SC} (b) and T and T_{amb} (c). Zooms of i_{SC} and v_{SC} at different temperatures: 28 °C (d), 40 °C (e) and 54 °C (f).

(Figure 6.25 (f)). In the three zooms, v_{SC} *mod.* accurately fits v_{SC} *meas.*, with RMSE values of 0.42 V (Figure 6.25 (d)), 0.63 V (Figure 6.25 (e)) and 0.49 V (Figure 6.25 (f)). These similar RMSE values indicate that the dependence of parameters R_s and C_{i0} on T, as proposed in the electric model, makes it possible to maintain the accuracy of the same in a wide range of SC operating temperatures.

Figure 6.25 (c) shows the thermal evolution of the SC throughout the test. While T_{amb} maintains an approximate constant value of around 26 °C, T increases due to the energy losses taking place in the SC. The thermal model prediction is considered to adequately reproduce the thermal evolution of the SC, given that a 2.229 °C RMSE is obtained. This error is basically due to the simplifications of the actual physical system, which are assumed in order to obtain the thermal circuit of Figure 6.19.

6.3.5.4 Operation of an SC bank integrated into a microgrid

This subsubsection validates the electro-thermal modelling of an SC bank operating in a real-life operating environment consisting of the electric microgrid described in Subsection 4.2.3.The ESS herein studied is a hydrogen-based energy storage system which complemented with SCs in order to enhance its capability and working conditions (see Figure 6.26 (a)). The hydrogen based system comprises four series-connected proton exchange membrane fuel cells

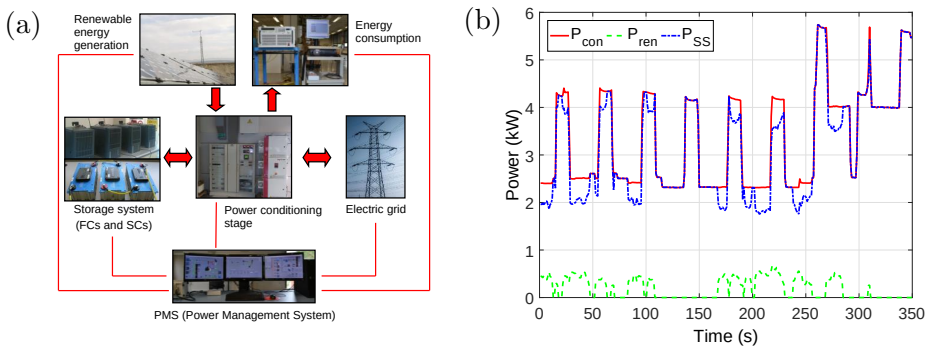

Figure 6.26: Microgrid used for the real-scenario model validation: schematic diagram of the electric microgrid (a) and power generated by the renewable sources (P_{ren}), power consumed (P_{con}) and power assumed by the microgrid storage system (P_{SS}) corresponding to 20:00 h on the 12th December 2012.

(PEM FCs) with a total rated power of 4.8 kW. The SC bank comprises three series connected BMOD0083 SCs which, in turn, are connected in parallel directly to the FCs, as shown in Figure 6.12 (a).

The experiment used for the validation of the electro-thermal modelling of the SC bank is the real microgrid operating interval of 350 s mentioned in Subsubsection 6.2.5.3 (see Figure 6.12 (b)). Figure 6.26 (b) shows the power consumed by the home (P_{con}), the power generated by the renewable system (P_{ren}) and the power supplied by the storage system (P_{SS}) for this time interval. P_{con} has a mean value close to 3 kW in the first 250 s of the test, which then rises to a mean value of approximately 4.5 kW. On the other hand, during the experiment P_{ren} records values between 0 W and 680 W with rapid, random variations inherent in the wind power resource. The storage system assumes the difference between P_{con} and P_{ren}, which is always positive in this case.

Figure 6.27 shows the currents and voltage in the storage system, comprising the FCs and SCs for the microgrid power profile represented in Figure 6.26 (b). Given that, in this experiment, the storage system is operating as a generator, a change has been made to the sign convention used in the equivalent circuit of Figure 6.18. Therefore, the current is positive when it leaves the SCs or FCs and is otherwise negative. Figure 6.27 (a) shows the storage system current (i_{SS}). Its variation range goes from a minimum value of 18 A to a maximum of 64 A at the end of the test. Part of this current is supplied by the FCs (i_{FC}) whilst the other part is supplied by the SCs (i_{SC}). The i_{FC} shows a smooth evolution throughout the test, as shown in Figure 6.27 (a),

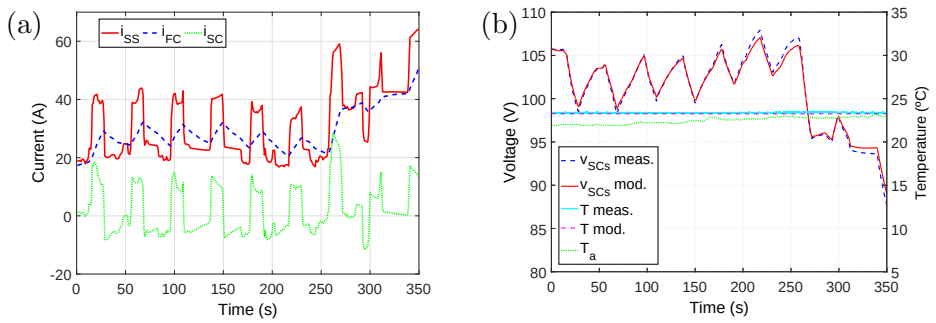

Figure 6.27: Experiment and simulation of the integration of a bank of SCs in the microgrid, corresponding to 20:00 h on the 12th December 2012. Storage system current (i_{SS}), SCs current (i_{SC}) and FCs current (i_{FC}) (a) and SCs voltage (v_{SCs}), SCs operating temperature (T) and ambient temperature T_{amb} (b).

with a mean value similar to the i_{SS}. On the contrary, the i_{SC} current shows more abrupt variations and a mean value close to 0 A. In other words, the SCs assume the rapid current variations, allowing the FCs to follow slower dynamics. In this respect, the incorporation of the SCs in the storage system, allows the FCs to operate with slower dynamics, thereby increasing their useful life.

Figure 6.27 (b) shows the storage system voltage, which is the same as for the SC bank (v_{SCs}), the SC operating temperature (T) and the ambient temperature of the room holding the storage system (T_{amb}). There are no great changes in v_{SCs} as the FCs do not allow this voltage to fall below 80 V. The maximum value of v_{SCs} during the test is 107 V (t = 257 s) and the minimum is 88.5 V (t = 350 s). The results obtained with the modelling of the SC bank voltage (v_{SCs} *mod.*) show an adequate and reliable behaviour compared to the voltage measured during the experiment ($v_{SCs\ meas.}$), with an RMSE in the v_{SCs} prediction of 0.457 V. The heating value of the SCs during the test is not very high, as the test was of short duration. Therefore, the thermal model is able to predict the operating temperature with an RMSE of just 0.125 ºC. From the analysis in this subsection, it can be concluded that the SC's electric and thermal models are scalable, allowing the connection of a number of SCs and, furthermore, they are accurate when simulating real-time operating environments in an electric microgrid.

6.4 Summary and outlook

As detailed in this chapter, SCs are an energy storage technology which is of increasing interest due to the growing need for robust ESSs able to manage

high power peaks. This chapter provides a broad overview of the technology with particular focus on the electrical characteristics. To do so, SCs are firstly compared with other storage technologies and are identified as devices that bridge the gap between batteries and conventional capacitors with regard to power and energy density. The physical principles that are the basis of SC performance (double layer, pseudocapacitance and faradaic processes) are also explained based on research papers published on these topics. These physical principles are then related to the electrical characteristics derived from each one, which is of particular interest for an optimal application of SCs in electrical systems. Subsequently, a compilation is made of the most promising materials used as electrodes and electrolytes, proposing a classification of the SCs based on these materials and also describing the electrical implications of the material properties.

A detailed analysis of the most noteworthy electrical phenomena observable in an SC is then presented. In this regard, capacitance and differential capacitance are described, and the difference between both parameters is clarified. The implications of charge distribution mechanisms along the electrode surface are covered, as well as the ohmic phenomena, which entail a voltage drop proportional to current. Electrical self-discharge and the high-frequency operation of SCs are also analysed based on their implications on SC performance. Given the importance of energy and power density for the analysis of ESSs, these two concepts are detailed and sensible expressions used in the literature to particularise their calculation for SCs are stated.

The most common modelling approaches are summarised in this chapter. The starting point is models based on electrochemical phenomena, which are the historical origin of the understanding of SCs. This is followed by a summary of the most important molecular modelling ideas, given the importance of these models for the SC design and manufacturing process. The next modelling trend is that of electrical circuit models, which are divided into transmission-line models, whose advantages and disadvantages are discussed, and simplified analytical models, which are electrical circuit models obtained by the simplification of physical equations. Finally, thermal modelling is also covered and the importance of thermal management for the safe performance and long lifetime of SCs is highlighted. In addition to the most important recent ideas related to each of these model approaches, some future research topics are highlighted, and experimental procedures for the characterization of the SC behaviour, analysed by each modelling technique, are critically described.

Besides, the SC manufacturing process is summarised, and a table with the key features of commercial products is provided, and the applications sug-

gested by the manufacturers are also addressed. An analysis of the current SC market divided into its four sectors (transport, energy, industrial and consumer electronics) is presented with recent examples of successful engineering applications in which SCs play a key role as ESSs, both by themselves and in combination with a battery or other ESS, as well as research papers in which improvements and new ideas for these needs are proposed.

Finally, an electrochemical–thermal model based on the physicochemical phenomena taking place in each cell is developed. For this purpose, we present an electric model and a thermal model in the form of electrical equivalent circuits in which each significant phenomenon is represented. The configuration of the SC electric model is principally based on the following phenomena: double layer; solvation and desolvation of the electrolyte ions; process dynamics of the ion penetration in the electrode pores; ohmic losses; and SC self-discharge. With regard to the thermal model, the SC has been considered to be a compact, homogeneous body which uniformly generates heat throughout. Taking account of the heat conduction and convection processes, the thermal model obtained is able to predict the SC operating temperature in relation to its operating mode. The prediction of the operating temperature has made it possible to introduce a thermal dependence in some of the electric model parameters in order to maintain its accuracy in a wide operating range.

The SC market is experiencing a remarkable expansion, which needs to be accompanied by engineering efforts to design the most advantageous storage system for each application, which may take advantage of the synergies arising from a combination of different storage technologies. Thus, the understanding and modelling of ageing mechanisms for different devices and the design of control strategies to minimise this effect are taking on increasing importance.

The high power capability, exceptional efficiency, decreasing price, ability to operate in hostile environments, low maintenance requirements and long lifetime offered by SCs are making this technology a desirable option for the increasing number of electrical applications requiring an outstanding ESS.

Chapter 7

Conclusions and future lines

You do not really understand something unless you can explain it to your grandmother.

– Albert Einstein

7.1 Conclusions

In the current scenario of both increasing electrification of the automotive sector and rising penetration of renewable energies, energy storage systems with high energy and power density, long lifetime and high efficiency are required to allow these changes. Lithium-ion batteries and supercapacitors are put forward as suitable ESSs for these applications for being modular and affordable systems offering a wide range of design and management alternatives.

During the past decade, the consumer electronic sector brought about the development of Li-ion batteries, being this type of ESS the most common option for electronic devices since the past decade. The recent rise of the electric vehicle market, requiring high energy density and an outstanding power–energy ratio are entailing a fast technology development and cost reduction of these batteries. Many technology outlooks predict Li-ion batteries to be a main option for electricity grid storage during the following years, given that the expected requirements coming from the increase of renewable energy generation share fit with the characteristics offered by Li-ion batteries.

The supercapacitor market has currently a smaller size than the Li-ion market. However, the high SC performance related to power density, life-

time, temperature range and high frequency operation also make these ESS an interesting option to be analysed for the design of hybrid ESS required in particular applications.

The updated review of the current state of both energy storage technologies accomplished through this thesis, with special emphasis on its applicability for engineering systems, reveals the improving performance and reducing costs that both technologies are undergoing. Specifically, the cost of Li-ion battery is sinking year after year, and SC are expected to experience an analogous effect during the upcoming years. Moreover, the variety of applications, including electric vehicles and electricity grid support, in which these elements are playing a main role, has been covered and explained.

These technologies have been analysed from a modelling point of view based on their operating principles. This has allowed the establishment of a relationship between the ESS operating principles and its electrical performance by means of electrochemical modelling. Therefore, the proposed models provide useful information about the most suitable management strategies for these systems. Effects such as the role played by the SEI (anode–electrolyte interphase) and the ion diffusion mechanisms in the variable equivalent resistance of a battery operating at different frequencies; the differences between the ion diffusion in the electrode and in the membrane in a Li-ion battery; and the influence of electrode porosity in the loss of usable capacitance of a SC for increasing frequency are some of the most important relationships analysed with the models herein proposed.

The thermal behaviour of both ESS has been also studied by means of the analysis and simplification of heat generation an dissipation processes. These models have been designed to be able to interact with the above-mentioned electrochemical model and enlarge their accuracy for wider operating temperature. The relationships between electrochemical and thermal phenomena are established, and particularly the influence of the operating temperature on the value of the main elements of the electrochemical model. These parameters determine in turn the generated heat and, therefore, the operating temperature.

After the proposal of these models for Li-ion batteries and SCs, parameter fitting procedures have been proposed. These fitting methods include a number of experimental tests that have been unequivocally described in order to allow its replica by any researcher with the equipment of an Electrical Engineering laboratory. After these characterisation experimental designs, parameter fitting methods for both Li-ion battery model and SC model have been proposed. These methods are divided into a number of well ordered and

clearly differentiated steps, which could be programmed in a software to allow an automatic calculation of the model parameters using the experimental measurements.

In addition, various trends proposed in the literature for SOC estimation have been analysed with a perspective of their inclusion in the battery BMS. Through this comparison, the benefits that a higher complexity in the estimation algorithm has on the estimation results are quantified. Therefore, each estimator has been addressed to be used in different applications depending on their requirements and characteristics, and the reliability of these methods has been experimentally measured.

The work described in the previous paragraphs has been validated through experimental tests by means of both a commercial Li-ion battery with a nominal voltage of 133 V and a capacity of 5.3 kWh, and a Maxwell supercapacitor (48 V, 82 F). With this aim, validation experiments have been designed to cover the whole operating range, including different temperatures, static and dynamic performance, high and low current, real-system requirements, etc. For the real scenario, an experimental microgrid located at the UPNA Renewable Energies Laboratory has been used, given the convenience of the Li-ion batteries and SCs for the requirements of electrical microgrids. The modelling accuracy for both ESSs slightly varies for different operating conditions, and the obtained results are satisfactory and useful to validate the proposed models.

Subsequently, an optimisation method to size Li-ion batteries has been proposed based on an algorithm for energy dispatch optimisation. This method has been applied to a a PV plant connected to the medium voltage grid. A realistic, mid-term regulative and economic scenario has been proposed and the usefulness of the optimisation tool to achieve the maximum revenue from an energy storage system has been quantified. This tool has important advantages. Firstly, it has a high versatility, since it can be adapted to very diverse scenarios through the inclusion of a model for each implied system. It can also be directly applied to engineering problem solving, given that it calculates both the battery size based on historical data series and an energy dispatch plan consisting in the power that has to be managed by the battery during each time step, which can be used as the input signal for the bidirectional battery power converter.

Finally, the importance that ageing phenomena have on the sizing, management and control of an energy storage system has been identified. An ageing model for Li-ion batteries has been proposed based on the ageing mechanisms identified in the literature and using the most common trend to build ageing

battery models. It is based on the division between calendar and cycle ageing, which effect on battery degradation is well distinguished. This ageing model has been validated by first simulating the normal operation of a commercial Li-ion battery system (Tesla Powerwall) and then comparing the model results with the manufacturer's guarantee. Due to time constrains, this ageing study has not been extended to experimental analysis.

7.2 Contributions

In this section, the main contributions of this thesis are presented

Predoctoral scholarship

The research presented in this thesis was awarded with public funding for the whole period of the thesis by means of a predoctoral scholarship for the training of university teachers given by the Spanish Ministry of Education, Culture and Sport. The call was published in the Spanish State Official Newsletter (BOE) on Thursday, 21 November, 2013, and the awarded scholarship code is FPU 13/00542.

Contributions to international journals

- A. Berrueta, A. Ursúa, P. Sanchis: *A comprehensive model for lithium-ion batteries: from the physical principles to an electrical model.* Energy, Submitted (under review).
- A. Berrueta, A. Ursúa, I. San Martín, A. Eftekhari, P. Sanchis: *Current state of supercapacitors, engineering applications, and future trends.* Progress in Energy and Combustion Science, Submitted (under review).
- A. Berrueta, I. San Martín, A. Hernández, A. Ursúa, P. Sanchis: *Electrothermal modelling of a supercapacitor and experimental validation.* Journal of Power Sources, 259, 154–165, (2014).

Contributions to international conferences

- A. Berrueta, I. San Martín, P. Sanchis and A. Ursúa: *Comparison of State-of-Charge Estimation Methods for Stationary Lithium-Ion Batteries.* In *IECON 2016 - 42nd Annual Conference of the IEEE Industrail Electronics Society*, pages 2010–2015, Florence (Italy), 2016.

- A. Berrueta, I. San Martín, P. Sanchis and A. Ursúa: *Hydrogen-lithium energy storage for a stand-alone microgrid.* In *21st World Hydrogen Energy Conference WHEC 2016*, Zaragoza (Spain), 2016.

- A. Berrueta, V. Irigaray, P. Sanchis and A. Ursúa: *Lithium-ion battery model and experimental validation.* In *2015 17th European Conference on Power Electronics and Applications (EPE'15 ECCE-Europe)*, Geneva (Switzerland), 2015.

- A. Berrueta, I. San Martín, A. Ursúa and P. Sanchis: *Static and dynamic characterization of a supercapacitor.* In *2nd International Forum on Progress and Trends in Battery and Capacitor Technologies. Power Our Future 2014*, Vitoria (Spain), 2014.

Participation in public R&D projects

- "Integration of renewable energy in the electricity grid by means of advance energy storage systems", R&D Navarre Plan, Government of Navarre, 2017.

- "Advanced electronic power converters for grid integration of wind and photovoltaic systems", R&D National Plan, DPI2016-80641-R, Spanish Ministry of Economy, Industry and Competitiveness, 2017–2019.

- "Hybridisation of advanced electricity storage systems for renewable energy plants", R&D National Plan, DPI2016-80642-R, Spanish Ministry of Economy, Industry and Competitiveness, 2016–2019.

- "Integration of advance energy storage systems in renewable-sources based microgrids", Caja Navarra call for R&D projects, Fundación Bancaria Caja Navarra, 2015–2016.

- "Technologies for the grid integration of renewable energies: power electronics, storage, energy management and interaction", R&D National Plan, DPI2013-42853-R, Spanish Ministry of Economy and Competitiveness, 2014–2017.

Supervision of undergraduate final year projects

Moreover, the research work done through the thesis has allowed the accomplishment of three undergraduate final year projects, which were co-directed by the author of this thesis. The projects and the students supervised are:

- A. Martínez de Narvajas: *Analysis of lithium-ion battery ageing*, Final year project, bachelor's degree in Industrial Engineering. UPNA, 2016.
- J. Mangado: *Electro-thermal characterization and modelling of a lithium-ion battery*, Final year project, bachelor's degree in Electrical Engineering. UPNA, 2015.
- V. Irigaray: *Electrochemical modelling and experimental validation of the electrical performance of a lithium-ion battery system*, Final year project, bachelor's degree in Electrical Engineering. UPNA, 2014.

7.3 Future lines

7.3.1 Design and implementation of hybrid electro-thermal energy storage systems to increase the share of renewable energy

The generalisation of electric energy storage to electro-thermal energy storage should be studied in order to increase the use of renewable energies. This concept has special interest in situations where electrical and thermal systems are settled together, for instance, in residential buildings or districts.

Traditionally, the electrical and thermal systems of residential buildings have been considered as independent and isolated systems, given that heating is usually fed by natural gas and it cannot interact with the electricity grid. However, the increasing willingness of reducing the use of fossil fuels is also affecting the heating sector. In order to achieve this goal, one of the best strategies is to use renewable electricity to cover at least part of the thermal demand of residential buildings by using heat pumps. As mentioned through the thesis, the main barriers for the utilisation of renewable energy at large scale are its intermittency, seasonality and highly dynamic behaviour. Therefore, energy storage technologies appear as the most promising solutions to overcome these barriers and increase the renewable fraction. In this context, there is a thrilling research area concerning the integration and best utilization of renewable energy, to satisfy the energy needs of residential buildings (heating, cooling and domestic hot water). And the best option to achieve this goal is a coupling of electrical and thermal energy storage technologies to a heat pump. The interest put on this technology is increasing and continuous improvements are reported.

An integration of the models proposed in this thesis with other models developed by different research groups concerning renewable energy genera-

tion, thermal energy storage, heat pumps and household consumption needs to be faced in order to tackle this future research line. Moreover, an interdisciplinary team should research different synergies that can be achieved from the joint design of an electro-thermal energy storage system, such as storing the heat evacuated by the electric ESS or using the thermal ESS to keep a constant and suitable temperature in the electric ESS. Moreover, besides the model proposed in this thesis, an improved version of the optimisation tool presented in Chapter 5 would turn into a key tool to size and manage the electro-thermal energy storage system, in such a way that the design criteria could be satisfied at a minimum cost.

7.3.2 In-the-loop SOC estimation algorithms

The study of state of charge estimators for Li-ion batteries accomplished throughout this thesis has made it possible to identify the most suitable characteristics of each algorithm for a particular application. This has been made by means of simulation and experimental validation. However, these algorithms have not been implemented in a real BMS to be run online while battery operation.

A particularly interesting field of study to quantify the benefits of each estimator is a microgrid. The most used management strategies for this kind of systems prevent the battery from being fully charged or discharged in such a way that there is always available capacity for either absorb energy surplus or provide unexpected power needs. Moreover, the battery is rarely kept in open circuit during several hours to allow the direct measurement of the open circuit voltage, given that home consumption is not usually interrupted. These issues, along with the interest of using cheap sensors that allow economic saves, put much interest on finding proper SOC estimation methods.

Therefore, an interesting study for a future research line would be to implement these estimators in the BMS of the experimental microgrid installed at UPNA and run the system continuously during several days or weeks. The improvements in the system performance and the effectiveness of the management strategies achieved by the inclusion of each SOC estimator could be quantified, as well as the associated BMS computational requirements. This real-field study would add an important extra value to the SOC estimator comparison made in this thesis, given that the problems associated with real sensors and characteristics of commercial BMS would be taken into account.

Moreover, this study would allow for the inclusion of heuristic improvements for the SOC estimators aimed at individualising these methods for each

particular renewable-energy application. This way, more useful estimators requiring lower computational effort are expected to be designed. These new algorithms, which could be already programmed in a BMS, would have a direct applicability to the improvement of both already installed microgrids and future plants.

7.3.3 Enhancements in battery size and energy dispatch optimisers

The energy dispatch optimiser reported in Chapter 5 is a non-linear heuristic optimiser that always reaches the battery dispatch plan that optimises the value of the objective function. This optimiser performs daily optimisations with hourly power variations. Therefore, the number of decision variables for each optimisation problem is 24 (the battery power during each hour of the day). Given that he computational time required for this optimisation exponentially increases with the number of decision variables, a time interval shorter than 1 hour is not feasible using this optimiser.

In order to account for faster dynamics in a renewable energy plant (cloudy sky, gusty wind, grid code requirements related to ramp following, voltage and frequency regulation, etc.) the optimisation interval should be reduced from 1 hour to 1 minute. This issue requires a radical change in the optimisation algorithm, which needs to handle, not 24, but 1440 decision variables. Given the proper design of the currently-used non-linear dynamic program algorithm and the multiple relative local optimums, a linearisation of the problem is expected to be required to handle such a large amount of decision variables. This linearisation would allow to use linear optimiser, such as Simplex, which are able to reach the optimal solution within a much shorter time compared to non-linear algorithm.

Besides, attention should be paid to the weather forecast. On the one hand, the effects that prediction errors have on the performance and revenue obtained by the renewable energy plant need to be quantified and related to the prediction algorithm and control strategy. On the other hand, forecast error compensation based on battery management should be analysed and taken into account for the energy dispatch and battery size optimisation. The quantification of these achievements would bring more interest in the optimiser from the applicability point of view, given that disturbances due to weather forecast errors are inherent to renewable energy generation.

Finally, the ageing of Li-ion batteries needs to be further analysed. Ageing experiments should be designed for several types of Li-ion batteries in order

to improve the accuracy of the proposed ageing model. To do so, a battery ageing experimental bench should be built at the Energy Storage Laboratory, where various cells could be cycled at a controlled temperature during several weeks or months while recording the measurements. Battery ageing is one of the main current concerns for companies engaged in battery assembly or management. Temperature control, assembly design, charge and discharge control and maximum and minimum allowed SOC are some of the hot topics that affect the selection of the best Li-ion battery, and they are all strongly dependent on the battery ageing, what proves the importance of an accurate knowledge of the ageing phenomena.

7.3.4 Designing of advanced power converters and management strategies for ESS based on the proposed models

The electrochemical and thermal models proposed for Li-ion batteries and SCs accurately predict the performance of these systems when subjected to particular working conditions. Moreover, if these models are combined with accurate ageing models, the reliability of the results would be increased.

Ingeper is the research group in which this thesis has been carried out. The name comes form the acronym in Spanish of *Electrical Engineering, Power Electronics and Renewable Energies*. The knowledge that the researchers of this group have about power electronic converters topologies and control could be combined with the above-mentioned battery models in order to design power converters that enhance the battery capabilities, allowing price reduction of the energy storage system. Topics such as the power converter commutation, maximum charging and discharging power and optimal current profile to allow a fast charging while keeping a long battery lifetime are some of the topics that are still to be studied and that can bring important improvements in markets such as electric vehicle charger stations and stationary ESSs for renewable energy plants.

7.3.5 Analyse design methods for hybrid Li-ion battery and SC energy storage systems

The improvement of the energy dispatch optimiser proposed in Subsection 7.3.3 would allow for the study of the hybridisation of different energy storage technologies by means of mathematical optimisation. This optimiser improvement is required to be tackled prior to the hybridisation analysis, given that the inclusion of new ESSs means a larger number of decision variables that cannot be handled by the current optimiser.

Due to their complementary characteristics, special interest may have the hybridisation of Li-ion batteries and SCs. The analysis of this issue would require the previous design of a SC ageing model. The robustness and long lifetime of SCs can enlarge the required experimental time, thereby hindering the design of a SC ageing model. However, the ageing model is crucial for the applicability of the optimisation algorithm, given that it determines the cost sharing of the energy storage system along its lifetime. Therefore, special effort should be placed in obtaining an accurate supercapacitor ageing model.

Given the wide range of characteristics offered by the different types of Li-ion batteries, the analysis of hybridisation options for several types of Li-ion batteries to be combined in an ESS is also interesting. Energy-oriented Li-ion batteries can be combined with power-oriented products with the aim of having a maximum performance of the ESS at a minimum price for each particular application.

Appendix A

Finite difference method. Application to heat conduction equation

A.1 Theoretical base of the method

This section explains the procedure followed for obtaining a finite difference expression from any differential equation [CHA87]. Only two general variables ξ and ν have been used because the results of the general heat transfer equation are also applied to two variables: space (x) and time (t).

Considering a function f with two independent variables:

$$f = f(\xi, \nu) \tag{A.1}$$

and an increment $\delta\xi$ in variable ξ, a forward Taylor expansion of the function at $\xi = \xi + \delta\xi, \nu = \nu$, in terms of its value at $\xi = \xi, \nu = \nu$, is:

$$f(\xi + \delta\xi, \nu) = f(\xi, \nu) + \delta\xi \left(\frac{\partial f}{\partial \xi}\right) + \frac{\delta\xi^2}{2}\left(\frac{\partial^2 f}{\partial \xi^2}\right)_{\xi,\nu} + \frac{\delta\xi^3}{6}\left(\frac{\partial^3 f}{\partial \xi^3}\right)_{\xi,\nu} + \vartheta\left(\delta\xi^4\right) \tag{A.2}$$

The last term of the expression indicates that subsequent terms are of the order of $\delta\xi^4$ or higher. If terms of the order of $\delta\xi^2$ or greater are neglected, the following forward finite difference approximation to the first derivative is

obtained, for a forward displacement $\delta\xi$ in the variable ξ.

$$\left[\left(\frac{\partial f}{\partial \xi}\right)_{\xi,\nu}\right]_f \approx \frac{1}{\delta\xi}\left[f(\xi+\delta\xi,\nu)-f(\xi,\nu)\right] \tag{A.3}$$

Similarly, for a forward displacement of $\delta\nu$ in the variable ν, the forward finite difference approximation for the first derivative is:

$$\left[\left(\frac{\partial f}{\partial \nu}\right)_{\xi,\nu}\right]_f \approx \frac{1}{\delta\nu}\left[f(\xi,\nu+\delta\nu)-f(\xi,\nu)\right] \tag{A.4}$$

Likewise, backward finite difference expressions for the first derivatives may be obtained by writing Taylor's expansions for an increment in ξ of $-\delta\xi$ or an increment of $-\delta\nu$ in ν:

$$f\left(\xi-\delta\xi,\nu\right)=f(\xi,\nu)-\delta\xi\left(\frac{\partial f}{\partial \xi}\right)+\frac{\delta\xi^2}{2}\left(\frac{\partial^2 f}{\partial \xi^2}\right)_{\xi,\nu}-\frac{\delta\xi^3}{6}\left(\frac{\partial^3 f}{\partial \xi^3}\right)_{\xi,\nu}+\vartheta\left(\delta\xi^4\right) \tag{A.5}$$

Again neglecting terms of order $\delta\xi^2$ and greater, the following expressions are obtained:

$$\left[\left(\frac{\partial f}{\partial \xi}\right)_{\xi,\nu}\right]_b \approx \frac{1}{\delta\xi}\left[f(\xi,\nu)-f(\xi-\delta\xi,\nu)\right] \tag{A.6}$$

$$\left[\left(\frac{\partial f}{\partial \nu}\right)_{\xi,\nu}\right]_b \approx \frac{1}{\delta\nu}\left[f(\xi,\nu)-f(\xi,\nu-\delta\nu)\right] \tag{A.7}$$

The central finite difference approximation to the second derivatives may be found by adding equations A.2 and A.5.

$$f\left(\xi+\delta\xi,\nu\right)+f\left(\xi-\delta\xi,\nu\right)=2f\left(\xi,\nu\right)+\delta\xi^2\left(\frac{\partial^2 f}{\partial \xi^2}\right)_{\xi,\nu}+\vartheta\left(\delta\xi^4\right) \tag{A.8}$$

When terms of the order of $\delta\xi^4$ and greater are neglected, the following expressions are obtained:

$$\left[\left(\frac{\partial^2 f}{\partial \xi^2}\right)_{\xi,\nu}\right]_{cent} \approx \frac{1}{\delta\xi^2}\left[f\left(\xi+\delta\xi,\nu\right)-2f\left(\xi,\nu\right)+f\left(\xi-\delta\xi,\nu\right)\right] \tag{A.9}$$

$$\left[\left(\frac{\partial^2 f}{\partial \nu^2}\right)_{\xi,\nu}\right]_{cent} \approx \frac{1}{\delta\nu^2}\left[f\left(\xi,\nu+\delta\nu\right)-2f\left(\xi,\nu\right)+f\left(\xi,\nu-\delta\nu\right)\right] \tag{A.10}$$

It is worth noting that the first derivative finite difference approximations neglect terms of the order of δ^2, while the second derivative approximations neglect terms of the order of δ^4. Furthermore, other approximations to the second derivative may be written, such as forward or backward. However, the central difference given here is most commonly used for heat conduction analyses [OZI94].

A.2 Application to heat conduction equation

Expression A.11 represents the heat conduction general equation [CHO98]. If the previous approximations are applied to it, a general expression for heat conduction expressed in finite differences can be obtained.

$$\lambda\left(\frac{\delta^2 T}{\delta x^2}+\frac{\delta^2 T}{\delta y^2}+\frac{\delta^2 T}{\delta z^2}\right)+\ \dot{q}=\rho\cdot cp\cdot\frac{\delta T}{\delta t} \tag{A.11}$$

In this study, the one-dimensional case is considered:

$$\lambda\frac{\delta^2 T}{\delta x^2}+\ \dot{q}=\rho\cdot cp\cdot\frac{\delta T}{\delta t} \tag{A.12}$$

As it has been explained, it is possible to write two finite difference expressions for the first derivative: forward and backward approximations. These expressions lead to two separate formulations of the finite difference method: explicit formulation and implicit formulation. It can be demostrated that, in the case of explicit formulation, if the chosen increment of time δt is too wide in relation with the increment of space δx, the solution can present an oscillating aspect that make the method useless [OZI94]. In order to avoid this problem, it is necessary to enormously restrict the time interval δt with respect the space interval δx, which inevitably increases the computational cost. In contrast, in the implicit solution, the increment of time does not need to be restricted regardless the chosen spacial increment. Hence, in this study implicit finite difference formulation has been chosen, as it is detailed now.

Implicit formulation is obtained expanding on the conduction equation in one-dimensional case (equation A.12) considering $x = x, t = t+\delta t$. If the first and second derivatives are replaced by equations A.7 and A.9, and in those f is substituted by T, ν by $t+\delta t$, ξ by x, $\delta\nu$ by δt and $\delta\xi$ by δx, the expression results in:

$$\frac{\lambda}{(\delta x)^2}\left[T\left(x+\delta x,t+\delta t\right)-2T\left(x,t+\delta t\right)+T\left(x-\delta x,t+\delta t\right)\right]+\dot{q} = \frac{\rho\cdot cp}{\delta t}\left[T\left(x,t+\delta t\right)-T\left(x,t\right)\right] \quad \text{(A.13)}$$

If subindexes a, b and c are used for expressing the position of the nodes in x, $(x-\delta x)$ and $(x+\delta x)$ respectively, T' represents temperature at time $t+\delta t$ and T expresses the temperature at time t, the previous expression changes to:

$$\frac{\lambda}{(\delta x)^2}\left({T_b}'-2{T_a}'+{T_c}'\right)+\dot{q_a}=\frac{\rho\cdot cp}{\delta t}\left({T_a}'-T_a\right) \quad \text{(A.14)}$$

This formulation allows obtaining the future temperature in point a $({T_a}')$ based on the actual temperature of that node (T_a) and the future temperatures of the surrounding points (T_i'). Equation A.14 can be rearranged in a standardized layout:

$$\frac{\lambda}{(\delta x)^2}\left({T_b}'-{T_a}'\right)+\frac{\lambda}{(\delta x)^2}\left({T_c}'-{T_a}'\right)+\dot{q_a}=\frac{\rho\cdot cp}{\delta t}\left({T_a}'-T_a\right) \quad \text{(A.15)}$$

Multiplying all the terms by the volume of node a $(V_a=S_a\delta x)$, where S_a is the area of node a, the following expression is obtained:

$$\frac{S_a\lambda}{\delta x}\left({T_b}'-{T_a}'\right)+\frac{S_a\lambda}{\delta x}\left({T_c}'-{T_a}'\right)+\dot{Q}_a=\frac{V_a\cdot\rho\cdot cp}{\delta t}\left({T_a}'-T_a\right) \quad \text{(A.16)}$$

Considering that $R_{i,j}$ is the thermal resistance between nodes i and j given by Equation A.17, so that $x_{i,j}$ is the distance between nodes, $A_{i,j}$ is the cross section between nodes and λ is the thermal conductivity of the medium. And considering that C is the thermal capacity of the medium given by Equation A.18, where *mass* represents the material's mass and *cp* its specific heat.

$$R_{i,j}=\frac{x_{i,j}}{\lambda S_{i,j}} \quad \text{(A.17)}$$

$$C=\rho\cdot V\cdot cp \quad \text{(A.18)}$$

The equation finally results in:

$$\frac{1}{R_{a,b}}\left({T_b}'-{T_a}'\right)+\frac{1}{R_{a,c}}\left({T_c}'-{T_a}'\right)+\dot{Q}_a=\frac{C_a}{\delta t}\left({T_a}'-T_a\right) \quad \text{(A.19)}$$

If this argumentation is extended to a larger number of surrounding nodes (the details of this extension are not explained in this thesis), the general equation for a node a surrounded by N nodes is expressed in Equation A.20, known as finite difference heat transfer equation.

$$\frac{1}{R_{a,1}}\left({T_1}' - {T_a}'\right) + ... + \frac{1}{R_{a_N}}\left({T_N}' - {T_a}'\right) + \dot{Q}_a = \frac{C_a}{\delta t}\left({T_a}' - {T_a}'\right) \qquad \text{(A.20)}$$

with

- $\dot{Q}_a$: Heat generation within node a.
- T_a: Temperature of central node a in time instant t.
- T_i with $i = 1, ..., N$: Temperature of the N surrounding nodes at time instant t.
- ${T_a}'$: Temperature of central node a at time instant $t + \delta t$.
- ${T_i}'$ with $i = 1, ..., N$: Temperature of the N surrounding nodes at time instant $t + \delta t$.
- $R_{a,i}$ with $i = 1, ..., N$: Thermal resistance between node a and each of the surrounding nodes.
- C_a: Themal capacity of node a.

Hence, the temperature of node a at time instant $t + \delta t$ is calculated based on the temperature of the node itself at instant t, and the temperatures of the N surrounding nodes at $t + \delta t$. This calculation also involves the physical characteristics of node a, represented by its thermal capacity (C_a), as well as the relation with the surrounding nodes expressed by the thermal resistances to node a ($R_{a,i}$). Finally, it appears a release or absorption of heat in the node itself $\left(\dot{Q}_a\right)$. If this equation is applied to each of the N nodes, the following system of equations results:

$$\boldsymbol{S}\ \boldsymbol{T}' = \boldsymbol{T} + \delta t \frac{\dot{\boldsymbol{Q}}}{\boldsymbol{C}} \qquad \text{(A.21)}$$

where

- $\boldsymbol{T}'$ is the vector with the $N + 1$ unknown temperatures at time instant $t + \delta t$.

- $\boldsymbol{T}$ is the vector with the $N+1$ temperatures at instant t.
- $\boldsymbol{C}$ is the vector with the $N+1$ thermal capacities.
- $\dot{\boldsymbol{Q}}$ is the vector in which all the heat fluxes are stored.
- $\boldsymbol{S}$ is the coefficient matrix of the system. Its dimensions are NxN. In positions (i,i).

Bibliography

[ABD14] Y. Abdul Quadir, T. Laurila, J. Karppinen, K. Jalkanen, K. Vuorilehto, L. Skogström, and M. Paulasto-Kröckel: *Heat generation in high power prismatic Li-ion battery cell with $LiMnNiCoO_2$ cathode material.* International Journal of Energy Research, 38(11):1424–1437, 2014.

[ABE08] A. Abedini and A. Nasiri: *Applications of super capacitors for PMSG wind turbine power smoothing.* In *2008 34th Annual Conference of IEEE Industrial Electronics*, pages 3347–3351, 2008.

[ACC16] Accuracy Research LLP: *Global Ultracapacitor Market Analysis and Trends – Industry Forecast to 2025.* technical report ACR12385, 2016.

[ADI] Adif, *Ferrolinera Project.* http://www.adif.es/es_ES/comunicacion_y_prensa/fichas_de_actualidad/ficha_actualidad_00072.shtml.

[AEM] AEMET and Gobierno de Navarra, *Meteorología y climatología de Navarra.* Online, http://meteo.navarra.es/estaciones/mapadeestaciones.cfm.

[AG16] AG: *Lithium Report 2016.* Report, Swiss Resource Capital AG, 2016.

[AL 00] S. Al Hallaj, R. Venkatachalapathy, J. Prakash, and J. R. Selman: *Entropy Changes Due to Structural Transformation in the Graphite Anode and Phase Change of the $LiCoO_2$ Cathode.* Journal of The Electrochemical Society, 147(7):2432–2436, 2000.

[AL 17] M. Al Zareer, I. Dincer, and M. A. Rosen: *Novel thermal management system using boiling cooling for high-powered lithium-ion battery packs for hybrid electric vehicles.* Journal of Power Sources, 363(Supplement C):291 – 303, 2017.

[ALB16] ALBEMARLE: *Global Lithium Market Outlook.* In *Goldman Sachs HCID Conference*, 2016.

[ALI17] ALISE, *Horizon 2020 research project*, 2017. Online, http://www.aliseproject.com/.

[ALL89] M. P. Allen and D. J. Tildesley: *Computer simulation of liquids.* Oxford university press, 1989. ISBN: 0-19-855375-7.

[AMI05] K. Amine, J. Liu, and I. Belharouak: *High-temperature storage and cycling of C-$LiFePO_4$/graphite Li-ion cells.* Electrochemistry Communications, 7(7):669 – 673, 2005.

[AND01] A. M. Andersson and K. Edström: *Chemical Composition and Morphology of the Elevated Temperature SEI on Graphite.* Journal of The Electrochemical Society, 148(10):A1100–A1109, 2001.

[APA10] S. Aparicio, M. Atilhan, and F. Karadas: *Thermophysical Properties of Pure Ionic Liquids: Review of Present Situation.* Industrial & Engineering Chemistry Research, 49(20):9580–9595, 2010.

[ARC16] D. Arcos Aviles, F. Guinjoan, M. P. Marietta, J. Pascual, L. Marroyo, and P. Sanchis: *Energy management strategy for a grid-tied residential microgrid based on Fuzzy Logic and power forecasting.* In *IECON 2016 - 42nd Annual Conference of the IEEE Industrial Electronics Society*, pages 4103–4108, 2016.

[ARC17] D. Arcos Aviles, J. Pascual, F. Guinjoan, L. Marroyo, P. Sanchis, and M. P. Marietta: *Low complexity energy management strategy for grid profile smoothing of a residential grid-connected microgrid using generation and demand forecasting.* Applied Energy, 205(Supplement C):69 – 84, 2017.

[ARI15] R. Arickx: *General Motors Company 2015 Global Business Conference*, 2015.

[ARO98] P. Arora, R. E. White, and M. Doyle: *Capacity Fade Mechanisms and Side Reactions in Lithium-Ion Batteries.* Journal of The Electrochemical Society, 145(10):3647–3667, 1998.

[AUR99] D. Aurbach, B. Markovsky, I. Weissman, E. Levi, and Y. Ein-Eli: *On the correlation between surface chemistry and performance of graphite negative electrodes for Li ion batteries.* Electrochimica Acta, 45(1):67 – 86, 1999.

[AUR05] D. Aurbach: *A review on new solutions, new measurements procedures and new materials for rechargeable Li batteries.* Journal of Power Sources, 146(1):71 – 78, 2005.

[BAH17] F. Bahiraei, M. Ghalkhani, A. Fartaj, and G.-A. Nazri: *A pseudo 3D electrochemical-thermal modeling and analysis of a lithium-ion battery for electric vehicle thermal management applications.* Applied Thermal Engineering, 125(Supplement C):904 – 918, 2017.

[BAL16] A. Balducci: *Electrolytes for high voltage electrochemical double layer capacitors: A perspective article.* Journal of Power Sources, 326:534 – 540, 2016.

[BAN11] T. M. Bandhauer, S. Garimella, and T. F. Fuller: *A Critical Review of Thermal Issues in Lithium-Ion Batteries.* Journal of The Electrochemical Society, 158(3):R1–R25, 2011.

[BAR01] A. J. Bard and L. R. Faulkner: *Electrochemical Methods: Fundamentals and Applications.* John Wiley & Sons, Inc, 2001. ISBN: 978-0-471-04372-0.

[BAR05] E. Barsoukov and J. R. Macdonald: *Impedance Spectroscopy: Theory, Experiment, and Applications.* John Wiley & Sons, Ltd., 3 ed., 2005. ISBN 978-0-471-64749-2.

[BAR17] S. Barsali, R. Giglioli, G. Lutzemberger, D. Poli, and G. Valenti: *Optimised operation of storage systems integrated with MV photovoltaic plants, considering the impact on the battery lifetime.* Journal of Energy Storage, 12:178 – 185, 2017.

[BAS83] S. Basu, *Ambient temperature rechargeable battery*, 1983. US Patent 4,423,125.

[BAZ14] S. J. Bazinski and X. Wang: *The Influence of Cell Temperature on the Entropic Coefficient of a Lithium Iron Phosphate (LFP) Pouch Cell.* Journal of The Electrochemical Society, 161(1):A168–A175, 2014.

[BEL57] R. Bellman: *Dynamic Programming.* Princeton University Press, Princeton, NJ, USA, 1 ed., 1957.

[BEN15] F. Bensmaine, O. Bachelier, S. Tnani, G. Champenois, and E. Mouni: *LMI approach of state-feedback controller design for a STATCOM–supercapacitors energy storage system associated with a wind generation.* Energy Conversion and Management, 96:463–472, 2015.

[BER85] D. Bernardi, E. Pawlikowski, and J. Newman: *A General Energy Balance for Battery Systems.* Journal of The Electrochemical Society, 132(1):5–12, 1985.

[BER14] A. Berrueta, I. San Martín, A. Hernández, A. Ursúa, and P. Sanchis: *Electrothermal modelling of a supercapacitor and experimental validation.* Journal of Power Sources, 259:154 – 165, 2014.

[BER15] A. Berrueta, V. Irigaray, P. Sanchis, and A. Ursúa: *Lithium-ion battery model and experimental validation.* In *Power Electronics and Applications (EPE'15 ECCE-Europe), 2015 17th European Conference on*, pages 1–8, 2015.

[BER16a] B. B. Berkes, A. Schiele, H. Sommer, T. Brezesinski, and J. Janek: *On the gassing behavior of lithium-ion batteries with NCM523 cathodes.* Journal of Solid State Electrochemistry, 20(11):2961–2967, 2016.

[BER16b] A. Berrueta, I. S. Martín, P. Sanchis, and A. Ursúa: *Comparison of State-of-Charge estimation methods for stationary Lithium-ion batteries.* In *IECON 2016 - 42nd Annual Conference of the IEEE Industrial Electronics Society*, pages 2010–2015, 2016.

[BHA15] N. Bhandari, R. Dua, L. Estevez, R. Sahore, and E. P. Giannelis: *A combined salt-hard templating approach for synthesis of multi-modal porous carbons used for probing the simultaneous effects of porosity and electrode engineering on EDLC performance.* Carbon, 87:29 – 43, 2015.

[BIZ15] A. Bizeray, S. Zhao, S. Duncan, and D. Howey: *Lithium-ion battery thermal-electrochemical model-based state estimation using orthogonal collocation and a modified extended Kalman filter.* Journal of Power Sources, 296(Supplement C):400 – 412, 2015.

[BLO03] I. Bloom, S. A. Jones, V. S. Battaglia, G. L. Henriksen, J. P. Christophersen, R. B. Wright, C. D. Ho, J. R. Belt, and C. G. Motloch: *Effect of cathode composition on capacity fade, impedance rise and power fade in high-power, lithium-ion cells.* Journal of Power Sources, 124(2):538 – 550, 2003.

[BLO17] N. Blomquist, T. Wells, B. Andres, J. Bäckström, S. Forsberg, and H. Olin: *Metal-free supercapacitor with aqueous electrolyte and low-cost carbon materials.* Scientific Reports, 7, 2017.

[BOH07a] O. Bohlen, J. Kowal, and D. U. Sauer: *Ageing behaviour of electrochemical double layer capacitors: Part I. Experimental study and ageing model.* Journal of Power Sources, 172(1):468 – 475, 2007.

[BOH07b] O. Bohlen, J. Kowal, and D. U. Sauer: *Ageing behaviour of electrochemical double layer capacitors: Part II. Lifetime simulation model for dynamic applications.* Journal of Power Sources, 173(1):626–632, 2007.

[BOR14] A. Bordes, K. Eom, and T. F. Fuller: *The effect of fluoroethylene carbonate additive content on the formation of the solid–electrolyte interphase and capacity fade of Li-ion full-cell employing nano Si-graphene composite anodes.* Journal of Power Sources, 257(Supplement C):163 – 169, 2014.

[BRA99] J. W. Braithwaite, A. Gonzales, G. Nagasubramanian, S. J. Lucero, D. E. Peebles, J. A. Ohlhausen, and W. R. Cieslak: *Corrosion of Lithium-Ion Battery Current Collectors.* Journal of The Electrochemical Society, 146(2):448–456, 1999.

[BRA07] E. J. Brandon, W. C. West, M. C. Smart, L. D. Whitcanack, and G. A. Plett: *Extending the low temperature operational limit of double-layer capacitors*. Journal of Power Sources, 170(1):225 – 232, 2007.

[BRA16] N. P. Brandon, J. Edge, M. Aunedi, P. G. Bruce, B. K. Chakrabarti, T. Esterle, J. W. Somerville, Y. L. Ding, C. Fu, P. S. Grant, et al.: *UK research needs in grid scale energy storage technologies*. White paper, Energy SUPERSTORE, Energy Storage Research Network and Engineering and Physical Science Research Council, 2016.

[BRA17] M. H. Braga, N. S. Grundish, A. J. Murchison, and J. B. Goodenough: *Alternative strategy for a safe rechargeable battery*. Energy Environ. Sci., 10:331–336, 2017.

[BRO03] M. Broussely, P. Blanchard, P. Biensan, J. Planchat, K. Nechev, and R. Staniewicz: *Properties of large Li ion cells using a nickel based mixed oxide*. Journal of Power Sources, 119(Supplement C):859 – 864, 2003.

[BRO05] M. Broussely, P. Biensan, F. Bonhomme, P. Blanchard, S. Herreyre, K. Nechev, and R. Staniewicz: *Main aging mechanisms in Li ion batteries*. Journal of Power Sources, 146(1):90 – 96, 2005.

[BRO15] T. Broussea, D. Bélangerc, and J. W. Long: *To Be or Not To Be Pseudocapacitive?* J. Electrochem. Soc., 162(5):A5185–A5189, 2015.

[BRU16] T. Bruen and J. Marco: *Modelling and experimental evaluation of parallel connected lithium ion cells for an electric vehicle battery system*. Journal of Power Sources, 310(Supplement C):91 – 101, 2016.

[BUC16] I. Buchmann: *Batteries in a portable world*. Cadex Electronics Inc., 2016. ISBN 978-0-9682118-4-7.

[BUR14] R. Burt, G. Birkett, and X. Zhao: *A review of molecular modelling of electric double layer capacitors*. Physical Chemistry Chemical Physics, 16(14):6519–6538, 2014.

[BUR15] A. Burke and H. Zhao: *Applications of supercapacitors in electric and hybrid vehicles*. In *5th European Symposium on Supercapacitor and Hybrid Solutions (ESSCAP), Brasov, Romania*, 2015.

[BUZ04] M. Buzzeo, R. Evans, and R. Compton: *Non-haloaluminate room-temperature ionic liquids in electrochemistry—A review*. ChemPhysChem, 5(8):1106–1120, 2004.

[CAI10] L. Cai and R. E. White: *An Efficient Electrochemical-Thermal Model for a Lithium-Ion Cell by Using the Proper Orthogonal Decomposition Method*. Journal of The Electrochemical Society, 157(11):A1188–A1195, 2010.

[CAI11] L. Cai and R. E. White: *Mathematical modeling of a lithium ion battery with thermal effects in COMSOL Inc. Multiphysics (MP) software*. Journal of Power Sources, 196(14):5985 – 5989, 2011.

[CAM10] M. B. Camara, H. Gualous, F. Gustin, A. Berthon, and B. Dakyo: *DC/DC Converter Design for Supercapacitor and Battery Power Management in Hybrid Vehicle Applications — Polynomial Control Strategy*. IEEE Transactions on Industrial Electronics, 57(2):587–597, 2010.

[CAM16] H. Camblong, S. Baudoin, I. Vechiu, and A. Etxeberria: *Design of a SOFC/GT/SCs hybrid power system to supply a rural isolated microgrid*. Energy Conversion and Management, 117:12–20, 2016.

[CAP15] C. Capasso, V. Sepe, O. Veneri, M. Montanari, and L. Poletti: *Experimentation with a ZEBRA plus EDLC based hybrid storage system for urban means of transport.* In *2015 International Conference on Electrical Systems for Aircraft, Railway, Ship Propulsion and Road Vehicles (ESARS)*, pages 1–6, 2015.

[CAR17] M. G. Carignano, R. Costa-Castelló, V. Roda, N. M. Nigro, S. Junco, and D. Feroldi: *Energy management strategy for fuel cell-supercapacitor hybrid vehicles based on prediction of energy demand.* Journal of Power Sources, 360:419 – 433, 2017.

[CAR18] J.-M. Cariolet, M. Colombert, M. Vuillet, and Y. Diab: *Assessing the resilience of urban areas to traffic-related air pollution: Application in Greater Paris.* Science of The Total Environment, 615(Supplement C):588 – 596, 2018.

[CAS16] A. Castaings, W. Lhomme, R. Trigui, and A. Bouscayrol: *Comparison of energy management strategies of a battery/supercapacitors system for electric vehicle under real-time constraints.* Applied Energy, 163:190–200, 2016.

[CAT12] Caterpillar, *Press release: Caterpillar announces development of largest hydraulic shovel*, 2012. http://www.cat.com/en_GB/news/machine-press-releases/caterpillar-announcesdevelopmentoflargesthydraulicshovel.html.

[CAZ16] P. Cazzola and M. Gorner: *Global EV outlook 2016.* Technical report, International Energy Agency, 2016.

[CEN07] Y. Cengel: *Heat Transfer: A Practica Approach.* McGraw-Hill, 2007. ISBN 9780073250359.

[CHA13] D. L. Chapman: *LI. A contribution to the theory of electrocapillarity.* The London, Edinburgh, and Dublin philosophical magazine and journal of science, 25(148):475–481, 1913.

[CHA87] A. J. Chapman: *Fundamentals of heat transfer.* Macmillan Publishing Company, New York, 1987.

[CHA98] E. J. Chaisson: *The cosmic environment for the growth of complexity.* Biosystems, 46(1):13 – 19, 1998.

[CHA13] M.-H. Chang, H.-P. Huang, and S.-W. Chang: *A New State of Charge Estimation Method for $LiFePO_4$ Battery Packs Used in Robots.* Energies, 6(4):2007–2030, 2013.

[CHA14] R. Chaari, O. Briat, and J.-M. Vinassa: *Capacitance recovery analysis and modelling of supercapacitors during cycling ageing tests.* Energy Conversion and Management, 82:37–45, 2014.

[CHE94] Y. Chen and J. W. Evans: *Three-Dimensional Thermal Modeling of Lithium-Polymer Batteries under Galvanostatic Discharge and Dynamic Power Profile.* Journal of The Electrochemical Society, 141(11):2947–2955, 1994.

[CHE96] Y. Chen and J. W. Evans: *Thermal Analysis of Lithium-Ion Batteries.* Journal of The Electrochemical Society, 143(9):2708–2712, 1996.

[CHE04] C. Chen, J. Liu, M. Stoll, G. Henriksen, D. Vissers, and K. Amine: *Aluminum-doped lithium nickel cobalt oxide electrodes for high-power lithium-ion batteries.* Journal of Power Sources, 128(2):278 – 285, 2004.

[CHE06a] M. Chen and G. A. Rincon-Mora: *Accurate electrical battery model capable of predicting runtime and I-V performance.* IEEE Transactions on Energy Conversion, 21(2):504–511, 2006.

[CHE06b] S.-C. Chen, Y.-Y. Wang, and C.-C. Wan: *Thermal Analysis of Spirally Wound Lithium Batteries.* Journal of The Electrochemical Society, 153(4):A637–A648, 2006.

[CHE13] Z. Chen, Y. Fu, and C. C. Mi: *State of Charge Estimation of Lithium-Ion Batteries in Electric Drive Vehicles Using Extended Kalman Filtering.* IEEE Transactions on Vehicular Technology, 62(3):1020–1030, 2013.

[CHE15] D. Chen, Q. Wang, R. Wang, and G. Shen: *Ternary oxide nanostructured materials for supercapacitors: A review.* Journal of Materials Chemistry A, 3(19):10158–10173, 2015.

[CHO98] Y. Cho, E. Ganic, J. Harnett, and W. Rohsenow: *Basic Concepts of Heat Transfer.* In *Handbook of Heat Transfer*, pages 1.1–1.37. McGraw-Hill Handbooks, New York, 3rd ed., 1998.

[CHO01] J. Cho, Y. J. Kim, T.-J. Kim, and B. Park: *Zero-Strain Intercalation Cathode for Rechargeable Li-Ion Cell.* Angewandte Chemie International Edition, 40(18):3367–3369, 2001.

[CHO02] S. S. Choi and H. S. Lim: *Factors that affect cycle-life and possible degradation mechanisms of a Li-ion cell based on $LiCoO_2$.* Journal of Power Sources, 111(1):130 – 136, 2002.

[CIC14] F. Ciccarelli, A. Del Pizzo, and D. Iannuzzi: *Improvement of energy efficiency in light railway vehicles based on power management control of wayside lithium-ion capacitor storage.* IEEE Transactions on Power Electronics, 29(1):275–286, 2014.

[CON99] B. E. Conway: *Electrochemical supercapacitors: Scientific fundamentals and technological applications.* New York, N.Y. Kluwer Academic, Plenum Publishers, 1999. ISBN: 978-1-4757-3058-6.

[CON14] M. Conte, A. Genovese, F. Ortenzi, and F. Vellucci: *Hybrid battery-supercapacitor storage for an electric forklift: a life-cycle cost assessment.* Journal of Applied Electrochemistry, 44(4):523–532, 2014.

[COW14] M. Cowell, R. Winslow, Q. Zhang, J. Ju, J. Evans, and P. Wright: *Composite carbon-based ionic liquid supercapacitor for high-current micro devices.* Journal of Physics: Conference Series, 557(1), 2014.

[CRO95] K. Croswell: *The alchemy of the heavens: searching for meaning in the Milky Way.* Anchor Books, 1995. ISBN 9780385472135.

[DAF10] B. Daffos, P.-L. Taberna, Y. Gogotsi, and P. Simon: *Recent Advances in Understanding the Capacitive Storage in Microporous Carbons.* Fuel Cells, 10(5):819–824, 2010.

[DE 63] R. de Levie: *On porous electrodes in electrolyte solutions.* Electrochimica Acta, 8(10):751 – 780, 1963.

[DE 89] R. de Levie: *On the impedance of electrodes with rough interfaces.* Journal of Electroanalytical Chemistry and Interfacial Electrochemistry, 261(1):1 – 9, 1989.

[DE 17] J. de Hoog, J.-M. Timmermans, D. Ioan-Stroe, M. Swierczynski, J. Jaguemont, S. Goutam, N. Omar, J. V. Mierlo, and P. V. D. Bossche: *Combined cycling and calendar capacity fade modeling of a Nickel-Manganese-Cobalt Oxide Cell with real-life profile validation.* Applied Energy, 200(Supplement C):47 – 61, 2017.

[D'E14] A. d'Entremont and L. Pilon: *First-principles thermal modeling of electric double layer capacitors under constant-current cycling.* Journal of Power Sources, 246:887–898, 2014.

[DEV14a] N. Devillers, S. Jemei, M.-C. Péra, D. Bienaimé, and F. Gustin: *Review of characterization methods for supercapacitor modelling*. Journal of Power Sources, 246:596–608, 2014.

[DEV14b] N. Devillers, M.-C. Péra, D. Bienaimé, and M.-L. Grojo: *Influence of the energy management on the sizing of Electrical Energy Storage Systems in an aircraft*. Journal of Power Sources, 270:391 – 402, 2014.

[DÍA12] F. Díaz González, A. Sumper, O. Gomis-Bellmunt, and R. Villafáfila-Robles: *A review of energy storage technologies for wind power applications*. Renewable and sustainable energy reviews, 16(4):2154–2171, 2012.

[DON15] G. Dong, X. Zhang, C. Zhang, and Z. Chen: *A method for state of energy estimation of lithium-ion batteries based on neural network model*. Energy, 90(Part 1):879 – 888, 2015.

[DOU02] D. H. Doughty, P. C. Butler, R. G. Jungst, and E. Roth: *Lithium battery thermal models*. Journal of Power Sources, 110(2):357 – 363, 2002.

[DOW17] J. Dow, *Tesla christens Buffalo solar factory "Gigafactory 2", will finalize locations of Gigafactory 3, 4 and possibly 5 this year*, 2017. Online, https://electrek.co/2017/02/22/tesla-christens-buffalo-solar-factory-gigafactory-2-will-finalize/-locations-of-gigafactory-3-4-and-possibly-5-this-year/.

[DRE16] W. Dreyer, C. Guhlke, and R. Muller: *A new perspective on the electron transfer: recovering the Butler–Volmer equation in non-equilibrium thermodynamics*. Phys. Chem. Chem. Phys., 18:24966–24983, 2016.

[DRI08] A. Driesse, P. Jain, and S. Harrison: *Beyond the curves: Modeling the electrical efficiency of photovoltaic inverters*. In *2008 33rd IEEE Photovoltaic Specialists Conference*, pages 1–6, 2008.

[DRU15] R. Drummond, D. A. Howey, and S. R. Duncan: *Low-order mathematical modelling of electric double layer supercapacitors using spectral methods*. Journal of Power Sources, 277:317 – 328, 2015.

[DRU17] R. Drummond, S. Zhao, D. Howey, and S. Duncan: *Circuit synthesis of electrochemical supercapacitor models*. Journal of Energy Storage, 10:48 – 55, 2017.

[DUD17] B. Dudley, *BP Statistical Review of World Energy*, 2017.

[DUF15] R. Dufo López and J. L. Bernal-Agustín: *Techno-economic analysis of grid-connected battery storage*. Energy Conversion and Management, 91:394 – 404, 2015.

[DVO14] D. Dvorak, H. Lacher, and D. Simic: *Thermal Modeling and Validation of a Lithium-Ion Battery Based on Electric Vehicle Measurements*. In *2014 IEEE Vehicle Power and Propulsion Conference (VPPC)*, pages 1–6, 2014.

[EDD13] A. Eddahech, M. Ayadi, O. Briat, and J.-M. Vinassa: *Online parameter identification for real-time supercapacitor performance estimation in automotive applications*. International Journal of Electrical Power & Energy Systems, 51:162–167, 2013.

[EDO16] C. Edouard, M. Petit, C. Forgez, J. Bernard, and R. Revel: *Parameter sensitivity analysis of a simplified electrochemical and thermal model for Li-ion batteries aging*. Journal of Power Sources, 325(Supplement C):482 – 494, 2016.

[EFT15a] A. Eftekhari and F. Molaei: *Carbon Nanotube-Assisted Electrodeposition. Part I: Battery Performance of Manganese Oxide Films Electrodeposited at Low Current Densities.* Journal of Power Sources, 274:1306–1314, 2015.

[EFT15b] A. Eftekhari and F. Molaei: *Carbon Nanotube-Assisted Electrodeposition. Part II: Superior Pseudo-Capacitive Behavior of Manganese Oxide Film Electrodeposited at High Current Densities.* Journal of Power Sources, 274:1315–1321, 2015.

[EFT16] A. Eftekhari, Y. Liu, and P. Chen: *Different roles of ionic liquids in lithium batteries.* Journal of Power Sources, 334(Supplement C):221 – 239, 2016.

[EFT17a] A. Eftekhari: *Supercapacitors utilising ionic liquids.* Energy Storage Materials, 9:47 – 69, 2017.

[EFT17b] A. Eftekhari and H. García: *The Necessity of Structural Irregularities for the Chemical Applications of Graphene.* Materials Chemistry Today, 4:1–16, 2017.

[EFT17c] A. Eftekhari, L. Li, and Y. Yang: *Polyaniline supercapacitors.* Journal of Power Sources, 347:86 – 107, 2017.

[EMM14] R. Emmett, M. Karakaya, R. Podila, M. Arcila-Velez, J. Zhu, A. Rao, and M. Roberts: *Can Faradaic processes in residual iron catalyst help overcome intrinsic EDLC limits of carbon nanotubes?* Journal of Physical Chemistry C, 118(46):26498–26503, 2014.

[EMS01] J. Emsley: *Nature's Building Blocks: An A–Z Guide to the Elements.* Oxford Pakistan Paperbacks Series. Oxford University Press, 2001. ISBN 9780198503415.

[EU16] EU, *Batteries 2020*, 2016. Online, http://www.batteries2020.eu/index.html.

[FAN16] G. Fan, K. Pan, M. Canova, J. Marcicki, and X. G. Yang: *Modeling of Li-Ion Cells for Fast Simulation of High C-Rate and Low Temperature Operations.* Journal of The Electrochemical Society, 163(5):A666–A676, 2016.

[FAR15a] S. Faraji and F. N. Ani: *The development supercapacitor from activated carbon by electroless plating – A review.* Renewable and Sustainable Energy Reviews, 42:823 – 834, 2015.

[FAR15b] A. Farmann, W. Waag, A. Marongiu, and D. U. Sauer: *Critical review of on-board capacity estimation techniques for lithium-ion batteries in electric and hybrid electric vehicles.* Journal of Power Sources, 281(Supplement C):114 – 130, 2015.

[FEN15] T. Feng, L. Yang, X. Zhao, H. Zhang, and J. Qiang: *Online identification of lithium-ion battery parameters based on an improved equivalent-circuit model and its implementation on battery state-of-power prediction.* Journal of Power Sources, 281(Supplement C):192 – 203, 2015.

[FER13] R. Ferrero, M. Marracci, and B. Tellini: *Single PEM Fuel Cell Analysis for the Evaluation of Current Ripple Effects.* IEEE Transactions on Instrumentation and Measurement, 62(5):1058–1064, 2013.

[FIC12] K. Fic, G. Lota, M. Meller, and E. Frackowiak: *Novel insight into neutral medium as electrolyte for high-voltage supercapacitors.* Energy Environ. Sci., 5:5842–5850, 2012.

[FIT15] G. Fitzgerald, J. Mandel, J. Morris, and H. Touati: *The economics of battery energy storage.* Technical report, Rocky Mountain Institute, 2015.

[FLE10] S. Fletcher, F. Sillars, R. Carter, A. Cruden, M. Mirzaeian, N. Hudson, J. Parkinson, and P. Hall: *The effects of temperature on the performance of electrochemical double layer capacitors.* Journal of Power Sources, 195(21):7484 – 7488, 2010.

[FLE14a] C. Fleischer, W. Waag, H.-M. Heyn, and D. U. Sauer: *On-line adaptive battery impedance parameter and state estimation considering physical principles in reduced order equivalent circuit battery models part 2. Parameter and state estimation.* Journal of Power Sources, 262(Supplement C):457 – 482, 2014.

[FLE14b] S. Fletcher, , V. J. Black, and I. Kirkpatrick: *A universal equivalent circuit for carbon-based supercapacitors.* Journal of Solid State Electrochemistry, 18(5):1377–1387, 2014.

[FLE17] S. Fletcher, I. Kirkpatrick, R. Dring, R. Puttock, R. Thring, and S. Howroyd: *The modelling of carbon-based supercapacitors: Distributions of time constants and Pascal Equivalent Circuits.* Journal of Power Sources, 345:247–253, 2017.

[FON16] P. Fontela: *The STORE project: Multiservice applications of storage for DSO applications (Spain).* In *Grid+Storage 5th regional workshop. Research and Innovation activities about energy storage integration in the electricity networks: ongoing activities at national level and future needs*, 2016.

[FRE] Freqcon, *Freqcon welcome page.* http://www.freqcon.de/.

[FRE01] D. Frenkel and B. Smit: *Understanding molecular simulation, 2^{nd} Ed.: From algorithms to applications*, volum 1. Academic press, 2001. ISBN: 9780122673511.

[FUL94] T. F. Fuller, M. Doyle, and J. Newman: *Relaxation Phenomena in Lithium-Ion-Insertion Cells.* Journal of The Electrochemical Society, 141(4):982–990, 1994.

[GAM15] P. Gambhire, N. Ganesan, S. Basu, K. S. Hariharan, S. M. Kolake, T. Song, D. Oh, T. Yeo, and S. Doo: *A reduced order electrochemical thermal model for lithium ion cells.* Journal of Power Sources, 290(Supplement C):87 – 101, 2015.

[GAO17] Y. Gao, J. Jiang, C. Zhang, W. Zhang, Z. Ma, and Y. Jiang: *Lithium-ion battery aging mechanisms and life model under different charging stresses.* Journal of Power Sources, 356(Supplement C):103 – 114, 2017.

[GER10] M. Gerard, J.-P. Poirot-Crouvezier, D. Hissel, and M.-C. Péra: *Ripple Current Effects on PEMFC Aging Test by Experimental and Modeling.* Journal of Fuel Cell Science and Technology, 8(2), 2010.

[GER15] R. German, A. Sari, P. Venet, O. Briat, and J.-M. Vinassa: *Study on specific effects of high frequency ripple currents and temperature on supercapacitors ageing.* Microelectronics Reliability, 55(9):2027 – 2031, 2015.

[GER16] R. German, A. Hammar, R. Lallemand, A. Sari, and P. Venet: *Novel Experimental Identification Method for a Supercapacitor Multipore Model in Order to Monitor the State of Health.* IEEE Transactions on Power Electronics, 31(1):548–559, 2016.

[GEV13] V. Gevorgian and S. Booth: *Review of PREPA Technical Requirements for Interconnecting Wind and Solar Generation.* Technical report, Massachusetts Institute of Technology (MIT), 2013.

[GHO12] O. Ghodbane, F. Ataherian, N.-L. Wu, and F. Favier: *In situ crystallographic investigations of charge storage mechanisms in MnO_2-based electrochemical capacitors.* Journal of Power Sources, 206:454 – 462, 2012.

[GHO13] A. Ghosh, V. T. Le, J. J. Bae, and Y. H. Lee: *TLM-PSD model for optimization of energy and power density of vertically aligned carbon nanotube supercapacitor.* Scientific reports, 3:2939, 2013.

[GOH14] C.-T. Goh and A. Cruden: *Bivariate quadratic method in quantifying the differential capacitance and energy capacity of supercapacitors under high current operation.* Journal of Power Sources, 265:291 – 298, 2014.

[GON16] A. González, E. Goikolea, J. A. Barrena, and R. Mysyk: *Review on supercapacitors: technologies and materials.* Renewable and Sustainable Energy Reviews, 58:1189–1206, 2016.

[GON17] R. Gonçalves, W. Christinelli, A. Trench, A. Cuesta, and E. Pereira: *Properties improvement of poly (o-methoxyaniline) based supercapacitors: Experimental and theoretical behaviour study of self-doping effect.* Electrochimica Acta, 228:57–65, 2017.

[GRA16] Grand View Research: *Ultracapacitor Market By Type , By Application And Segment Forecasts To 2024.* technical report 978-1-68038-965-4, 2016.

[GRE71] W. Greatbatch, J. H. Lee, W. Mathias, M. Eldridge, J. R. Moser, and A. A. Schneider: *The Solid-State Lithium Battery: A New Improved Chemical Power Source for Implantable Cardiac Pacemakers.* IEEE Transactions on Biomedical Engineering, BME-18(5):317–324, 1971.

[GRE92] W. Greatbatch and C. Holmes: *The lithium/iodine battery: A historical perspective.* PACE - Pacing and Clinical Electrophysiology, 15(11 II):2034–2036, 1992.

[GRE16] A. Greco and X. Jiang: *A coupled thermal and electrochemical study of lithium-ion battery cooled by paraffin/porous-graphite-matrix composite.* Journal of Power Sources, 315(Supplement C):127 – 139, 2016.

[GRI13] Grid code: *Minimum technical requirements of interconnection of PV facilities.* technical report, Puerto Rico Electric Power Authority, 2013.

[GRI14] Grid code: *Reglas generales de interconexión al sistema el'ectrico nacional — Requerimientos técnicos para interonexión de centrales solares fotovoltaicas al sistema eléctrico nacional.* technical report, Mexican Comission for Energy Regulation (CRE), 2014.

[GRI15] J. Griffin, A. Forse, W.-Y. Tsai, P.-L. Taberna, P. Simon, and C. Grey: *In situ NMR and electrochemical quartz crystal microbalance techniques reveal the structure of the electrical double layer in supercapacitors.* Nature Materials, 14(8):812–819, 2015.

[GRY05] G. Gryglewicz, J. Machnikowski, E. Lorenc-Grabowska, G. Lota, and E. Frackowiak: *Effect of pore size distribution of coal-based activated carbons on double layer capacitance.* Electrochimica Acta, 50(5):1197 – 1206, 2005.

[GU14a] W. Gu, Z. Sun, X. Wei, and H. Dai: *A new method of accelerated life testing based on the Grey System Theory for a model-based lithium-ion battery life evaluation system.* Journal of Power Sources, 267(Supplement C):366 – 379, 2014.

[GU14b] W. Gu and G. Yushin: *Review of nanostructured carbon materials for electrochemical capacitor applications: Advantages and limitations of activated carbon, carbide-derived carbon, zeolite-templated carbon, carbon aerogels, carbon nanotubes, onion-like carbon, and graphene.* Wiley Interdisciplinary Reviews: Energy and Environment, 3(5):424–473, 2014.

[GU15] L. Gu, D. Xiao, Y.-S. Hu, H. Li, and Y. Ikuhara: *Atomic-Scale Structure Evolution in a Quasi-Equilibrated Electrochemical Process of Electrode Materials for Rechargeable Batteries.* Advanced Materials, 27(13):2134–2149, 2015.

[GUA03] H. Gualous, D. Bouquain, A. Berthon, and J. Kauffmann: *Experimental study of supercapacitor serial resistance and capacitance variations with temperature.* Journal of Power Sources, 123(1):86 – 93, 2003.

[GUA09] H. Gualous, H. Louahlia-Gualous, R. Gallay, and A. Miraoui: *Supercapacitor thermal modeling and characterization in transient state for industrial applications.* IEEE Transactions on industry applications, 45(3):1035–1044, 2009.

[GUA11] H. Gualous, H. Louahlia, and R. Gallay: *Supercapacitor characterization and thermal modelling with reversible and irreversible heat effect.* IEEE Transactions on power electronics, 26(11):3402–3409, 2011.

[GUA14] T. Guan, P. Zuo, S. Sun, C. Du, L. Zhang, Y. Cui, L. Yang, Y. Gao, G. Yin, and F. Wang: *Degradation mechanism of $LiCoO_2$/mesocarbon microbeads battery based on accelerated aging tests.* Journal of Power Sources, 268(Supplement C):816 – 823, 2014.

[GUA16] H. Gualous, H. Chaoui, and R. Gallay: *Supercapacitor calendar aging for telecommunication applications.* In *Telecommunications Energy Conference (INTELEC), 2016 IEEE International*, pages 1–5. IEEE, 2016.

[GUI06] P. Guillemet, Y. Scudeller, and T. Brousse: *Multi-level reduced-order thermal modeling of electrochemical capacitors.* Journal of Power Sources, 157(1):630–640, 2006.

[GUO10] G. Guoy: *Constitution of the electric charge at the surface of an electrolyte.* J Physique, 9:457–67, 1910.

[GUO10] G. Guo, B. Long, B. Cheng, S. Zhou, P. Xu, and B. Cao: *Three-dimensional thermal finite element modeling of lithium-ion battery in thermal abuse application.* Journal of Power Sources, 195(8):2393 – 2398, 2010.

[GUO11a] M. Guo, G. Sikha, and R. E. White: *Single-Particle Model for a Lithium-Ion Cell: Thermal Behavior.* Journal of The Electrochemical Society, 158(2):A122–A132, 2011.

[GUO11b] M. Guo and R. E. White: *Thermal Model for Lithium Ion Battery Pack with Mixed Parallel and Series Configuration.* Journal of The Electrochemical Society, 158(10):A1166–A1176, 2011.

[GUO17] Y. Guo, W. Li, H. Yu, D. F. Perepichka, and H. Meng: *Flexible Asymmetric Supercapacitors via Spray Coating of a New Electrochromic Donor – Acceptor Polymer.* Advanced Energy Materials, 7(2):1601623–n/a, 2017.

[GUT67] F. Gutmann, A. M. Hermann, and A. Rembaum: *Solid-State Electrochemical Cells Based on Charge Transfer Complexes.* Journal of The Electrochemical Society, 114(4):323–329, 1967.

[HAD09] I. Hadjipaschalis, A. Poullikkas, and V. Efthimiou: *Overview of current and future energy storage technologies for electric power applications.* Renewable and Sustainable Energy Reviews, 13(6-7):1513 – 1522, 2009.

[HAL99] S. A. Hallaj, H. Maleki, J. Hong, and J. Selman: *Thermal modeling and design considerations of lithium-ion batteries.* Journal of Power Sources, 83(1):1 – 8, 1999.

[HAN14] C. A. Hans, V. Nenchev, J. Raisch, and C. Reincke-Collon: *Minimax Model Predictive Operation Control of Microgrids.* {IFAC} Proceedings Volumes, 47(3):10287 – 10292, 2014. 19th {IFAC} World Congress.

[HAO16] C. Hao, X. Wang, Y. Yin, and Z. You: *Analysis of Charge Redistribution During Self-discharge of Double-Layer Supercapacitors.* Journal of Electronic Materials, 45(4):2160–2171, 2016.

[HAR58] W. S. Harris: Ph. D. thesis, University of California, Berkeley, UCRL–8381, 1958.

[HAY12] W. Haynes: *CRC Handbook of Chemistry and Physics, 93rd Edition*. CRC Handbook of Chemistry and Physics. Taylor & Francis, 2012. ISBN 9781439880494.

[HE11] H. He, R. Xiong, X. Zhang, F. Sun, and J. Fan: *State-of-Charge Estimation of the Lithium-Ion Battery Using an Adaptive Extended Kalman Filter Based on an Improved Thevenin Model*. IEEE Transactions on Vehicular Technology, 60(4):1461–1469, 2011.

[HE13] Y.-B. He, M. Liu, Z.-D. Huang, B. Zhang, Y. Yu, B. Li, F. Kang, and J.-K. Kim: *Effect of solid electrolyte interface (SEI) film on cyclic performance of $Li_4Ti_5O_{12}$ anodes for Li ion batteries*. Journal of Power Sources, 239(Supplement C):269 – 276, 2013.

[HEL79] H. Helmholtz: *Studien über electrische Grenzschichten*. Annalen der Physik, 243(7):337–382, 1879.

[HEL15] M. Helmlinger, *PMP9766 Test Report — Supercapacitor Backup Power Supply With Active Cell Balancing*, 2015.

[HER13] W. Hermann, *Rigid cell separator for minimizing thermal runaway propagation within a battery pack*, 2013. US Patent 8,481,191.

[HMA16] S. Hmam, J.-C. Olivier, S. Bourguet, and L. Loron: *A cycle-based and multirate approach for power system simulation application to the ageing estimation of a supercapacitor-based ferry*. Journal of Energy Storage, 8:175 – 184, 2016.

[HOH64] P. Hohenberg and W. Kohn: *Inhomogeneous Electron Gas*. Phys. Rev., 136:B864–B871, 1964.

[HOK13] A. Hoke, A. Brissette, S. Chandler, A. Pratt, and D. Maksimovic: *Look-ahead economic dispatch of microgrids with energy storage, using linear programming*. pages 154–161, 2013. Cited By 7.

[HOL01] C. F. Holmes: *The role of lithium batteries in modern health care*. Journal of Power Sources, 97(Supplement C):739 – 741, 2001.

[HU12] X. Hu, S. Li, and H. Peng: *A comparative study of equivalent circuit models for Li-ion batteries*. Journal of Power Sources, 198(Supplement C):359 – 367, 2012.

[HU16] C. Hu, E. Zhao, N. Nitta, A. Magasinski, G. Berdichevsky, and G. Yushin: *Aqueous solutions of acidic ionic liquids for enhanced stability of polyoxometalate-carbon supercapacitor electrodes*. Journal of Power Sources, 326:569 – 574, 2016.

[HUA01] H. Huang, S.-C. Yin, and L. F. Nazar: *Approaching Theoretical Capacity of $LiFePO_4$ at Room Temperature at High Rates*. Electrochemical and Solid-State Letters, 4(10):A170–A172, 2001.

[HUA17] H.-H. Huang, H.-Y. Chen, K.-C. Liao, H.-T. Young, C.-F. Lee, and J.-Y. Tien: *Thermal-electrochemical coupled simulations for cell-to-cell imbalances in lithium-iron-phosphate based battery packs*. Applied Thermal Engineering, 123(Supplement C):584 – 591, 2017.

[HUD01] J. Huddleston, A. Visser, W. Reichert, H. Willauer, G. Broker, and R. Rogers: *Characterization and comparison of hydrophilic and hydrophobic room temperature ionic liquids incorporating the imidazolium cation*. Green Chemistry, 3(4):156–164, 2001.

[HUN17] P. Hunziker and L.-E. Cederman: *No extraction without representation: The ethno-regional oil curse and secessionist conflict*. Journal of Peace Research, 54(3):365–381, 2017.

[HYB] HybridCARS, *Tesla projects battery costs could drop to $100/kWh by 2020.* Online, http://www.hybridcars.com/tesla-projects-battery-costs-could-drop-to-100kwh-by-2020/.

[IEA16] IEA: *Utility of the future.* Technical report, International Energy Agency, 2016.

[IEC15] IEC 61427−2: *Secondary cells and batteries for renewable energy storage. General requirements and methods of test. Part 2: on-grid applications.* Standard, International Electrotechnical commission, 2015.

[IOX] Ioxus, *Products overview.* http://www.ioxus.com/english/products/.

[IPC13] IPCC: *Intergovernmental Panel on Climate Change, Fifth Assessment Report (AR5).* WMO, IPCC Secretariat, 2013.

[ISL14a] M. M. Islam, V. S. Bryantsev, and A. C. T. van Duin: *ReaxFF Reactive Force Field Simulations on the Influence of Teflon on Electrolyte Decomposition during Li/SWCNT Anode Discharge in Lithium–Sulfur Batteries.* Journal of The Electrochemical Society, 161(8):E3009–E3014, 2014.

[ISL14b] M. S. Islam and C. A. J. Fisher: *Lithium and sodium battery cathode materials: computational insights into voltage, diffusion and nanostructural properties.* Chem. Soc. Rev., 43:185–204, 2014.

[ITO05] Y. Itou and Y. Ukyo: *Performance of $LiNiCoO_2$ materials for advanced lithium-ion batteries.* Journal of Power Sources, 146(1):39 – 44, 2005.

[JAF17] S. Jaffe: *Vulnerable Links in the Lithium-Ion Battery Supply Chain.* Joule, 1(2):225 – 228, 2017.

[JAL15] K. Jalkanen, J. Karppinen, L. Skogström, T. Laurila, M. Nisula, and K. Vuorilehto: *Cycle aging of commercial NMC/graphite pouch cells at different temperatures.* Applied Energy, 154(Supplement C):160 – 172, 2015.

[JAN17] M. Janssen and R. van Roij: *Reversible Heating in Electric Double Layer Capacitors.* Phys. Rev. Lett., 118:096001, 2017.

[JEO07] S. Jeong, Y. Lim, Y. Choi, G. Cho, K. Kim, H. Ahn, and K. Cho: *Electrochemical properties of lithium sulfur cells using PEO polymer electrolytes prepared under three different mixing conditions.* Journal of Power Sources, 174(2):745 – 750, 2007.

[JI13] Y. Ji, Y. Zhang, and C.-Y. Wang: *Li-Ion Cell Operation at Low Temperatures.* Journal of The Electrochemical Society, 160(4):A636–A649, 2013.

[JIA16] J. Jiang, S. Liu, Z. Ma, L. Y. Wang, and K. Wu: *Butler–Volmer equation-based model and its implementation on state of power prediction of high-power lithium titanate batteries considering temperature effects.* Energy, 117(Part 1):58 – 72, 2016.

[JOH98] B. A. Johnson and R. E. White: *Characterization of commercially available lithium-ion batteries.* Journal of Power Sources, 70(1):48 – 54, 1998.

[JOH16] A. Johnston, *Tesla Starts Off 2016 By Producing & Delivering Powerwall*, 2016. Online, https://cleantechnica.com/2016/01/08/tesla-starts-off-2016-producing-delivering-powerwall/.

[JON89] R. O. Jones and O. Gunnarsson: *The density functional formalism, its applications and prospects.* Rev. Mod. Phys., 61:689–746, 1989.

[JUN11] M. Jung and K. A. Williams: *Effect of dynamic operation on chemical degradation of a polymer electrolyte membrane fuel cell.* Journal of Power Sources, 196(5):2717 – 2724, 2011.

[KÄB13] S. Käbitz, J. B. Gerschler, M. Ecker, Y. Yurdagel, B. Emmermacher, D. André, T. Mitsch, and D. U. Sauer: *Cycle and calendar life study of a graphite|$LiNi_{1/3}Mn_{1/3}Co_{1/3}O_2$ Li-ion high energy system. Part A: Full cell characterization.* Journal of Power Sources, 239(Supplement C):572 – 583, 2013.

[KAI16] K.-P. Kairies, D. Haberschusz, J. van Ouwerkerk, J. Strebel, O. Wessels, D. Magnor, J. Badeda, and D. U. Sauer: *Wissenschaftliches Mess- und Evaluierungsprogramm Solarstromspeicher.* Jahresbericht, RWTH Aachen, 2016.

[KAL05] P. Kalyani and N. Kalaiselvi: *Various aspects of $LiNiO_2$ chemistry: A review.* Science and Technology of Advanced Materials, 6(6):689 – 703, 2005.

[KAN92] R. Kanno, Y. Kawamoto, Y. TaAAkeda, S. Ohashi, N. Imanishi, and O. Yamamoto: *Carbon fiber as a Negative Electrode in Lithium Secondary Cells.* Journal of the Electrochemical Society, 139(12):3397–3404, 1992.

[KAN11] H. Kanchev, D. Lu, F. Colas, V. Lazarov, and B. Francois: *Energy management and operational planning of a microgrid with a PV-based active generator for smart grid applications.* IEEE transactions on industrial electronics, 58(10):4583–4592, 2011.

[KAR08] D. K. Karthikeyan, G. Sikha, and R. E. White: *Thermodynamic model development for lithium intercalation electrodes.* Journal of Power Sources, 185(2):1398 – 1407, 2008.

[KAW02] T. Kawamura, A. Kimura, M. Egashira, S. Okada, and J.-I. Yamaki: *Thermal stability of alkyl carbonate mixed-solvent electrolytes for lithium ion cells.* Journal of Power Sources, 104(2):260 – 264, 2002.

[KEL17] K. Kelty, C. Kishiyama, and S. Stewart, *Low temperature fast charge of battery pack*, 2017. US Patent 9,694,699.

[KIM06] D.-H. Kim and J. Kim: *Synthesis of $LiFePO_4$ Nanoparticles in Polyol Medium and Their Electrochemical Properties.* Electrochemical and Solid-State Letters, 9(9):A439–A442, 2006.

[KIM15a] B. C. Kim, J.-Y. Hong, G. G. Wallace, and H. S. Park: *Recent Progress in Flexible Electrochemical Capacitors: Electrode Materials, Device Configuration, and Functions.* Advanced Energy Materials, 5(22):1500959–n/a, 2015.

[KIM15b] S. T. Kim, S. Bae, Y. C. Kang, and J. W. Park: *Energy Management Based on the Photovoltaic HPCS With an Energy Storage Device.* IEEE Transactions on Industrial Electronics, 62(7):4608–4617, 2015.

[KÖH17] C. Köhler, A. Steiner, Y.-M. Saint-Drenan, D. Ernst, A. Bergmann-Dick, M. Zirkelbach, Z. Ben Bouallègue, I. Metzinger, and B. Ritter: *Critical weather situations for renewable energies - Part B: Low stratus risk for solar power.* Renewable Energy, 101:794–803, 2017.

[KOM08] Komatsu, *Press release: Komatsu Introduces the World's First Hydraulic Excavator: Hybrid Evolution Plan for Construction Equipment*, 2008. http://www.komatsu.com/CompanyInfo/press/2008051315113604588.html.

[KOR13] R. Korthauer: *Handbuch Lithium-Ionen-Batterien.* Springer Berlin Heidelberg, 2013. ISBN 9783642306525.

[KÖT06] R. Kötz, M. Hahn, and R. Gallay: *Temperature behavior and impedance fundamentals of supercapacitors*. Journal of Power Sources, 154(2):550–555, 2006.

[KOT17] S. Kotra and M. K. Mishra: *A Supervisory Power Management System for a Hybrid Microgrid With HESS*. IEEE Transactions on Industrial Electronics, 64(5):3640–3649, 2017.

[KUM08] K. Kumaresan, G. Sikha, and R. E. White: *Thermal Model for a Li-Ion Cell*. Journal of The Electrochemical Society, 155(2):A164–A171, 2008.

[KUM15] S. Kumagai, K. Mukaiyachi, and D. Tashima: *Rate and cycle performances of supercapacitors with different electrode thickness using non-aqueous electrolyte*. Journal of Energy Storage, 3:10 – 17, 2015.

[KUN15] M. Kunowsky, C. Linares-Solano, A. Garcia-Gomez, V. Barranco, J. M. Rojo, and J. D. Carruthers: *Applications for CO_2-Activated Carbon Monoliths: II. EDLC Electrodes*. International Journal of Applied Ceramic Technology, 12:E127–E132, 2015.

[KUR16] N. Kurra, Q. Jiang, A. Syed, C. Xia, and H. N. Alshareef: *Micro-Pseudocapacitors with Electroactive Polymer Electrodes: Toward AC-Line Filtering Applications*. Applied Materials & Interfaces, 8:12748–12755, 2016.

[KWO16] S. Kwon, B.-S. Kim, S.-G. Kim, B.-J. Lee, M.-S. Kim, and J. Jung: *Preparation of nano-porous activated carbon aerogel using a single-step activation method for use as high-power EDLC electrode in organic electrolyte*. Journal of Nanoscience and Nanotechnology, 16(5):4598–4604, 2016.

[LAB] S. N. Laboratories, *PVPerformance: Modeling collaborative*. Online, https://pvpmc.sandia.gov/applications/pv_lib-toolbox/.

[LAJ07] W. Lajnef, J.-M. Vinassa, O. Briat, S. Azzopardi, and E. Woirgard: *Characterization methods and modelling of ultracapacitors for use as peak power sources*. Journal of Power Sources, 168(2):553 – 560, 2007.

[LAM14] S. Lamichhane and N. Mithulananthan: *Influence of wind energy integration on low frequency oscillatory instability of power system*, 2014.

[LEE12] D. Lee and R. Baldick: *Limiting Ramp Rate of Wind Power Output using a Battery Based on the Variance Gamma Process*. In *International Conference on Renewable Energies and Power Quality (ICREPQ'12)*, pages 1591–1596, 2012.

[LEE14] H. Lee, M. Yanilmaz, O. Toprakci, K. Fu, and X. Zhang: *A review of recent developments in membrane separators for rechargeable lithium-ion batteries*. Energy Environ. Sci., 7:3857–3886, 2014.

[LEH16] N. Lehmann, A. Lever, D. Sanders, M. Ravishankar, M. Ashcroft, G. Strbac, M. Aunedi, F. Teng, and D. Pudjianto: *Can storage help reduce the cost of a future UK electricity system?* White paper, Carbon Trust and Imperial Collage of London, 2016.

[LEI10] C. Lei and C. Lekakou: *Carbon-based nanocomposite EDLC supercapacitors*. volum 1, pages 176–179, 2010. ISBN: 978-143983401-5.

[LEI14] Y.-H. Lei and G. Michaels: *Do giant oilfield discoveries fuel internal armed conflicts?* Journal of Development Economics, 110(Supplement C):139 – 157, 2014. Land and Property Rights.

[LEP15] F. LePort, *Battery pack pressure monitoring system for thermal event detection*, 2015. US Patent 9,083,064.

[LI01] J. Li, E. Murphy, J. Winnick, and P. Kohl: *Studies on the cycle life of commercial lithium ion batteries during rapid charge-discharge cycling.* Journal of Power Sources, 102(1):294 – 301, 2001.

[LI10] W. Li, G. Joos, and J. Belanger: *Real-Time Simulation of a Wind Turbine Generator Coupled With a Battery Supercapacitor Energy Storage System.* IEEE Transactions on Industrial Electronics, 57(4):1137–1145, 2010.

[LI12a] J. Li, B. Jia, M. Mazzola, and M. Xin: *On-line battery state of charge estimation using Gauss-Hermite quadrature filter.* In *2012 Twenty-Seventh Annual IEEE Applied Power Electronics Conference and Exposition (APEC)*, pages 434–438, 2012.

[LI12b] S. Li, G. Feng, P. F. Fulvio, C. Hillesheim, Patrick, C. Liao, S. Dai, and P. T. Cummings: *Molecular dynamics simulation study of the capacitive performance of a binary mixture of ionic liquids near an onion-like carbon electrode.* The journal of physical chemistry letters, 3(17):2465–2469, 2012.

[LI14] J. Li and M. A. Danzer: *Optimal charge control strategies for stationary photovoltaic battery systems.* Journal of Power Sources, 258:365 – 373, 2014.

[LI15] X. Li, S.-Y. Choe, and W. T. Joe: *A reduced order electrochemical and thermal model for a pouch type lithium ion polymer battery with $LiNi_xMn_yCo_{1-x-y}O_2/LiFePO_4$ blended cathode.* Journal of Power Sources, 294(Supplement C):545 – 555, 2015.

[LI16a] B. Li, F. Dai, Q. Xiao, L. Yang, J. Shen, C. Zhang, and M. Cai: *Activated Carbon from Biomass Transfer for High-Energy Density Lithium-Ion Supercapacitors.* Advanced Energy Materials, 6(18):1600802–n/a, 2016.

[LI16b] L. Li, J. Zhang, Z. Peng, Y. Li, C. Gao, Y. Ji, R. Ye, N. D. Kim, Q. Zhong, Y. Yang, H. Fei, G. Ruan, and J. M. Tour: *High-Performance Pseudocapacitive Microsupercapacitors from Laser-Induced Graphene.* Advanced Materials, 28(5):838–845, 2016.

[LI16c] Y. Li and Y. Han: *A new perspective on battery cell balancing: Thermal balancing and relative temperature control.* In *2016 IEEE Energy Conversion Congress and Exposition (ECCE)*, pages 1–5, 2016.

[LI17a] H. Li, Y. Hou, F. Wang, M. R. Lohe, X. Zhuang, L. Niu, and X. Feng: *Flexible All-Solid-State Supercapacitors with High Volumetric Capacitances Boosted by Solution Processable MXene and Electrochemically Exfoliated Graphene.* Advanced Energy Materials, 7(4):1601847–n/a, 2017.

[LI17b] J. Li, J. Guo, X. Zhang, Y. Huang, and L. Guo: *Asymmetric Supercapacitors with High Energy and Power Density Fabricated Using $LiMn_2O_4$ Nano-rods and Activated Carbon Electrodes.* International Journal of Electrochemical Science, 12(2):1157–1166, 2017.

[LI17c] J. Li, X. Yuan, C. Lin, Y. Yang, L. Xu, X. Du, J. Xie, J. Lin, and J. Sun: *Achieving High Pseudocapacitance of 2D Titanium Carbide (MXene) by Cation Intercalation and Surface Modification.* Advanced Energy Materials, 1:1602725–n/a, 2017.

[LI17d] J. Li, G. Zhang, C. Fu, L. Deng, R. Sun, and C.-P. Wong: *Facile preparation of nitrogen/sulfur co-doped and hierarchical porous graphene hydrogel for high-performance electrochemical capacitor.* Journal of Power Sources, 345:146 – 155, 2017.

[LIA03] B. Y. Liaw, E. Roth, R. G. Jungst, G. Nagasubramanian, H. L. Case, and D. H. Doughty: *Correlation of Arrhenius behaviors in power and capacity fades with cell impedance and heat generation in cylindrical lithium-ion cells.* Journal of Power Sources, 119(Supplement C):874 – 886, 2003.

[LIA04] B. Y. Liaw, G. Nagasubramanian, R. G. Jungst, and D. H. Doughty: *Modeling of lithium ion cells—A simple equivalent-circuit model approach.* Solid State Ionics, 175(1):835 – 839, 2004. Fourteenth International Conference on Solid State Ionics.

[LIN14] F. Lin, I. Markus, D. Nordlund, T.-C. Weng, M. Asta, H. Xin, and M. Doeff: *Surface reconstruction and chemical evolution of stoichiometric layered cathode materials for lithium-ion batteries.* Nature communications, 5:3529, 2014.

[LIU10] P. Liu, J. Wang, J. Hicks-Garner, E. Sherman, S. Soukiazian, M. Verbrugge, H. Tataria, J. Musser, and P. Finamore: *Aging Mechanisms of $LiFePO_4$ Batteries Deduced by Electrochemical and Structural Analyses.* Journal of The Electrochemical Society, 157(4):A499–A507, 2010.

[LIU16] K. Liu and J. Wu: *Boosting the Performance of Ionic-Liquid-Based Supercapacitors with Polar Additives.* Journal of Physical Chemistry C, 120(42):24041–24047, 2016.

[LIU17a] C. Liu, C. Zhang, H. Fu, X. Nan, and G. Cao: *Exploiting High-Performance Anode through Tuning the Character of Chemical Bonds for Li -Ion Batteries and Capacitors.* Advanced Energy Materials, 7(1):1601127–n/a, 2017.

[LIU17b] H. Liu, L. Liao, Y.-C. Lu, and Q. Li: *High Energy Density Aqueous Li-Ion Flow Capacitor.* Advanced Energy Materials, 7(1):1601248–n/a, 2017.

[LOG15] P.-O. Logerais, M. Camara, O. Riou, A. Djellad, A. Omeiri, F. Delaleux, and J. Durastanti: *Modeling of a supercapacitor with a multibranch circuit.* International Journal of Hydrogen Energy, 40(39):13725–13736, 2015.

[LOM17] P. Lombardi and F. Schwabe: *Sharing economy as a new business model for energy storage systems.* Applied Energy, 188:485–496, 2017.

[LOP17] J. Lopez Sanz, C. Ocampo-Martinez, J. Álvarez-Flórez, M. Moreno-Eguilaz, R. Ruiz-Mansilla, J. Kalmus, M. Gräeber, and G. Lux: *Thermal Management in Plug-In Hybrid Electric Vehicles: A Real-Time Nonlinear Model Predictive Control Implementation.* IEEE Transactions on Vehicular Technology, 66(9):7751–7760, 2017.

[LS] LS Ultracapacitor, *Product.* http://www.ultracapacitor.co.kr/?enc=L3N1Yi9wcm9kdWN0L3N1YjFfMS5odG1s.

[LYS15] V. Lystianingrum, B. Hredzak, V. G. Agelidis, and V. S. Djanali: *On estimating instantaneous temperature of a supercapacitor string using an observer based on experimentally validated lumped thermal model.* IEEE Transactions on Energy Conversion, 30(4):1438–1448, 2015.

[LYU16] X. Lyu, F. Su, and M. Miao: *Two-ply yarn supercapacitor based on carbon nanotube/stainless steel core-sheath yarn electrodes and ionic liquid electrolyte.* Journal of Power Sources, 307:489–495, 2016.

[MAG14] B. Magoro and T. Khoza: *Grid connection code for renewable power plants (RPPs) connected to the electricity transmission system (TS) or the distribution system (DS) in South Africa.* Grid code, National Energy Regulator of South Africa (NERSA), 2014.

[MAJ18] K. J. Maji, A. K. Dikshit, M. Arora, and A. Deshpande: *Estimating premature mortality attributable to PM2.5 exposure and benefit of air pollution control policies in China for 2020*. Science of The Total Environment, 612(Supplement C):683 – 693, 2018.

[MAL14] Y. Maletin, N. Stryzhakova, S. Zelinsky, S. Chernukhin, D. Tretyakov, S. Tychina, and D. Drobny: *Electrochemical Double Layer Capacitors and Hybrid Devices for Green Energy Applications*. Green, 4(1-6):9–17, 2014.

[MAL15] Y. Maletin, N. Stryzhakova, S. Zelinskyi, S. Chernukhin, D. Tretyakov, H. Mosqueda, N. Davydenko, and D. Drobnyi: *New Approach to Ultracapacitor Technology: What it Can Offer to Electrified Vehicles*. Journal of Energy and Power Engineering, 9(6):585–591, 2015.

[MAR09] P. Mars, *Supercapacitors for SSD backup power*, 2009. Technical report.

[MAR12] J. Marcos, L. Marroyo, E. Lorenzo, and M. García: *Smoothing of PV power fluctuations by geographical dispersion*. Progress in Photovoltaics: Research and Applications, 20(2):226–237, 2012.

[MAR14a] J. Marcicki and X. G. Yang: *Model-Based Estimation of Reversible Heat Generation in Lithium-Ion Cells*. Journal of The Electrochemical Society, 161(12):A1794–A1800, 2014.

[MAR14b] J. Marcos, I. de la Parra, M. García, and L. Marroyo: *Control Strategies to Smooth Short-Term Power Fluctuations in Large Photovoltaic Plants Using Battery Storage Systems*. Energies, 7(10):6593, 2014.

[MAR14c] J. Mardall and P. Yeomans, *Battery Pack Base Plate Heat Exchanger*, 2014. US Patent App. 13/736,217.

[MAR16] J. Marcos, I. de la Parra, M. García, and L. Marroyo: *Simulating the variability of dispersed large PV plants*. Progress in Photovoltaics: Research and Applications, 24(5):680–691, 2016.

[MAS17] G. Masson: *2016 Snapshot of global photovoltaic markets*. technical report, IEA – International Energy Agency, 2017.

[MAXa] Maxwell Technologies, *Maxell Ultracapacitors*. http://www.maxwell.com/products/ultracapacitors/.

[MAXb] Maxwell Technologies, *Ultracapacitors: transforming the grid*.

[MAZ11] Mazda, *Press release: Mazda 'i-ELOOP' Capacitor-Based Brake Energy Regeneration System*, 2011. http://www2.mazda.com/en/publicity/release/2011/201111/111125a.html.

[MÉG15] O. Mégel, J. L. Mathieu, and G. Andersson: *Scheduling distributed energy storage units to provide multiple services under forecast error*. International Journal of Electrical Power & Energy Systems, 72:48 – 57, 2015. The Special Issue for 18th Power Systems Computation Conference.

[MER12] C. Merlet, C. Péan, B. Rotenberg, P. A. Madden, P. Simon, and M. Salanne: *Simulating supercapacitors: Can we model electrodes as constant charge surfaces?* The journal of physical chemistry letters, 4(2):264–268, 2012.

[MEY00] J. P. Meyers, M. Doyle, R. M. Darling, and J. Newman: *The impedance response of a porous electrode composed of intercalation particles*. Journal of The Electrochemical Society, 147(8):2930–2940, 2000.

[MIC06] H. Michel: *Temperature and dynamics problems of ultracapacitors in stationary and mobile applications.* Journal of Power Sources, 154(2):556 – 560, 2006.

[MIL10] J. R. Miller, R. Outlaw, and B. Holloway: *Graphene double-layer capacitor with ac line-filtering performance.* Science, 329(5999):1637–1639, 2010.

[MIL11] J. Miller: *Ultracapacitor Applications.* Energy Engineering Series. Institution of Engineering and Technology, 2011. ISBN: 9781849190718.

[MIL16] J. R. Miller: *Engineering electrochemical capacitor applications.* Journal of Power Sources, 326:726–735, 2016.

[MIL17] L. Millet, M. Bruch, P. Raab, S. Lux, and M. Vetter: *Isothermal calorimeter heat measurements of a 20Ah lithium iron phosphate battery cell.* In *2017 Twelfth International Conference on Ecological Vehicles and Renewable Energies (EVER)*, pages 1–7, 2017.

[MIN15] L. I. Minchala Avila, L. E. Garza-Castañón, A. Vargas-Martínez, and Y. Zhang: *A Review of Optimal Control Techniques Applied to the Energy Management and Control of Microgrids.* Procedia Computer Science, 52:780 – 787, 2015.

[MIN16] H. Miniguano, A. Barrado, C. Raga, A. Lázaro, C. Fernández, and M. Sanz: *A comparative study and parameterization of supercapacitor electrical models applied to hybrid electric vehicles.* In *Electrical Systems for Aircraft, Railway, Ship Propulsion and Road Vehicles & International Transportation Electrification Conference (ESARS-ITEC), International Conference on*, pages 1–6. IEEE, 2016.

[MIZ81] K. Mizushima, P. Jones, P. Wiseman, and J. Goodenough: *Li_xCoO_2 ($0<x\leq 1$): A new cathode material for batteries of high energy density.* Solid State Ionics, 3(Supplement C):171 – 174, 1981.

[MOA13] S. Moayedi, F. Cingoz, and A. Davoudi: *Accelerated simulation of high-fidelity models of supercapacitors using waveform relaxation techniques.* IEEE Transactions on Power Electronics, 28(11):4903–4909, 2013.

[MOR04] M. J. Moran and H. N. Shapiro: *Fundamentals of Engineering Thermodynamics.* John Wiley & Sons, Inc, 2004. ISBN 84-291-4313-0.

[MOS72a] J. Moser, *Solid state lithium-iodine primary battery*, 1972. US Patent 3,660,163.

[MOS72b] J. Moser and A. Schneider, *Primary cells and iodine containing cathodes therefor*, 1972. US Patent 3,674,562.

[MOT14] S. N. Motapon, L. A. Dessaint, and K. Al-Haddad: *A Comparative Study of Energy Management Schemes for a Fuel-Cell Hybrid Emergency Power System of More-Electric Aircraft.* IEEE Transactions on Industrial Electronics, 61(3):1320–1334, 2014.

[MUL13] G. Mulder, D. Six, B. Claessens, T. Broes, N. Omar, and J. V. Mierlo: *The dimensioning of PV–battery systems depending on the incentive and selling price conditions.* Applied Energy, 111:1126 – 1135, 2013.

[MÜN14] W. Münchgesang, P. Meisner, G. Yushin, D. C. Meyer, and T. Leisegang: *Supercapacitors specialities–Technology review.* In *AIP Conference Proceedings*, volum 1597, pages 196–203. AIP, 2014.

[MUN16] A. Mundy and G. L. Plett: *Reduced-order physics-based modeling and experimental parameter identification for non-Faradaic electrical double-layer capacitors.* Journal of Energy Storage, 7:167 – 180, 2016.

[NAD15] A. Nadeau, M. Hassanalieragh, G. Sharma, and T. Soyata: *Energy awareness for supercapacitors using Kalman filter state-of-charge tracking.* Journal of Power Sources, 296:383–391, 2015.

[NAG99] G. Nagasubramanian, D. Ingersoll, D. Doughty, D. Radzykewycz, C. Hill, and C. Marsh: *Electrical and electrochemical performance characteristics of large capacity lithium-ion cells.* Journal of Power Sources, 80(1):116 – 118, 1999.

[NEA16] A. R. Neale, S. Murphy, P. Goodrich, C. Schütter, C. Hardacre, S. Passerini, A. Balducci, and J. Jacquemin: *An ether-functionalised cyclic sulfonium based ionic liquid as an electrolyte for electrochemical double layer capacitors.* Journal of Power Sources, 326:549 – 559, 2016.

[NEJ16] S. Nejad, D. Gladwin, and D. Stone: *A systematic review of lumped-parameter equivalent circuit models for real-time estimation of lithium-ion battery states.* Journal of Power Sources, 316(Supplement C):183 – 196, 2016.

[NES] Nesscap Ultracapacitors, *Nesscap products.* http://www.nesscap.com/product/p_overview.jsp.

[NEW95] J. Newman: *Optimization of Porosity and Thickness of a Battery Electrode by Means of a Reaction-Zone Model.* Journal of The Electrochemical Society, 142(1):97–101, 1995.

[NEW17] New Energy Outlook 2017.: *Bloomberg new energy finance's annual long-term economic forecast of the world's power sector.* Forecast, Bloomberg, 2017.

[NIE13] P. Niehoff, E. Kraemer, and M. Winter: *Parametrisation of the influence of different cycling conditions on the capacity fade and the internal resistance increase for lithium nickel manganese cobalt oxide/graphite cells.* Journal of Electroanalytical Chemistry, 707(Supplement C):110 – 116, 2013.

[NIT15] N. Nitta, F. Wu, J. T. Lee, and G. Yushin: *Li-ion battery materials: present and future.* Materials Today, 18(5):252 – 264, 2015.

[NOT13] A. Nottrott, J. Kleissl, and B. Washom: *Energy dispatch schedule optimization and cost benefit analysis for grid-connected, photovoltaic-battery storage systems.* Renewable Energy, 55:230–240, 2013. Cited By 46.

[NOZ09] H. Nozaki, K. Nagaoka, K. Hoshi, N. Ohta, and M. Inagaki: *Carbon-coated graphite for anode of lithium ion rechargeable batteries: Carbon coating conditions and precursors.* Journal of Power Sources, 194(1):486 – 493, 2009.

[OBE17] A. M. Obeidat, M. A. Gharaibeh, and M. Obaidat: *Solid-state supercapacitors with ionic liquid gel polymer electrolyte and polypyrrole electrodes for electrical energy storage.* Journal of Energy Storage, 13:123 – 128, 2017.

[OLA17] B. D. Olaszi and J. Ladanyi: *Comparison of different discharge strategies of grid-connected residential PV systems with energy storage in perspective of optimal battery energy storage system sizing.* Renewable and Sustainable Energy Reviews, 75:710 – 718, 2017.

[O'N15] L. O'Neill, C. Johnston, and P. S. Grant: *Enhancing the supercapacitor behaviour of novel Fe_3O_4/FeOOH nanowire hybrid electrodes in aqueous electrolytes.* Journal of Power Sources, 274:907 – 915, 2015.

[OUY15] M. Ouyang, W. Zhang, E. Wang, F. Yang, J. Li, Z. Li, P. Yu, and X. Ye: *Performance analysis of a novel coaxial power-split hybrid powertrain using a CNG engine and supercapacitors.* Applied Energy, 157:595 – 606, 2015.

[OZI94] M. Ozisik: *Finite Difference Methods in Heat Transfer*. CRC Press, Boca Raton, 1st editio ed., 1994.

[PAD97] A. K. Padhi, K. S. Nanjundaswamy, and J. B. Goodenough: *Phospho-olivines as Positive-Electrode Materials for Rechargeable Lithium Batteries*. Journal of The Electrochemical Society, 144(4):1188–1194, 1997.

[PAE13] E. Paek, A. J. Pak, and G. S. Hwang: *A computational study of the interfacial structure and capacitance of graphene in [BMIM][PF_6] ionic liquid*. Journal of The Electrochemical Society, 160(1):A1–A10, 2013.

[PAL95a] C. R. Pals and J. Newman: *Thermal Modeling of the Lithium/Polymer Battery: I. Discharge Behavior of a Single Cell*. Journal of The Electrochemical Society, 142(10):3274–3281, 1995.

[PAL95b] C. R. Pals and J. Newman: *Thermal Modeling of the Lithium/Polymer Battery: II. Temperature Profiles in a Cell Stack*. Journal of The Electrochemical Society, 142(10):3282–3288, 1995.

[PAL16] M. R. Palacín and A. de Guibert: *Why do batteries fail?* Science, 351(6273), 2016.

[PAN] Panasonic Corp, *Electric Double Layer Capacitors (Gold Capacitors)*. https://industrial.panasonic.com/ww/products/capacitors/edlc.

[PAN13] H. Pan, Y.-S. Hu, and L. Chen: *Room-temperature stationary sodium-ion batteries for large-scale electric energy storage*. Energy Environ. Sci., 6:2338–2360, 2013.

[PAR12] J.-K. Park: *Principles and Applications of Lithium Secondary Batteries*. John Wiley & Sons, Ltd., 2012. ISBN 978-3-527-33151-2.

[PAR15] I. Parra, J. Marcos, M. García, and L. Marroyo: *Storage requirements for PV power ramp-rate control in a PV fleet*. Solar Energy, 118:426 – 440, 2015.

[PAR16a] I. Parra, J. Marcos, M. García, and L. Marroyo: *Improvement of a control strategy for PV power ramp-rate limitation using the inverters: Reduction of the associated energy losses*. Solar Energy, 127:262 – 268, 2016.

[PAR16b] Y. Parvini, J. B. Siegel, A. G. Stefanopoulou, and A. Vahidi: *Supercapacitor electrical and thermal modeling, identification, and validation for a wide range of temperature and power applications*. IEEE Transactions on Industrial Electronics, 63(3):1574–1585, 2016.

[PAR17] K. Parida, V. Bhavanasi, V. Kumar, J. Wang, and P. S. Lee: *Fast charging self-powered electric double layer capacitor*. Journal of Power Sources, 342:70 – 78, 2017.

[PAS13] J. Pascual, I. San Martín, A. Ursúa, P. Sanchis, and L. Marroyo: *Implementation and control of a residential microgrid based on renewable energy sources, hybrid storage systems and thermal controllable loads*. In *Energy Conversion Congress and Exposition (ECCE), 2013 IEEE*, pages 2304–2309. IEEE, 2013.

[PAS15] J. Pascual, J. Barricarte, P. Sanchis, and L. Marroyo: *Energy management strategy for a renewable-based residential microgrid with generation and demand forecasting*. Applied Energy, 158(Supplement C):12 – 25, 2015.

[PEÑ17] J. C. Peña, *ACS logra la mayor adjudicación de todas las subastas renovables: 1550 MW fotovoltaicos*, 2017. https://www.elconfidencial.com/empresas/2017-07-26/forestalia-se-lleva-316mw-en-la-subasta-de-renovables-de-fotovoltaica_1421073/.

[PEA16] C. Pean, B. Rotenberg, P. Simon, and M. Salanne: *Multi-scale modelling of supercapacitors: From molecular simulations to a transmission line model.* Journal of Power Sources, 326:680 – 685, 2016.

[PEG15] J. Pegueroles Queralt, F. D. Bianchi, and O. Gomis-Bellmunt: *A power smoothing system based on supercapacitors for renewable distributed generation.* IEEE Transactions on Industrial Electronics, 62(1):343–350, 2015.

[PÉR16] I. Pérez Arriaga, C. Knittel, R. Miller, and R. Tabors: *Next Generation Wind and Solar Power: From cost to value.* Technical report, International Energy Agency, 2016.

[PIE16] M. Pierro, F. Bucci, M. De Felice, E. Maggioni, A. Perotto, F. Spada, D. Moser, and C. Cornaro: *Deterministic and Stochastic Approaches for Day-Ahead Solar Power Forecasting.* Journal of Solar Energy Engineering, 139, 2016.

[PIL16] G. Pilatowicz, H. Budde-Meiwes, J. Kowal, C. Sarfert, E. Schoch, M. Königsmann, and D. U. Sauer: *Determination of the lead–acid battery's dynamic response using Butler-Volmer equation for advanced battery management systems in automotive applications.* Journal of Power Sources, 331:348 – 359, 2016.

[POH15] S. Pohlmann, T. Olyschläger, P. Goodrich, J. A. Vicente, J. Jacquemin, and A. Balducci: *Mixtures of Azepanium Based Ionic Liquids and Propylene Carbonate as High Voltage Electrolytes for Supercapacitors.* Electrochimica Acta, 153:426 – 432, 2015.

[PUR14] J. Purewal, J. Wang, J. Graetz, S. Soukiazian, H. Tataria, and M. W. Verbrugge: *Degradation of lithium ion batteries employing graphite negatives and nickel–cobalt–manganese oxide + spinel manganese oxide positives: Part 2, chemical–mechanical degradation model.* Journal of Power Sources, 272:1154 – 1161, 2014.

[QU98] D. Qu and H. Shi: *Studies of activated carbons used in double-layer capacitors.* Journal of Power Sources, 74(1):99 – 107, 1998.

[QU11] L. Qu and W. Qiao: *Constant Power Control of DFIG Wind Turbines With Supercapacitor Energy Storage.* IEEE Transactions on Industry Applications, 47(1):359–367, 2011.

[RAF07] F. Rafik, H. Gualous, R. Gallay, A. Crausaz, and A. Berthon: *Frequency, thermal and voltage supercapacitor characterization and modeling.* Journal of power sources, 165(2):928–934, 2007.

[RAM03] P. Ramadass, B. Haran, R. White, and B. N. Popov: *Mathematical modeling of the capacity fade of Li-ion cells.* Journal of Power Sources, 123(2):230 – 240, 2003.

[RAM16] S. Ramachandran, A. Khandelwal, K. S. Hariharan, B.-C. Kim, and K. Y. Kim: *Rapid Analysis of Charging Profiles of Lithium Ion Batteries Using a Hybrid Simplified Electrochemical Model.* Journal of The Electrochemical Society, 163(6):A1101–A1111, 2016.

[RAN17] T. Randall, *Tesla Flips the Switch on the Gigafactory*, 2017. Online, https://www.bloomberg.com/news/articles/2017-01-04/tesla-flips-the-switch-on-the-gigafactory.

[RAW14] P. Rawlinson, N. Herron, B. Edwards, and G. Goetchius, *Vehicle battery pack thermal barrier*, 2014. US Patent 8,875,828.

[REC] R. Recycler, *Press release: A revolutionary new technology.* http://www.rockster.at/index.php?option=com_content&view=article&id=152%3Ar1100de&catid=4%3Anews&Itemid=7&lang=en.

[RED10] T. Reddy: *Linden's Handbook of Batteries, 4th Edition*. McGraw-Hill Education, 2010. ISBN 9780071624190.

[REN17] G. Ren, J. Liu, J. Wan, Y. Guo, and D. Yu: *Overview of wind power intermittency: Impacts, measurements, and mitigation solutions*. Applied Energy, 204:47 – 65, 2017.

[REZ17] D. Rezzak and N. Boudjerda: *Management and control strategy of a hybrid energy source fuel cell/supercapacitor in electric vehicles*. International Transactions on Electrical Energy Systems, 27(6):e2308–n/a, 2017.

[RIC00] B. Ricketts and C. Ton-That: *Self-discharge of carbon-based supercapacitors with organic electrolytes*. Journal of Power Sources, 89(1):64 – 69, 2000.

[ROS92] E. Rossen, C. Jones, and J. Dahn: *Structure and electrochemistry of $Li_xMn_yNi_{1-y}O_2$*. Solid State Ionics, 57(3):311 – 318, 1992.

[ROS11] M. A. Roscher and D. U. Sauer: *Dynamic electric behavior and open-circuit-voltage modeling of $LiFePO_4$-based lithium ion secondary batteries*. Journal of Power Sources, 196(1):331 – 336, 2011.

[ROT04] E. Roth and D. Doughty: *Thermal abuse performance of high-power 18650 Li-ion cells*. Journal of Power Sources, 128(2):308 – 318, 2004.

[ROU94] J. Rouquerol, D. Avnir, C. W. Fairbridge, D. H. Everett, J. M. Haynes, N. Pernicone, J. D. F. Ramsay, K. S. W. Sing, and K. K. Unger: *Recommendations for the characterization of porous solids*. technical report, International Union of Pure and Applied Chemistry, 1994.

[ROU96] A. Rougier, P. Gravereau, and C. Delmas: *Optimization of the Composition of the $Li_{1-z}Ni_{1+z}O_2$ Electrode Materials: Structural, Magnetic, and Electrochemical Studies*. Journal of The Electrochemical Society, 143(4):1168–1175, 1996.

[SAA14] I. Saadoune, S. Difi, S. Doubaji, K. Edström, and P. E. Lippens: *Electrode materials for sodium ion batteries: A cheaper solution for the energy storage*. In *2014 International Conference on Optimization of Electrical and Electronic Equipment (OPTIM)*, pages 1078–1081, 2014.

[SAB15] J. Sabatier, J. M. Francisco, F. Guillemard, L. Lavigne, M. Moze, and M. Merveillaut: *Lithium-ion batteries modeling: A simple fractional differentiation based model and its associated parameters estimation method*. Signal Processing, 107(Supplement C):290 – 301, 2015.

[SAI01] Y. Saito, K. Takano, K. Kanari, A. Negishi, K. Nozaki, and K. Kato: *Comparative study of thermal behaviors of various lithium-ion cells*. Journal of Power Sources, 97(Supplement C):688 – 692, 2001.

[SAK09] M. A. Sakka, H. Gualous, J. V. Mierlo, and H. Culcu: *Thermal modeling and heat management of supercapacitor modules for vehicle applications*. Journal of Power Sources, 194(2):581 – 587, 2009.

[SAL15] A. Salvadori, D. Grazioli, and M. Geers: *Governing equations for a two-scale analysis of Li-ion battery cells*. International Journal of Solids and Structures, 59(Supplement C):90 – 109, 2015.

[SAN06] S. Santhanagopalan, Q. Guo, P. Ramadass, and R. E. White: *Review of models for predicting the cycling performance of lithium ion batteries*. Journal of Power Sources, 156(2):620 – 628, 2006.

[SAN13] I. San Martín: *Integración de energías renovables y almacenamiento energético en microrredes eléctricas*. Ph. D. thesis, Universidad Pública de Navarra, 2013.

[SAN14] I. San Martín, A. Ursúa, and P. Sanchis: *Modelling of PEM Fuel Cell Performance: Steady-State and Dynamic Experimental Validation.* Energies, 7(2):670–700, 2014.

[SAR04] G. Sarre, P. Blanchard, and M. Broussely: *Aging of lithium-ion batteries.* Journal of Power Sources, 127(1-2):65–71, 2004.

[SAU13] D. U. Sauer: *Marktanreizprogramm für dezentrale Speicher insbesondere für PV-Strom.* Short report, RWTH Aachen, 2013.

[SCA17] A. Scalia, F. Bella, A. Lamberti, S. Bianco, C. Gerbaldi, E. Tresso, and C. F. Pirri: *A flexible and portable powerpack by solid-state supercapacitor and dye-sensitized solar cell integration.* Journal of Power Sources, 359:311 – 321, 2017.

[SCH57] J. Schrama: *On the phenomenological theory of linear relaxation processes.* Uitg. Excelsior, 1957.

[SCH99] S. Scharner, W. Weppner, and P. Schmid-Beurmann: *Evidence of Two-Phase Formation upon Lithium Insertion into the $Li_{1.33}Ti_{1.67}O_4$ Spinel.* Journal of The Electrochemical Society, 146(3):857–861, 1999.

[SCH06] J. Schiffer, D. Linzen, and D. U. Sauer: *Heat generation in double layer capacitors.* Journal of Power Sources, 160(1):765–772, 2006.

[SCH13] J. Schmalstieg, S. Käbitz, M. Ecker, and D. U. Sauer: *From accelerated aging tests to a lifetime prediction model: Analyzing lithium-ion batteries.* In *2013 World Electric Vehicle Symposium and Exhibition (EVS27)*, pages 1–12, 2013.

[SCH14] J. Schmalstieg, S. Käbitz, M. Ecker, and D. U. Sauer: *A holistic aging model for Li(NiMnCo)O_2 based 18650 lithium-ion batteries.* Journal of Power Sources, 257:325 – 334, 2014.

[SCH15] S. F. Schuster, T. Bach, E. Fleder, J. Müller, M. Brand, G. Sextl, and A. Jossen: *Nonlinear aging characteristics of lithium-ion cells under different operational conditions.* Journal of Energy Storage, 1:44 – 53, 2015.

[SCH16] C. Schütter, T. Husch, V. Viswanathan, S. Passerini, A. Balducci, and M. Korth: *Rational design of new electrolyte materials for electrochemical double layer capacitors.* Journal of Power Sources, 326:541 – 548, 2016.

[SCH17] J. Schmitt, A. Maheshwari, M. Heck, S. Lux, and M. Vetter: *Impedance change and capacity fade of lithium nickel manganese cobalt oxide-based batteries during calendar aging.* Journal of Power Sources, 353:183 – 194, 2017.

[SCR13] B. Scrosati, K. Abraham, W. van Schalkwijk, and J. Hassoun: *Lithium Batteries: Advanced Technologies and Applications.* The ECS Series of Texts and Monographs. Wiley, 2013. ISBN 9781118615393.

[SED15] V. Sedlakova, J. Sikula, J. Majzner, P. Sedlak, T. Kuparowitz, B. Buergler, and P. Vasina: *Supercapacitor equivalent electrical circuit model based on charges redistribution by diffusion.* Journal of Power Sources, 286:58–65, 2015.

[SEO16] H. Seo, S.-G. Kim, J. Jung, and M.-S. Kim: *Preparation and characterization of carbon aerogel activated with KOH and CO_2: Effect of pore size distribution on electrochemical properties as EDLC electrodes.* Polymer (Korea), 40(4):577–586, 2016.

[SHA10] P. Sharma and T. Bhatti: *A review on electrochemical double-layer capacitors.* Energy Conversion and Management, 51(12):2901 – 2912, 2010.

[SHE16] J.-F. Shen, Y.-J. He, and Z.-F. Ma: *A systematical evaluation of polynomial based equivalent circuit model for charge redistribution dominated self-discharge process in supercapacitors.* Journal of Power Sources, 303:294–304, 2016.

[SID15] A. Sidhu, A. Izadian, and S. Anwar: *Adaptive Nonlinear Model-Based Fault Diagnosis of Li-Ion Batteries.* IEEE Transactions on Industrial Electronics, 62(2):1002–1011, 2015.

[SIE10] Siemens AG, *Sitras SES: Stationary energy storage system for DC traction power supply*, 2010. https://w3.usa.siemens.com/mobility/us/Documents/en/rail-solutions/railway-electrification/dc-traction-power-supply/sitras-ses-en.pdf.

[SIM14] P. Simon, Y. Gogotsi, and B. Dunn: *Where Do Batteries End and Supercapacitors Begin?* Science, 343(6176):1210–1211, 2014.

[SIN] Sinautec, *Sinautec Automobile Technologies.* http://www.sinautecus.com/.

[SMA07] M. Smart, J. Whitacre, B. Ratnakumar, and K. Amine: *Electrochemical performance and kinetics of $Li_{1+x}(Co_{1/3}Ni_{1/3}Mn_{1/3})_{1-x}O_2$ cathodes and graphite anodes in low-temperature electrolytes.* Journal of Power Sources, 168(2):501 – 508, 2007.

[SMI10] A. J. Smith, J. C. Burns, S. Trussler, and J. R. Dahn: *Precision Measurements of the Coulombic Efficiency of Lithium-Ion Batteries and of Electrode Materials for Lithium-Ion Batteries.* Journal of The Electrochemical Society, 157(2):A196–A202, 2010.

[SMI16] V. Smil: *Energy Transitions: Global and National Perspectives, 2nd Edition.* ABC-CLIO, 2016. ISBN 9781440853258.

[SOE13] K. Soeda, M. Yamagata, S. Yamazaki, and M. Ishikawa: *Application of Chitosan-based Gel Electrolytes with Ionic Liquids for High-Performance and Safe Electric Double Layer Capacitors.* Electrochemistry, 81(10):867–872, 2013.

[SON00] L. Song and J. W. Evans: *Electrochemical-Thermal Model of Lithium Polymer Batteries.* Journal of The Electrochemical Society, 147(6):2086–2095, 2000.

[SON14a] M.-S. Song, R.-H. Kim, S.-W. Baek, K.-S. Lee, K. Park, and A. Benayad: *Is $Li_4Ti_5O_{12}$ a solid-electrolyte-interphase-free electrode material in Li-ion batteries? Reactivity between the $Li_4Ti_5O_{12}$ electrode and electrolyte.* J. Mater. Chem. A, 2:631–636, 2014.

[SON14b] Z. Song, H. Hofmann, J. Li, J. Hou, X. Han, and M. Ouyang: *Energy management strategies comparison for electric vehicles with hybrid energy storage system.* Applied Energy, 134:321 – 331, 2014.

[SON17] Z. Song, J. Hou, S. Xu, M. Ouyang, and J. Li: *The influence of driving cycle characteristics on the integrated optimization of hybrid energy storage system for electric city buses.* Energy, 135:91 – 100, 2017.

[SOU15] M. Soumya, G. Binitha, P. Praveen, K. Subramanian, Y. Lee, V. S. Nair, and N. Sivakumar: *Electrochemical Performance of PbO_2 and PbO_2–CNT Composite Electrodes for Energy Storage Devices.* Journal of nanoscience and nanotechnology, 15(1):703–708, 2015.

[SPE14] V. R. Spena Visentini, L. M. Carlotti Zarpelon, and R. N. Faria: *Self-Discharge and Microstructure of Supercapacitors Tested at Room Temperature and at 333 K.* In *Advanced Powder Technology IX*, volum 802 of *Materials Science Forum*, pages 427–432. Trans Tech Publications, 2014.

[SPO03] R. Spotnitz and J. Franklin: *Abuse behavior of high-power, lithium-ion cells.* Journal of Power Sources, 113(1):81 – 100, 2003.

[SPO07] R. M. Spotnitz, J. Weaver, G. Yeduvaka, D. Doughty, and E. Roth: *Simulation of abuse tolerance of lithium-ion battery packs.* Journal of Power Sources, 163(2):1080 – 1086, 2007.

[SPY00] R. Spyker and R. Nelms: *Classical equivalent circuit parameters for a double-layer capacitor.* IEEE transactions on aerospace and electronic systems, 36(3):829–836, 2000.

[SRI99] V. Srinivasan and J. Weidner: *Mathematical modeling of electrochemical capacitors.* Journal of the Electrochemical Society, 146(5):1650–1658, 1999.

[SRI04] V. Srinivasan and J. Newman: *Discharge Model for the Lithium Iron-Phosphate Electrode.* Journal of The Electrochemical Society, 151(10):A1517–A1529, 2004.

[STE24] O. Stern: *The theory of the electrolytic double-layer.* Z. Elektrochem, 30(508):1014–1020, 1924.

[STE00] D. A. Stevens and J. R. Dahn: *High Capacity Anode Materials for Rechargeable Sodium-Ion Batteries.* Journal of The Electrochemical Society, 147(4):1271–1273, 2000.

[STE14] M. Steuer, U. Fahl, and A. Voß: *Curtailment: an option for cost-efficient integration of variable renewable generation.* technical report, The INSIGHT_E project, 2014.

[STE17a] A. Steiner, C. Köhler, I. Metzinger, A. Braun, M. Zirkelbach, D. Ernst, P. Tran, and B. Ritter: *Critical weather situations for renewable energies - Part A: Cyclone detection for wind power.* Renewable Energy, 101:41 – 50, 2017.

[STE17b] D. Steingart, *Redox without Redox*, 2017. Online, https://medium.com/the-unfortunate-tetrahedron/a-potential-big-deal-in-batteries-298c7ad9543a.

[STM12] STMicroelectronics, *Press Release: STMicroelectronics Breaks through LED Camera Flash Limitations*, 2012. http://www.cap-xx.com/wp-content/uploads/2015/04/ST-Microelectronics-Breaks-through-LED-Camera-Flash-Limitations.pdf.

[STR14] D. I. Stroe, M. Świerczyński, A. I. Stan, R. Teodorescu, and S. J. Andreasen: *Accelerated Lifetime Testing Methodology for Lifetime Estimation of Lithium-Ion Batteries Used in Augmented Wind Power Plants.* IEEE Transactions on Industry Applications, 50(6):4006–4017, 2014.

[STR15] J. Straubel, E. Berdichevsky, D. Lyons, T. Colson, M. Eberhard, I. Wright, and R. Ferber, *Battery mounting and cooling system*, 2015. US Patent 9,065,103.

[STU04] T. Stuart and A. Hande: *HEV battery heating using AC currents.* Journal of Power Sources, 129(2):368 – 378, 2004.

[SUN09] Y.-K. Sun, S.-T. Myung, B.-C. Park, J. Prakash, I. Belharouak, and K. Amine: *High-energy cathode material for long-life and safe lithium batteries.* Nat. Mater ., 8:320–324, 2009.

[SUN15] W. Sun, X. Rui, M. Ulaganathan, S. Madhavi, and Q. Yan: *Few-layered $Ni(OH)_2$ nanosheets for high-performance supercapacitors.* Journal of Power Sources, 295:323 – 328, 2015.

[SUP] Supreme Power Solutions, *SPS CAP.* http://spscap.com/en/.

[SWI16] M. Swierczynski, D. I. Stroe, E. M. Laserna, E. Sarasketa-Zabala, J. M. Timmermans, S. Goutam, and R. Teodorescu: *The Second Life Ageing of the NMC/C Electric Vehicle Retired Li-Ion Batteries in the Stationary Applications*. ECS Transactions, 74(1):55–62, 2016.

[SZU08] A. Szumanowski and Y. Chang: *Battery Management System Based on Battery Nonlinear Dynamics Modeling*. IEEE Transactions on Vehicular Technology, 57(3):1425–1432, 2008.

[TAN16] D. Tang, S. Hu, F. Dai, R. Yi, M. L. Gordin, S. Chen, J. Song, and D. Wang: *Self-Templated Synthesis of Mesoporous Carbon from Carbon Tetrachloride Precursor for Supercapacitor Electrodes*. ACS Applied Materials & Interfaces, 8(11):6779–6783, 2016.

[TAT14] E. Tatsukawa and K. Tamura: *Activity correction on electrochemical reaction and diffusion in lithium intercalation electrodes for discharge/charge simulation by single particle model*. Electrochimica Acta, 115(Supplement C):75 – 85, 2014.

[TEC16] TechNavio: *Global Automotive Ultracapacitor Market 2016 – 2020*. technical report 3941007, 2016.

[TES] Tesla, *Tesla Powerwall*. Online, https://www.tesla.com/powerwall?redirect=no.

[TEV13] T. Tevi, H. Yaghoubi, J. Wang, and A. Takshi: *Application of poly (p-phenylene oxide) as blocking layer to reduce self-discharge in supercapacitors*. Journal of Power Sources, 241:589 – 596, 2013.

[TEV15] T. Tevi and A. Takshi: *Modeling and simulation study of the self-discharge in supercapacitors in presence of a blocking layer*. Journal of Power Sources, 273:857 – 862, 2015.

[THA98] M. M. Thackeray, Y. Shao-Horn, A. J. Kahaian, K. D. Kepler, E. Skinner, J. T. Vaughey, and S. A. Hackney: *Structural Fatigue in Spinel Electrodes in High Voltage (4 V)$Li/Li_xMn_2O_4$ Cells*. Electrochemical and Solid-State Letters, 1(1):7–9, 1998.

[THO01] K. E. Thomas, C. Bogatu, and J. Newman: *Measurement of the Entropy of Reaction as a Function of State of Charge in Doped and Undoped Lithium Manganese Oxide*. Journal of The Electrochemical Society, 148(6):A570–A575, 2001.

[THO03a] E. Thomas, H. Case, D. Doughty, R. Jungst, G. Nagasubramanian, and E. Roth: *Accelerated power degradation of Li-ion cells*. Journal of Power Sources, 124(1):254 – 260, 2003.

[THO03b] K. E. Thomas and J. Newman: *Thermal Modeling of Porous Insertion Electrodes*. Journal of The Electrochemical Society, 150(2):A176–A192, 2003.

[TIM16] J. M. Timmermans, A. Nikolian, J. D. Hoog, R. Gopalakrishnan, S. Goutam, N. Omar, T. Coosemans, J. V. Mierlo, A. Warnecke, D. U. Sauer, M. Swierczynski, D. I. Stroe, E. Martinez-Laserna, E. Sarasketa-Zabala, J. Gastelurrutia, and N. Nerea: *Batteries 2020 — Lithium-ion battery first and second life ageing, validated battery models, lifetime modelling and ageing assessment of thermal parameters*. In *2016 18th European Conference on Power Electronics and Applications (EPE'16 ECCE Europe)*, pages 1–23, 2016.

[TIP14] S. Tippmann, D. Walper, L. Balboa, B. Spier, and W. G. Bessler: *Low-temperature charging of lithium-ion cells part I: Electrochemical modeling and experimental investigation of degradation behavior*. Journal of Power Sources, 252(Supplement C):305 – 316, 2014.

[TOR15] D. Torregrossa, K. E. Toghill, V. Amstutz, H. H. Girault, and M. Paolone: *Macroscopic indicators of fault diagnosis and ageing in electrochemical double layer capacitors.* Journal of Energy Storage, 2:8 – 24, 2015.

[TOR16a] D. Torregrossa and M. Paolone: *Modelling of current and temperature effects on supercapacitors ageing. Part I: Review of driving phenomenology.* Journal of Energy Storage, 5:85 – 94, 2016.

[TOR16b] D. Torregrossa and M. Paolone: *Modelling of current and temperature effects on supercapacitors ageing. Part II: State-of-Health assessment.* Journal of Energy Storage, 5:95 – 101, 2016.

[TRA71] S. Trasatti and G. Buzzanca: *Ruthenium dioxide: A new interesting electrode material. Solid state structure and electrochemical behaviour.* Journal of Electroanalytical Chemistry and Interfacial Electrochemistry, 29:A1–A5, 1971.

[TRA09] S. Trasatti: *Electrochemical theory — Electrokinetics.* In J. Garche (ed.), *Encyclopedia of Electrochemical Power Sources*, pages 23 – 31. Elsevier, Amsterdam, 2009. ISBN 978-0-444-52745-5.

[TRI15] S. Trieste, S. Hmam, J.-C. Olivier, S. Bourguet, and L. Loron: *Techno-economic optimization of a supercapacitor-based energy storage unit chain: Application on the first quick charge plug-in ferry.* Applied Energy, 153:3 – 14, 2015.

[TRO15] J. Trovão and C. Antunes: *A comparative analysis of meta-heuristic methods for power management of a dual energy storage system for electric vehicles.* Energy Conversion and Management, 95:281–296, 2015.

[TSI13] Y. Tsividis and J. Milios: *A detailed look at electrical equivalents of uniform electrochemical diffusion using nonuniform resistance-capacitance ladders.* Journal of Electroanalytical Chemistry, 707(Supplement C):156 – 165, 2013.

[TU06] J. Tu, X. Zhao, G. Cao, D. Zhuang, T. Zhu, and J. Tu: *Enhanced cycling stability of $LiMn_2O_4$ by surface modification with melting impregnation method.* Electrochimica Acta, 51(28):6456 – 6462, 2006.

[URS12] A. Ursúa and P. Sanchis: *Static-dynamic modelling of the electrical behaviour of a commercial advanced alkaline water electrolyser.* International Journal of Hydrogen Energy, 37(24):18598 – 18614, 2012.

[VAN99] E. Vangioni Flam and M. Cassé: *Cosmic Lithium-Beryllium-Boron Story.* Astrophysics and Space Science, 265(1):77–86, 1999.

[VAQ12] S. Vaquero, R. Díaz, M. Anderson, J. Palma, and R. Marcilla: *Insights into the influence of pore size distribution and surface functionalities in the behaviour of carbon supercapacitors.* Electrochimica Acta, 86:241 – 247, 2012.

[VAT10] J. Vatamanu, O. Borodin, and G. D. Smith: *Molecular insights into the potential and temperature dependences of the differential capacitance of a room-temperature ionic liquid at graphite electrodes.* Journal of the American Chemical Society, 132(42):14825–14833, 2010.

[VEN03] S. Venkatraman, Y. Shin, and A. Manthiram: *Phase Relationships and Structural and Chemical Stabilities of Charged $Li_{1-x}CoO_{2-\delta}$ and $Li_{1-x}Ni_{0.85}Co_{0.15}O_{2-\delta}$ Cathodes.* Electrochemical and Solid-State Letters, 6(1):A9–A12, 2003.

[VER96] M. W. Verbrugge and B. J. Koch: *Modeling Lithium Intercalation of Single-Fiber Carbon Microelectrodes.* Journal of The Electrochemical Society, 143(2):600–608, 1996.

[VER14] G. Vertiz, M. Oyarbide, H. Macicior, O. Miguel, I. Cantero, P. F. de Arroiabe, and I. Ulacia: *Thermal characterization of large size lithium-ion pouch cell based on 1d electro-thermal model.* Journal of Power Sources, 272(Supplement C):476 – 484, 2014.

[VET05] J. Vetter, P. Novák, M. Wagner, C. Veit, K.-C. Möller, J. Besenhard, M. Winter, M. Wohlfahrt-Mehrens, C. Vogler, and A. Hammouche: *Ageing mechanisms in lithium-ion batteries.* Journal of Power Sources, 147(1):269 – 281, 2005.

[VIN] VINATech, *Supercapacitor Solution.* http://www.vina.co.kr/eng/product/supercap.html.

[VOI15] I. Voicu, H. Louahlia, H. Gualous, and R. Gallay: *Thermal management and forced air-cooling of supercapacitors stack.* Applied Thermal Engineering, 85:89–99, 2015.

[WAA13] W. Waag, S. Käbitz, and D. U. Sauer: *Experimental investigation of the lithium-ion battery impedance characteristic at various conditions and aging states and its influence on the application.* Applied Energy, 102(Supplement C):885 – 897, 2013.

[WAA14] W. Waag, C. Fleischer, and D. U. Sauer: *Critical review of the methods for monitoring of lithium-ion batteries in electric and hybrid vehicles.* Journal of Power Sources, 258:321 – 339, 2014.

[WAF14] E. Waffenschmidt: *Dimensioning of Decentralized Photovoltaic Storages with Limited Feed-in Power and their Impact on the Distribution Grid.* Energy Procedia, 46:88 – 97, 2014. 8th International Renewable Energy Storage Conference and Exhibition (IRES 2013).

[WAG06] M. Wagemaker, D. Simon, E. Kelder, J. Schoonman, C. Ringpfeil, U. Haake, D. Lützenkirchen-Hecht, R. Frahm, and F. Mulder: *A Kinetic Two-Phase and Equilibrium Solid Solution in Spinel $Li_{4+x}Ti_5O_{12}$.* Advanced Materials, 18(23):3169–3173, 2006.

[WAN07] Y. Wang, W. Jiang, T. Yan, and G. A. Voth: *Understanding ionic liquids through atomistic and coarse-grained molecular dynamics simulations.* Accounts of chemical research, 40(11):1193–1199, 2007.

[WAN11a] H. Wang and L. Pilon: *Accurate Simulations of Electric Double Layer Capacitance of Ultramicroelectrodes.* The Journal of Physical Chemistry C, 115(33):16711–16719, 2011.

[WAN11b] J. Wang, P. Liu, J. Hicks-Garner, E. Sherman, S. Soukiazian, M. Verbrugge, H. Tataria, J. Musser, and P. Finamore: *Cycle-life model for graphite-$LiFePO_4$ cells.* Journal of Power Sources, 196(8):3942 – 3948, 2011.

[WAN12] Q. Wang, P. Ping, X. Zhao, G. Chu, J. Sun, and C. Chen: *Thermal runaway caused fire and explosion of lithium ion battery.* Journal of Power Sources, 208(Supplement C):210 – 224, 2012.

[WAN14a] J. Wang, Y.-c. K. Chen-Wiegart, and J. Wang: *In Situ Three-Dimensional Synchrotron X-ray Nanotomagraphy of the (De)Lithiation Processes in Tin Anodes.* Angewandte Chemie International Edition, 53(17):4460–4464, 2014.

[WAN14b] J. Wang, J. Purewal, P. Liu, J. Hicks-Garner, S. Soukazian, E. Sherman, A. Sorenson, L. Vu, H. Tataria, and M. W. Verbrugge: *Degradation of lithium ion batteries employing graphite negatives and nickel–cobalt–manganese oxide + spinel manganese oxide positives: Part 1, aging mechanisms and life estimation.* Journal of Power Sources, 269:937 – 948, 2014.

[WAN14c] L. Wang, L. Chen, B. Yan, C. Wang, F. Zhu, X. Jiang, Y. Chao, and G. Yang: *In situ preparation of SnO_2@polyaniline nanocomposites and their synergetic structure for high-performance supercapacitors.* Journal of Materials Chemistry A, 2(22):8334–8341, 2014.

[WAN14d] W. Wang, M. Cheng, Y. Wang, B. Zhang, Y. Zhu, S. Ding, and W. Chen: *A novel energy management strategy of onboard supercapacitor for subway applications with permanent-magnet traction system.* IEEE Transactions on Vehicular Technology, 63(6):2578–2588, 2014.

[WAN16a] Y. Wang, Y. Song, and Y. Xia: *Electrochemical capacitors: mechanism, materials, systems, characterization and applications.* Chem. Soc. Rev., 45:5925–5950, 2016.

[WAN16b] Y. Wang, D. Yang, X. Zhang, and Z. Chen: *Probability based remaining capacity estimation using data-driven and neural network model.* Journal of Power Sources, 315(Supplement C):199 – 208, 2016.

[WEN14] J. Weniger, J. Bergner, and V. Quaschning: *Integration of PV power and load forecasts into the operation of residential PV battery systems*, 2014.

[WER15] S. Werkstetter, *Ultracapacitor Usage in Wind Turbine Pitch Control Systems*, 2015. Maxwell Technologies, Inc.

[WHI78] M. Whittingham: *Chemistry of intercalation compounds: Metal guests in chalcogenide hosts.* Progress in Solid State Chemistry, 12(1):41 – 99, 1978.

[WIL13] N. Williard, W. He, C. Hendricks, and M. Pecht: *Lessons Learned from the 787 Dreamliner Issue on Lithium-Ion Battery Reliability.* Energies, 6(9):4682–4695, 2013.

[WIN03] M. Winter, K.-C. Moeller, and J. Besenhard: *Carbonaceous and Graphitic Anodes.* In Gholam-Abbas, Nazri, Gianfranco, and Pistoia (editors), *Lithium Batteries Science and Technology.* Springer US, 2003. ISBN 978-1-4020-7628-2.

[WU10] Z.-S. Wu, W. Ren, D.-W. Wang, F. Li, B. Liu, and H.-M. Cheng: *High-Energy MnO_2 Nanowire/Graphene and Graphene Asymmetric Electrochemical Capacitors.* ACS Nano, 4(10):5835–5842, 2010.

[WU12] S.-L. Wu, W. Zhang, X. Song, A. K. Shukla, G. Liu, V. Battaglia, and V. Srinivasan: *High Rate Capability of $Li(Ni_{1/3}Mn_{1/3}Co_{1/3})O_2$ Electrode for Li-Ion Batteries.* Journal of The Electrochemical Society, 159(4):A438–A444, 2012.

[WU14] B. Wu, M. A. Parkes, V. Yufit, L. D. Benedetti, S. Veismann, C. Wirsching, F. Vesper, R. F. Martinez-Botas, A. J. Marquis, G. J. Offer, and N. P. Brandon: *Design and testing of a 9.5 kWe proton exchange membrane fuel cell–supercapacitor passive hybrid system.* International Journal of Hydrogen Energy, 39(15):7885 – 7896, 2014.

[XIN12] L. Xing, J. Vatamanu, O. Borodin, and D. Bedrov: *On the atomistic nature of capacitance enhancement generated by ionic liquid electrolyte confined in subnanometer pores.* The journal of physical chemistry letters, 4(1):132–140, 2012.

[XIO16] X.-b. Xiong, J.-y. Zhang, J. Ma, X.-r. Zeng, H. Qian, and Y.-y. Li: *Fabrication of porous nickel (hydr)oxide film with rational pore size distribution on nickel foam by induction heating deposition for high-performance supercapacitors.* Materials Chemistry and Physics, 181:1 – 6, 2016.

[XU04] K. Xu: *Nonaqueous Liquid Electrolytes for Lithium-Based Rechargeable Batteries.* Chemical Reviews, 104(10):4303–4418, 2004.

[XU11] B. Xu, C. R. Fell, M. Chi, and Y. S. Meng: *Identifying surface structural changes in layered Li-excess nickel manganese oxides in high voltage lithium ion batteries: A joint experimental and theoretical study.* Energy Environ. Sci., 4:2223–2233, 2011.

[XU15] H. Xu, X. Hu, H. Yang, Y. Sun, C. Hu, and Y. Huang: *Flexible Asymmetric Micro-Supercapacitors Based on Bi_2O_3 and MnO_2 Nanoflowers: Larger Areal Mass Promises Higher Energy Density.* Advanced Energy Materials, 5(6):1401882–n/a, 2015.

[YAN14] N. Yang, X. Zhang, and G. Li: *State-of-charge estimation for lithium ion batteries via the simulation of lithium distribution in the electrode particles.* Journal of Power Sources, 272(Supplement C):68 – 78, 2014.

[YAN16a] H. Yang and Y. Zhang: *A task scheduling algorithm based on supercapacitor charge redistribution and energy harvesting for wireless sensor nodes.* Journal of Energy Storage, 6:186 – 194, 2016.

[YAN16b] I. Yang, S.-G. Kim, S. H. Kwon, J. H. Lee, M.-S. Kim, and J. C. Jung: *Pore size-controlled carbon aerogels for EDLC electrodes in organic electrolytes.* Current Applied Physics, 16(6):665 – 672, 2016.

[YAN16c] N. Yang, X. Zhang, B. Shang, and G. Li: *Unbalanced discharging and aging due to temperature differences among the cells in a lithium-ion battery pack with parallel combination.* Journal of Power Sources, 306(Supplement C):733 – 741, 2016.

[YAN18] S. Yang, Y. Ma, F. Duan, K. He, L. Wang, Z. Wei, L. Zhu, T. Ma, H. Li, and S. Ye: *Characteristics and formation of typical winter haze in Handan, one of the most polluted cities in China.* Science of The Total Environment, 613(Supplement C):1367 – 1375, 2018.

[YAZ99] R. Yazami: *Surface chemistry and lithium storage capability of the graphite-lithium electrode.* Electrochimica Acta, 45(1):87 – 97, 1999.

[YE16] S. Ye, L. Zhu, I.-J. Kim, S.-H. Yang, and W.-C. Oh: *Characterization of expanded graphene nanosheet as additional material and improved performances for electric double layer capacitors.* Journal of Industrial and Engineering Chemistry, 43:53–60, 2016.

[YOS87] A. Yoshino, K. Sanechika, and T. Nakajima, *Secondary battery*, 1987. US Patent 4,668,595.

[YOS07] M. Yoshida, Y. Tsukamoto, T. Matsuda, Y. Dougan, and K. Ueno: *Introducing Electric-powered Forklift Truck "New ARION" Series.* Technical report, Komatsu, 2007.

[YOU16] M. Yousaf, H. T. H. Shi, Y. Wang, Y. Chen, Z. Ma, A. Cao, H. E. Naguib, and R. P. S. Han: *Novel Pliable Electrodes for Flexible Electrochemical Energy Storage Devices: Recent Progress and Challenges.* Advanced Energy Materials, 6(17):1600490–n/a, 2016.

[YUN] Yunasko, *Ultracapacitor Product Line.* http://yunasko.com/en/products.

[ZEN15] Y. Zeng, Y. Han, Y. Zhao, Y. Zeng, M. Yu, Y. Liu, H. Tang, Y. Tong, and X. Lu: *Advanced Ti-Doped Fe_2O_3@PEDOT Core/Shell Anode for High-Energy Asymmetric Supercapacitors.* Advanced Energy Materials, 5(12):1402176–n/a, 2015.

[ZEN16] Y. Zeng, M. Yu, Y. Meng, P. Fang, X. Lu, and Y. Tong: *Iron-Based Supercapacitor Electrodes: Advances and Challenges.* Advanced Energy Materials, 6(24):1601053–n/a, 2016.

[ZER16] A. Zervos: *Renewables 2016 global status report.* Technical report, REN21 Renewable Energy Policy Network for the 21st Century, 2016.

[ZHA04] S. Zhang, K. Xu, and T. Jow: *Electrochemical impedance study on the low temperature of Li-ion batteries.* Electrochimica Acta, 49(7):1057 – 1061, 2004.

[ZHA12] W. Zhang, Y. H. Qu, and L. J. Gao: *Performance of PbO_2/activated carbon hybrid supercapacitor with carbon foam substrate.* Chinese Chemical Letters, 23(5):623 – 626, 2012.

[ZHA13] F. Zhang, T. Zhang, X. Yang, L. Zhang, K. Leng, Y. Huang, and Y. Chen: *A high-performance supercapacitor-battery hybrid energy storage device based on graphene-enhanced electrode materials with ultrahigh energy density.* Energy Environ. Sci., 6:1623–1632, 2013.

[ZHA14a] X. Zhang, H. Xue, Y. Xu, H. Chen, and C. Tan: *An investigation of an uninterruptible power supply (UPS) based on supercapacitor and liquid nitrogen hybridization system.* Energy Conversion and Management, 85:784–792, 2014.

[ZHA14b] R. Zhao, J. Gu, and J. Liu: *An investigation on the significance of reversible heat to the thermal behavior of lithium ion battery through simulations.* Journal of Power Sources, 266(Supplement C):422 – 432, 2014.

[ZHA15a] L. Zhang, Z. Wang, X. Hu, F. Sun, and D. G. Dorrell: *A comparative study of equivalent circuit models of ultracapacitors for electric vehicles.* Journal of Power Sources, 274:899 – 906, 2015.

[ZHA15b] S. Zhang and N. Pan: *Supercapacitors Performance Evaluation.* Advanced Energy Materials, 5(6):1401401–n/a, 2015.

[ZHA15c] H. Zhao, Q. Wu, S. Hu, H. Xu, and C. N. Rasmussen: *Review of energy storage system for wind power integration support.* Applied Energy, 137:545 – 553, 2015.

[ZHA16a] L. Zhang, K. Tsay, C. Bock, and J. Zhang: *Ionic liquids as electrolytes for nonaqueous solutions electrochemical supercapacitors in a tempeature range of 20 ^oC–80 ^oC.* Journal of Power Sources, 324:615–624, 2016.

[ZHA16b] X. Zhang, Y. Wang, D. Yang, and Z. Chen: *An on-line estimation of battery pack parameters and state-of-charge using dual filters based on pack model.* Energy, 115(Part 1):219 – 229, 2016.

[ZHA16c] X. Zhang, Z. Zhang, H. Pan, W. Salman, Y. Yuan, and Y. Liu: *A portable high-efficiency electromagnetic energy harvesting system using supercapacitors for renewable energy applications in railroads.* Energy Conversion and Management, 118:287–294, 2016.

[ZHA16d] N. Zhao, N. Schofield, and W. Niu: *Energy storage system for a port crane hybrid power-train.* IEEE Transactions on Transportation Electrification, 2(4):480–492, 2016.

[ZHE99] T. Zheng, A. S. Gozdz, and G. G. Amatucci: *Reactivity of the Solid Electrolyte Interface on Carbon Electrodes at Elevated Temperatures.* Journal of The Electrochemical Society, 146(11):4014–4018, 1999.

[ZHE15] Y. Zheng, M. Ouyang, L. Lu, J. Li, Z. Zhang, and X. Li: *Study on the correlation between state of charge and coulombic efficiency for commercial lithium ion batteries.* Journal of Power Sources, 289(Supplement C):81 – 90, 2015.

[ZHE16] L. Zheng, L. Zhang, J. Zhu, G. Wang, and J. Jiang: *Co-estimation of state-of-charge, capacity and resistance for lithium-ion batteries based on a high-fidelity electrochemical model.* Applied Energy, 180(Supplement C):424 – 434, 2016.

[ZHO14] L. Zhong, C. Zhang, Y. He, and Z. Chen: *A method for the estimation of the battery pack state of charge based on in-pack cells uniformity analysis.* Applied Energy, 113(Supplement C):558 – 564, 2014.

[ZHO15] C. Zhong, Y. Deng, W. Hu, J. Qiao, L. Zhang, and J. Zhang: *A review of electrolyte materials and compositions for electrochemical supercapacitors.* Chemical Society Reviews, 44(21):7484–7539, 2015.

[ZHU11] Y. Zhu, S. Murali, M. D. Stoller, K. J. Ganesh, W. Cai, P. J. Ferreira, A. Pirkle, R. M. Wallace, K. A. Cychosz, M. Thommes, D. Su, E. A. Stach, and R. S. Ruoff: *Carbon-Based Supercapacitors Produced by Activation of Graphene.* Science, 332(6037):1537–1541, 2011.

[ZHU13] H. Zhu, Z. Jia, Y. Chen, N. Weadock, J. Wan, O. Vaaland, X. Han, T. Li, and L. Hu: *Tin Anode for Sodium-Ion Batteries Using Natural Wood Fiber as a Mechanical Buffer and Electrolyte Reservoir.* Nano Letters, 13(7):3093–3100, 2013.

[ZHU14] J. Zhu, W. Zu, G. Yang, and Q. Song: *A novel electrochemical supercapacitor based on $Li_4Ti_5O_{12}$ and $LiNi_{1/3}Co_{1/3}Mn_{1/3}O_2$.* Materials Letters, 115:237 – 240, 2014.

[ZHU15] G. Zhu, K. Wen, W. Lv, X. Zhou, Y. Liang, F. Yang, Z. Chen, M. Zou, J. Li, Y. Zhang, and W. He: *Materials insights into low-temperature performances of lithium-ion batteries.* Journal of Power Sources, 300(Supplement C):29 – 40, 2015.

[ZUB00] L. Zubieta and R. Bonert: *Characterization of double-layer capacitors for power electronics applications.* IEEE Transactions on Industry Applications, 36(1):199–205, 2000.

Nomenclature

Symbols

$\bar{j}_{Li}$	Lithium flow	$\mathrm{m\,s^{-1}}$
$\dot{m}$	Mass flow	$\mathrm{kg\,s^{-1}}$
$\dot{Q}$	Heat	W
$\dot{q}$	Volumetric heat generation	$\mathrm{W\,m^{-3}}$
α	Calendar ageing parameter	$\mathrm{year^{-1}}$
α	Transfer coefficient	–
β	Cycle ageing parameter	–
Δ	Variation	–
δ	Finite difference	–
ϵ	Material permitivity	–
η	Efficiency	p.u.
γ	Activity coefficient	–
λ	Thermal conductivity	$\mathrm{W\,K^{-1}m^{-1}}$
μ	Chemical potential	$\mathrm{J\,mol^{-1}}$
ν	General variable	–
ω	Frequency	$\mathrm{rad\,s^{-1}}$
Φ	Diameter	m
Ψ	Exponent of CPE	–
ρ	Density	$\mathrm{kg\,m^{-3}}$
τ	Time constant	s
θ	Electrode host material	–
θ	Parameter vector	–
ϑ	Taylor series remainder	–
ξ	General variable	–
A	Generic chemical species	–
a	Chemical activity	–
a	Constant fitting coefficient	–
B	Generic chemical species	–
b	Constant fitting coefficient	–
C	Battery capacity	Ah
C	Capacitance	F
c	Concentration of a species	–
$Cost$	Economic cost	€
cp	Specific heat	$\mathrm{J\,kg^{-1}K^{-1}}$
CPE	Constant phase element	Ω
CT	Charge throughtput	Ah
D	Fick's diffusion coefficient	$\mathrm{m^2\,s^{-1}}$
d	Double layer length	m
DOD	Depth of discharge	p.u.
E	Energy	J
F	Faraday constant	$\mathrm{C\,mol^{-1}}$
f	$F/(R \cdot T)$	$\mathrm{V^{-1}}$
f	General function	–
G	Gibbs free energy	J
g	Inflation	p.u.
H	Enthalpy	J
h	Convection coefficient	$\mathrm{W\,m^{-2}K^{-1}}$

I	Constant current	A	R	Thermal resistance	$\mathrm{K\,W^{-1}}$
i	Current	A	r	Radial coordinate	m
IR	Interest rate	p.u.	Rev	Annual revenue	€
J	Objective function	€	$RMSE$	Root mean square error	–
j	Imaginary unit	–	S	Surface area	$\mathrm{m^2}$
K	Fitting parameter	–	s	frequency variable	$\mathrm{s^{-1}}$
k	Reaction rate constant	$\mathrm{s^{-1}}$	SOC	Battery state of charge	p.u.
L	Width of a cell	m	SOH	Battery state of health	p.u.
l	Spatial coordinate	m	T	Temperature	K
$Life$	Lifetime of the battery	Years	t	Simmulation time	s
n	Generic number	–	V	Volume	$\mathrm{m^3}$
n	Number of exchanged electrons	–	v	Terminal voltage	V
NPV	Net Present Value	€	vel	Reaction speed	$\mathrm{mol\,l^{-1}\,s^{-1}}$
O	Oxidant chemical species	–	x	Molar fraction	–
P	Power	W	x	Spatial coordinate	m
PC	Price	€	Y	Admitance	S
Q	Equivalent full cycles	–	y	Spatial coordinate	m
q	Charge	C	Z	Impedance	Ω
R	Gas constant	$\mathrm{J\,mol^{-1}\,K^{-1}}$	z	Charge	–
R	Reductant chemical species	–	z	Spatial coordinate	m
R	Resistance	Ω	C	Thermal capacitance	$\mathrm{J\,K^{-1}}$

Subscripts

$_0$	Initial (with time) or independent (for fitting) value	$_{amb}$	Ambient
$_1$	First order dependency	$_{arc}$	Parallel connection of R_{ct} and CPE_{dl}
$_2$	Second order dependency	$_{av}$	Adiabatic vessel
$_\eta$	Polarization	$_A$	Activation energy
$_\psi$	Unoccupied host material	$_a$	Anode
$_\zeta$	Intercalated species	$_{bat}$	Battery
$_{act}$	Activation	$_{bulk}$	Relative to the volume of the electrolyte
$_{air}$	Air property	$_b$	Backward

$_{cell}$	Cell
$_{cent}$	Central
$_{ch}$	Charging
$_{cold}$	Cold side
$_{cond}$	Heat conduction
$_{conv}$	Convection
$_{conv}$	Power converter
$_{con}$	Consumption
$_{CPE}$	Constant phase element
$_{ct}$	Charge transfer process
$_{cyc}$	Average cycle value
$_{C}$	Capacitance
$_{c}$	Cathode
$_{c}$	Coulombic
$_{DC}$	Direct current
$_{dif}$	Differential
$_{dif}$	Diffusion phenomena
$_{dis}$	Discharging
$_{dl}$	Double layer
$_{DOD}$	Depth of discharge
$_{dyn}$	Dinamic phenomena
$_{d}$	Mid-term branch
$_{elec}$	Electricity
$_{elec}$	Electrode
$_{eq}$	Equilibrium state
$_{ev}$	Evacuated
$_{exp}$	Exponential
$_{ex}$	Exchange
$_{e}$	Energy
$_{fan}$	Cooling fan
$_{FC}$	Fuel cell
$_{F}$	Faradaic
$_{f}$	Forward
$_{gen}$	Generated
$_{grid}$	Electricity grid
$_{hot}$	Hot side
$_{INT}$	Non-ideal interactions between the Li ions and the electrode
$_{inv}$	Inverter
$_{I}$	Current
$_{i}$	Current
$_{i}$	Immediate branch
$_{i}$	Internal
$_{j}$	Different chemical species
$_{k}$	Counter
$_{leak}$	Leakage
$_{Li}$	Lithium
$_{loss}$	Power losses
$_{l}$	Counter
$_{l}$	Long-term branch
$_{max}$	Maximum
$_{mem}$	Membrane
$_{min}$	Minimum
$_{net}$	Net value
$_{N}$	Nominal
$_{O\&M}$	Opperation and maintenance
$_{OC}$	Open circuit
$_{ohm}$	Ohmic phenomena
$_{opt}$	Optimal value
$_{peak}$	Peak value
$_{PR}$	Plate resistor
$_{PV*}$	Photovoltaic with storage system
$_{PV}$	Photovoltaic
$_{p}$	Particle
$_{R_i}$	Internal resistance
$_{rea}$	Reaction

$_{ren}$	Renewable energy generation
$_{R}$	Rated value
$_{SC}$	Supercapacitor
$_{SEI}$	Solid–electrolyte interface
$_{sink}$	Heat sink
$_{SOC}$	State of charge
$_{SS}$	Storage system
$_{sur}$	Surface
$_{s}$	Series
$_{s}$	Solid
$_{Th}$	Thermal process
$_{tl}$	Transmission line
$_{T}$	Temperature
$_{u}$	Usable fraction
$_{V}$	Voltage
$_{wt}$	Wind tunnel
$_{x}$	Inflection point

Superscripts

*	Maximum allowed or available
$^{+}$	Unit positive charge
$^{-}$	Unit negative charge
^{0}	Reference conditions
$^{+\delta}$	Partial positive charge
$^{-\delta}$	Partial negative charge
^{avg}	Average value

Abbreviations

Φ	Diameter
AC	Alternating current
ACN	Acetonitryle
Ah-c	Amper-hour counting method
Asym.	Asymmetric
BMS	Battery management system
BSO	Battery Size Optimiser
CAGR	Compound Annual Growth Rate
CC	Constant current
CPE	Constant phase element
CV	Constant voltage
DC	Direct current
DMC	Dimethyl carbonate
DOD	Depth of discharge
DOE	U.S. Department of Energy
DPS	Digital signal processor
EC	Ethylene carbonate
EDO	Energy Dispatch Optimiser
EIS	Electrochemical Impedance Spectroscopy
EM	Electrochemical model
EMC	Ethylmethyl carbonate
EOL	End of life
ESS	Energy Storage System
FC	Fuel cell
FRA	Frequency Response Analyser
LCO	$LiCoO_2$
LFP	$LiFePO_4$
LFP	Lithium iron phosphate
LIB	Lithium ion battery
LiPO	Lithium–polymer

LMO	$LiMnO_2$ or $LiMn_2O_4$
LNO	$LiNiO_2$
LTO	$Li_4Ti_5O_{12}$
meas.	Measured variable
mod.	Modelled variable
MPP	Maximum Power Point
MPPT	Maximum Power Point Tracker
NCA	$LiNiCoAlO_2$
NMC	$LiNiMnCoO_2$
NMO	$Li(Ni_{0.5}Mn_{0.5})O_2$
NPV	Net present value
OC	Observer and controller method
PANI	Polyaniline
PC	Propylene carbonate
PEM	Proton exchange membrane
PV	Photovoltaic
PV+	Photovoltaic with storage system
RMSE	Root mean square error
SC	Supercapacitor
SEI	Solid–electrolyte interface
SHE	Standard hydrogen electrode
SOC	Battery state of charge
SOH	Battery state of health
Sym.	Symmetric
UPNA	Public University of Navarre

This thesis has been subsidised by the FPU Program of the Spanish Ministry of Education, Culture and Sport with the scholarship FPU 13/00542. Moreover, funding from the Spanish Ministry of Economy, Industry and Competitiveness has been used under the research and development projects DPI2016–80641–R, DPI2016–80642–R and DPI2013–42853–R and from the Government of Navarre under the research and development project "Integration of renewable energy in the electricity grid by means of advance energy storage systems".